Modelling and Analysis of Hydrogen Storage in Nanostructured Solids for Sustainable Energy Systems

Bimbo, Nuno

Award date:
2013

Awarding institution:
University of Bath

Modelling and Analysis of Hydrogen Storage in Nanostructured Solids for Sustainable Energy Systems

Submitted by Nuno Maria Marques dos Santos Bimbo
for the degree of Doctor of Philosophy

University of Bath
Department of Chemical Engineering
April 2013

Signed
Date

Abstract

As societies depart from current economic models which are built around affordable and easily accessible fossil fuels to energy systems increasingly based on the use of renewable energies, the need grows for a wide-scale clean and sustainable energy vector. Hydrogen fulfils most of the needed requirements, but implementation and large scale penetration, especially for mobile applications, is precluded by technical issues. Among these, arguably the most complex is how to safely, economically and efficiently store hydrogen. Storage in a porous material offers some attractive features, which include fast kinetics, reversibility and moderate energy penalties.

A new methodology to analyse hydrogen adsorption isotherms in microporous materials is presented in this thesis. The methodology is applied to hydrogen adsorption in different classes of high-surface area materials but could in principle be used for any supercritical fluid adsorbed onto a microporous material. To illustrate the application of the methodology, high-pressure hydrogen adsorption isotherms of four different materials were analysed, metal-organic frameworks MIL-101 and NOTT-101 and carbons AX-21 and TE7. The analysis extracts important information on the adsorptive capacities of the materials and compares them with conventional storage methods, which include compression, liquefaction and cryogenic compression. The methodology also aids in the calculation of the thermodynamics of adsorption, providing a more accurate calculation method than currently reported techniques, demonstrated with the calculation of the differential isosteric enthalpies for metal-organic framework NOTT-101.

NMR and INS are used in a novel way at the same operating conditions of sorption experiments to validate the findings of the analysis. Both methods provide a qualitative validation for the analysis. Remarkably, the INS reveals that the adsorbed hydrogen in TE7 is in a solid-like state. GCMC simulations were also used to compare with the application and findings of the methodology, using silicalite-1 as a test material.

Preface

I have long waited to write these lines – it is done and soon will be submitted! It was written in land and air, in three different countries and I am very happy on how it turned out.

I'm writing this preface because I wanted to attach something personal to this thesis, which meant so much for me in the last three years and I wanted to document and leave in writing what I felt about my time here. I can say that I was very happy in Bath and coming here to do a PhD was probably the best decision I have ever made. This time in Bath was so enjoyable for many reasons, but especially because of my work – it is excellent when you are working on something you thoroughly enjoy and believe, with hard-working, intelligent people who support and encourage you and on something you think will bring about the greater good. Sir Bertrand Russell says that all the conditions of happiness are realized in the man of science, since he has an activity which utilizes his abilities to the full and achieves results which appear important not only to himself but to the general public, and I guess I could not agree more.

Even though this journey was not always great and there were ups and downs, it was a labour of love and I am really happy with the outcome. I think the project was, from the very beginning, an excellent fit and it turned out an extraordinary experience for me to complete this PhD. There are two people who I would especially like to acknowledge - I am obviously forever indebted to my academic supervisor, Dr Tim Mays, who accepted me as his student and always provided me with the necessary support. He was truly outstanding on every step of the way and I am very glad that things worked out this way. The other person I would like to especially acknowledge is Dr Valeska Ting, who was a Postdoctoral Assistant and is now a Prize Fellow in the University. I do not think it would have been possible to write this thesis without their contribution. Even more, they served as outstanding mentors and they taught me (I hope) how to become a good researcher.

I am also grateful to my friends, especially to Alan, Alejandro Iain, Simon and Pete, which made my time in Bath fun and enjoyable. Life is not only work and I will always have very fond memories of Bath.

My family was also, as always, extremely encouraging and supportive and I cannot wait to see them so that we can celebrate. Finally, Ana Maria, my angel, who has been extremely supportive and has given me everything in these last months. I feel that this thesis is also hers, for all the support she has given me.

I dedicate this thesis to my father Luis, my mother Isabel, my brothers Luis and João and to my lovely Ana Maria.

Bath, April 2013

Table of Contents

Additional Information (in electronic format)

- Additional Information A

Additional Background – Energy storage and uses of hydrogen

- Additional Information B

The Levenberg-Marquardt algorithm

- Additional Information C

The van't Hoff relation

- Additional Information D

Filling factor

- Additional Information E

NMR experimental setup, analysis and deconvolution

- Additional Information F

INS spectra at 4 and 100 K and 0.016 MPa

- Additional Information G

Technical specification sheet for silicalite-1

List of figures

List of tables

Dissemination

Journal publications

The author has participated in five manuscripts, three of which are currently published (1, 2 and 3), one is accepted for publication and available online (4) and one is to be submitted for publication (5). The journal publications 1 and 3 constitute the main results presented in Chapter 4 (Results and Analysis), while publication 5 are the INS results presented in Chapter 5 (Validation of the Methodology Using Experimental Techniques). The author contributed to publication 2, which reported the characterisation of TE7 and standardisation of experimental sorption techniques and to publication 4, which dealt with the analysis and application of the constant density of adsorbate model presented in Chapter 5 to a variety of materials.

1. Bimbo, N.; Ting, V.P.; Hruzewicz-Kolodziejczyk, A. and Mays, T.J. (2011). Analysis of hydrogen storage in nanoporous materials for low carbon energy applications, *Faraday Discussions*, 151, 59-74

2. Hruzewicz-Kolodziejczyk, A. ; Ting, V.P. ; Bimbo, N. and Mays, T.J. (2012). Improving comparability of hydrogen storage capacities of nanoporous materials, *International Journal of Hydrogen Energy*, 37, 2728-2736

3. Sharpe, E. J.; Bimbo, N; Ting, V. P.; Burrows, A.D.; Jiang, D. and Mays, T.J. (2013) Supercritical hydrogen adsorption in nanostructured solids with hydrogen density variation in pores. *Adsorption – Journal of the International Adsorption Society*, 19, 2-4, 643-652

4. Bimbo, N; Ting, V.P.; Sharpe, J.E. and Mays, T.J. (2012) Analysis of optimal conditions for adsorptive hydrogen storage in microporous solids, *Colloids and Surfaces A: Physicochemical and Engineering Aspects* (in press) doi:10.1016/j.colsurfa.2012.11.008

5. Ting, V.P.; Ramirez-Cuesta, A.J.; Bimbo, N.; Sharpe, J.E. and Mays, T.J. (2013) Direct evidence for solid-like hydrogen adsorbed in microporous carbon at supercritical temperatures, *Energy and Environmental Science* (to be submitted)

Conference and workshop presentations

The author has participated in the following conference and workshop presentations, which reported most or some of the work presented in this thesis. The underline indicates the presenter(s) and they are in chronological order starting from the oldest.

1. University of Bath Meeting of Minds, June 2010, Bath, UK
   Sustainability, Hydrogen and Nanotechnology - How new nanoengineered materials can make the hydrogen economy possible
   N. Bimbo

2. American Institute of Chemical Engineers (AIChe) Annual Meeting, Salt Lake City, UT, USA, November 2010
   Improving Comparability of Hydrogen Storage Capacities of Nanoporous Materials
   V.P.Ting, N.Bimbo, A. Neczaj-Hruzewicz, L. Fisher, S. Rigby, A.D. Burrows and T.J. Mays

3. University of Bath Faculty of Engineering and Design Research Students Showcase, Bath, May 2011
   A semi-empirical analysis of hydrogen storage in new nanoporous materials
   N. Bimbo

4. 3rd UK-SHEC Researchers Workshop, Bath, September 2011
   Hydrogen's next top model – modelling hydrogen storage in porous materials
   N. Bimbo

5. Bath Royal Literary and Scientific Institution Speaking of Research, Bath, October 2011
   There is plenty of room at the bottom – Nanoengineered materials for hydrogen storage
   V.P Ting, N. Bimbo, A. Hruzewicz-Kołodziejczyk

6. 6th International Workshop Characterization of Porous Materials, Delray Beach, Florida, USA, April-May 2012
   Novel evaluation of nanoporous hydrogen storage materials using adsorption, nuclear magnetic resonance and inelastic neutron scattering
   N. Bimbo, V.P.Ting, R.J.Anderson, A.J. Ramirez-Cuesta, J. Sharpe, A. Kleinhammes, Y. Wu and T.J. Mays

7. Institute of Chemical Engineers(IChemE) Fluid Separations Special Interest Group Research Event "What's new in fluid separations?", Air Products, Basingstoke, UK May 2012
   Analysis of hydrogen storage through adsorption in high-surface area materials
   N. Bimbo (invited talk)

8. ISSHAC-8, 8th International Symposium on Effects of Surface Heterogeneity in Adsorption and Catalysis on Solids, Krakow, Poland, August 2012
   Hetereogeneity of supercritical hydrogen adsorption in nanostructured solids
   J. E. Sharpe, V.P. Ting, N.Bimbo, A.D. Burrows, D. Jiang, A.Godula-Jopek and T.J.Mays

Poster presentations

The author has participated in the following poster presentations, again in chronological order, with the underline indicating the presenter(s).

1. 10th International Materials Chemistry Conference, Manchester, UK, July 2011
   High-pressure experimental data collection, analysis and modelling of hydrogen storage on nanoporous materials
   N. Bimbo, A. Hruzewicz-Kolodziejczyk, V. P. Ting, T. J. Mays
2. 6th International Workshop Characterization of Porous Materials, Delray Beach, Florida, USA, April-May 2012
   Metal-organic framework materials for hydrogen storage in aerospace applications
   I. Y. Ahmet, J.E. Sharpe, Va.P. Ting, N. M. Bimbo, A. D. Burrows, A. Godula-Jopek and T. J. Mays

Accepted abstracts

At the time of writing, the author has the following accepted abstracts, as posters and oral presentations.

Poster presentation:

1. ChemEngDayUK 2013, Imperial College, London, March 2013
   Hydrogen Energy Research in the Department of Chemical Engineering, University of Bath, UK
   N. Bimbo, S. Owens, J. Sharpe, A. Noguera-Diaz, A. Rushworth, M. Smith, M. Berry, P. Hayes and T. J. Mays

2. FOA11 - 11th International Symposium on the Fundamentals of Adsorption, Baltimore, MD, USA, May 2013
   A New Generalised Model for Supercritical Sorption in Nanoporous Materials
   J. E. Sharpe, N. Bimbo, A. José Noguera-Diaz, V. P. Ting and T. J. Mays

Oral presentations:

1. FOA11 - 11th International Symposium on the Fundamentals of Adsorption, Baltimore, MD, USA, May 2013
   Isosteric Enthalpies for Hydrogen Adsorbed on Nanoporous Materials at High Pressures
   N. Bimbo, J.E. Sharpe, V. P.Ting and T. J. Mays

Awards:

The author has received the following award during the course of his Doctorate.

1. EPSRC Project Studentship associated with UK-SHEC (UK Sustainable Hydrogen Energy Consortium)

2. University of Bath's Faculty of Engineering and Design Research Students Showcase 2011 – 2nd prize for best presentation

3. Royal Academy of Engineering International Travel Grant to attend the AIChE Annual Meeting in Salt Lake City, UT, USA (£600 award)

4. Royal Society of Chemistry Conference Bursary to attend Faraday Discussions 151 – Hydrogen Storage Materials (£150 award)

5. Royal Society of Chemistry Conference Bursary for the 10th International Materials Chemistry Conference (£150 award)

6. Selected as a member of the 2nd cohort of the University of Bath's Faculty of Engineering and Design Fellowship Academy

7. IChemE Fluid Separation Special Interest Group – Conference and Short Course Grants for the attendance of the 6th International Workshop on Characterisation of Porous Materials in Delray Beach, FL, USA (£500 award)

8. IChemE Fluid Separations Special Interest Group Research Event "What's new in Fluid Separations", Basingstoke, UK – 3rd prize for best presentation

Acknowledgements

Many people participated in the work presented here with their knowledge, insight and hard work and it would simply not have been possible to write this thesis without their contribution. I am most grateful for all the people that contributed and I hope I have included everyone who has helped.

My most grateful thanks go to two people – my academic supervisor Dr Tim Mays and collaborator and former postdoctoral research assistant in our research group (now a University of Bath Prize Fellow) Dr Valeska Ting. Tim was an extraordinary supervisor, who always had patience and guided me through all the stages of a PhD. He always had time and patience for my questions and served as an outstanding mentor. I will forever be indebted to him for accepting me as his student.

Valeska was also outstanding in her help and contribution. Like Tim, much of the work presented in this thesis is also hers, since she contributed in experimental acquisition of data, analysis, ideas and discussions. She provided assistance every step of the way and always had time to read and comment on my work. I am truly indebted to both of them for their work and patience and for teaching me how to do science.

I am also very thankful to the remaining members of my research group – Anna, Jess, Simon and Antonio – which also contributed and helped me with the work presented here. Anna was very helpful throughout my studies and provided help and encouragement when needed. Jess was very helpful in discussions concerning modelling and on the exchange of ideas. Antonio and Andrew were very helpful in the later stages of the PhD, especially the silicalite-1 studies.

I would also like to help the technicians team in Chemical Engineering, especially Fernando Acosta and Robert Brain, who were always ready to help. Dr Anne Dailly generously provided the sorption data for NOTT-101. Thanks also to Luke Keenan, who helped with MOF synthesis (results not presented in this thesis) and to Tom Shapley, for providing assistance with the use of Aquila (the High Performance Computer in the University of Bath). Thanks also to Linjiang Chen and Dr Tina

Düren in the University of Edinburgh for assistance with the MUSIC code and to Prof Randall Snurr from Northwestern University, USA, for providing the code. Prof Stephen Parker from the Department of Chemistry of the University of Bath was also very helpful with discussions concerning molecular simulations.

Dr Timmy Ramirez-Cuesta at ISIS, RAL was very helpful with the INS experiment, as was Dr Robert Anderson, now at the University of Hawaii, with the NMR data.

The TE7 carbon beads were provided by MAST Carbon (MAST Carbon International, UK) and the AX-21 was acquired from Anderson Company (Anderson Development Company, MI, USA). The material is available nowadays under licence by Kansai Coke and Chemicals (Kansai Coke and Chemicals Co. Amagasaki, Japan) under the commercial name Maxsorb. MIL-101 was synthesised in the Department of Chemistry of the University of Bath by Dr Dongmei Jiang and Jessica Sharpe under the guidance of Dr Andrew Burrows.

Sorption data acquired in Bath for the TE7 carbon beads, AX-21 and MIL-101 was done by Dr Valeska Ting and Anna Hruzewicz-Kołodwijeczyk, with characterisation of the TE7 - BET specific surface area, pore size distribution, helium pycnometry measurements and thermal gravimetric analysis - done by Anna Hruzewicz-Kołodwijeczyk. AX-21 and MIL-101 were characterised – BET specific surface area and helium pycnometry measurements - by Dr Valeska Ting.

Data for the NOTT-101 was provided by Dr Anne Dailly from the Chemical and Environmental Sciences Laboratory, General Motors Corporation, Warren, MI, 48090, USA.

NMR spectra experiments for the TE7 carbon beads were done at the University of North Carolina at Chapel Hill by Dr Robert J Anderson (now at Department of Medicine, John A. Burns School of Medicine, University of Hawai'i), under the guidance of Prof Alfred Kleinhammes and Prof Yue Wu. The data of the NMR spectra of the PEEK carbons and the AX-21 were provided by Dr Robert J Anderson and Prof Alfred Kleinhammes. The PEEK carbon high-pressure hydrogen excess isotherms were tested in the University of Bath by Dr Valeska Ting.

Inelastic neutron scattering experiments were done at STFC Rutherford Appleton Laboratory with help from instrument scientist Dr Anibal J (Timmy) Ramirez-Cuesta. User support was provided by Chris Goodway and Mark Kibble. The experiment was designed by Dr Valeska Ting and Dr Anibal J Ramirez-Cuesta. Data collection was done by Dr Valeska Ting, Jessica Sharpe and the author. The experiment was allocated beam time under proposal RB1210041.

A sample of silicalite-1 was provided by Zeochem ® (Zeochem AG, Uetikon am See, Switzerland). Computational simulations were done by the author in Aquila, the high-performance computing system of the University of Bath. The MUSIC code was provided by Prof Randall Snurr at Northwestern University, Evanston, IL, USA.

Silicalite high-pressure sorption results were performed by the author, Antonio Noguera, Andrew Physick and Dr Valeska Ting. Silicalite BET specific surface area was done by Andrew Physick, Dr Valeska Ting and Antonio Noguera.

Finally, I would like to thank the people that read parts or the whole of the thesis and provided feedback and comments. So many thanks to Dr Tim Mays, Dr Valeska Ting, Andrew Rushworth, my hoursemates Cat Clarke and Alan Carroll, Vânia Moreira João, Luis and Ana Maria.

Nomenclature

Acronyms

AAO-TC	Anodic-Aluminium Oxide Templated Carbons
AFC	Alkaline Fuel Cell
BET	Brunauer-Emmett-Teller
BDC	Benzene dicarboxylate
BTB	Benzene tribenzoate
BTC	Benzene tricarboxylate
CAES	Compressed Air Energy Storage
CCDC	Cambridge Crystallographic Data Centre
CDC	Carbide-Derived Carbons
CIO	Carbon Inverse Opals
CMP	Conjugated Microporous Polymer
COF	Covalent Organic Frameworks
DA	Dubinin-Astakhov
DMFC	Direct Methanol Fuel Cell
DOE	Department of Energy (as in USA DOE)
DR	Dubinin-Radushkevich
EOS	Equation of State
ESRF	European Synchrotron Radiation Facility
FCV	Flow Control Valve
FH	Feynman-Hibbs
FID	Free Induction Decay
GCMC	Grand Canonical Monte Carlo
GDP	Gross Domestic Product
GM	General Motors
GSE	Gibbs Surface Excess
HCP	Hypercrosslinked Polymer
HDI	Human Development Index
HIFAR	High Flux Australian Reactor
ILL	Institute Laue-Langevin

IMF	International Monetary Fund
INS	Inelastic Neutron Scattering
IPCC	Intergovernmental Panel on Climate Change
IPNS	Intense Pulsed Neutron Source (Argonne)
IUPAC	International Union of Pure and Applied Chemistry
ITER	International Thermonuclear Experimental Reactor
KENS	Neutron Scattering Facility (Japan)
LJ	Lennard-Jones
LNG	Liquefied Natural Gas
MCFC	Molten Carbonate Fuel Cells
MFI	Morderite Inverted Framework
MIL	Matérial Institut Lavoisier
MOF	Metal-Organic Frameworks
MUSIC	Multi-Purpose Simulation Code
MWCNT	Multi-Walled Carbon Nanotube
NIST	National Institute of Standards and Technology
NMR	Nuclear Magnetic Resonance
OECD	Organisation for Economic Co-operation and Development
OMC	Ordered Mesoporous Carbons
PAF	Porous Aromatic Frameworks
PAFC	Phosphoric Acid Fuel Cells
PCV	Pressure Control Valve
PEEK	Poly Ether Ether Ketone
PEMFC	Proton-Exchange Membrane Fuel Cells
PHES	Pumped Hydro Energy Storage
PIM	Polymer of Intrinsic Microporosity
PPN	Porous Polymer Network
PSE	Pressure Safety Element
PSV	Pressure Sustaining Valve
PV	Photo-Voltaic
RAL	Rutherford Appleton Laboratory (UK)
SINQ	Paul Scherrer Institute Spallation Neutron Source (Switzerland)
SNS	Spallation Neutron Source (Oak Ridge)
SOFC	Solid Oxide Fuel Cells

SRSR	Sum of the Root Squared Residuals
STP	Standard Pressure and Temperature
SWCNT	Single Walled Carbon Nanotube
TC	Templated Carbons
TCBPB	Tris[40-carboxy(1,10-biphenyl)-4-yl] benzene
TMS	Tetramethylsilane [$Si(CH_3)_4$]
UK	United Kingdom
UN	United Nations
USA	United States of America
ZIF	Zeolitic Imidazolate Framework
ZSM-5	Zeolite Socony Mobil - 5
ZTC	Zeolite Templated Carbons

Symbols

A_P	J mol^{-1}	Polanyi's adsorption potential
A_n	-	Parameters for the rational function fit
a_H	J mol^{-1}	Helmholtz energy
b	MPa^{-1}	Affinity constant
b_0	MPa^{-1}	Entropic factor in the van't Hoff relation
c	-	Heterogeneity parameter
D_i	-	Regression coefficient for the Leachman's EOS
d_i	-	Regression coefficient for the Leachman's EOS
E	J	Energy
E_i	J	Energy of state *i*
f	-	Filling factor
k	-	Parameter for the pseudo-vapour pressure relation
k_H	MPa^{-1}	Henry's constant
M	g mol^{-1}	Molar mass
m	-	Surface heterogeneity for DA and DR equation
m_A	wt. %	Absolute amount
m_{ads}	g	Mass of adsorbate
m_E	wt. %	Excess amount
m^0_{ads}	g	Reference dry mass of adsorbent

m_{H_2}	g	Mass of hydrogen
m_P	wt. %	Total amount
m_S	g	Mass of solid adsorbent
n	-	Number of points
N	-	Number of molecules
n_a^{max}	wt. %	Limiting absolute capacity
n_b	wt. %	Bulk amount
n_e	wt. %	Excess amount adsorbed
n_e^{max}	wt. %	Excess maximum amount
P	MPa	Pressure
P_{BE}	MPa	Pressure at break-even point
P_e^0	MPa	Pressure when excess quantity is zero
P_e^{max}	MPa	Pressure when excess reaches maximum
p_i	-	Regression coefficient for the Leachman's EOS
P_0	MPa	Vapour pressure
Q^0_{st}	J mol^{-1}	Characteristic energy of adsorption
R^2	-	Coefficient of correlation
r	Å	Intermolecular separation distance
T	K	Temperature
t_i	-	Regression coefficient for the Leachman's EOS
$u_{FH}(r)$	J	Feynman-Hibbs effective potential as function of r
$u_{LJ}(r)$	J	Lennard-Jones potential as a function of r
V	m^3	Volume
V_A	m^3	Volume of adsorbed phase
V_B	m^3	Volume of bulk gas
V_C	m^3	Volume of container
V_D	m^3	Displaced volume
V_P	cm^3 g^{-1}	Volume of the pore
v_a	m^3 mol^{-1}	Molar volume of state a
v_b	m^3 mol^{-1}	Molar volume of state b
wt. %	$\frac{m(H_2)}{m^0_{ads}} \times 100$	Sample-specific weight percent
y_i	-	Regression coefficient for the Leachman's EOS
x_m	wt. %	Absolute calculated with methodology (for SRSR)

x_n	wt. %	Absolute calculated with NMR (for SRSR)
Z	-	Compressibility factor
Z_A	Å	Potential field of the solid
$Z(r)$	Å	Distance to solid surface
$Z(t)$	-	Partition function
∇^2	-	Laplace operator

Greek symbols

α_H	-	Reduced Helmholtz energy
α_H^0	-	Ideal gas contribution to reduced Helmholtz energy
α_H^r	-	Residual contribution to reduced Helmholtz energy
α_E	J mol^{-1}	Enthalpic factor (for DA and DR)
β_E	J mol^{-1} K^{-1}	Entropic factor (for DA and DR)
β_i	-	Regression coefficient for the Leachman's EOS
β_T	J^{-1} ($1/k_bT$)	Inverse of Boltzmann's constant times temperature
δ	-	Reduced density
Δh_{ab}	J mol^{-1}	Change in enthalpy from state *a* to state *b*
$\Delta \upsilon_{ab}$	mol cm^{-3}	Change in molar volume from state *a* to state *b*
ε	J	Potential well depth of interaction
θ	-	Fractional filling
μ	J mol^{-1}	Chemical potential
μ_m	-	Reduced mass
ρ	Kg m^{-3}	Density
$\overline{\rho_A}$	Kg m^{-3}	Average adsorbed density
$\overline{\rho_A}^{\lim}$	Kg m^{-3}	Limiting average adsorbed density
ρ_A	Kg m^{-3}	Density of adsorbate
ρ_B	Kg m^{-3}	Density of the bulk phase
ρ_c	Kg m^{-3}	Density at critical point
ρ_s	Kg m^{-3}	Density of the solid
σ	Å	Collision diameter
τ	-	Reduced temperature
υ_A	cm^3 g^{-1}	Specific pore volume

χ^2_{red}	-	Reduced chi-square

Physical constants and conversion factors

eV	J	= 1.602×10^{-19}	electron-Volt
h	J s	= 6.626×10^{-34}	Planck constant
$\hbar$	J s	= 1.055×10^{-34}	Reduced Planck constant
k_b	J K^{-1}	= 1.381×10^{-23}	Boltzmann constant
M (H_2)	g mol^{-1}	= 2.016	Molar mass of hydrogen
N_A	mol^{-1}	= 6.022×10^{23}	Avogadro's constant
R	J mol^{-1} K^{-1}	= 8.314	Molar gas constant
π	-	= 3.1415	pi

Declaration of authorship

The author was funded by an Engineering and Physical Sciences Research Council (EPSRC) Project Studentship from the SUPERGEN United Kingdom Sustainable Hydrogen Energy Consortium, grant reference EP/J016454/1.

The worked presented in this thesis, except where otherwise noted, was done by the author with supervision and guidance from his academic supervisor, Dr Timothy J Mays, Senior Lecturer of Chemical and Materials Engineering in the Department of Chemical Engineering of the University of Bath.

Most of the work reported in this thesis has been published in journal articles and presented at conferences, as indicated in the dissemination section. Copyrighted material in this thesis is identified and used with permission from the copyright owner.

Theories are nets cast to catch what we call "the world": to rationalise, to explain and to master it. We endeavour to make the mesh ever finer and finer"

Sir Karl R. Popper *in* The Logic of Scientific Discovery

Chapter One

Introduction

1. Introduction

1.1. Scope and motivation

A sufficient, secure and affordable supply of energy is one of the major problems that humanity faces on the turn of the 21st century, along with the provision of food, access to clean, drinkable water and appropriate living spaces. While fossil fuels have fuelled progress since the Industrial Revolution, they are becoming scarcer and more difficult to explore, which will inevitably impact upon their price. Proven fossil fuel reserves are likely to last for at least another century, but problems associated with their use, the most important of which is climate change due to greenhouse gas emissions, have prompted the study of low-carbon alternative sources of energy. Developed economies are currently facing a significant challenge, since they have to depart from their current energy system, which is based on energy conversion from fossil fuels and underpin their economies on a low-carbon, sustainable energy system.

Due to its abundance on the Earth's crust and the fact that it does not release any harmful emissions, hydrogen is being considered as a possible wide-scale energy vector, and would fit ideally within this low-carbon sustainable energy system. There are still major technical and scientific hurdles to overcome, arguably the most important of these is how to efficiently, economically and securely store hydrogen for later use. Storage of hydrogen is an area that has received considerable attention in the last decade and has been the driver for many interesting scientific developments. An area that has known substantial development is the synthesis and study of new porous materials for gas storage and separation, with newly synthesised materials such as metal-organic frameworks garnering widespread attention from the scientific community in recent years. The number of different porous materials grows by the day and many of these materials have been identified as promising hydrogen storage materials. However, operating conditions are still stringent, and due to hydrogen's physical properties, significant storage in a porous material only occurs at moderate pressures (above 0.1 MPa) and cryogenic temperatures (usually 77 K).

This thesis concerns the modelling and analysis of hydrogen storage in nanoporous materials for sustainable, low-carbon energy systems. It proposes a simple methodology to analyse high-pressure hydrogen isotherms, estimating the total quantity of adsorbate within a porous material. It could, in principle, be applied to any high-pressure adsorption of any fluid above its critical point. Based on this methodology, varied temperature isotherms of a range of distinct materials are analysed, highlighting, among other parameters, the maximum capacities, density within the pores and comparison with alternative storage techniques. To improve the understanding of the energetics of hydrogen adsorption, the isosteric enthalpies of adsorption are also calculated for the materials, using a variety of different methods. Finally, the methodology to estimate total quantities is assessed using alternative experimental techniques (nuclear magnetic resonance and inelastic neutron scattering) and grand canonical Monte Carlo simulations for adsorbed phases.

1.2. Structure of thesis

This thesis is divided into eight chapters, including this Introduction (Chapter 1). Chapter 2 introduces the background and motivation for the work. Rather than an extensive and lengthy review of the subject, it aims to cover key aspects that lead to the main topic of the thesis, which include energy, sustainability, the use of hydrogen as an energy vector, storage of hydrogen and analysis of sorption isotherms. This is done using the most recent references from authoritative sources, which give context for the work presented in the following pages. Chapter 3 presents the materials and methods used in the thesis, including the proposed model and methodology for the analysis of sorption isotherms, providing the theoretical background for it, as well as the experimental methods used for obtaining the sorption isotherms. Chapter 4 is the main results section of the thesis, including the representative datasets of different hydrogen storage materials that were analysed and tested. The analysis includes the application of the model using different IUPAC type I equations, the analysis of the parameters from the fitting, comparison with alternative storage methods and an investigation on the energetics of adsorption, calculating the differential isosteric enthalpies of adsorption by applying both the methodology proposed in this thesis and methods reported in the literature. In Chapter 5, the methodology is assessed and

validated using alternative experimental techniques. The experimental techniques used are nuclear magnetic resonance and inelastic neutron scattering and a comparison between the observed results from both methods and the models is put forth. Chapter 6 compares the methodology with computational simulations, namely grand canonical Monte Carlo simulations for adsorbed phases. A study using different assumptions for the simulations and the experimental results and applied methodology is presented for a sample of silicalite-1. Chapter 7 discusses the main results and observations reported in this thesis. Chapter 8 presents concluding remarks and suggests directions for further work.

Chapter Two

Background

2. Background

2.1. Introduction

This chapter will introduce and review in detail the motivation and background for the thesis. The chapter starts with a general review on energy and energy technologies. Problems associated with energy conversion from fossil fuel sources are highlighted, notably anthropogenic climate change caused by greenhouse gas emissions. New energy technologies that address these problems are discussed. The use of hydrogen as a wide-scale energy vector, as part of a future sustainable energy system is introduced. The element, current applications, and clean production, storage, distribution and end-use are all reviewed. A section is dedicated to hydrogen storage and the range of techniques in use or being developed for efficient storage. Emphasis is put on storing hydrogen in porous materials, the subject of this thesis, introducing some of the different classes of materials used in adsorptive storage. The chapter concludes with the aims and objectives of the thesis.

2.2. Energy technologies

Current global trends in energy supply and consumption are patently unsustainable – environmentally, economically, socially (...) What is needed is nothing short of an energy revolution.

Executive Summary, World Energy Outlook 2008

Energy technologies are the cornerstone of development in modern civilization. Contemporary societies have evolved mostly relying on energy conversion from fossil fuels, which has prompted economic, social and environmental problems, with the most notorious being anthropogenic climate change. The need for energy in upcoming decades due to population and economic growth will leave the world with an energy problem, since more energy will be needed to meet the continuous demand while fossil fuels have to be phased out due to their inherent problems. As the above quote, from the World Energy Outlook states, the world requires nothing short of an energy

revolution, as the need grows to change the current energy system to a cleaner and more sustainable one. Future energy landscapes will surely continue to be shaped by the use of fossil fuels but the share of renewable energies will continue to grow. This demands wide-scale energy storage, to balance the intermittency of renewable energies and demand fluctuations observed in the electric grid and for fuel applications in the transport sector. The transport sector will necessarily undergo drastic changes, since emissions will have to be abated. This will prompt the use of alternative power sources for mobile applications, a sector which is responsible for around a quarter of overall harmful atmospheric gas emissions.

2.2.1. Energy and development

Energy is essential for human life, since it is vital for supplying our most basic needs, including provision of food, shelter, heating and transport. Modern civilisation has come to depend on energy for everything and it is difficult to think of one single activity that does not involve the use of energy. Whenever new forms of energy conversion were mastered, a massive step forward in terms of progress ensued. Foremost examples of this are the discovery of fire, the use of the steam engine that started the industrial revolution or the splitting of the atom and the nuclear age. These are fine illustrations that show how critical the efficient exploitation of new sources of energy is to mankind and how it can lead to overall improvement in well-being and quality of life.

In developed countries[1], the provision of safe and secure energy is a mandate of the government and a crucial part of government policy. Unfortunately, access to safe and secure energy is not the case throughout the world and many countries still lack this provision. In developing countries, some of them rich in energy resources, easy access

[1] According to the UN, there is no established convention for the definition of developed and developing countries. There are many different classifications (UN, IMF, World Bank) for what a developed country is and which countries are developed. Due to the nature of energy statistics, the classification adopted in this thesis is that OECD countries will be considered developed countries and non-OECD countries will be considered developing countries. OECD stands for Organisation for Economic Co-Operation and Development and it is formed by 34 countries, including all of Western and Central Europe, all of North America, Poland, Estonia, Turkey, Israel, Chile, New Zealand, Australia, Japan and South Korea.

to energy is still amiss and most people rely on arcane methods of energy exploration to feed and heat themselves. This contrasts with what is observed in other parts of the world, where there is an extremely high per capita consumption of energy. Current methods of energy conversion and consumption have shaped our economic model since, in developed countries, access to non-expensive sources of energy made possible a number of luxuries. The list is endless, but the affordability of energy made possible the relatively inexpensive transport of people and goods, which form the basis for the centralisation of manufacturing, production and agriculture. Economies of scale work in such a way that it is more economical nowadays to produce materials, food, raw and fine chemicals and other products in far-away countries and then import them to where they will be consumed. This is all based on the presumption of affordable energy, which made a strong imprint on our current economic model.

One instant observation upon the analysis of energy technologies and usage is how well energy consumption correlates with the status of development in a country. The link between energy use, economic expansion and general well-being is evident and can be easily observed by noting the energy demand from countries with a high Gross Domestic Product (GDP) or that score highly in the UN's Human Development Index (HDI) and their energy consumption. The HDI is a composite classification, ranging from 0 to 1, created by the United Nations, which scores the level of development in a country by taking into account a number of different measures, which range from infant mortality to per capita wealth [2]. When analysing energy consumption, we find on that one end of the list high GDPs, high ratings on HDI and high energy consumption are present in countries such as the United States of America, Norway, Iceland, Japan and most of the developed countries. On the other end of the list, low GDPs, low scores on HDI and low energy consumption are present in countries like Mozambique, Nepal or Haiti. Regardless of how this connection is framed, it seems obvious to conclude that, as countries develop and their economies grow, they will consume more energy.

Table 2.1 – HDI ranking and score and per capita GDP and energy consumption for some countries. Data taken from the World Bank Indicators and the United Nations Development Programme [2].

	HDI [2] (2011)		GDP per capita Current US dollars [3]	Per capita Energy consumption kg oil equivalent (2010) [3]
	Ranking	Score	(2011)	
Norway	1	0.943	98,102	6,637
USA	4	0.910	48,112	7,164
United Kingdom	28	0.863	39,038	3,254
Nepal	157	0.458	619	341
Haiti	158	0.454	726	229
Eritrea	177	0.349	482	142
Mozambique	184	0.322	531	436

Table 2.1 shows per capita GDPs from 2011 in current US dollars, the per capita energy consumption in 2010 (in kg oil equivalent) and the HDI ranking and score on a number of countries from 2011. If developing countries are to reach the standard of living of OECD countries, their energy consumption is very likely to increase, as observed for all the countries throughout their history.

Seeing how well energy consumption correlates with economic development, it is reasonable to expect that more economic development will boost energy demand. Economic growth is by far the most important factor for energy demand [4]. Even with the recent global economic downturn, it is very likely that the world's GDP will grow significantly in upcoming decades, and this economic growth will most likely come from developing countries. The world's GDP is expected to increase significantly, and it is currently estimated (as of 31st October 2012, according to the World Bank statistics) at 70 trillion US dollars at current prices. This will grow, according to different sources, at various rates throughout the world, and according to the 2010 World Energy Outlook , the 2008-2035 compound average annual growth rate of real GDP for the world will be 3.2 %, with 1.8 % in OECD countries and 4.6 % in non-OECD countries. The highest economic development for the same period according to the same source will come from India (6.4 % of real GDP growth) and China (5.4 % of real GDP growth). Exxon-Mobil puts OECD GDP growth to 2040 at an annual rate of 2 %, while non-OECD countries will grow much faster, at 4.5 % a year [4], with similar figures being reported by the International Energy

Outlook [6] (compiled by the Department of Energy of the United States of America – US DOE), with OECD average annual GDP growth at 2.1 % between 2006 and 2035 and non-OECD average annual GDP growth at 4.6 %, expressed in purchasing power parity. As populations in developing countries escape poverty, growth will mostly come from non-OECD countries, with developed economies growing more modestly.

Alongside economic growth, another key factor to consider for future energy demand is the expected population growth until the mid-21st century. According to estimates, there will be around 9 billion people living on the Earth by 2050. The World Population Prospects report [7] issued by the United Nations Population Division sets population, as of July 2011, at 6.97 billion people, with a predicted 9.3 billion people by 2050. These estimates have been highlighted and supported by other reports, including the World Energy Outlook and the International Energy Outlook, with the latter predicting a world population of 8.5 billion people by 2035 [6]. According to the UN, World Bank and the United States Department of Energy statistics, the continent that will grow the fastest in population is Africa, with growth ranging from 1.7 to 2.0 % a year in the different reports [6, 7]. Expected economic growth for developing countries and their consequential increase in energy use will put a massive strain on energy demand in forthcoming years. Population is expected to rise to 9 billion people until it plateaus, due to an expected decrease in fertility rates [7] and economic growth is predicted to boom in several developing regions of the world. Developing countries are therefore forecast to meet developed countries' patterns of energy consumption. This growth in energy demand is likely to be met using a variety of energy sources. However, as has been the case since the Industrial Revolution, energy converted from fossil fuels is expected to play a major part in meeting the upcoming demand for the next decades. Referring again to the epigraph, the current and predicted trends for energy consumption are economically, socially and environmentally unsustainable and a big shift towards a different energy system has to occur in the upcoming decades, at the risk of major social and economic issues.

In the last two centuries, the world has witnessed unparalleled growth both in population and economy, largely due to the advance of the industrial age. Consequently, energy consumption also grew extensively and at a greater pace than population and economy. If the world population quadrupled since 1870, the world's

energy consumption increased by a factor of 60 [8]. Since the Second World War, energy consumption increased even more sharply than before and this period corresponded to major economic growth, especially in developed economies. In Figure 2.1, the world energy consumption since the 1870 until 2000 is presented and a massive increase can be observed, especially after the Second World War. The energy sources used in the beginning of the Industrial Revolution were mostly coal and biomass. The United Kingdom, which was the first industrialised country in the world, took full advantage of the technological advances brought by the modern age and from its coal reserves, which were used to power their economic development. After the Second World War, oil accounted an increasing share of the world's primary energy sources and nowadays, there is an increase in natural gas consumption.

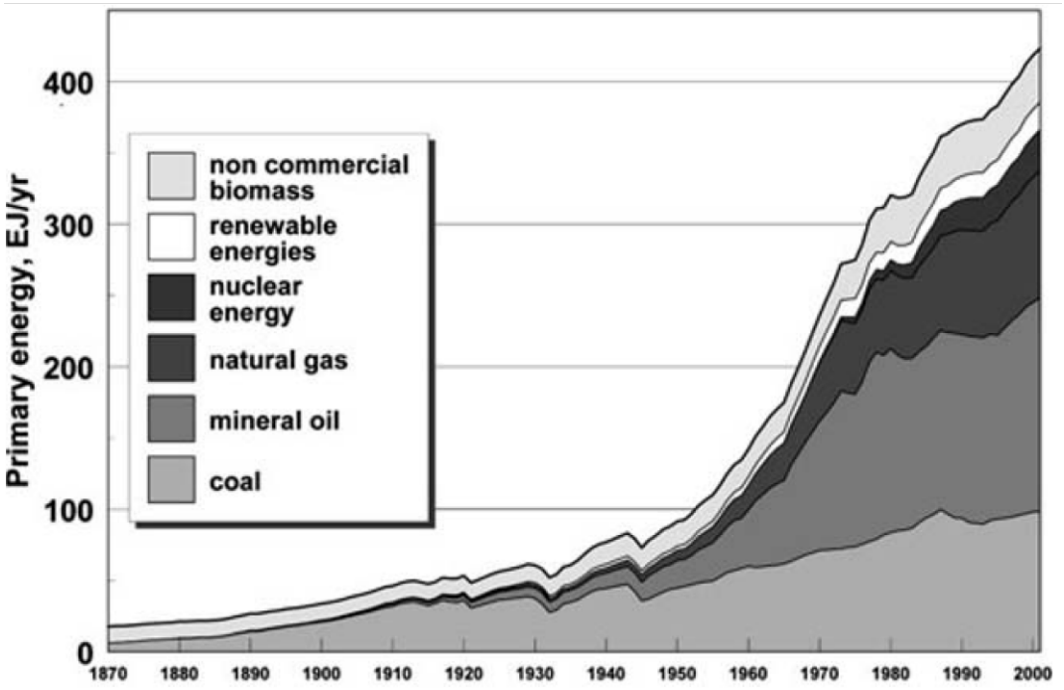

Figure 2.1 – World energy consumption in Exa Joules (10^{18}) since the Industrial Revolution by source. Reprinted from [8] and used with permission from Elsevier.

Coal, oil and natural gas are fossil fuels, since they are organic vestiges that were decomposed in the Earth's crust for millions of years. As they are organic remnants, they are mostly hydrocarbons. They are considered primary sources of energy since, even if the energy content was produced using the sun and natural processes in the Earth's mantle, they can be easily converted to energy. There are many factors contributing to fossil fuels' popularity, with the most important ones being their affordability, their availability, their ease of transportation, their high energy content

and the simple mechanisms involved in converting their chemical energy into other forms of energy, such as heat, mechanical or electrical energy [9]. The technologies involved are, in most cases, straightforward transformations, especially combustion, which can be used to provide heat or to power turbines or engines.

As observed in the last section, energy demand is expected to grow in upcoming decades, due to significant economic development and population growth until 2050. There are a variety of models to estimate future energy consumption, but most authoritative reports, including the World Energy Outlook from the International Energy Agency, the International Energy Outlook from the Department of Energy in the United States and reports compiled by energy companies, like Exxon-Mobil's "The Outlook for Energy: A view to 2040" all predict increased energy demand for upcoming decades [4, 6].

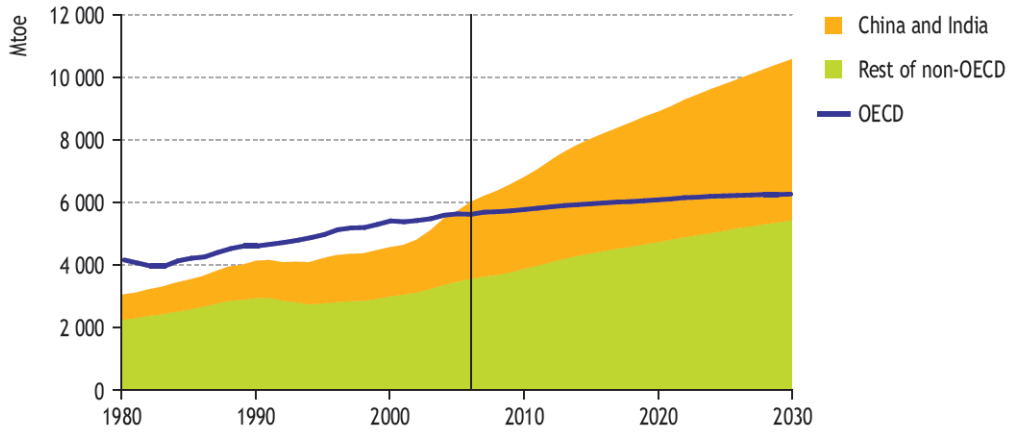

Figure 2.2 – Predicted energy demand until 2030 in China, India, OECD and non-OECD countries in Million tonnes of oil equivalent. Reprinted with permission from World Energy Outlook © OECD/IEA 2008.

Based on the Reference Scenario from the World Energy Outlook 2008 [1], future energy demand will come mostly from non-OECD countries, especially India and China, as it can be observed from Figure 2.2. The same report estimates the average annual rate of growth for energy demand in the world to be 1.6 % for the 2006-2030 period, with 0.5 and 2.4 % annual rate of growth for OECD and non-OECD countries, respectively. Energy demand annual rate of growth for the same period will be 3.0 % for China and 3.5 % for India.

Fossil fuel reserves are extensive and they are likely to last for decades at current consumption. In BP's Statistical Review of World Energy 2012, proven worldwide reserves of oil are 1,662 billion barrels of oil at 2011, which are likely to last more than 50 years at a daily consumption of 88,034 thousand barrels of oil, which was the daily worldwide oil consumption in 2011 [10]. Proven natural gas reserves are 208.4 trillion cubic metres and they are expected to last for 60 years, based on current yearly consumption of 3,222 billion cubic metres [10]. Proven coal reserves are 860,938 million tonnes, between anthracite, bituminous and sub-bituminous and lignite. These are predicted to last 112 years, if divided by the production in 2011 [10]. It is also important to note that these are proven reserves, in all cases, and there might be untapped fossil fuel reserves elsewhere in the world. While proven reserves might be able to meet consumption for many decades, there are some reports that the world is reaching peak oil production [11-13]. The hypothesis of peak oil was first reported by Hubbert [14], who warned about the possibility of reaching peak oil.

The abovementioned energy problem has several components – economic and population growth for the next decades will put a massive strain on energy demand on fossil fuels, which are limited and will become more expensive to explore and extract. This will inevitable slow or prevent economic growth in countries. Widespread use of fossil fuels has also generated a number of environmental problems. Fossil fuels' impacts and associated problems are the subject of the next section.

2.2.2. Impacts of non-renewable energy technologies

There are looming energy problems facing the world. Countries have become increasingly reliant on fossil fuels for energy conversion and these carry a number of problems, with economic, social and especially environmental impacts caused by their use. They are primary sources of energy, currently used for around 85 % of all energy consumed in the world [5], with all the different sectors relying on fossil fuels for energy conversion. There are several issues to consider with the use of fossil fuels that urge societies to move away from their use. Their impact is more pronounced when considering environmental aspects, since massive consumption of fossil fuels caused a number of environmental harms. A transition to an economy that does not have

fossil fuels as its core will one day happen and, since they are responsible for many environmental effects that will be soon discussed, the sooner the current energy system is replaced by a sustainable one, the better.

The first main issue with fossil fuels is that they are non-renewable energies, meaning that there is a finite supply of them on Earth [15]. Despite being able to meet demand for many decades to come, they are limited, which means that one day they will simply run out. Apart from their vast but still limited supply, there are inherent problems with their use, mostly related to environmental impacts caused by their consumption and issues to deal with energy security [15], which is related to importing energy from other countries. In addition to being limited, they are also becoming harder and more expensive to explore, due to the need of taping into more fossil fuels reserves to keep up with current demand [15]. Whereas in the past fossil fuel extraction was relatively simple and straightforward in some regions of the world, their value has propelled investments in off-shore oil platforms, which in some cases can go as deep as 5,000 metres. The need for more sources of energy has also put in play some technologies that were not considered until recently, due to their energy-intensive nature and the environmental damage they cause [16, 17]. These include shale oil, fracking of natural gas and heavy oil sands, all of which are environmentally damaging to produce but are or will be developed in the near future. All of this reflects on fuel prices, since more investment, and usually private investment, is put into these technologies that needs to be recovered.

Another issue to consider is that fossil fuel reserves are unequally distributed among the different nations. This unequal distribution prevents countries and regions, with Europe being a good example, of being energy self-sufficient and therefore having to rely on foreign countries for energy provision. Some of the countries rich in fossil fuel reserves are very unstable, poor and corrupt, which only adds to lack of energy security for the rest of the nations [15]. The security of a primary energy supply is something that is viewed very seriously by governments and the concentration of energy reserves in unstable parts of the world has taken governments to invest in alternative sources of energy so that they can diversify their energy mix. Also, energy insecurity due to production problems and reserves located in unstable regions of the

world, particularly the Middle East, causes fossil fuel's prices to be extremely volatile [15].

Apart from issues related to energy security and limited reserves, the use of fossil fuels carries great environmental harms. The most notorious environmental damage caused by the use of fossil fuels is anthropogenic climate change, which is predicted to have catastrophic consequences for the Earth [18]. In addition to climate change, fossil fuels cause additional environmental damage and are responsible for acid precipitation, stratospheric ozone depletion and air pollution, among other problems [19, 20]. The main problem with the use of fossil fuels is the pollutants they emit into the environment, especially carbon monoxide (CO), carbon dioxide (CO_2), methane (CH_4), nitric oxide (NO) and nitrogen dioxide (NO_2), nitrous oxide (N_2O), sulphur dioxide (SO_2), chlorofluorocarbons (CFCs) and ozone (O_3) [20]. Fossil fuels' use in various applications causes the emission of these substances to the atmosphere, causing deleterious effects.

In acid rain, some pollutants, especially SO_2 and NO_x, are produced by combustion of fossil fuels. Coal electric power generation produces 70 % of SO_2 emissions and transport vehicles are responsible for NO_x emissions, which are emitted to the atmosphere [20]. These pollutants react in the atmosphere and sometimes travel great distances, precipitating on local environments that are very sensitive to excessive acidity. Ozone depletion is also due to the emission of pollutants originating in energy conversion from fossil fuels. Emission of CFCs and NO_x causes the stratospheric ozone layer to deplete, since these pollutants react with the ozone present, causing damaging levels of UV radiation reaching the surface of the Earth [20]. Another issue is the air quality in cities and industrial areas, which has been a major problem to consider since the Industrial Revolution. The particulates present in the air, in areas that are greatly industrialised or with a great number of vehicles in the roads cause health problems [20]. There are also environmental disasters that can be attributed to the use of fossil fuels, especially oil tanker accidents or offshore oil platforms that explode and spill oil into the ocean. The Exxon-Valdez disaster and the recent Deepwater Horizon accident are two good examples of environmental disasters that significantly affect the local flora and fauna.

Apart from the environmental problems just mentioned, one of the main issues caused by fossil fuels is anthropogenic climate change [19, 21, 22]. Some pollutants are denominated greenhouse gases, due to their known contribution to the greenhouse gas effect. The most long-lived greenhouse gases are CO_2, CH_4, N_2O and halocarbons, a group of gases that contains fluorine, chlorine or bromine [22]. The atmospheric concentration of these gases affects the absorption, scattering and emission of the sun's radiation within the atmosphere and at the Earth's surface. This results in positive or negative changes in the energy balance, which can warm or cool the global climate [22].

The Intergovernmental Panel on Climate Change (IPCC), an organisation composed of hundreds of scientists, has concluded that there is significant climate change and it is almost certainly due to anthropogenic sources. There is now solid evidence that substantive damage is caused by the greenhouse gas effect, which has been altering the global climate [22]. Some observable events are the occurrence of more extreme weather events, such as droughts and heat waves. Conversely, it is reported that cold days, cold nights and frosts have become less frequent around the globe, while hot days and hot nights are more frequent [22]. Another important consequence is the ocean acidification, which leads to the loss of ecosystems [23]. The IPCC reports that global climate warming is unequivocal, as evident from observation of increases in global average air and ocean temperatures, widespread melting of snow and icing and a rising global average sea level [22]. Additionally, a consequence of reducing the snow cover is reducing the albedo, lowering the ice-albedo feedback phenomena [24], leading to more climate warming. Some of the most evident and observable consequences of climate change are highlighted in Figure 2.3.

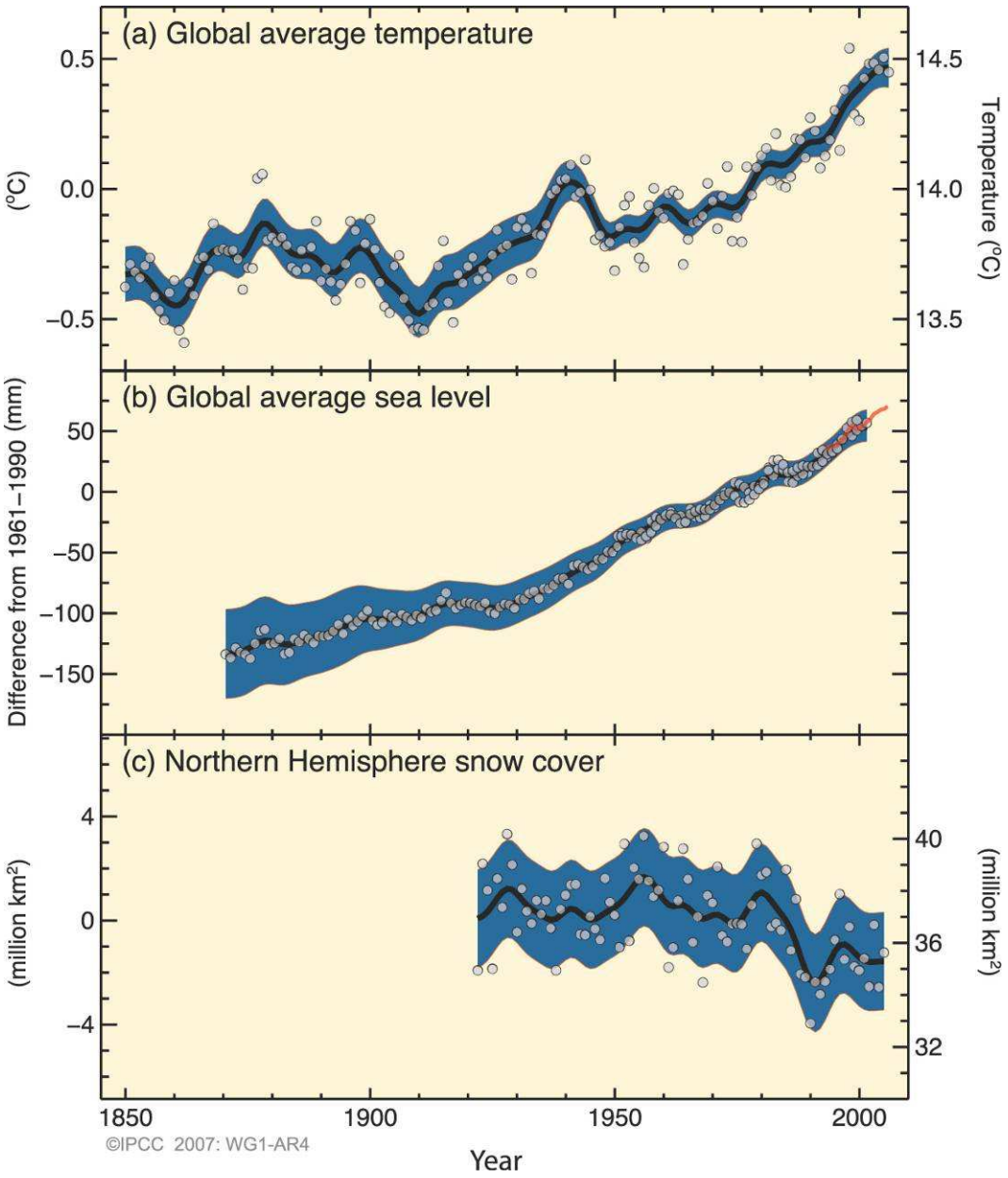

Figure 2.3 – Observed changes in (a) global average surface temperature, (b) global average sea level from tide gauge (blue) and satellite (red) data and (c) Northern Hemisphere snow cover for March-April. All changes are relative to corresponding averages for the period 1961-1990. Smoothed curves represent decadal average values while circles show yearly values. The shaded areas are the uncertainty intervals estimated from a comprehensive analysis of known uncertainties (a and b) and from the time series (c). Reprinted from reference [22] and used with permission.

After great concern raised by scientists, governments began to take notice and there are now several measures in place that aim to mitigate climate change, by reducing global greenhouse gas emissions. Governments have agreed to gradually decarbonise their economies and most of them have made pledges to reduce emissions by as much as 80 % relative to 1990 levels, for example, the 2008 Climate Change Act in the United Kingdom [25]. These pledges are in place in several countries of the world,

and in Europe there is a pledge from every country to reduce emissions by 20 % by 2020 [22, 26]. Climate change has been considered one of the biggest menaces facing mankind. Even financially, it should be dealt with as soon as possible, as the UK's Stern Review on the Economics of Climate Change concluded [27]. This was a report which aimed at providing an economic assessment of the impacts of climate change. Its conclusions are clear – "The scientific evidence is now overwhelming: climate change is a serious global threat, and it demands an urgent global response. (…) From all these perspectives, the evidence gathered by the Review leads to a simple conclusion: the benefits of strong and early action far outweigh the economic costs of not acting" [27]. Even economically, there are strong reasons why everything should be done now to prevent catastrophic consequences later. There is every reason why the economy should migrate to a sustainable, clean alternative, which would stop dependency on fossil fuels. This new energy system should convert, transport, store and use energy in a clean, sustainable way, so not producing any harmful emissions. Additionally, it should also use preferentially unlimited sources of energy or at least, sources that are not likely to deplete in the next centuries.

The need for a sustainable, clean, secure and affordable energy system is urgent. To achieve this, governments have to comply with their pledges and decarbonise their energy systems, migrating from an almost complete dependency on fossil fuels to other sources of energy that do not have harmful consequences. A good way forward is to introduce more renewable energies for energy generation and control emissions wherever possible, in all the different sectors. Renewable sources of energy are the topic of the next section of this thesis.

2.2.3. Renewable energies

As observed in the former section, environmental problems associated with energy conversion from fossil fuels have prompted the development of alternative sources of energy. Renewable energy sources are not completely carbon-free, because of the materials used to manufacture them, but can in principle generate energy without the emission of greenhouse gases. Renewable energies are almost unlimited, since they depend on natural phenomena such as solar radiation, tides and geothermal energy

and they are at the core of a future sustainable and clean energy system, which is a major pillar for sustainable development. Sustainable development should be the main aim, ensuring that greenhouse gas emissions are controlled and that the problems created by the use of fossil fuels are solved. Sustainability has known a number of definitions, perhaps the most famous is the one which is expressed in the UN's commissioned report to the Brundtland Commission [28], which defines sustainability as "development that meets the needs of the present without compromising the ability of future generations to meet their own needs" [28]. A similar definition, albeit more focused on economic aspects has been put forward by Economics Nobel Laureate Paul Solow, who defined sustainability as "an obligation to conduct ourselves so that we leave to the future the option or the capacity to be as well off as we are" [29].

The Executive Summary on the World Energy Outlook 2008 emphasises this, and it affirms that "It is not an exaggeration to claim that the future of human prosperity depends on how successfully we tackle the two central energy challenges facing us today: securing the supply of reliable and affordable energy; and effecting a rapid transformation to a low-carbon, efficient and environmentally benign system of energy supply." [1]. Renewable energies are beginning to be used in large scale and globally, including traditional uses of biomass, they are responsible for around 13 % of the total energy supply . They consist of technologies that harness and convert energy from natural phenomena that occur on the Earth, which can be sunlight, wind, waves, precipitation, tides, geothermal heat and biomass conversion [30]. There are many different ways to harness all these different sources and their potential is massive. In fact, renewable energies can in principle supply all our energy needs many times over [31]. Still, nowadays they account only for a small percentage of energy converted worldwide, but with an increasing share . There are some issues related with the use of renewable energies, mostly to do with their intermittence and accessibility. This creates numerous technical and economical problems, although significant research is underway to develop and explore new technologies. For this reason, renewable energies are at different stages of development, with some, like hydropower, considered mature technologies, while others are still in an exploratory phase. The main renewable energies can be divided into the following categories - wind power, biomass, solar energy, hydropower, geothermal and ocean energy [30].

It is also important to highlight nuclear energy in energy generation, which in some countries produces more than half of electricity generated (in France, it produces more than 75 % of the generated electricity [32]). There is some debate whether nuclear energy is clean, but some have argued that greenhouse gas emissions from the nuclear sector are comparable to renewable energy sources [33]. Nonetheless, energy generated in a nuclear fission reactor relies on uranium to produce energy. Uranium is, like other fuels, not equally distributed among countries, so nuclear energy has some issues related to accessibility, affordability, resilience and safety in comparison with renewable energy technologies [34]. Another very interesting energy power source is fusion energy, which is believed to be the most promising long-term nuclear power source [35]. The International Thermonuclear Experimental Reactor (ITER) has been commissioned and will test the feasibility of fusion power [36]. ITER is predicted to be finished in 2019 [37].

Renewable energy technologies are numerous and offer great potential. While they are not completely trouble-free, and still not competitive in comparison with energy generated from fossil fuels, great expectations reside on some of these technologies to unlock their full potential and provide clean, sustainable energy at competitive prices. It should be the goal of every government to migrate towards a sustainable, clean energy system, mainly because of the problems created by fossil fuels and due to pledges and commitments already signed. However, the case is that energy converted from renewable sources is still marginal in the overall energy mix, and according to the different scenarios, their future growth in the share of energy production is not as sharp as wished . Renewable energies can offer clean, renewable and unlimited energy to meet upcoming energy demand and in some cases, they just need bigger incentives to be commercially attractive.

Notwithstanding the major benefits they bring about, renewable energies also have some underlying problems associated with their use. Apart from the environmental and ecological harms the installation of some of these technologies might create, one problem that spans across most of these technologies is their intermittency and their unpredictability [30]. It is also important to point out that some of these technologies cannot be deployed instantly for energy conversion, which makes their use in the electric grid troublesome [38]. In fact, on some occasions, the wind turbines have to

be shut down because there is no need for the energy they generate. Electricity has to be created the moment it is consumed, which means that intermittent renewable energies cannot be plugged instantly on the electric grid when they are needed. Intermittency, unpredictability and unavailability to stream renewable energies on the grid the second they are needed creates the need for proper energy storage [39]. Energy storage technologies would play a crucial role in this, by converting this excess energy generated from renewable sources at times when it is not required and store it. Later, at peak demand times, this stored energy could be easily dispensed back to the electric grid at the moment it was needed. If proper energy storage is in place, energy generated from renewable technologies would not go to waste and could be stored for later use. Also, clean energy storage is also needed to power vehicles, since a major source of pollutants emission is the transport sector. Transport sector emissions vary from country to country, but they account for 24 % of total emissions in the UK for 2012 and 28 % for the United States in the 1990-2009 period [40, 41]. A future sustainable energy system, due to its reliance on intermittent renewable energies and to the need to decarbonise the transport sector, would definitely need proper energy storage. The different technologies for energy storage, whether mature or currently being developed, are the subject of the next section in this chapter.

2.2.4. Energy storage

As just noted, a clean and sustainable energy system will likely require proper energy storage. There is the need for governments to reduce their dependency of fossil fuels, making energy conversion from renewable sources increasingly important for electricity generation. Most renewable energies are intermittent by nature, and they have to produce electricity whilst coping with the unpredictability of energy demand by the consumer. Efficient energy storage, which would be available to be plugged in quickly and on demand is necessary, since it would avoid wastages of produced energy. There are clear economic and environmental advantages for appropriate energy storage and, if inexistent, renewable energies could never provide a big share of energy generation, since baseline production of energy cannot rely on intermittent energy sources [42]. There are many means to store energy when it is in surplus. The more common energy storage systems are pumped hydro energy storage, compressed

air energy storage, flywheel energy storage, superconducting magnetic energy storage, thermal energy storage, energy storage in batteries, supercapacitor energy storage and hydrogen energy storage [42]. More background information on the different types of energy storage can be found in Additional Information A.

Energy storage systems are usually assessed by a number of characteristics, with the most critical being the storage capacity (quantity of available energy in the storage system after charging), length of time of discharge and power transmission rate (time needed to extract the stored energy), efficiency (ratio of released energy and stored energy), durability (number of cycles of charge/discharge with minimal loss of performance), autonomy (amount of time the system can release energy), cost, adaptation to energy source (adapted to the applications, which can be low, mid or high power, permanent, renewable), fast response times for energy stored, self-discharge (storage energy that is dissipated over non-use time), mass and volume densities of energy (energy stored per unit mass and per unit volume), necessary equipment (which can include control and monitoring equipment), operational constraints (safe to operate, operating temperature and pressure), environmental aspects, reliability and others, including maintenance and design [38, 42]. Also quite important is the type of energy storage application, which can be stationary or portable and the duration of energy storage, which can be short or long term [38]. The different energy storage technologies are at different stages of technical maturity, with Pumped Hydro Energy Storage (PHES) and lead-acid batteries considered mature technologies with a number of applications already deployed [42].

An alternative way of storing energy is to use hydrogen. Off-peak electricity could be used to produce hydrogen *via* water electrolysis, which is stored for later use [38]. One of the advantages of using hydrogen as energy storage means is the multitude of routes to produce, store and use the hydrogen. Hydrogen is an abundant element on Earth, present in water, biomass and hydrocarbons, so there are plenty of hydrogen sources for production. The hydrogen is stored and when there is additional need for electricity in the electric grid, it can be used in a fuel cell to produce electricity. Among its many advantages, hydrogen offers energy storage which is transportable, highly versatile, efficient, clean, with high energy density, an ability to be implemented in systems over a wide range of scales (from kW to multi-MW scale),

independent system charge and discharge rate, independent storage capacity, modular construction with the ability of adding extra modules later and the potential for the excess hydrogen produced with off-peak electricity to be used in vehicles [42, 43]. Some of the drawbacks of using hydrogen to store energy include fuel cells costs, which are still somewhat costly per kW (6-20 USD per kWh) [42]. Investment costs are high and life expectancy is limited, mostly in power network applications [38]. Details on production, storage and use of hydrogen, in either a fuel cell or a heat engine are discussed in the next section of this chapter.

The energy and power density of the different storage systems is also very important, and a plot of the different energy storage technologies is shown in Figure 2.4. This type of plot (power density as a function of energy density) is also known as the Ragone plot. The figure illustrates that the different energy storage systems have different characteristics, and their power and energy densities are different by several orders of magnitude. This has made some of these technologies more suited for certain applications than others and, for every energy storage case, which are different in power (from some kW to hundreds of MW), duration (energy that only needs to be stored for seconds to energy that needs to be stored for months), rate of discharge of power and availability (from energy that needs to be connected in less than one second to energy that can be connected in days) there are different technologies that can be applied.

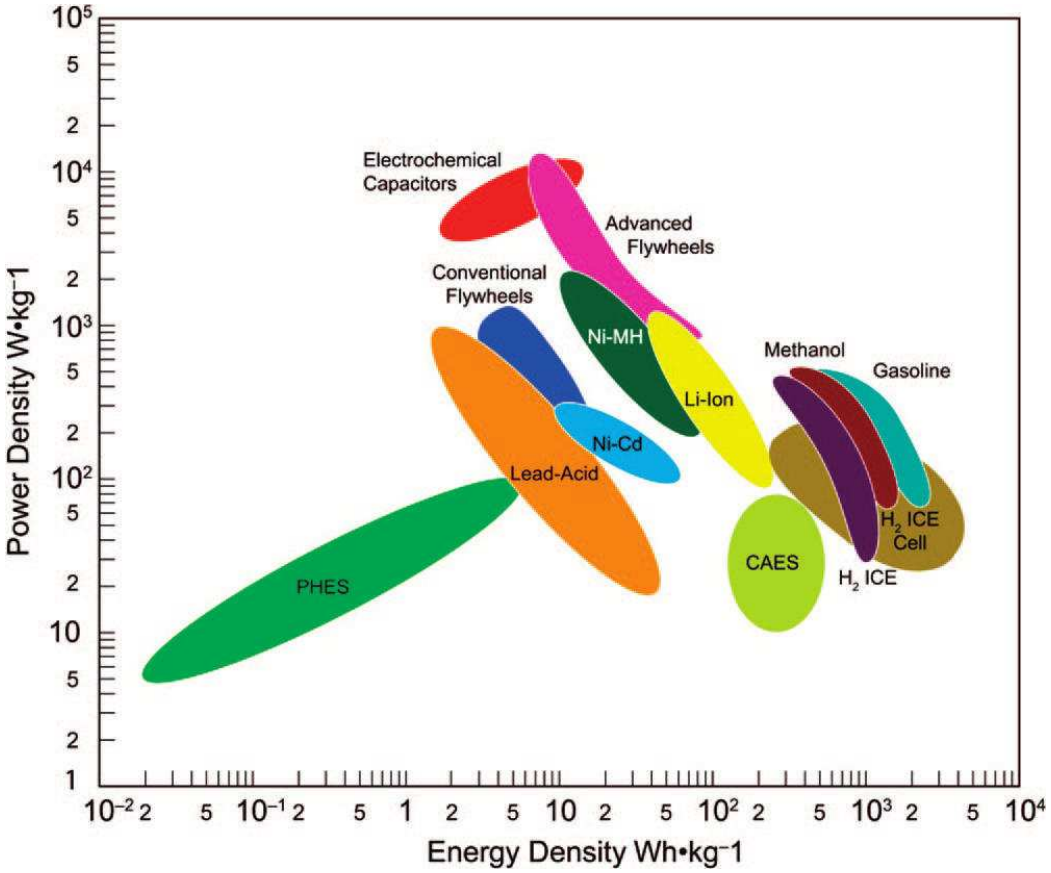

Figure 2.4 - Ragone plot for different energy storage mediums, including pumped hydro energy storage (PHES), lead-acid batteries, nickel-cadmium batteries, nickel-metal hydride batteries (Ni-MH), conventional and advanced flywheels, electrochemical capacitors, Li-ion batteries, compressed air energy storage (CAES), methanol, gasoline, hydrogen internal combustion engine and hydrogen fuel cell. Reprinted with permission from [44]. Copyright 2010 American Chemical Society.

Despite the development of many different energy storage systems, none has been designed so far that meets all the demands of an ideal energy storage system – maturely developed, having a long lifetime, low cost, high energy density and efficiency and environmentally clean [42]. Hydrogen, in conjunction with a fuel cell, can be an attractive energy store and can be used to decarbonise the transport sector, since it has limited impact on the environment. Despite its relevance as energy store to balance intermittent renewable energy sources, hydrogen is perhaps even more important as a sustainable energy vector in the transport sector.

2.3. Hydrogen as a sustainable energy vector

Hydrogen as a sustainable, wide-scale energy vector is still dependent on a number of technological breakthroughs, as well as overcoming social and economic issues, including the acceptance by the population of hydrogen and the need for proper infrastructure. The main technical issues concerning the use of hydrogen as a sustainable energy vector are sustainable production of hydrogen, efficient and safe storage and distribution, and environmentally benign and affordable use in a fuel cell or heat engine. This section discusses sources and current applications of hydrogen, clean and sustainable production, storage, delivery and infrastructure, and end-use in a fuel cell or heat engine. The "hydrogen economy" is a term often used to characterise a wide-scale implementation of hydrogen as a sustainable energy vector.

2.3.1. Hydrogen: sources and current applications

Hydrogen is the lightest element in the periodic table and the most abundant in the universe, with estimates of more than 90 % of the atoms and more than 75 % of the universe's mass being hydrogen [45]. Hydrogen was the first element created in the Big Bang 13.7 billion years ago and all heavier elements are made of hydrogen and helium, which are fusing inside stars [45]. In the Earth's crust, hydrogen has a prevalence of only 0.88 % in mass and 15.4 % on atomic concentration. It is the third most common element by atomic percentage in the Earth's crust after oxygen and silicon and the ninth most common in mass [46], but it is seldom present in molecular form and is instead found bound to other elements. Molecular hydrogen or di-hydrogen (H_2) can be found in some volcanic gases, in natural gases and trapped in rocks and meteorites. It is massively more common found bounded to other elements, such as part of water (11.2 wt. % on Earth). It is a ever present element in organic chemistry, abundant in organic compounds, including fossil fuels. Also, 10 wt. % of the human body is hydrogen [46].

Hydrogen is a large scale chemical commodity with a variety of applications. Current worldwide production is between 50 and 60 million tonnes of hydrogen, which

roughly corresponds to between 550 and 675 billion (10^9) at STP cubic metres produced annually [47, 48]. This hydrogen is mostly produced industrially, from coal, oil and natural gas [49].

There are many different methods of industrial production of hydrogen from coal and hydrocarbons. One former major source of hydrogen was coke oven gas, which in the first half of the twentieth century used to provide most of the hydrogen for ammonia synthesis and coal liquefaction. Coal gasification is another industrial process used to manufacture hydrogen. Coal is gasified with high-purity oxygen, at high temperatures and pressures to generate synthesis gases, rich in carbon monoxide and hydrogen. There is a variety of feedstocks and methods to produce hydrogen, depending on the operating conditions [49]. Partial oxidation of hydrocarbons is another route for industrial hydrogen production. Hydrogen can be produced by partial oxidation of any liquid hydrocarbon, but the production is only economically practical when using heavy residues from petrochemical processes [49]. Gaseous hydrocarbons can be used as feedstocks as well, using partial oxidation and producing carbon monoxide and hydrogen. Another major industrial process for hydrogen production is catalytic reforming of hydrocarbons, which involve the reaction of hydrocarbons with steam to produce carbon monoxide and hydrogen [49].

Natural gas is the most important feedstock for catalytic steam reforming and steam methane reforming is the cheapest industrial method for producing hydrogen, accounting for half of the total production [49, 50]. In refineries, hydrogen is generated in some processes and needed in others, so most of the produced hydrogen is consumed in the refinery that produces it [49]. One main last industrial process for hydrogen production is in the petrochemical processes area. In steam cracking for olefin, hydrogen is generated as a byproduct in the production of ethylene and propene from ethane, naptha or gas oil. In acetylene production, hydrogen is also generated as a byproduct using thermal cracking of methane, naphta or liquefied petroleum gas [49]. As a chemical commodity, hydrogen is used in a variety of industrial processes. Import and export amounts of hydrogen are usually residual and merchant hydrogen (hydrogen that is produced and sold on the market) accounts for 10 % of the total hydrogen produced [49]. Hydrogen is usually produced onsite and

immediately consumed in industrial processes (captive hydrogen), in either addition (hydrogenation) or reduction processes [49].

One major use of hydrogen is in ammonia synthesis. Ammonia is used mostly as a feedstock for fertiliser production, but there are some industrial uses of ammonia, such as the production of nitric acid, plastics and fibres, explosives, dyes and pharmaceuticals [51]. Hydrogen is also used in refinery processes to increase the hydrogen content in heavy crude oil fractions and in producing lighter fractions by reducing molecular mass [51]. A number of coal refinement processes also use hydrogen, namely coal hydrogenation, hydropyrolysis and hydrogenating coal gasification. Carbon monoxide and hydrogen constitute synthesis gas, which is also an industrial use of hydrogen [51]. Synthesis gas is used in the production of special chemical products, such as methanol synthesis, Fischer-Tropsch synthesis, oxo synthesis and methane synthesis. Hydrogen is also common in organic chemistry, for synthesising chemicals and intermediates [51].

In inorganic chemistry, hydrogen is used for the production of hydrogen peroxide in the catalytic hydrogenation of anthraquinone and its derivatives [51]. Also important are the production of hydrochloric acid and hydroxylamine. Another area for the industrial use of hydrogen is metallurgy, where it is used to reduce iron ore and as a reducing agent in powder metallurgy processes and in the recovery of copper from sulfidic ores [51]. Finally, hydrogen is used for high temperature oxy-hydrogen flames, which are used for cutting and welding in metallurgy, as a plasma for heating purposes, in cutting and welding in metal processing, in semiconductor production to dope the silicon, in water treatment for denitrification, as an alloying element in metals to produce desired chemical properties, to increase the transition temperature of superconducting alloys and as a carrier and fuel gas in gas chromatography [51]. Liquid hydrogen, due to its extremely low temperature, is also used as a refrigerant in bubble chambers and for the cooling of superconducting metals below transition temperatures [51].

2.3.2. Clean production, storage, infrastructure and use of hydrogen

As just observed in the previous section, industrial hydrogen is mostly produced from oil, coal and natural gas, which are fossil fuels. Despite widespread production in industry and its use as a chemical commodity, hydrogen as a sustainable energy vector would require a steep increase in production. To fulfil its ambitions as a sustainable and clean energy vector and fuel, it would entail that it is sustainably produced, stored, distributed and used. This means using renewable energy and renewable sources to produce molecular hydrogen, which due to the availability of clean sources of energy and to the ubiquity of hydrogen, result in numerous sustainable pathways to produce hydrogen [52]. Various alternatives have been considered and one of the best known examples for sustainable production of hydrogen is the electrolysis of water powered by wind turbines. This offers several advantages over other sustainable methods of production, since wind turbines are already installed and are producing energy, which, in some cases, might not even feed into the electric grid. Any energy generated while the wind turbines are offline could be used to electrolyse water and produce hydrogen, and this could be stored for later use.

Clean and sustainable hydrogen production uses electric, thermal, biochemical, photonic, electro-thermal, photo-thermal, photo-electric, photo-biochemical and thermo-biochemical sources. These forms of energy can be derived from renewable sources of energy, nuclear energy and from energy recovery processes [53]. Electrolysis of water has been used for more than 100 years and it accounts for around 5 % of the total hydrogen production [49]. An electrolysis cell with an electrolyte is used and the overall cell reaction consists in splitting water into hydrogen and oxygen. Because pure water has very low conductivity, an aqueous solution of potassium or sodium hydroxide, sodium chloride or hydrochloric acid is used, which generates other products besides hydrogen and oxygen depending on the solution [49]. Electric current flows through the electrolysis cell and generates hydrogen at the cathode and oxygen at the anode. Electrolysis therefore requires a source of energy, which to be sustainable has to be a clean, renewable source and a source of hydrogen, which is

usually water. If hydrogen is used in a hydrogen fuel cell, with only water as its product, producing energy through electrolysis would close the water cycle, since the water used to produce molecular hydrogen would be later restored once it is used in a fuel cell. Electrolysis can also be done at high temperatures (high-temperature electrolysis) in which a combination of a thermal source and electric power are used to split the water molecule [53]. Electrolysis is also used together with photovoltaics (PV) in PV-electrolysis, in which PV panels generate the electricity that drives the electrolyser. In photo-electro-chemical methods, heterogeneous catalysts are used in one electrode that is exposed to solar radiation [53]. A slight modification of this method consists of using semiconductors materials, which generate an electric field upon absorption of photons with energy greater than the semiconductors' bandgap. The generated electric field is then used to electrolyse water and split it into oxygen and hydrogen. One advantage of this method is that the solar energy absorption and water electrolysis are integrated in a single unit [53].

Apart from electrolysis, there are other hydrogen production methods that use water as a source of hydrogen. Another common method for producing hydrogen is using thermal energy, in which water is heated up to very high temperatures (over 2,500 K at ambient pressures) and splits into oxygen and hydrogen [49]. Thermochemical water cleavage also involves heating water to very high temperatures and using chemical reactions (which can include redox reactions) to split the water molecule [49]. Photocatalysis is another hydrogen production method that uses water as a source of hydrogen. In photocatalysis, solar radiation is captured and used in conjunction with catalysts to split the water molecule. Biological routes for producing hydrogen from water are bio-photolysis, in which bacteria and microbes photo-generate hydrogen from water, enzymatic processes with polysaccharides to generate energy and artificial photosynthesis, in which modified molecules mimic photosynthesis and generate hydrogen from water [53].

Another important source of hydrogen is biomass. Hydrogen is present in organic compounds and can be produced from a variety of biomass feedstocks. Methods for producing hydrogen using biomass include thermocatalysis, in which feedstocks such as wood sawdust and sugar cane bagasse are gasified using water and heat, forming hydrogen; thermochemical processes, in which biomass is converted to syngas and

hydrogen is separated; reforming of biofuels, in which liquid biofuels are converted to hydrogen and dark fermentation of biomass, in which anaerobic fermentation is done in the absence of light on organic wastes, using microbes to generate hydrogen [53]. Bio-photolysis, photo-fermentation, artificial photosynthesis and thermophilic digestion are examples of systems that use biomass as a raw material to produce hydrogen [53]. Other raw materials from which hydrogen can be produced include hydrogen sulphide (H_2S), which can be cracked at high temperatures and using catalysts (thermocatalysis) or split in cyclical reactions (thermochemical processes) [53]. The hydrogen sulphide is extracted from the sea or derived from other industrial processes. The only needs for production of hydrogen are sources of hydrogen, which can be water, biomass or other chemicals and a source of energy or heat, which can be any source, but to comply with the sustainability requirement, has to be clean and sustainable.

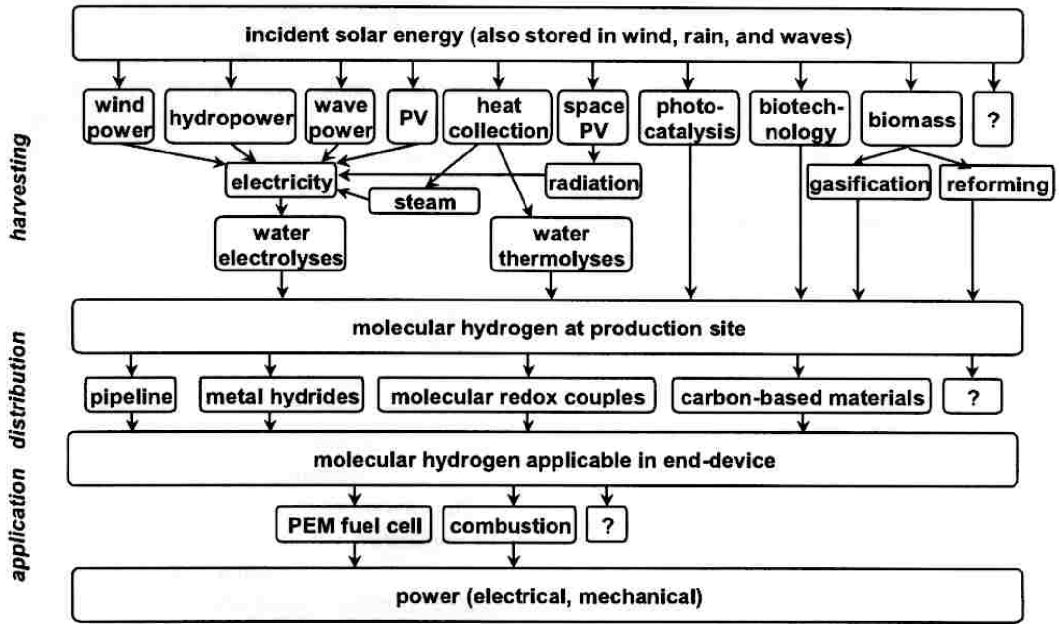

Figure 2.5 – Sustainable hydrogen chain, taken from Gosselink [52]. Reprinted with permission from the International Hydrogen Energy Association.

Figure 2.5 illustrates the sustainable hydrogen chain, with a multitude of production storage and distribution pathways, until the hydrogen is finally used in a fuel cell, in combustion or in other method to extract electrical or mechanical energy.

Another important aspect of the use of hydrogen as an energy vector is the storage of hydrogen. In order to be a clear alternative to electricity as an energy vector, the produced hydrogen has to be stored for later use. This requires proper infrastructure to distribute it, especially when concerning mobile applications. The storage problem is arguably the biggest technological problem preventing widespread use of hydrogen as an energy vector [54]. As already observed in this chapter, energy storage is a compelling problem and if an efficient, clean, easily converted and easily used method for storing energy existed, a variety of problems could be solved. Storage of hydrogen is at the core of the use of hydrogen as an energy vector and, despite other aspects of hydrogen as a sustainable energy vector all meriting research, hydrogen cannot be implemented without an appropriate solution for its storage [55]. The storage is a problem because, despite being the chemical fuel with the highest energy density per mass, hydrogen has a very low volumetric density (that is, the quantity of hydrogen per volume) at normal pressures and temperatures. For a significant amount of hydrogen to be stored, the volumetric density has to be significantly enhanced to reduce the occupied volume [56]. This is especially relevant for mobile applications, since vehicles running on hydrogen have a limitation in their volume and any containment method for hydrogen cannot occupy a large volume in the car. There are many different alternatives for storing hydrogen, with mature methods consisting of compressed hydrogen in cylinders and liquefaction of hydrogen to enhance the volumetric density [56]. Some alternatives are being studied, which involve chemical storage or adsorption in a porous material. Hydrogen storage is the topic of this thesis, so it is discussed in more detail in section 2.4 of this Background.

Distribution of hydrogen requires proper infrastructure to be built, and this is not a minor issue. A transition towards the use of hydrogen as a wide scale energy vector would require an infrastructure to distribute the hydrogen for end-uses. However, due to specific needs, a hydrogen infrastructure has to be built at a significant cost and before significant demand is in place. This is what has been called the “chicken-and-egg” problem, since no infrastructure will be built without significant demand for hydrogen and there will not be a significant demand for hydrogen until proper infrastructure is built [57]. The infrastructure issue is also another big problem to solve on the roadmap towards the “hydrogen economy”.

One of the aspects of the infrastructure issue is the argument between centralised and decentralised production. Decentralising hydrogen production would mean that hydrogen is produced on-site by reforming or electrolysis or even on-board in fuel cell vehicles [57]. This would only happen in the first stages of hydrogen use, especially in mobile vehicles, since once a fleet of fuel cell vehicles is in place, demand for hydrogen will be high enough so that the decentralised production sites are connected with pipelines. The downsides inherent to the decentralised approach are that environmental benefits can be reduced (reforming natural gas on-site would make technologies like carbon capture and sequestration unlikely) and the loss of efficiencies due to smaller-sized electrolysis units. This transition issue is vital for the change required in our energy system – there is a current energy supply chain built for electricity, natural gas and petrol. Creating a new integrated hydrogen supply chain to deliver hydrogen where it is needed is no easy task. This is because the production and storage facilities, methods for transporting hydrogen, fuelling stations for hydrogen-powered vehicles and technologies that convert hydrogen into energy for end-use all have to be designed in an efficient, clean, sustainable and economical manner [58].

If conveniently stored, hydrogen can be used in either an internal combustion engine, or a hydrogen-powered fuel cell to provide mechanical power to drive the car [59]. It can also be used in gas turbines or in rockets. Hydrogen has the highest energy content per mass basis of any chemical fuel, with a mass energy of around 3 times of gasoline [54]. One of the most efficient uses for hydrogen, either in a stationary or mobile application is the fuel cell, which is likely to be used in the transport sector to decarbonise it. More information on the uses of hydrogen on a fuel cell or a heat engine can be found in Additional Information A. The high energy content and the increased efficiency of fuel cells make them a much more efficient way of powering a vehicle than the diesel or gasoline internal combustion engine [55]. The main advantages of the hydrogen fuel cell system is that it is more efficient, more stable, durable and more silent than an internal combustion engine [60]. Another upside on the use of fuel cells is that they can use a variety of fuels, usually hydrocarbons, but, if used with hydrogen, its only product is water so there is no emission of harmful greenhouse gases [60]. If a large share of fuel cell vehicles were on the road, there would be fewer emissions associated with the transport sector. This springs from the

fact that fossil fuels are used mostly for powering vehicles and dependency on fossil fuels has to be eradicated, because of economic and environmental reasons already discussed in this chapter. Alternatives like electric vehicles, powered on batteries, still lack sufficient energy stored to power a vehicle for extended ranges [61]. Additionally, electric vehicles have long recharging times [61].

Finally, a word must be said about the social issues concerning a transition towards a "hydrogen economy". In order for hydrogen to be implemented as a wide scale energy vector, there has to be public acceptance and awareness of the technology [59]. Hydrogen raises issues, and it has been observed that the public is especially concerned with the safety and economics of hydrogen [62]. These have to be dealt with appropriately, and demonstration projects have come a long way in clearing hesitations or concerns the public has expressed regarding hydrogen technologies [59].

2.4. Hydrogen storage

Hydrogen storage is an intense and active research field and, as said, it is arguably the biggest technical hurdle for the implementation of hydrogen as a sustainable, clean energy vector. This is due to hydrogen's physical properties, which make it a very low density gas at ambient pressures and temperatures. There are established technologies to store hydrogen but there is intense research underway to develop storage alternatives that bring the operating conditions closer to ambient, hence making storage of hydrogen more affordable. This section presents hydrogen storage technologies, introducing physical properties of hydrogen, current storage methods and research on new hydrogen storage alternatives.

2.4.1. Physical properties of molecular hydrogen

Hydrogen has three naturally occurring isotopes (protium, deuterium and tritium), which share the same number of protons (one) but have a differing number of neutrons. Protium does not have a neutron and is by far the most common isotope, with a 99.985 % atomic percentage on the Earth's crust. Deuterium has one neutron

and it is a stable isotope with 156 ppm (atomic) percentage on the Earth [46]. Tritium is radioactive and has two neutrons, having a half-time of 12.7 years. It is much less prevalent, with only traces found in the atmosphere [46]. Molecular hydrogen also has two spin isomers, parahydrogen and orthohydrogen, due to the relative orientation of the nuclear proton spin of the two atoms. This means that the spin isomers populate differently according to the temperature and they equilibrate at a given temperature [46]. Orthohydrogen (the parallel aligned spins) is the highest energy state, so it will have a higher percentage at higher temperatures. In Fig.2.6, the relative percentages in equilibrium of para- and orthohydrogen are shown. The equilibrium ratios will depend on temperature, and at room temperature there is a ratio of approximately 3:1 of ortho- to para-hydrogen, which is called normal hydrogen. The spin isomers have approximately equal ratios at 77 K and at lower temperatures the percentage of parahydrogen increases, until at approximately 20 K, most of the equilibrium consists of parahydrogen.

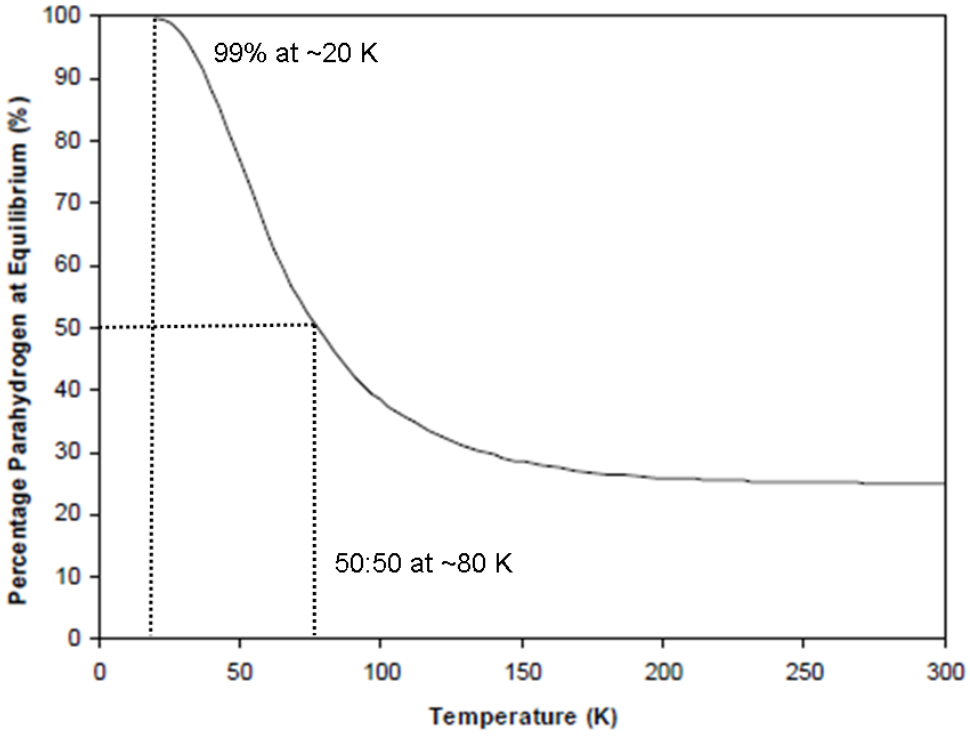

Figure 2.6 - Parahydrogen and orthohydrogen equilibrium ratios as a function of temperature. Adapted from Goldman et al. [63] and used with permission from Elsevier.

Parahydrogen and orthohydrogen possess slightly different properties. While their densities are approximately equal, they differ on other characteristics, including

thermodynamic properties. The heat capacity is one that has been studied and where some differences have been observed [64].

In Table 2.2, some of the properties of atomic and molecular hydrogen are shown. As it can be observed, molecular hydrogen has a density at 273.15 K and 1.013 MPa of 0.08988 kg m^{-3}. Even at the triple point, molecular hydrogen has a density of 77.21 kg m^{-3}, which is less than one tenth of the density of water at normal pressures and temperatures. The density at normal pressures and temperatures and the physical properties of hydrogen make it a very difficult gas to store efficiently. If hydrogen is to be used as energy store, its volumetric density has to be significantly increased. The calculated necessary hydrogen to drive 500 kms is 4 kg [54], which at normal pressures and temperatures occupies around 60 m^3, impracticable for a mobile application. The challenge is to improve on the volumetric hydrogen density, which means that 4 kg of H_2 have to occupy as lower volume as possible. There are conventional methods already developed and used, which include compression of hydrogen gas in cylinders, typically at 35 or 70 MPa or liquefaction of hydrogen at 20 K and there are some alternatives being researched, including solid-state storage in a chemical compound or adsorption in a porous material [65].

Table 2.2 Properties of atomic and molecular hydrogen. From Leachman et al. and Christmann [64, 67].

Property	type/Unit	
Molar mass	g mol^{-1}	Molecular - 2.01588
Isotopes and abundance	% (in atomic basis)	Protium - ^1H – 99.985 Deuterium - ^2H – 156 ppm Tritium - ^3H – trace amounts
Triple point temperature and pressure	K ; MPa	13.95 ; 0.0721
Critical point temperature and pressure	K ; MPa	33.18 ; 13.00
Critical density	mol dm^{-3}	15.4
Density at liquid-vapour critical point	kg m^{-3}	30.12
Density at triple point	kg m^{-3}	77.21
Density at 273.15 K and 1.013 MPa	kg m^{-3}	0.08988
Normal boiling point	K	20.39
Melting entropy	J mol^{-1} K^{-1}	8.41
Heat of fusion at 13.9 K	J mol^{-1}	117.2
Heat of vaporisation at 18 K	J mol^{-1}	912.5
Crystal structure of solid H_2		hcp/fcc

Efficient, high density hydrogen storage remains largely unsolved. There is still a great deal of research to be done in assessing all the different hydrogen storage materials and how they compare with other methods currently in use. While there are still many technical issues to be solved if hydrogen is to be considered a prospective technology for energy storage, including efficiency and price of fuel cells, safety considerations, clean production using waste, wind or sunlight, arguably the biggest problem and the main hurdle for wide-scale use of hydrogen is how to store it in an efficient, safe and economic manner. In light of this, hydrogen storage systems will be discussed in the next pages of this thesis.

2.4.2. Hydrogen storage systems

The high energy content per mass of hydrogen makes it an ideal alternative to use as a wide-scale sustainable energy vector. The hydrogen-fuel cell combination is a very attractive solution for the decarbonisation of the transport sector, but, as already discussed, H_2 storage is still a problem for mobile applications. Despite hydrogen's high energy content on a mass basis (lower heating value of 120 MJ kg^{-1}), it has a very low volumetric density, hence a low energy content on a volume basis at STP (8.7 MJ L^{-1}, which compares with gasoline's 32 MJ L^{-1}) [56]. For mobile applications, it is of the utmost importance that the volumetric density of hydrogen is enhanced, so the challenge is to design a complete hydrogen storage system which occupies a small portion of volume and mass in the car, of the order of a conventional fuel tank. The density at normal pressure and temperature is very low, so the storage system will probably require low temperatures, high pressures or a combination of both for the uptake and/or storage of hydrogen [68]. There are many other requirements, including the ability to charge and discharge hydrogen (cycles) in a short of time and the resilience to withstand many cycles without changing the material [69]. Equally important to make it a viable option as a hydrogen storage system is the need to be efficient, low cost and produced with non-toxic and sustainable materials [69].

Hydrogen storage systems are usually divided into two main areas – physical storage and chemical storage [68]. For physical storage, no strong chemical bonds (covalent or ionic) are observed between the hydrogen and the host material. Mature methods,

such as liquefaction and compression of hydrogen, are physical methods for storing hydrogen [68]. Physical adsorption (or physisorption) is also considered a physical storage method, since no strong bonds are formed and hydrogen maintains its molecular identity [68]. In physical adsorption, highly porous materials are used to store hydrogen, which is adsorbed on the surfaces of the materials. In chemical storage, hydrogen dissociates into atomic hydrogen and usually forms a strong chemical bond with the host material, either as H^0 (*e.g.*, an interstitial), H^+ in ionic systems or covalent H. Examples of chemical storage include metal and complex hydrides.

Shown in Figure 2.7 are the different hydrogen storage system options with the representative materials. As it can be seen, they all require different operating conditions and different energy inputs to release hydrogen.

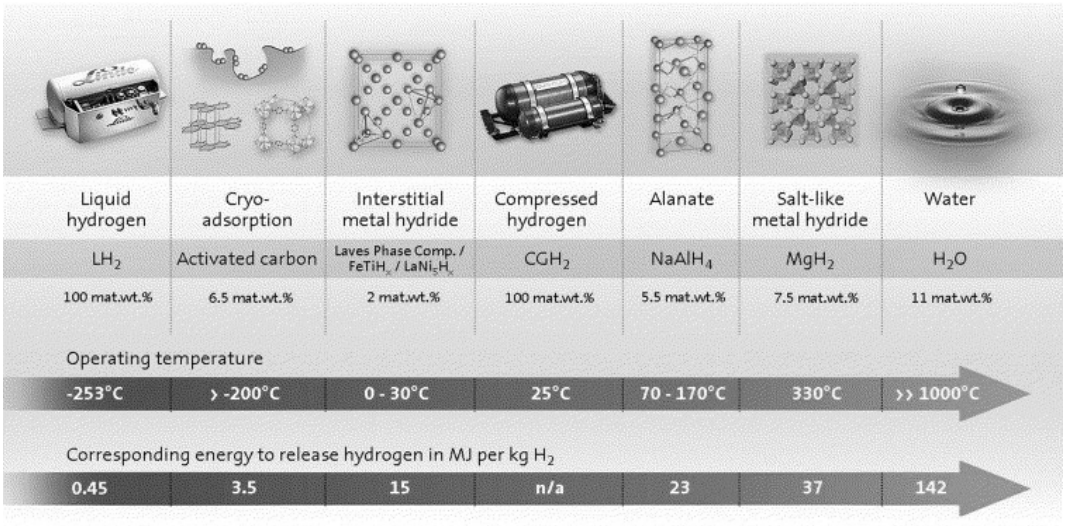

Figure 2.7 – Different hydrogen storage methods, their operating conditions and their energy release. Reprinted from [68] and used with permission from Elsevier.

Hydrogen storage systems, if they are to be fully utilised for powering mobile applications, have to comply with a certain number of requirements. A useful set of requirements are the United States Department of Energy (DOE) targets for on-board storage of hydrogen for light-duty vehicles [69]. DOE targets are for hydrogen storage systems, which include all the balance-of-plant components, such as the tank, material, valves, regulators, piping, mounting brackets, insulation, added cooling capacity and others.

The current targets, updated in September 2009, are presented in Table 2.3. Although volumetric and gravimetric capacities are usually highlighted, equally important are cost, operating temperatures for storage and delivery, number of cycles, delivery pressure, efficiency and kinetics of refilling the storage system. The purity of the hydrogen used and losses are also accounted for. These targets were optimised to allow for driving ranges greater than 300 miles (~ 480 km) on a single fill of the system, while meeting packaging, cost, safety and performance requirements to compete with comparable vehicles available on the market [69]. All the targets are also supposed to be met simultaneously for the storage system, not just the material, so balance-of-plant components have to be taken into account.

Table 2.3 – Some of the DOE revised targets for onboard storage of light-duty vehicles [69].

Storage parameter	Units	2010	2017	Ultimate
Gravimetric capacity	g H_2 / kg system	4.5	5.5	7.5
Volumetric capacity	g H_2 / L system	28	40	70
Cost	\$/gge[1] at pump	3-7	2-4	2-4
Operating temperature	^oC	-30 to 50	-40 to 60	-40 to 60
Delivery temperature (min/max)	^oC	-40/85	-40/85	-40/85
Cycle life	Cycles	1000	1500	1500
Minimum delivery pressure from system (FC/ICE)	bar	5/35	5/35	3/35
Maximum delivery pressure from system (FC/ICE)	bar	12/100	12/100	12/100
Onboard efficiency	%	90	90	90
Well to powerplant efficiency	%	60	60	60
System fill time (5 kg)	min	4.2	3.3	2.5
% H_2	%	99.97	99.97	99.97
Loss of useable H	%	0.1	0.05	0.05

[1] gge stands for gasoline gallon equivalent and it is the amount of fuel it takes to equal the energy content in a liquid gallon of gasoline.

Hydrogen storage systems using known materials still fall short on many of these targets. For this reason, the search for prospective hydrogen storage systems has mostly relied on synthesising and modifying materials to achieve the desired properties. As an example of this, in a recent Faraday Discussions on Hydrogen Storage Materials three main outcomes emerged – "Hydrogen storage is still an unsolved problem with significant challenges remaining to be met; research is driven by the US DOE targets, though these targets are probably not optimal outside the USA (and perhaps not even there) and all the focus is on automotive applications, which may not be the best use for the technology" [70]. There is a considerable research effort on finding suitable hydrogen storage materials, which has driven a great deal of material synthesis research. Some good examples are new synthetic high-surface area materials, which have been, in some cases, driven by research for finding improved hydrogen storage materials. Metal-Organic Frameworks (MOFs), which will be discussed in the next section of this thesis, are a good example of synthetic materials whose main driver was hydrogen storage. Another area which has known considerable developments is metal and complex hydride research. The search for high hydrogen gravimetric and high hydrogen volumetric materials has also prompted hydride materials synthesis and research.

Recently, the DOE assessed three different storage alternatives against the requirements for the materials [71]. The materials assessed were representative of each different type of storage material, which were the AX-21 "superactivated" carbon for the cryo-adsorbent systems, the fluid phase ammonia borane for the chemical hydride systems and sodium alanate ($NaAlH_4$) for metal hydrides, which were benchmarked against all the requirements of the DOE 2010 targets. The benchmarking against the requirements is shown in Figure 2.8, Figure 2.9 and Figure 2.10.

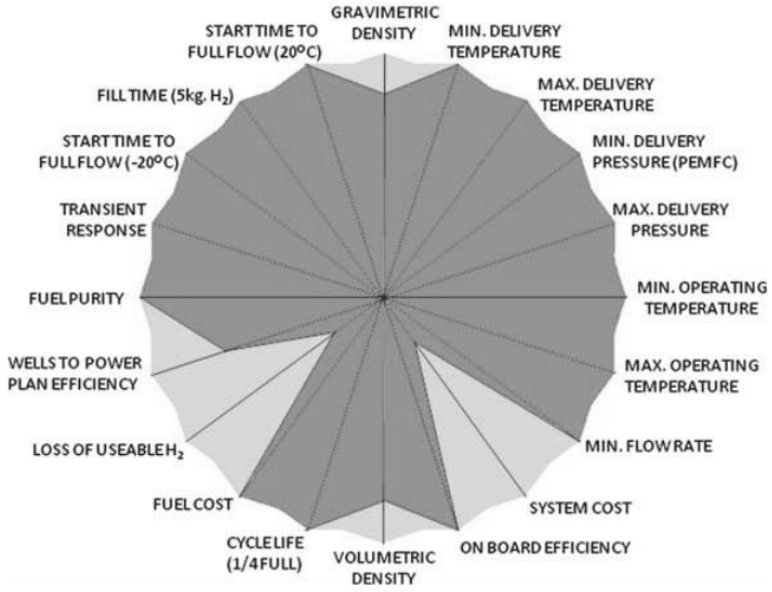

Figure 2.8 - A representative cryo-adsorbent (AX-21) against the DOE's 2010 targets. Reprinted from [71] with permission.

In Figure 2.8, a cryoadsorbent system is assessed, using AX-21 "superactivated" carbon. The system is shown to meet completely 15 requirements – minimum and maximum delivery temperature, minimum and maximum delivery pressure, minimum and maximum operating temperature, minimum full flowrate, on-board efficiency, cycle-life, fuel cost, fuel purity, transient response, start time to full flow at -20 and 20 ^{o}C and fill time. The system has 3 targets at 40 % of the requirement – gravimetric and volumetric density and wells to power plant efficiency - and has two targets below 40 % - system cost and loss of useable hydrogen.

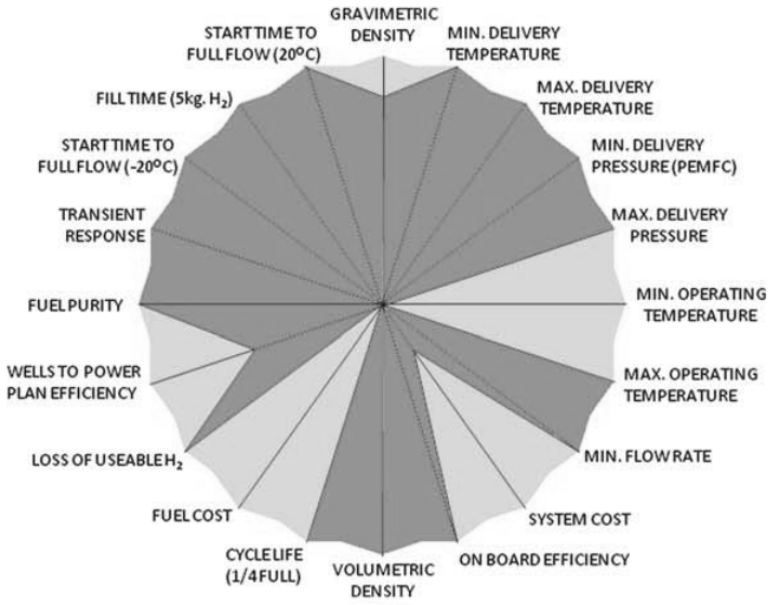

Figure 2.9 – A representative chemical hydride (ammonia borane) against the DOE's 2010 targets. Reprinted from [71] with permission.

In Figure 2.9, the evaluation of a chemical hydride system – ammonia borane, H_3NBH_3 – is shown to meet and fully satisfy 15 requirements – minimum and maximum delivery temperature, minimum and maximum delivery pressure, maximum operating temperature, minimum full flowrate, on-board efficiency, volumetric density, cycle-life, loss of usable H_2, fuel purity, transient response, start time to full flow at -20 and 20 ^{o}C, and fill time. Two requirements are above 40 % - gravimetric density and wells to power plant efficiency, one target is below 40 % - system cost – and two targets are undetermined – minimum operating temperature and fuel cost.

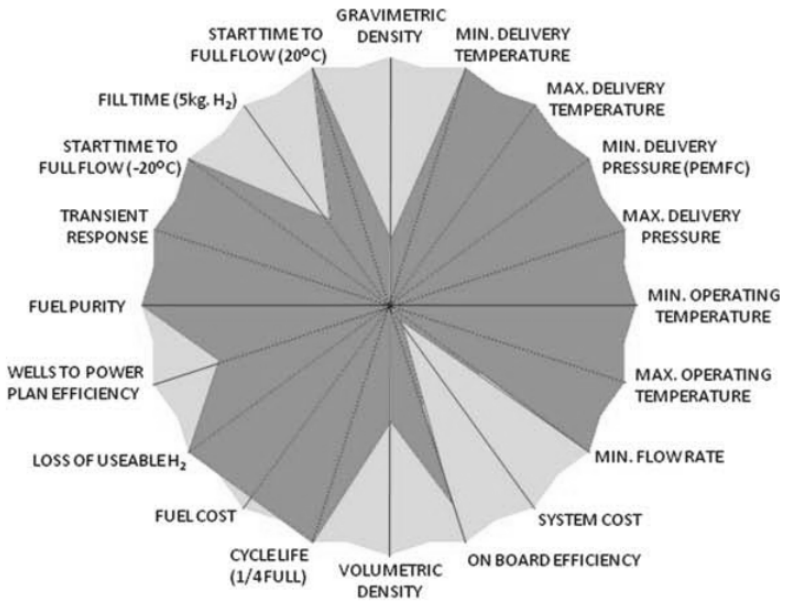

Figure 2.10 – A representative metal hydride system ($NaAlH_4$) against the DOE's 2010 targets. Reprinted from [71] with permission.

As it can be observed, metal-hydride systems fully fulfil 13 criteria – minimum and maximum delivery temperature, minimum and maximum delivery pressure, minimum and maximum operating pressure, minimum flowrate, cycle-life, loss of useable H_2, fuel purity, transient response and start time to full flow at -20 and 20 ^{o}C – meet five requirements above 40 % - on-board efficiency, volumetric density, fuel cost, wells to power plant efficiency and fill time – and are below 40 % requirements on two targets - gravimetric density and system cost.

In recent years, there has been considerable effort and the number of prospective hydrogen storage materials has experienced tremendous growth. Meeting all the requirements from the DOE remains elusive, despite some fantastic developments, either for adsorbent materials with ultra-high surface areas or for new hydride materials. Different hydrogen storage systems are explained in the following pages, starting with mature methods like compression and liquefaction, discussing the different types of chemical storage and other methods for storing hydrogen currently being developed. Adsorptive storage of hydrogen is discussed separately in the next section, as it is the hydrogen storage method considered in this thesis.

2.4.3. Mature methods – compression and liquefaction for hydrogen storage

Two mature methods used in industry to store hydrogen by increasing its volumetric density are compression and liquefaction. Compression is the industry standard for storing hydrogen and it involves increasing the pressure at ambient temperature up to 35 or 70 MPa, with the hydrogen stored in a cylinder. The cylinders are designed to withstand high pressures, with volumetric densities of contained gas ranging from 20 to 50 kg m^{-3}, and gravimetric densities (for the system) in the range of 5 to 10 % [72]. Standard compression has been used for industrial applications since it is a fairly mature method so there is availability of materials and standards for production, safety and transport. Compression is an obvious choice for storing hydrogen, since compressing hydrogen from 35 MPa decreases the storage volume by 99.6 % [72]. This can be even further pressurised to decrease the volume, but it increases the compression work and carries safety concerns. Nonetheless, compressed gaseous hydrogen also exists at 70 MPa. There are different types of compressed gaseous hydrogen cylinders, mostly made from steel and aluminium alloys. The choice of material is relevant, since molecular hydrogen can dissociate at metal surfaces and atomic hydrogen is known to diffuse into the materials and cause embrittlement. Cylinders are usually classified as Type I (made of stainless steel or aluminium), with volumes ranging from 2.5 to 50 dm^3 [72], Type II and Type III containers (made from composite materials, which can have a thin layer of steel, aluminium or carbon fibre to achieve the desired properties) and Type IV, which are also composite materials, but lighter materials than Type II or III [72]. The different types of hydrogen tanks have different operating pressures (typically 35 or 70 MPa), with volumes varying from 50 to 200 dm^3 and volumetric densities ranging from 16 kg H_2 m^{-3} to 26 kg H_2 m^{-3} [72]. Safety concerns on compression storage include hydrogen embrittlement of metals at room temperature, a temperature rise in fast filling processes and potential risks such as diffusion, deflagration and detonation after accidental hydrogen leakage [73].

Another method that could be used for storing hydrogen involves using cryogenic compression. This method has also been investigated as a potential hydrogen storage

system and its proponents argue that it has increased advantages over many methods. Cryogenic compression could significantly increase volumetric density, but adds the need for the cylinder to be at extremely low temperatures, typically at normal liquid nitrogen temperature (~ 77 K). Insulated pressure vessels have the capacity to operate at low temperatures (as low as 20 K) and at high pressures (up to 24.8 MPa) [74]. Compressed hydrogen at 80 K and 24.8 MPa is nearly as dense as liquid hydrogen, so it can be used for long-range mobile applications without excessive weight, volume or concerns regarding the low temperatures used in liquefaction. While there are issues related to losses of hydrogen, these are not as serious as in the liquid form, since temperatures involved are higher. The vessel, however, has to withstand high pressures while being insulated at the same time. Cryogenic vessels are an attractive solution for the storage of hydrogen, since they combine properties from both room temperature compression and liquefaction of hydrogen. Furthermore, some issues related to liquefaction are not as significant in cryogenic compression and there is also the extra alternative of simply compressing the hydrogen if the low temperature option is not available.

Liquefaction is another mature method for storing hydrogen. In liquefaction, hydrogen is cooled below its boiling point, thus turning into a liquid. One of the main advantages when considering liquid hydrogen storage is the high volumetric capacity, since liquid hydrogen has a volumetric density higher than 70 kg m^{-3}. There are several issues to consider in liquefied hydrogen storage for mobile applications, with the main ones relating to the energy penalty associated with the low temperatures involved and the safety and boil-off of liquid hydrogen [68]. The boil-off is an issue especially during refuelling, since liquid hydrogen boils off readily when exposed to heat and this causes a pressure rise in the storage tank. To keep the tank at the desired pressure, this hydrogen vapour is vented from the storage system, which involves a significant loss of energy. Since some of the liquid hydrogen also vaporises in the storage system, this decreases the overall efficiency. An additional drawback of liquid hydrogen is, if inactive for a long period of time, the hydrogen will boil off. This dormancy issue can be observed when the vehicles are parked for a long time and even multi-layered vacuum insulation has not prevented this from happening [75]. On the other hand, liquid hydrogen has been considered for large scale storage of hydrogen or when long range transport is needed, much the same way as liquefied

natural gas (LNG) because it allows for higher volumetric storage densities [76]. Even if it carries a high energy penalty associated with low temperatures, the benefits of liquefying hydrogen and transporting it with high volumetric densities counterbalance the drawbacks. LNG can be seen as an example, since in 2002, 26 % of all natural gas traded internationally was in its liquid form [76]. In Table 2.4, the parameters for the different storage systems, with densities of hydrogen, system requirements, operating conditions, as well as other properties from the storage system are depicted.

Table 2.4 – Parameters for storage vessels – compressed hydrogen, cryogenic pressured vessel and liquid hydrogen tank. From [77].

Parameter (unit)	**Compressed H_2 cylinder**	**Cryogenic pressured vessel**	**Liquid hydrogen tank**
External volume (dm^3)	237	126	135
Internal volume (dm^3)	216	81.2	78.5
Maximum Pressure (MPa)	34.4	34.4	0.69
Total mass of H_2 (kg)	5	5.17	5
Volumetric density (kg H_2 m^{-3})	21.1	41.1	37.1
Insulation thickness (cm)	-	1	5
Total vessel weight (kg)	37.0	66.0	31.3
Maximum vehicle range (km)	640	640	640

As seen in Table 2.4, cryogenic pressured vessels are an attractive solution for the storage problem and they offer the highest volumetric density. The only downside for cryogenic compression is the weight of the vessel, which is somewhat higher than liquid hydrogen tanks and compressed cylinders, but storing the same amount of hydrogen (~ 5 kg) with much less volume occupied in the vessel. Also, the insulation of the vessels and the boil-off are less significant, since the operating temperature is higher than the one used in liquid hydrogen tanks.

2.4.4. Storing hydrogen as a chemical

Another intensively researched area for hydrogen storage has been storage in a chemical compound. In this type of storage, molecular hydrogen dissociates and reacts with an element, forming a hydride compound which in some cases has high gravimetric hydrogen density. There is extensive literature on hydrogen storage in hydrides and they are typically divided into conventional metal hydrides, complex hydrides and chemical hydrides. In some cases, high gravimetric capacities can be attained, but the dehydrogenation of the materials is still difficult, since it involves high temperatures [56, 68]. While the materials are stable when hydrogen is stored and most materials store H_2 at ambient pressures and temperatures, the temperatures needed for dehydrogenation of the materials are typically very high. There are also some reversibility issues with some of them, meaning that not all of the capacity can be used after a number of cycles. As previously mentioned, chemical storage differs from physical storage since it involves dissociation of the hydrogen molecule. In solid-state chemical storage, the hydrogen molecule is first attracted to the surface of the metal, leading to a physisorbed state. When it is close to the surface, it dissociates and forms a hydrogen-metal bond, making the hydrogen molecules chemically adsorbed (chemisorption). The chemisorbed hydrogen has high mobility and can form a different phase with the host material at high coverage [78]. In the next step of the process, the hydrogen can jump to the subsurface layer and diffuse into the interstitial sites [78].

Most metals, intermetallic compounds and alloys react with hydrogen and form solid hydrides. The distinction between the different types of hydrides for hydrogen storage is not clear, but they can be categorised as conventional metal hydrides, complex hydrides and chemical hydrides [78-80]. Conventional metal hydrides are compounds formed by reaction of hydrogen with a metal or metal alloy, which are usually stable at ambient conditions. When the structure of the metal does not topologically change, the compounds are named interstitial hydrides, since the H atoms are inserted in the interstitial sites. Examples of interstitial hydrides include PdH, (Vi-Ti-Fe)H_2 and $LaNi_5H_x$. When a new structure forms upon hydrogen absorption, the hydrides are

called structural hydrides, with magnesium hydride (MgH_2) and AlH_3 being good examples [79].

Complex hydrides are another type of solid hydrogen storage system. Complex hydrides are ionic hydrogen compounds which have a metal cation (usually a lightweight alkali or alkaline earth Li, Na, Mg or Ca) and hydrogen "complex" anions, such as borohydrides (BH_4^-), alanates (AlH_4^-) and amides (NH_2^-). The hydrogen atoms are covalently or ionically bonded to the central atoms [79]. Examples of high capacity complex hydrides include borohydrides, alanates, nitrides, amides and imides [80]. Alanates are compounds formed with aluminium, which usually dissociate in two steps. A good example of an alanate is magnesium alanate [$Mg(AlH_4)_2$], which has a gravimetric capacity of 9.3 wt. % [81]. Borohydrides (BH_4^-) are another type of complex hydrides and one which has high gravimetric density materials. Lithium borohydride ($LiBH_4$), for instance, has a gravimetric capacity of 13.9 wt.%, but these materials suffer from the high dehydrogenation temperatures, which prevents their use [79]. Nitrides, amides and imides are all based on the N-H system and good examples are the lithium imide (Li_2NH), lithium amide ($LiNH_2$) and lithium nitride (Li_4NH). Other materials that have been considered apart from lithium include magnesium, calcium and cesium [80]. However, these materials have some considerable drawbacks, including the temperatures involved, sensitivity to air and moisture and the ammonia formed upon dehydrogenation, which can poison the fuel cell [80].

Arguably, the materials that have received the most attention are the magnesium hydrides, the sodium alanates and the borohydrides. As mentioned, one of the main problems with using hydride materials are the temperatures of dehydrogenation [79]. Kinetics and diffusion in the materials are not optimum, which means that more research has to be conducted to overcome some of these issues [79]. Nonetheless, hydride storage is a very active field of research and could provide interesting solutions for hydrogen storage.

In Table 2.5, the volumetric and gravimetric densities of some example hydrides are presented. Although some of these properties are very interesting for hydrogen storage systems, the temperatures involved add a substantial drawback to these

systems. In addition, for some cases there are issues related with reversibility of the materials, meaning that they cannot withstand many hydrogenation and dehydrogenation cycles.

Table 2.5 – Volumetric and gravimetric densities and absorption/desorption temperature for metal and complex hydrides.

Hydride	Gravimetric capacity wt.%	Volumetric capacity g H_2 L^{-1}	Absorption/desorption temperature ^oC	References
$LaNi_5H_6$	1.49	108	12	[82]
MgH_2	7.7	109	195	[83]
$LiBH_4$	13.9	93	322	[83]
$Mg(AlH_4)_2$	9.3	72.3	110-200 – 1st 240-380 – 2nd	[81]
$Mg(BH_4)_2$	14.82	146.5	320	[81]
$NaBH_4$	10.57	113.1	505	[81]

Amine-borane adducts have also been investigated as hydrogen storage systems and a simple ammonia-borane BH_3NH_3 contains 19.6 wt. % in hydrogen, which can be delivered at 130 ^oC in a multistep decomposition process. Since the decomposition is exothermic, these materials are not suited for reversible on-board hydrogen storage [68]. Chemical storage of hydrogen also encompasses research into liquid hydrogen carriers, which consist of the hydrogenation and dehydrogenation of cyclic hydrocarbons (benzene and cyclohexane), toluene and methylcyclohexane or naphthalene and decalin. These systems have reasonable storage capacities between 6.1 wt. % (for methylcyclohenaxe) and 7.1 wt. % (cyclohexane) or 7.2 wt. % for decalin and volumetric densities between 47 and 65 kg m^{-3}. These also carry some problems, since, for rehydrogenation, the required temperatures are above 300 ^oC and the hydrocarbon cannot be regenerated on-board [68].

2.5. Adsorptive storage of hydrogen

Adsorptive storage of hydrogen is a possible alternative to conventional methods because it can store large quantities of hydrogen without incurring high energy and materials' penalties. In comparison with mature methods such as liquefaction or compression of hydrogen, adsorption of hydrogen has the inherent advantage of requiring less stringent operating conditions. Nonetheless, since adsorptive storage

also involves lower temperatures and higher pressures than ambient, careful study, analysis and comparison with other methods has to be done. Also, the benefits in amounts stored at milder conditions have to be weighed against a number of other requirements, like weight and density of the adsorbent, adequate diffusion for fast charging and discharging of hydrogen, cost, reliability and safety. The growing number of new porous materials has made adsorptive storage one of the best prospective technologies to store hydrogen. In this section, physisorption of hydrogen in porous materials is reviewed and some materials that have been studied for hydrogen storage are introduced and discussed.

2.5.1. Physisorption of hydrogen on a porous material

Compression is usually done at 35 or 70 MPa, making the cylinders that can withstand those pressures very heavy and bulky for light-duty vehicles [84]. The temperatures required for hydrogen's liquefaction are usually around 20 K, due to the physical properties of molecular hydrogen and there is a large energy penalty involved in attaining temperatures in that range [84]. The storage conditions involved in these two methods also require that the storage system has to withstand high pressures or low temperatures for a large duration of time. Additionally, as already observed, safety is an issue, since a large compressed cylinder or a very cold system might not provide the most appropriate and safe storage system, especially when considering mobile applications. Due to all these shortcomings, a system that could store equal amounts of hydrogen without the need of high pressures or low temperatures would pose as a very attractive alternative. Adsorptive storage in a high-surface area porous material has been studied since it can compete with these alternatives in amounts stored, at milder operating conditions of temperature and pressure than its counterparts. One of the advantages of using adsorption to store hydrogen is that the storage is fast and completely reversible, with the hydrogen not dissociating and maintaining its molecular form [84]. The storage works without any temperature change and only requires a pressure increase and drop to store and release the hydrogen. Although failing to meet some requirements for an ideal hydrogen storage system, as already discussed previously, adsorbing hydrogen in a high-surface area material is one of the most intensively researched areas for hydrogen storage.

Adsorption is a physical phenomenon that occurs at the surface of a solid porous material. Adsorption can be differentiated between chemical adsorption (chemisorption) and physical adsorption (physisorption). In chemisorption, the molecule usually dissociates at the surface, with enthalpies of adsorption equalling enthalpies of reaction (~100 kJ mol^{-1}) [78]. Physisorption does not involve the dissociation of molecules at the surface, which means that molecules maintain their molecular identity. In physisorption, the enthalpies of adsorption are usually very weak, between 5-15 kJ mol^{-1} [84]. Physisorptive storage of hydrogen relies on weak van der Waals forces, specifically London dispersion forces (or instantaneous dipole forces), present in the induced polarisation of the molecules due to delocalisation of the electron cloud [78]. This means London forces are present even in molecules that do not have permanent polarity. This surface effect is enhanced in porous materials, since London forces created by the overlapping potential of the walls in the pores attract molecules to the surface. Even a weak interacting molecule like hydrogen has dispersion forces, which create instantaneous polarity and are attracted to the surface of the material, especially to the pores, which is where the overlapping potential is created. This effect enhances the concentration of adsorbate in the pore [68].

Solid-gas adsorption systems are composed of three distinct parts – the adsorbent, which is the solid material with porosity, the adsorptive, which is the gas and the adsorbate, which is the enhanced concentration of the gas in the vicinity of the surface due to the adsorptive forces. Adsorption is a very active research subject and it has seen applications in various areas, including physics, chemistry, biology and engineering. It is the basis for many industrial processes, such as wastewater treatment, gas separation and purification and catalysis. Experimentally, adsorption is oftern measured in pressure-composition-temperature (PCT) diagrams, with the most common the adsorption isotherm, which involves the measurement of the adsorptive capacity, *i.e.*, molar quantity in a material, at constant temperature with increasing pressure. The isotherms depend on the system, temperature and conditions. They can be grouped into 6 main types, as described by the International Union of Pure and Applied Chemistry (IUPAC) [85].

In Figure 2.11, the representative six different types of isotherms according to IUPAC are shown. The differences in isotherms are linked to the material and type of interaction.

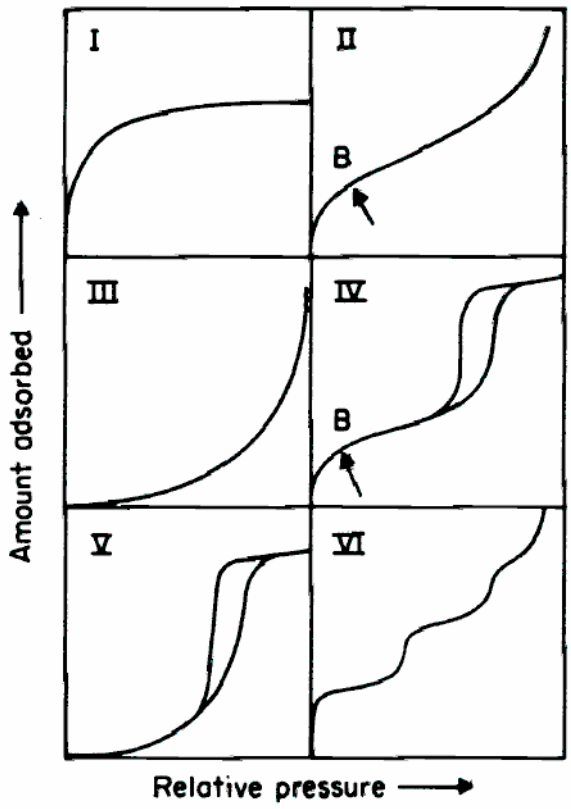

Figure 2.11 – Types of physisorption isotherms. From [85] and used with permission of IUPAC©.

There is an important distinction to make, regarding the adsorbent materials. The nature of the interactions and therefore, the adsorption isotherms, depend greatly on the structural morphology of the material, especially its pore size. Materials are classified by IUPAC according to their pore size, which can be in the micropore (pores below 2 nm), mesopore (pores with sizes between 2 and 50 nm) and macropore range (pores with sizes bigger than 50 nm) [85].

An IUPAC type I isotherm is characteristic of adsorption in a microporous material. Type I equations have a horizontal asymptote, which they approach monotonically and are obtained when adsorption is in monolayers (one layer) or few molecular layers. They are also indicative of chemisorption, since as uptakes approach the asymptote, it indicates that the active sites on the surface are being occupied. Type II sorption isotherms are usually obtained for non-porous or macroporous adsorbents,

where mono or multilayer adsorption can occur. Type III isotherms are rare, but they can occur when adsorbent-adsorptive interactions are weak and adsorptive-adsorptive interactions dominate. Type IV isotherms usually occur in mesoporous materials and they have a characteristic hysteresis loop, due to pore condensation. Hysteresis and pore condensation are also present in type V isotherms, but they differ from type IV because the initial part of the isotherm is related to the type III isotherms, which are indicative of weak interactions between adsorbent and adsorptive. Finally, type VI isotherms are stepwise multilayer adsorption on a uniform, non-porous surface, especially for symmetrical, non-polar adsorptives [85]. Donohue and Aranovich expanded on this isotherm classification, including subcritical, near critical and supercritical isotherms for some of the different types. Supercritical adsorption in a microporous material, as indicated by Donohue and Aranovich, does not have a monotonic crescent Gibbs isotherm (or excess isotherm) [86].

As discussed in the physical properties section, hydrogen is a very low interacting molecule and this is reflected in its extremely low melting and boiling point. The forces involved in adsorptive storage are very weak and no bond with the host material is observed, making adsorptive storage very dependent on the temperature of the system. This means that significant storage only occurs at extremely low temperatures and high pressures. The storage capacity also depends on the materials' characteristics, like its pore volume and its specific surface area, usually measured with nitrogen at 77 K and using the Brunauer-Emmett-Teller (BET) method [87]. Both the micropore volume (available volume in the pores below 2 nm) and the BET specific surface area seem to correlate well with hydrogen uptake at 77 K [88]. For adsorptive storage of hydrogen, the emphasis is put on testing or synthesising materials with a high-surface area and pore volumes adequate for the storage of hydrogen. In the last decade, there has been a surge in materials with increased surface areas to serve as prospective hydrogen storage materials. From new synthetic materials, like metal-organic frameworks (MOFs) and derivatives, to porous polymers and carbon materials, including nanotubes or graphene, all have been proposed as possible hydrogen storage materials.

Adsorption, due to the nature of the hydrogen-solid interaction, depends on the surface chemistry and porosity of the material. For hydrogen, the low energies of

interactions involved require a high-surface area made mostly with small pores and low temperatures and pressures for the uptake to be of any significance [88]. These requirements mean that only high-surface area materials with pores in the micropore region would be suitable as prospective hydrogen storage materials and that the operating conditions required would still be different from ambient conditions. The challenge is to find better hydrogen storage materials and bring the operating conditions as close to ambient as possible, to minimise the energy and materials penalties associated with low temperatures and high pressures. Different porous materials have been discovered and studied over the years, the main ones being zeolites and carbons. Recently, new synthetic materials were discovered which improved vastly on specific surface area. At the forefront of this new wave of synthetic materials are MOFs, which have received considerable attention in the last years.

For hydrogen storage materials, the uptakes are closely connected to the available pore volume and surface area. The challenge is to synthesise materials, with the porous structure in the micropore range (some authors argue that 0.7 nm is the pore size ideal for hydrogen adsorption [89-96]) to improve the thermodynamics of the interaction and possibly bring the temperatures closer to ambient [97]. Prospective adsorptive hydrogen storage materials are discussed in the next part of this chapter, with an introduction to MOFs, carbon materials and other porous materials which have studied for hydrogen storage.

2.5.2. Metal-organic Frameworks

MOFs are a new class of synthetic materials which have been recently discovered. They are sometimes referred to as porous coordination polymers or hybrid porous solids [98]. MOFs are porous crystalline materials which consist of molecular building blocks composed of metal centres joined by organic linkers materials with permanent porosity [99]. The variety of linkers and metal centres has made possible for a huge number of these materials to have been synthesised and their properties studied [100]. Due to the possibility of building molecules with large void spaces within them, an important application of MOFs and one of the first ones to be studied

has been gas storage [101]. MOFs however, have the potential to find applications in catalysis [102], gas separation and sensing [103]. Their magnetic properties and luminescence are also being studied for prospective applications [103]. MOFs have also found applications in biology, especially in drug delivery systems and in imaging [104-108].

Table 2.6 - Some properties of high surface area MOFs.

MOF	Metal and organic linker	BET specific surface area / $m^2\ g^{-1}$	Micropore volume$^+$ / $cm^3\ g^{-1}$	Excess H_2 uptake, in wt.% (*T*,*P*)	Ref.
MOF-5	Zinc metal centres joined by benzene dicarboxyate linkers	3,800	1.55	7.1 (77 K, 4 MPa)	[99, 109]
ZIF-8	Zinc metal centres joined by imidazolate linkers	1,947	0.63	3.1 (77 K, 5.5 MPa)	[110]
UMCM-2	Zinc metal centres joined by benzenetribenzoate and thieno thiophene-dicarboxylate	5,200	2.32	6.9 (77 K, 4.6 MPa)	[111]
MOF-177	Zinc metal centres connected by benzenetribenzoate linkers	4,630	1.69	7.3 (77 K, 5.2 MPa)	[112, 113]
MIL-101	Chromium metal centres joined by benzene dicarboxylate linkers	4,230	2.15	6.1 (77 K, 8 MPa)	[114-116]
NOTT-101	Copper metal centres joined by terphenyl tetracarboxylic linkers	2,247	1.08	6.06 77 K, 2 MPa)	[117]
MOF-210	Zinc metal centres joined by a mixture of benzene tribenzoate and biphenyl dicarboxylate linkers	6,240	3.6	8.6 (77 K, 8 MPa)	[118]
NU-100	Copper centres joined by hexacarboxylate linkers	6,143	2.82	9.95 (77 K, 5.6 MPa)	[119]

$^+$Micropore volumes for MOF-5, MOF-210 and NU-100 were calculated from Grand Canonical Monte Carlo simulations of adsorbed N_2. Pore volumes for ZIF-8, UMCM-2, MOF-177 and NOTT-101 are the crystallographic pore volumes. Pore volume for MIL-101 was calculated using the nitrogen adsorption at 77 K and the Dubinin-Radushkevich method [120, 121].

MOFs have been pushing the boundaries on high-surface area materials, with some recently synthesised MOFs reaching extremely high specific surface areas. The first

MOF with permanent porosity was reported in 1999 (MOF-5) [122] and ever since, thousands have been synthesised and used in a number of applications. MOF synthesis has been a very active research area in synthetic chemistry in recent years. Some landmark MOFs have been synthesised, becoming quite popular due to their high BET specific surface area. The first reported MOF was MOF-5 in 1999, which had a BET specific surface area of 3,800 m^2 g^{-1} [122]. In the last years MOFs have been synthesised with BET specific surface areas in excess of 6,000 m^2 g^{-1}. Prominent MOFs include UMCM-2 [111], MOF-177 [112], MIL-101 [116], NOTT-101 [117], MOF-210 [118] and NU-100 [119]. One variation of MOF materials are Zeolitic Imidazolate Frameworks (ZIFs) [110]. These materials follow the structure of zeolites, but instead of silica and alumina tetrahedral units, they are composed of transition metals and imidazolate units. One of the advantages of ZIFs is that they are chemically and thermally stable, while offering high surface areas. ZIF-8 has a BET specific surface area of 1,947 m^2 g^{-1} and excess hydrogen uptake of 3.1 wt. % at 77 K and 5.5 MPa [110]. These MOF materials and an example ZIF material (ZIF-8) [110], their BET specific surface area, pore volumes and hydrogen uptakes are presented in Table 2.6.

As can be observed in the table, MOFs have reached extremely high BET specific surface areas, pore volumes and hydrogen uptakes, making them candidates of choice for hydrogen storage materials. It has recently been suggested that the theoretical limit for BET specific surface areas in MOFs is above 14,000 m^2 g^{-1} [123], which means that, despite the spectacular advances seen in materials' synthesis, there might still be a long way to go in synthesising MOFs with higher BET specific surface areas. The premise for MOFs synthesis is to create rigid, repeating frameworks with solvents in the void volumes, which are then removed without collapsing of the structure [124]. In order to achieve this, the structures have to be rigid enough to cope with the large void fractions within them. One important step is the activation of MOFs for gas sorption studies, which has been achieved with thermal activation or, when solvents are non-volatile, solvent exchange or supercritical carbon dioxide activation [125].

In addition to this, MOFs add the facility of being, in principle, completely tuneable. The variety of linkers and metal centres and the possibility of post-synthetic modification of the materials, means that a material could be completely tuned for

hydrogen adsorption. Some authors identified the different factors contributing to higher hydrogen uptakes. Rowsell and Yaghi reported a number of different hydrogen storage strategies for MOFs [126]. At the top of the list are materials which possess high porosity with a suitable pore size. Smaller pore sizes are more appropriate for hydrogen storage, as they increase the density of the adsorbed hydrogen [126]. Another technique to improve hydrogen adsorption in MOFs is impregnation with a non-volatile guest or catenation by another identical framework [126]. Impregnation with some elements provides additional attractive sites, which could improve the energetics of adsorption and bring temperatures closer to ambient [126]. Catenation is another technique that can be used to enhance hydrogen adsorption. Catenation in MOFs can be of two forms – interweaving and interpenetration [126]. The differences in the two reside in the framework displacement – it is maximally displaced in interpenetration and it is minimally displaced in interweaving [126]. Although catenation reduces the diameter in the pores, it can provide optimal porous morphologies for hydrogen adsorption – high surface areas with small pore sizes [126]. Interweaving reinforces the structure of the frameworks but interpenetration is considered more suitable for hydrogen adsorption, since it maximizes the exposed surfaces of the frameworks [126]. Another attractive structural feature in MOFs and one that has been explored to maximize uptakes of hydrogen is the existence of open metal sites in the frameworks [127, 128]. MOFs are synthesised with metal centres, which in some cases have terminal ligands bounded to them. If proper activation is done on the material, these terminal ligands can be removed from the framework without collapsing the structure. These coordinated unsaturated metal centres can be part of the periodic array of the MOF and are preferential sites for hydrogen adsorption [126].

Another important feature present in MOFs is the structural change that can be induced in some materials [129, 130]. A prominent example of this is the flexibility displayed by some materials upon adsorption of a gas, which induces a dynamic change in the material. These changes can include stretching, rotating, “breathing” and scissoring mechanisms [129]. As discussed by Fletcher et al., gating and step changes processes involve structural transformations of the material upon adsorption of hydrogen, which can all be interesting routes to explore in the design of hydrogen storage materials [129].

Spillover is another technique that has been studied for hydrogen storage [131-133]. This is a phenomenon known for decades and especially important in catalysis. In hydrogen storage, structures are doped with noble metals, which cause the hydrogen to dissociate and migrate to the carbon layers [131-133]. Spillover, according to some authors, is completely reversible, since the hydrogen turns to its molecular form upon desorption and it can be done on carbon and MOF supports. The application on hydrogen storage resides in the fact that it can enhance the uptakes, even at room temperature. However, spillover for hydrogen storage has been controversial, with authors arguing the enhanced results and the proposed mechanism [134-137]. Doping MOFs is also interesting for hydrogen adsorption, especially the insertion of Li in the structures [138-140]. The cation exchange of Li^+ increases the accessible pore volume in the structure but lowers the adsorption enthalpy, due to higher pore sizes [140].

Summarising, MOFs are one of the most promising classes of hydrogen storage materials, because of the immense realm of possibilities they offer. Not only can MOFs surpass other known materials in terms of pore volumes and surface areas, they are extremely tuneable, which means that structures can be optimally designed for higher hydrogen uptakes. Industrial applications for MOFs are also being studied, as well as the synthesis scale-up of these compounds [141, 142].

2.5.3. Carbon materials

Carbon materials are probably the most studied class of adsorbent materials, with numerous applications in catalysis, gas separation and storage and others. There are many advantages of using carbon adsorbents, and their popularity is due to price, availability, durability and specific properties [143]. Carbon materials have long been known as adsorbents for chemical processes. They are being considered as potential hydrogen storage materials because of their low cost, accessibility, recycling characteristics, low density, geometrical variety, extensive pore structure, stability and because they can undergo structural modifications using different preparations, carbonizations and activations [144]. The allotropes of carbon that have been investigated for hydrogen storage are activated carbons, single-walled carbon nanotubes, multi-walled carbon nanotubes, nanohorns, nanofibers, graphene (strictly,

it is not an allotrope, since it is a single planar sheet of sp^2 bonded carbon atoms), templated carbons and carbide-derived carbons [145]. The differences in these materials consist on the packing of the carbon atoms. For activated carbon, the carbons are layered in sheets (graphene sheets) which are packed tightly and create a porous structure [145]. The packing of the graphene sheets makes activated carbons amorphous, meaning that they have no defined long-range macro structure. The synthesis and activation methods adopted can lead to large differences in porosity of the materials. Many different carbons have been synthesised from a huge variety of precursors that are then oxidised to create the carbon structure [145].

For hydrogen storage in microporous activated carbons, there has been some disparity of theoretical and experimentally measured uptakes, due to chemical and structural complexity and heterogeneity of the activated carbons. Room temperature adsorption of hydrogen in microporous carbons has not exceeded 1 wt.%, even at pressures as high as 10 MPa for high surface area materials. A good example of a microporous activated carbon is AX-21, the "superactivated" microporous carbon that showed 5.2 wt. % excess hydrogen uptake at 77 K and 2.9 MPa [146]. Poly ether ether ketone carbons (PEEK carbons) are another class of microporous carbon materials. They result from the burning of poly ether ether ketone in CO_2 or steam, resulting in high surface area microporous carbons, with BET specific surface areas ranging from 500 to 3,200 $m^2\ g^{-1}$ [147]. Their excess hydrogen uptakes were found to be 3.0 and 2.2 wt. % for PEEK-ST-9-70 and PEEK-CO_2-9-26 at 0.2 MPa and 77 K [147].

Another class of carbon material which has been extensively studied for hydrogen storage are carbon nanotubes. These can be single- (SWCNT) or multi-walled carbon nanotubes (MWCNT) and they have been subject to a number of different studies on hydrogen adsorption. There has been many contradicting reports in hydrogen storage on carbon nanotubes and the interest they once elicited has somewhat dwindled. The disparity observed in many reports, probably due to purity of samples or experimental error, makes a consensus between the different experiments very difficult to reach. Uptakes for SWCNT and MWCNT have been reviewed and they range from 0.1 to 21 wt. % [144, 145]. As an example SWCNT, one sample of highly pure SWCNT (HiPco^{TM}, Carbon Nanotechnologies Inc., USA) was treated with nitric acid (SWCNT-HNO_3) and showed a 1.8 wt. % uptake at 0.1 MPa and 77 K [148].

However, hydrogen storage in carbon nanotubes is still investigated, despite the interest being much less than it was a decade ago. In 1997, carbon nanotubes reported hydrogen uptakes of above 30 wt. % in a study by Dillon and colleagues [149] but lack of confirmation of these results by other laboratories has somewhat discredited these results. Graphitic nanofibres are another class of carbon materials studied for hydrogen storage. These nanofibres are graphene sheets arranged in parallel, perpendicular or angular orientation with respect to the axis, with just the graphene edges exposed [144]. Graphitic nanofibres showed large uptakes of hydrogen, even at room temperature, but it has been strongly suggested that this might be due to the impurity of the fibres, which are usually synthesised in the presence of catalysts. Catalysts present in the structure would bind strongly to the hydrogen, and contribute to higher uptakes [144]. Graphene is another type of carbon material that has been considered for hydrogen storage. Graphene is a two-dimensional, one-atom thick crystal composed of carbon atoms, which are arranged in honeycomb geometry, and it possesses extraordinary properties, including strength, flexibility and electronic conduction [150]. The properties of graphene make it an ideal material with many applications and it has also been studied as a potential hydrogen storage material. If only a monolayer of hydrogen is formed on the surface of graphene, the gravimetric density is limited at 3.3 wt. % (doubled if the two sides of the graphene are considered) [150]. The volumetric density however, depends on the packing of the graphene sheets. Uptakes for graphene layers with an optimal separation can be higher, with theoretical studies predicting 6 wt. % at 77 K and 0.1 MPa [151].

Nowadays, promising hydrogen uptakes in carbon materials are seen in templated carbons. Templated carbons (TCs) are materials which are carbonised in the presence of a template, which can create nanoporosity in the samples [152]. They vary according to the template used and they can use anodic-aluminium oxide as a template (AAO-TCs), carbon inverse opals (CIOs), which use close packed spheres to template the carbons, ordered mesoporous carbons (OMCs), which use hard mesoporous silicas as templates and zeolite templated carbons (ZTCs), which use zeolites as templates for carbons [152]. An example of these materials is the OMC CS48, which is a carbon derived from a sucrose precursor and templated with MCM-48. The silica was impregnated with sucrose and sulphuric acid, heated for carbonisation and then dissolved [153]. The obtained surface area was 2,390 m^2 g^{-1} for the OMC CS48 and

the excess hydrogen uptake was 3.5 wt. % at 77 K and 1 MPa [153]. An example of the ZTC is the CB850h, which was synthesised *via* chemical vapour deposition of an acetonitrile precursor and zeolite β as the hard template, and heated at 850 ^{o}C [154]. CB850h was further heated under nitrogen flow. This material exhibited a surface area of 3,150 m^2 g^{-1} and an hydrogen uptake of 5.7 wt. % at 77 K and 1 MPa [154].

Another class of specifically tuned materials are carbide-derived carbons (CDCs) [155, 156]. These materials are formed from carbon precursors which are transformed into carbon by physical or chemical processes, which can be thermal decomposition or halogenation [155]. A variety of carbide precursors can be used (SiC, TiC, Mo_2C, VC) and the porosity depends on the precursor used. The differences in pore sizes make the CDCs useful for identifying the pore volumes more appropriate for hydrogen adsorption [89, 90, 93-95]. A CDC that displayed a high hydrogen capacity was recently reported. Zirconium CDC (Zr-CDC) was synthesised and heated at 800 ^{o}C and chlorinated [96]. It was then mixed with KOH and heat treated under nitrogen flow, with temperatures ranging from 600 to 900 ^{o}C [96]. The sample with the highest uptake was the one heated at 900 ^{o}C, Zr-CDC-KOH-900 [96]. The properties of different carbon adsorbents tested for hydrogen storage are compiled in Table 2.7.

Table 2.7 – Properties of some example carbon adsorbents.

Material	**BET specific surface area / m^2 g^{-1}**	**Micropore volume^{+} / cm^3 g^{-1}**	**Excess H_2 uptake, in wt.% (*T*,*P*)**	**Ref.**
AX-21	2,780	0.86	5.2 (77 K, 2.9 MPa)	[146]
SWCNT – HNO_3	710	-	1.8 (77 K, 0.1 MPa)	[148]
OMC CS48	2,390	0.68	3.5 (77 K, 1 MPa)	[153]
ZTC CB850h	3,150	1.95	6.9 (77 K, 2 MPa)	[154]
Zr-CDC-KOH-900	2,447	1.47	6.2 (77 K, 2 MPa)	[157]
PEEK-ST-9-70	1,956	0.89	3.0 (77 K, 0.2 MPa)	[147]

$^{+}$Determined using a 77 K N_2 isotherm and the Dubinin-Radushkevich method [120, 121] for all the carbons, except the Zr-CDC-KOH-900, which used 77 K N_2 isotherm and plot analysis and PEEK-ST-9-70, which used 77 K N_2 isotherm and Density Functional Analysis.

2.5.4. Other porous materials for adsorptive storage of hydrogen

Adsorptive storage of hydrogen has also been the subject of study for other classes of porous materials. A good example is the use of zeolites for hydrogen adsorption. Zeolites have long been used in research and industry due to their properties – they are stable materials, with nanoscale pores and can be suited for many applications, from gas separations to catalysis and storage. Unfortunately, they have been quickly discarded for hydrogen storage, since their BET specific surface area is in the order of 300 to 400 m^2 g^{-1} and the corresponding uptakes were not commensurate with the capacities needed for wide-scale adsorptive storage. Niejkamp and colleagues analysed zeolites, aluminas and silicas, as well as a number of carbon sorbents [158]. The tested materials Zeolite L, Zeolite ZSM-5 and zeolite ferrierite had hydrogen uptakes between 0.5 and 0.7 wt. % at 0.1 MPa and 77 K [158]. The tested silicas and aluminas did not have any microporosity, so the hydrogen uptakes were even more modest. The conclusion seems to be that zeolite materials have limited micropore volumes and, unlike other materials, there is not much room for optimisation of the porous structure [88].

Porous polymers have also been studied as possible hydrogen storage materials. These include polymers of intrinsic microporosity (PIMs), conjugated microporous polymers (CMPs), hypercrosslinked polymers (HCPs) and porous aromatic frameworks (PAFs) [159]. PIMs were first synthesised in 2002 by Budd and McKeown, with PIM-1 having a BET specific surface area of 950 m^2 g^{-1} [160]. Sherrington and colleagues reported a "Davankov type" HCP with a surface area of up to 2,000 m^2 g^{-1} in 2006 [161]. The first CMPs were reported by Cooper and colleagues in 2007 [162]. Finally, in 2009, a PAF was synthesised with a BET specific surface area of 5,640 m^2 g^{-1} [163]. PIMs are porous polymers that try to mimic the structure of activated carbon, by using very rigid polymers that cannot fill space efficiently and create voids within their structure, giving them porosity [164]. PIMs BET specific surface areas range from 850 to 1,200 m^2 g^{-1} and their hydrogen uptakes go as high as 2.71 wt. % for Trip-PIM at 1 MPa and 77 K [165]. HCPs are highly rigid crosslinked polymers with small pore volumes and high surface areas. Their BET specific surface areas range

from 700 to 1,500 m^2 g^{-1}[159]. Hydrogen uptakes in HCPs can be as high as 3.04 wt. % in HCPs Davankov resins at 77 K and 1.5 MPa [166]. CMPs are a subclass of HCPs, with the difference that they consist of extended conjugated networks of multiple carbon-carbon bonds and/or aromatic rings [159]. CMPs have between 600 and 1,200 m^2 g^{-1} and the highest reported hydrogen uptake (without doping with other elements) within CMPs is 1.50 wt. % for HPOP-1, at 0.11 MPa and 77 K [167].

Some porous polymers have been reported to be amongst the highest reported surface area materials. PAFs are materials whose design premise was to imitate the structure of diamond, but instead of carbon-carbon bonds, the building blocks would be phenyl rings. PAF-1 was successfully synthesised using two phenyl rings as replacements for the carbon-carbon bond [163]. The material exhibited an extremely high BET specific surface area of 5,600 m^2 g^{-1} and a pore volume of 2.46 cm^3 g^{-1} and had a hydrogen uptake of 7.0 wt. % at 77 K and 4.8 MPa [163]. Recently, more PAFs have been synthesised but none reached the extraordinary properties of PAF-1 [168]. The highest surface area material (~ 6,500 m^2 g^{-1}) that has been reported in literature is PPN-4, with PPN standing for porous polymer network [169]. PPNs were synthesised based on the approach followed by PAFs, with the difference that, instead of using the phenyl rings as tetrahedral monomers, analogues were created using other quadricovalent building centres [169]. For PPN-4, tetrakis(4-bromophenyl)silane was used, which yielded an impressive BET specific surface area of 6,461 m^2 g^{-1} and a hydrogen uptake of 9.1 wt. % at 77 K and 5.5 MPa [169].

A class of materials which derive from MOFs and are considered porous polymers are Covalent-Organic Frameworks (COFs). These are assembled much the same way as MOFs, but instead of a metal centre, they are composed entirely of lightweight elements (hydrogen, boron, oxygen, silicon and carbon) which form strong covalent bonds with the organic linkers [170]. These structures are very interesting and some have been studied for hydrogen adsorption [171]. COFs have increased BET specific surface areas and micropore volumes and quite interesting hydrogen uptakes, and, due to the use of lightweight elements, can reduce the framework weight and increase the gravimetric density of hydrogen. The first reported COFs, COF-1 and COF-5, had BET specific surface areas of 711 m^2 g^{-1} and 1,590 m^2 g^{-1}, respectively [170]. Highest surface area reported COFs are COF-102 and COF-103, with BET specific surface

areas of 3,620 and 3,530 m^2 g^{-1}, respectively [172]. Their reported excess hydrogen uptakes are 7.16 and 6.98 wt. % at 77 K and 4 MPa [172].

Table 2.8 – Properties of zeolites and porous polymers.

Material	BET specific surface area / m^2 g^{-1}	Micropore volume[+] / cm^3 g^{-1}	Excess H_2 uptake, in wt.% (*T*,*P*)	Ref.
Zeolite ZSM-5	431	0.28	0.72 (77 K, 0.1 MPa)	[158]
Trip-PIM	850	0.78	2.71 (77 K, 1 MPa)	[165]
HCP Davankov resins	1,042	0.87	3.04 (77 K, 1.5 MPa)	[166]
COF-102	3,620	1.55	7.16 (77 K, 4 MPa)	[172]
COF-103	3,530	1.54	6.98 (77 K, 4 MPa)	[172]
PAF-1	5,600	2.46	7.0 77 K, 4.8 MPa)	[163]
PPN-4	6,461	2.90	9.1 (77 K, 5.5 MPa)	[169]

[+] **All measured using 77 K N_2 isotherm. The HCP Davankov used the Horvath-Kawazoe method, the COFs were determined using the Dubinin-Radushkevich method [120, 121] and the PPN-4 was determined using Density Functional Analysis .**

In Table 2.8, the summary of the properties of zeolites and porous polymers used for hydrogen storage is shown. As it can be observed, some of these are very interesting hydrogen storage adsorbents and they are amongst the highest reported surface area materials.

2.5.5. Analysing hydrogen adsorption isotherms

The vast and growing number of materials tested for adsorptive storage, which are still unable to meet the stringent and elusive DOE targets for onboard storage in light-duty vehicles, as well as the complexity of adsorption phenomena and the need to relate to specific materials' characteristics require sophisticated analysis of the adsorptive behaviour of materials. This means that analysis and modelling have to be applied so that adsorptive capacities and thermodynamic behaviour are modelled and some guidance is given on synthesis of materials with enhanced characteristics for hydrogen adsorption.

Modelling adsorptive behaviour is conspicuous in literature, in many different branches of science, and some known equations, like the Langmuir, the Sips or the Dubinin equations have been used extensively in a variety of studies. For hydrogen adsorptive storage the reports are fewer, but the modelling of adsorptive hydrogen storage materials is not by any means new and there is very active ongoing research in a number of groups, the most prolific being Richard Chahine's research group at the Université of Québec at Trois-Rivéres [173-180] and Anne Dailly's research at the General Motors Chemical and Environmental Sciences Laboratory [181-187]. A number of other authors have also modelled experimental isotherms [88, 188-190], with the goal of correlating specific materials' properties with hydrogen uptakes. This analysis is often done with experimental data acquired in-house and with models that have been developed to analyse adsorption of hydrogen on porous materials.

Chahine and colleagues were one of the first groups to analyse hydrogen adsorption on porous materials. Experimental data were acquired in-house and models were developed to analyse the isotherms. This has focused mostly on the use of the DA equation and modified forms [174-176], although the Langmuir and Ono-Kondo lattice approach [178, 179] have also been applied to the isotherm analysis. The DA model has been used on H_2 adsorption of AX-21 [174], MOF-5, SWCNT and IRH-33 (a coconut shell activated carbon) [176] with the goal of extracting parameters, like the maximum capacity of the material and the pore volume, and to calculate the isosteric enthalpies. In a different report, MOF Al-TCBPB (where TCBPB stands for tris[40-carboxy(1,10-biphenyl)-4-yl] benzene) was analysed using the high-pressure excess hydrogen isotherms and the modified DA model [191]. The isosteric enthalpies were also calculated both a van't Hoff relation and the DA model. Comparisons with compression and isothermal delivery and charging using modelling and the modified DA equation model were also done, by calculating the absolute quantity on AX-21, activated carbon CNS-201 and MOF $Cu_3(BTC)_2$, where BTC stands for benzene tricarboxylate [173]. In another study, the density of the adsorbed hydrogen using also the modified DA model was assessed to be in the high liquid range (78.6 kg m^{-3} for MOF-177) [192]. Recently, Chahine and colleagues have applied the Sips, Tóth, Langmuir and Freundlich equations to the analysis of Al, Cr, Fe, and Ga-BTB (where BTB stands for benzenetribenzoate) MOFs and obtaining fitting parameters for all the

equations [193]. However, there was no distinction on the application of the equations between excess and absolute adsorption – the distinction between the absolute and excess is mentioned in the journal publication but the analysis does not focus on this – and these were only applied in the low pressure range (below 1 MPa) with the goal of comparing the simulated isotherms with the experimental results. The same research group also used modifications of the Dubinin and of the potential theory for analysing hydrogen storage in AX-21 [194]. The multicomponent potential theory of adsorption was extended by introducing a temperature dependent Dubinin potential parameter that allowed the use in adsorption isotherms of supercritical gases, including hydrogen, nitrogen and methane [194]. Recently, the same group has focused on the application of their analytical models to other gases [180] and on mass transfer issues for hydrogen storage [195-200].

Dailly and colleagues also routinely use modelling and analysis of hydrogen storage in porous materials. The DA modified model reported by Chahine and colleagues is the one used in most of their analysis. Their work has been focused on the analysis of experimental excess isotherms for hydrogen storage materials. As an example, isotherms of MOF-177 [185], MOF-5 [183] and Cu_2(BPTC) and Cu_2(TPTC) [186] - where BPTC and TPTC stand for 3,3',5,5' biphenyl tetracarboxylate and 3,3',5,5' terphenyl tetracarboxylate - were collected and analysed. Cu_2(BPTC) is also called NOTT-101 and it was also used in this thesis. The experimental data was collected from 50-77 K for the MOF-177 and from 50-100 K for the IRMOF-1 and the Cu_2(BPTC) and Cu_2(TPTC). All the isotherms were collected up to 4 MPa. The analysis in these four materials showed adsorbed densities in the high range of liquid densities, yielding densities of 56, 69, 54 and 59 kg m^{-3} for the MOF-177, MOF-5 and Cu_2(BPTC) and Cu_2(TPTC). In all cases, it was concluded that an incompressible phase with bulk liquid hydrogen density was forming in the pores of the analysed materials. This was further studied on another report, which included MOFs Zn(BDC) and Zn (BTB), AX-21 and molecular sieve Y [184]. For all the materials and using the same analysis, the adsorbed phase density reached 67, 56, 61 and 54 kg m^{-3} for Zn(BDC), Zn (BTB), AX-21 and molecular sieve Y, respectively. Analysis of the correlations between pore volumes and BET specific surface areas were also done in the same publication [184]. In other study, experimental excess hydrogen isotherms for MOF-177 in powder, pellets of AX-21, Basolite Z377 in powder and in pellets

were analysed [181]. The obtained densities for the DA model were 59 and 66 kg m^{-3} for the powder and pellet version of Basolite Z377, respectively. A more recent report focused on the same aspects – analysis done using the modified DA model on UMCM-1 and NOTT-112, with isotherms in the range 50-77 K and from 0 to 40 bar [187]. The outcomes are the same as in previous reports from the same authors, with the maximum capacities and pore volumes calculated and the densities reaching 56 kg m^{-3} and 74 kg m^{-3} for the UMCM-1 and NOTT-112. The results of the modelling, according to the authors, provided further evidence of an incompressible state within the pore that possesses densities of the same order of magnitude of liquid hydrogen.

Other authors have also used modelling on hydrogen isotherms to evaluate storage materials. Tedds et al. [189] analysed isotherms of activated carbon Takeda 4A carbon, MOFs IRMOF-1 and Cu-BTC, zeolite NaX and microporous polymer Methyl Trip PIM up to 1.5 MPa and from 77 K to room temperature. The equations used were the Tóth and the Sips, with the maximum capacity values, pore volumes and adsorbed phase densities estimated for all using both equations. The adsorbed densities calculated using the Tóth equation ranged from 43 kg m^{-3} for the Takeda 4A carbon to 108 kg m^{-3} for the Methyl Trip-PIM. The isosteric enthalpies of adsorption using both the virial and Clausius-Clapeyron equation and the usable capacities for all the materials were also determined. Elsewhere, Thomas has focused on the identification of structural characteristics of the materials' and the correlation with their hydrogen uptake capacities [88, 188]. The hydrogen uptake at 77 K and 1 bar was correlated with surface area, total pore volume and micropore volume in carbons, zeolites, MOFs and porous polymers [88]. More recently, the same author reviewed hydrogen storage in MOFs, correlating the hydrogen uptake at 77 K and 1 bar with the BET surface area [188]. The hydrogen uptake at saturation or close to saturation was also correlated with the BET specific surface area, the Langmuir surface area and the total pore volume. In another recent report, hydrogen storage in MOF-5 composites was also analysed for 77 K to room temperature and up to 6 MPa [190]. The modified DA model reported by Chahine and others was used, along with the UNILAN and Tóth model. The UNILAN was considered the model giving the most accurate description of the system. The volumetric storage of hydrogen, and the calculation of deliverable hydrogen, and the differential enthalpy were all reported for the MOF-5 composites.

As just observed in this section, the majority of analysis has focused on the use of the Dubinin equations and especially of the Dubinin-Astakhov equation for analysis of hydrogen adsorption on porous materials. The Dubinin equations were designed assuming a pore filling mechanism with a subcritical adsorptive which would condense in the pores. Hydrogen is mostly tested at supercritical conditions, so there are some inadequacies in using the Dubinin equations, mainly the fact that the equations use a vapour pressure P_0. This vapour pressure is inexistent in a supercritical fluid, so an approximation above the critical point is used, usually the relation provided by Amankwah and Schwarz [201]. The analysis presented in other work has also aimed at providing insights into the nature of the adsorbed phase and some authors have concluded, using analysis, that adsorbed hydrogen can have a density higher than the low range of liquid densities for hydrogen.

As seen in this section, modelling experimental excess data for hydrogen can offer important insights into the nature of hydrogen adsorption and the properties of the material. While the development of new synthetic prospective materials for hydrogen storage is surely important, analysing the experimental data obtained by conventional adsorption techniques can provide a wealth of information. The adsorption isotherm differs from material to material, which means that analysing under certain ranges might not provide the true capacity of a material. Also, since the operating ranges are usually in the high-pressure range for hydrogen storage in a microporous material, there might be significant differences between absolute and excess quantities. This difference means that experimental sorption equipment provides insufficient data, since the absolute quantity of hydrogen stored in a given material cannot be accounted for. For practical reasons, when designing a storage system and when comparing the different materials, the absolute quantity is the amount that should be reported for a material. Modelling can also be used to predict capacities at different operating ranges and to estimate the thermodynamic properties of a material, which, if known, can be tailored for specific applications.

Predicting the maximum capacities for a material and assessing total amounts stored, accessing thermodynamic information and estimating uptakes at different conditions are all available from experimental data when proper modelling and analysis are applied to the isotherms. This information is necessary to evaluate the different

adsorptive storage materials and, since, through modelling, different storage methods can be compared, can even confirm hydrogen storage in a porous material as a valid alternative for wide-scale storage of hydrogen.

2.6. Aims and objectives of the thesis

Energy demand is one of the main challenges facing humanity at this turn of century. While energy demand is increasing, due to strong population and economic growth, sources of energy are becoming more expensive and difficult to explore and most of these carry grave environmental impact. A wide range of technologies are currently being explored that mitigate environmental effects, but, as it has already been observed, large changes in energy conversion, storage, distribution and consumption have to be adopted soon to avoid catastrophic consequences.

A means to store energy, which is widely available and can be easily converted is of the utmost necessity. Hydrogen is the most likely candidate for a wide-scale sustainable energy vector, since it fulfils most of the needed requirements, but full implementation and large scale penetration still depends on a number of technological breakthroughs, arguably the biggest one being how to safely, efficiently and economically store it. While there is no clear cut answer to the storage problem and every different method carries some drawbacks, storing it in a porous material offers attractive features, since it is completely reversible and stores hydrogen in its molecular form, while maintaining milder operating conditions of pressure and temperature than other conventional storage methods. These issues were reviewed in detail to set to context for this work in the background of this thesis. This thesis is framed within the storage of hydrogen in porous materials subject, specifically on the modelling and analysis of hydrogen storage in nanoporous materials and its main aim is to further knowledge in this area for a sustainable energy system setting. Modelling and analysing experimental data is of great importance, because it can benchmark and point to better prospective hydrogen storage materials, identifying capacities for the full operating range of pressure and temperature for any given material. Designing improved storage systems can also be done, if experimental data is analysed and thermodynamic properties calculated. The thermodynamic nature of the systems is

crucial when designing a storage system, especially at cryogenic temperatures, where maintaining tight temperature controls is vital. Finally, modelling and analysis can also help in the comparison with alternative storage methods, and assess if there is any benefit of using an adsorbent to store hydrogen.

The **aim** of this thesis is:
To develop a generalised methodology that models and analyses hydrogen adsorption in microporous materials at high pressures (> 1 MPa) and supercritical conditions (> 33 K). The methodology should use an analytical model for experimental excess data and calculate the excess and absolute quantities for different operating ranges of pressure and temperature, using the fewest number of adjustable parameters.

To meet this aim, the following **objectives** have been set:

I) Develop a methodology that can be applied to excess hydrogen isotherms of different porous materials, by using an analytical model with a small number of parameters.

II) Use the analytical model to predict the excess and absolute capacities of a material for different operating ranges.

III) Test the methodology in a number of experimental excess hydrogen datasets for different classes of porous materials.

IV) Compare adsorptive storage with alternative storage methods.

V) Estimate the thermodynamic properties of a material and improve on the accuracy of current methods used to estimate enthalpies of adsorption.

VI) Validate the methodology using experimental and computational techniques.

Chapter Three

Materials and Methods

3. Materials and Methods

3.1. Introduction

This section reports the materials and methods used in this thesis. The chapter starts with the gas sorption data section, which includes an explanation of the adsorbent materials used in this work, the experimental setup used for obtaining the hydrogen isotherm data and the characterisation done on the experimental samples – BET (Brunauer-Emmett-Teller) specific surface area and helium pycnometry. The adsorbent materials are introduced, with an explanation of their synthesis, characterisation and activation.

The methodology and model which are the main part of this thesis are explained in this chapter, with an introduction to excess and absolute isotherms, the critical points in supercritical adsorption, the equation of state used to determine hydrogen's properties, the methodology used and the different type I equations applied with the method. The chapter ends by illustrating how to apply the methodology to experimental hydrogen excess sorption data.

3.2. Gas sorption data

3.2.1. Experimental methods

The BET specific surface area measurements were obtained using low-pressure nitrogen sorption measurements at 77 K with a Micromeritics ASAP 2020 (Micromeritics Instrument Corporation, Norcross, GA, USA) volumetric gas sorption analyser. The ASAP 2020, which stands for Accelerated Surface Area and Porosimetry System, is a volumetric sorption system with two analysis ports and two degassing ports that can work with a variety of gases in the 0 to 0.1 MPa range. The specific surface area was calculated using the British Standard guidelines for the BET method, with linear regression applied to data in the 0.05-0.3 P/P_O relative pressure

range [202]. The micropore volume was determined using the Dubinin-Radushkevich method applied to the N_2 isotherm at 77 K, up to 0.1 MPa [120, 121].

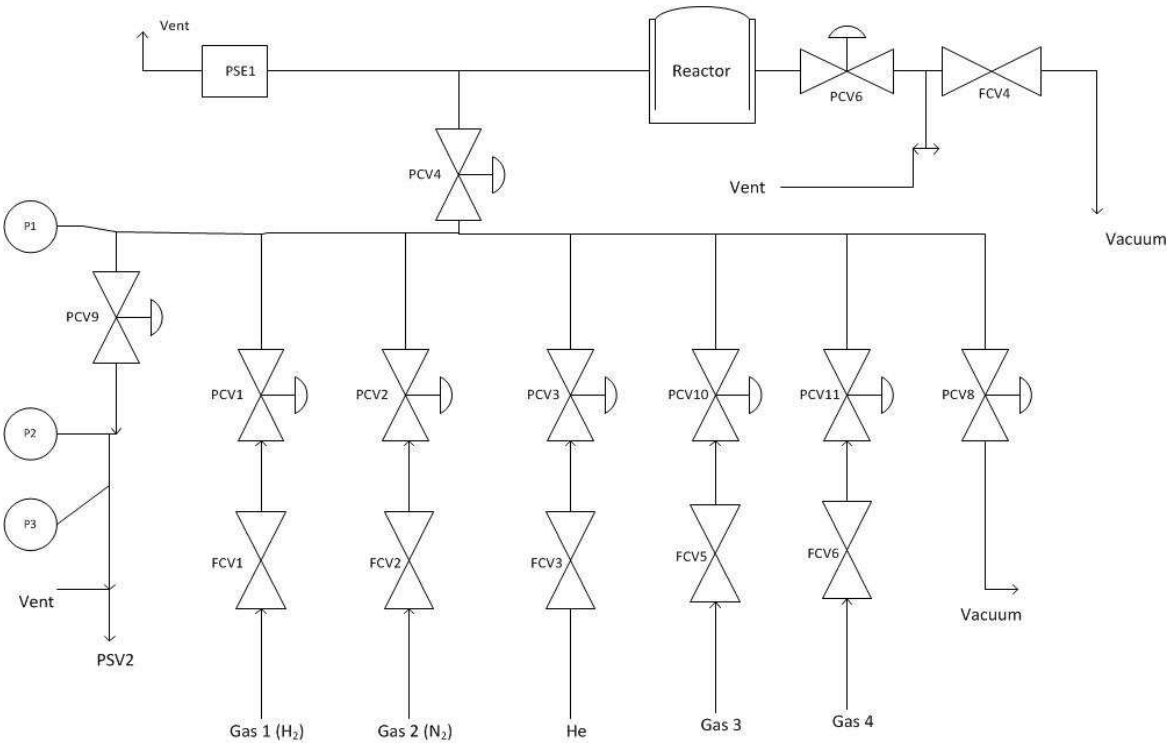

Figure 3.1 - Schematic of the HTP-1 sorption analyser. PCV stands for pressure control valve, FCV stands for flow control valve, PSE stands for pressure safety element and PSV stands for pressure sustaining valve.

The high-pressure hydrogen sorption studies were done on a Hiden HTP-1 volumetric gas sorption analyser (Hiden Isochema, Warrington, UK). This is a Sievert's type apparatus that calculates the amount adsorbed by dosing a known volume of gas and calculating the pressure drop at equilibrium. The schematics for the hydrogen dosing of the HTP-1 are shown in Figure 3.1. When dosing gases, the volume of the dosing chamber until PCV4 is known. Gas 1 is then dosed by opening FCV1 and PCV1 until the desired pressure P1 is attained. FCV1 and PCV1 close, PCV4 opens to expose the sample and the software waits until the gas pressure reaches equilibrium. The adsorbed quantity is then calculated with a molar balance. High-purity hydrogen (Air Products BIP-Plus, 99.99996%) was used and the temperature control was provided with a recirculating liquid nitrogen sample cell. The helium space corrections were done on the samples after the analyses and the full degas cycle.

The skeletal density, which is also called the true density and is the volume of the sample, excluding the space available for the probe gas, divided by the sample's mass, was measured at room temperature using a helium pycnometer (Micromeritics AccuPyc1330, Micromeritics Instrument Corporation, Norcross, GA, USA). The skeletal volume is determined using helium pycnometry by dosing helium into a sample and determining all the volume that is accessible to the gas. The sample's mass is determined using an accurate laboratory scale and the density is determined by dividing the mass over the skeletal volume. The skeletal density is used to determine the displaced volume of samples in containers.

3.3. The adsorbents – synthesis, characterisation and activation

As mentioned in the Background of this thesis (Chapter 2), materials could be crucial in solving the hydrogen storage problem. There are a number of issues to consider for each adsorbent, from price and availability to kinetics and capacity, and this constitutes only a small number of the actual requirements of any prospective hydrogen storage material [69]. Materials synthesis and characterisation is not the subject of this thesis, but due to the importance of adsorbents in the problem and their specificities, the next section is devoted to the synthesis, characterisation and sorption measurements of the materials studied and analysed in this thesis.

In this work, the method and analysis are applied to 4 different materials, two high-surface area activated carbons and two metal-organic frameworks. The two activated carbons were TE7 and AX-21, the latter a well studied high-surface area activated carbon powder and the former a material proposed by our research group as a standard reference material for hydrogen storage [203]. The two metal-organic frameworks chosen were MIL-101 and NOTT-101, two intensely studied, high-capacity metal-organic frameworks [114-117, 186, 204]. The sorption data for TE7, AX-21 and MIL-101 was collected in-house at the University of Bath and the sorption data for NOTT-101 was obtained at the Chemical and Environmental Sciences Laboratory at General Motors Research and Development Centre [186].

The TE7 carbon beads are a commercial available microporous activated carbon from MAST Carbon (MAST Carbon International, Basingstoke, United Kingdom). They are a steam-activated phenolic resin-based carbon, with a BET nitrogen specific surface area of 960 ± 50 m^2 g^{-1}. This was measured with a low-pressure sorption nitrogen isotherm at 77 K using a Micromeritics ASAP 2020 analysis system, where the uncertainty is the standard error of the BET measurements. This surface area was calculated using the British Standard guidelines for the BET method [202], with the data points relevant to the regression in the 0.05 to 0.3 relative pressure range. The micropore volume as evaluated by the Dubinin-Radushkevich (DR) [120, 121] method applied to the nitrogen isotherm at 77 K is 0.43 ± 0.03 cm^3 g^{-1} and the skeletal density was determined as 1.90 ± 0.03 g cm^{-3} using a He pycnometer. Prior to sorption studies, the sample was degassed at 623 K for 8 hours under a vacuum of 0.1 mPa. As we have reported, these are considered to be the optimum activation and de-gas conditions for this material [203].

The AX-21 activated carbon is another commercially available high-surface area carbon, obtained from Anderson Company (Anderson Development Company, MI, USA). It has been extensively studied for sorption studies [178, 205, 206] and it has become a standard reference activated carbon for adsorption, sometimes referred to as a "superactivated" carbon. It is synthesised using a carbon precursor and potassium hydroxide, from a process patented by Standard Oil Company (later to be known as Amoco Corporation). The material is available nowadays under licence by Kansai Coke and Chemicals (Kansai Coke and Chemicals Co., Amagasaki, Japan) under the commercial name Maxsorb. A BET specific surface area analysis on the material revealed a surface area of 2,440 ± 48 m^2 g^{-1}, which is comparable to reported values from the literature [175, 205]. The skeletal density was 2.23 g cm^{-3}, as measured by helium pycnometry. The micropore volume from literature for this material was 1.03 cm^3 g^{-1}, as determined by the Dubinin-Radushkevich method [120, 121]. Prior to sorption analysis, the material was degassed at 473 K for 24 hours under vacuum.

MIL-101 is a chromium-based metal-organic framework (MOF) first synthesised in the Institut Lavoisier in France . MIL-101(Cr) (MIL, Matérial Institut Lavoisier) was synthesised in-house, using an adapted procedure from Férey et al. [116]. The synthesis was done with 0.33 g of terephtalic acid [C_6H_4-1,4.$(CO_2H)_2$] added to 0.8 g

of chromium (III) nitrate (nonahydrate) [$Cr(NO_3)_3 9H_2O$] in a Teflon-lined autoclave, with 10 mL distilled water and a stirrer bar. It was then heated to 453 K for 8 hours and left to cool overnight. The resulting white powder was washed with deionised water and vacuum filtered to form a liquid, which was then centrifuged three times in water for 10 minutes at 11,000 rpm and left to dry. Prior to gas sorption studies, the material was dried in a vacuum oven and degassed at 423 K for 4 hours. The measured BET specific surface area was 2,885 ± 105 $m^2\ g^{-1}$. The material was then resolvated in H_2O and dried using the same procedure as before, showing no loss of porosity as indicated by the repeated BET specific surface area analysis. The skeletal density measured using helium pycnometry was 1.69 g cm^{-3}. The reported specific pore volume was measured according to the Gurvich rule [207] at P/P_0=0.95 and it was 1.51 $cm^3\ g^{-1}$ [208]. The Gurvich rule determines the pore volume by assuming that the amount adsorbed at the plateau is the adsorption capacity and then uses the molar volume to obtain the pore volumes of the samples [121]. MIL-101 shows a very interesting tri-modal pore size distribution, with the small pores having an inner diameter of 7 Å, the medium pores with a diameter of 29 Å and the large pores having a diameter of 34 Å [208].

The second metal-organic framework analysed in this study is Cu_2(3,3',5,5' terphenyl tetracarboxylate), also called Cu_2(tptc) or NOTT-101. NOTT-101 is microporous MOF composed of a paddle-wheel structural unit linked by a terphenyl connector. This material has a reported BET specific surface area of 2,510 $m^2\ g^{-1}$, measured in the 0.05-0.15 P/P_O range [186]. This material was synthesised at the University of Nottingham following the method proposed by Schröder et al. [117]. Figure 3.2 below displays the crystal arrangement of NOTT-101, with the paddle-wheel structure shown in the middle of the diagram and the three-connected terphenyl linkers. The figure was obtained using the crystallographic information file from the Cambridge Crystallographic Data Centre and Mercury 2.4 (Mercury CCDC, Copyright 2010).

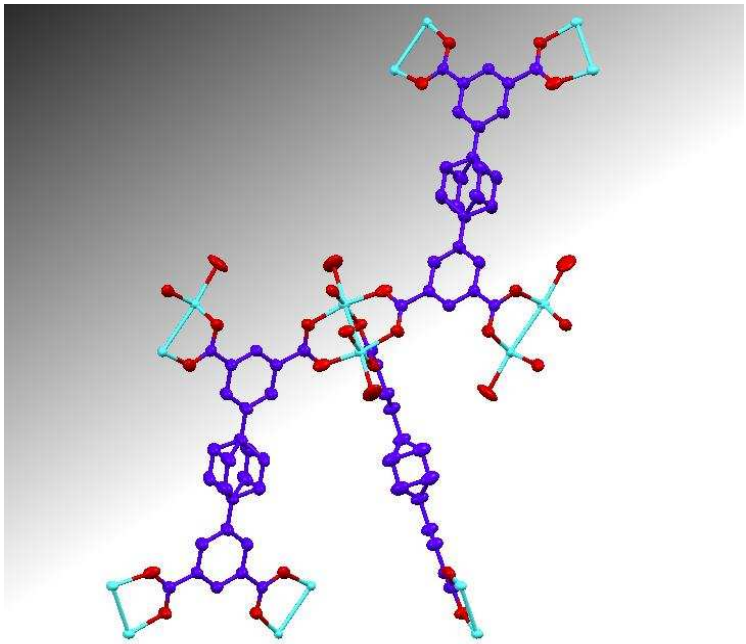

Figure 3.2 –Cu_2(tptc) or NOTT-101 viewed along the a axis using the crystallographic file. Chemical elements are: light blue – copper (Cu); dark blue – carbon (C); red – oxygen (O). Hydrogen atoms are not shown.

Prior to sorption studies, the material was activated at 373 K under vacuum. The BET specific surface area and the hydrogen isotherms were measured at the Chemical and Environmental Sciences Laboratory, General Motors Research and Development Centre, Warren, MI, USA. The BET specific surface area was measured using a Quantachrome Autosorb-1 automated gas-sorption apparatus and the data points used were in the P/P_0 range of 0.05 to 0.15. The hydrogen isotherms were measured using a PCT-Pro 2000 from Hy-Energy LLC, which is an automated Sievert's apparatus, used in conjunction with a continuous-flow cryostat with a liquid helium flow. Ultra-high purity hydrogen and helium (99.999%) from Airgas Inc. were used. The isotherms were measured in the 50-87 K range, with pressures up to 4 MPa [186]. Hydrogen isotherm data were generously provided by Dr Anne Dailly from General Motors Research and Development Centre (GM Research and Development Centre, Warren, MI, USA).

Table 3.1 summarises the material properties of the adsorbents used in this study. Except where otherwise stated, these properties were measured in the Department of Chemical Engineering of the University of Bath, with the BET Specific Surface area measured using the British Standard BET range [202] (0.05-0.3 P/P_O) on a nitrogen

isotherm at 77 K, the micropore volume measured using the Dubinin-Radushkevich analysis on a nitrogen isotherm at 77 K and the skeletal density measured using helium pycnometry. Details on the experimental methods are in the previous section.

Table 3.1 - Material properties of the adsorbents. Errors, where shown, indicate the standard error from the experiment

Adsorbent	BET Specific Surface Area / $m^2\ g^{-1}$	Micropore Volume / $cm^3\ g^{-1}$	Skeletal density / $g\ cm^3$
TE7	960 ± 50	0.43 ± 0.03	1.90 ± 0.03
AX-21	2,440 ± 48	1.03 [209]	2.23
MIL-101	2,885 ± 105	1.51[a]	1.69
NOTT-101	2,510[b]	1.083[c], 0.886[d]	1.67[e]

[a] Specific pore volume as calculated by the Gurvich rule on a nitrogen isotherm at 77 K when P/P_0 is at 0.95 [208].

[b] Measured on a N_2 isotherm at 77 K over the 0.05-0.15 P/P_0 range using a Quanthachrome Autosorb-1[186].

[c] Pore volume calculated using Platon/Solv, calculated crystallographic pore volume [117].

[d] Pore volume calculated using N_2 sorption at 78 K [117].

[e] Determined using helium sorption isotherms at 273 K [117].

3.4. The model

3.4.1. Critical points in high-pressure adsorption

Adsorption is the material enhancement of a fluid (gas, liquid or vapour) in the vicinity of a solid surface [121], as it was already mentioned in the Background (Chapter 2). This enhancement depends on the chemical and physical composition of the surface and is therefore not uniform. This non-uniform adsorbate density makes adsorption difficult to express quantitatively. To facilitate the measurement of adsorption, a mathematical transformation has to be introduced, the so-called Gibbs Surface Excess (GSE). The GSE is the experimental variable for measuring sorption equilibria and kinetics from all available measurement methods – volumetric, gravimetric, chromatographic and others [210].

The GSE (or simply, the excess) was introduced by Williard J. Gibbs [121, 211] and introduces an arbitrary interface between the solid and the fluid. To measure the GSE experimentally, a probe gas has to be used, with the assumption that it does not adsorb. Helium gas is typically used, but this assumption of non-adsorbing helium at room temperature has been disputed [212-214]. On a typical solid-gas adsorption experiment, after the void volume is quantified using helium, a known volume of the adsorptive gas is dosed onto the sample and, once equilibrium is reached and the pressure does not change anymore, a mass balance is carried out to calculate the adsorbed amount. Because helium was used to estimate the available space for adsorption, the calculated adsorbed amount is always in excess of this helium volume, hence the name.

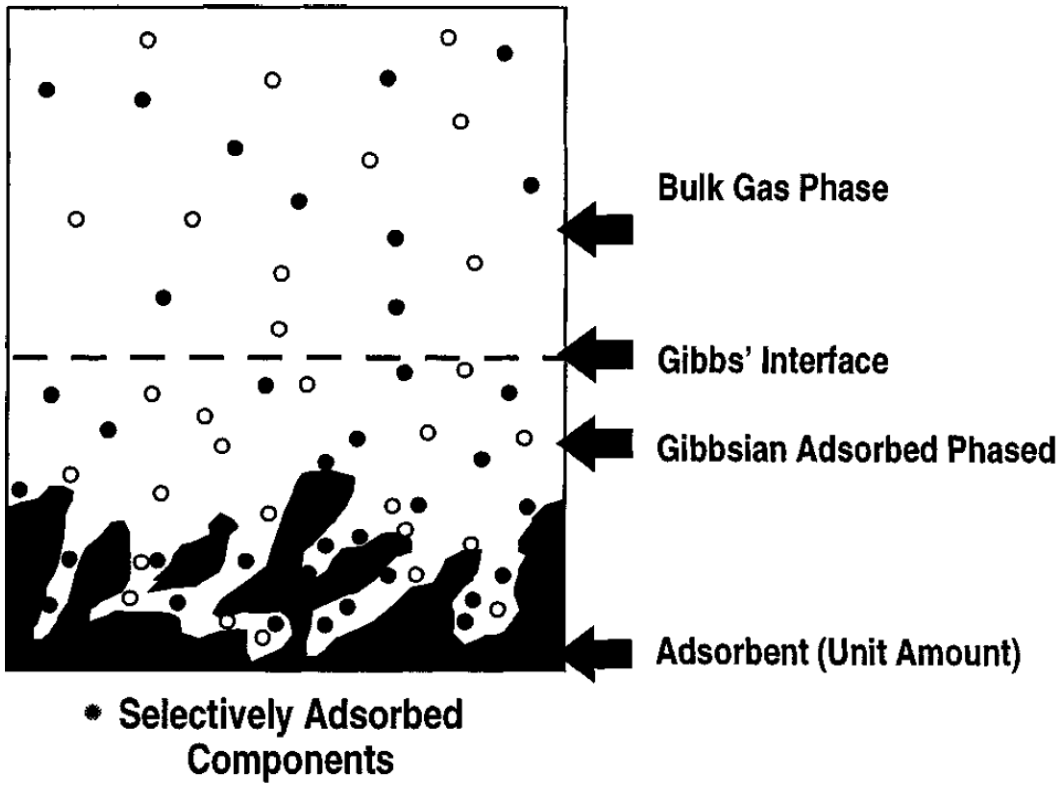

Figure 3.3 - Gibbs interface and adsorbed phase in multicomponent adsorption. Reprinted from [215] with permission from John Wiley and Sons.

For this reason, and as the diagram in Figure 3.3 and Figure 3.4 show, the GSE does not take into account the adsorbed amount in the potential field of the solid that has the same density as the bulk gas. However, since adsorption is an equilibrium phenomena, the adsorbed amount is the amount where the chemical potential is equal

everywhere and in equilibrium with the bulk fluid. The total quantity within the potential field of the solid is the absolute amount adsorbed and this is the quantity that expresses the total amount of gas within the porous material. The GSE is solely a mathematical transformation to help with the experimental setup, therefore not a separate thermodynamic phase, just a partition of the absolute amount adsorbed. Most of the adsorptive experiments are done at room temperatures and at pressures not exceeding 2 MPa, so the differences between absolute and excess amounts at these conditions are not significant and are usually ignored. In Figure 3.4, the excess and bulk in the potential field of the solid Z_A constitute the absolute amount adsorbed.

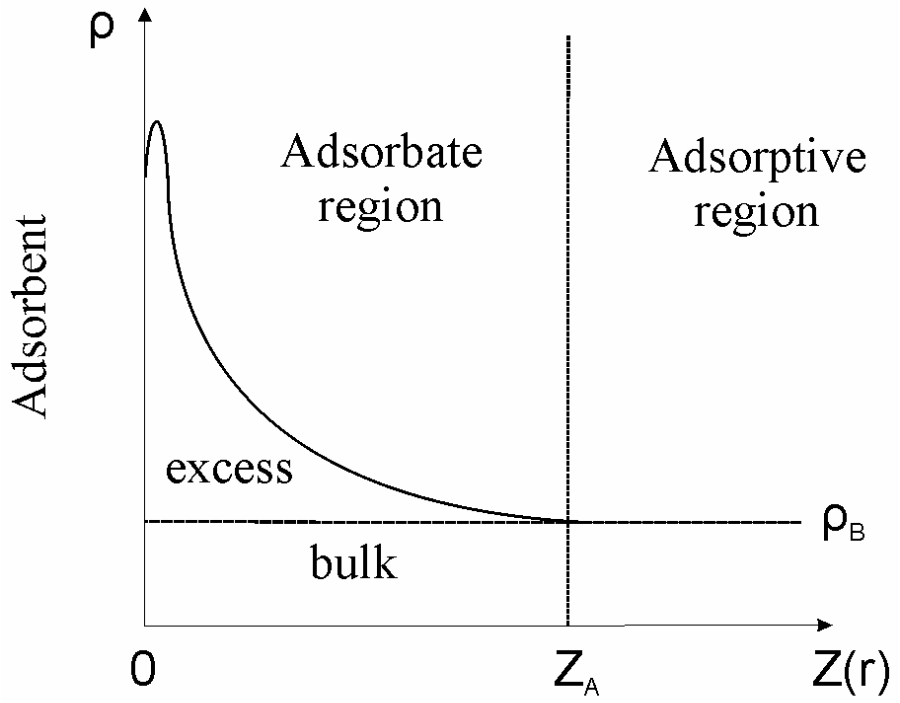

Figure 3.4 – Absolute and excess adsorption. The *y*-axis is the density of the gas, the *x*-axis is the distance to the surface. The excess plus bulk quantity contained within distance Z_A is the absolute adsorption.

It is a completely different situation with hydrogen storage. Most experiments are done above hydrogen's critical point of 33 K, so there is no pressure limit due to condensation. The cryogenic conditions and the high pressures, make the difference between absolute and excess amount very significant, and even more important since the amounts of hydrogen stored in a material using adsorption are comparatively very small. To design appropriate adsorptive storage systems for hydrogen, it is very important to quantify as accurately as possible the total amount of hydrogen contained

in a given solid-state material. Hydrogen is weakly interacting, making its liquid-vapour temperature critical point very low (~ 33 K), which means hydrogen adsorption isotherms are usually measured in the gas phase (*i.e.* supercritical or above its critical point). As Donohue and Aranovich observed, excess isotherms for supercritical fluids are not monotonic and at high pressures they reach a maximum point, after which they decrease with increasing pressures [86]. This behaviour, with a steep increase at low pressures, reaching a maximum and then starting to decrease is due to the rate of filling of the pore by adsorbate, which depends on the porosity of the sample. In the low pressure range, the rate of increase of adsorbate in the pore is much higher than in the bulk gas, making the isotherm steep in the beginning. Gradually, this rate becomes less pronounced and when the isotherm reaches the maximum point, this means the rate of increase of adsorbate in the pore equals the rate of increase in density in the bulk adsorptive. Afterwards, the pace of increase in density in the bulk adsorptive is higher than in the pore and as consequence, the excess isotherm starts to decrease. Eventually, at very high pressures, the excess amount will equal zero and at this pressure, P_e^0, the average adsorbate density $\overline{\rho_A}$ is equal to the bulk density of the adsorptive ρ_B, as shown in Eq.3.1.

$$\left(\rho_B = \overline{\rho_A}\right)_{P=P_e^0} \qquad \text{Eq.3.1}$$

The absolute amount adsorbed, on the other hand, which reflects the total quantity of adsorbate within the potential field of the solid is always increasing, so the isotherm monotonically rises, following a IUPAC type I behaviour and approaching an asymptote, which is the limiting absolute capacity (n_a^{max}). The diagram in Fig
ure 3.5 can be applied not only to hydrogen, which is supercritical at temperatures above 33 K, but to other supercritical fluids, like CO_2, oxygen and nitrogen, as long as the temperature is above the vapour-liquid critical point, which is 304.25, 154.6 and 126.3 K for CO_2, oxygen and nitrogen are respectively.

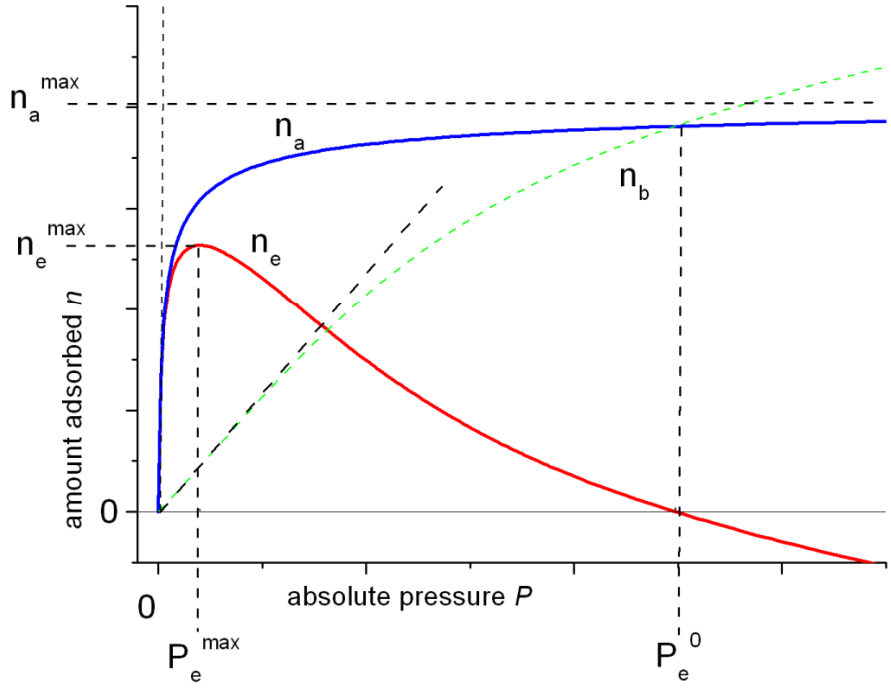

Figure 3.5 – Critical points in high-pressure adsorption of a supercritical fluid. The blue line is the absolute isotherm n_a, the red line is the excess isotherm n_e, the green line is the bulk quantity of adsorptive n_b, black small-dashed line is the bulk quantity if it obeyed the ideal-gas law and the vertical dashed line is the Henry's law gradient on the absolute isotherm. The upper and lower horizontal dashed lines correspond to n_a^{max} and n_e^{max} respectively and the vertical dashed lines on the left and right represent P_e^{max} and P_e^0, respectively. Adapted from Bimbo et al. [216].

The above figure illustrates high-pressure adsorption above the adsorptive's critical temperature. Critical points can clearly be identified in the graph, such as the excess maximum (n_e^{max}), the limiting absolute capacity (n_a^{max}), the pressure corresponding to the excess maximum (P_e^{max}) and the pressure at which the excess equals zero (P_e^0). The diagram shows these points in a case where the excess isotherm becomes negative before the absolute quantity reaches its limiting value, meaning that the densities of the adsorbed and bulk phase are identical before the pore reaches its limiting capacity.

At sufficiently high temperatures or at sufficiently low pressures, the amount adsorbed should have a linear relation with the absolute pressure. This means that, at lower temperatures, as shown in Eq.3.2, the quantity obeys a linear relationship with pressure and with k_h, which is called the Henry's constant. This is called obeying the Henry's Law limit and it can be seen in the diagram in Figure 3.5. Another important implication is that when the excess reaches a maximum, the gradient of the absolute

adsorbed quantity (n_a) is equal to the gradient of the bulk quantity (n_b), as shown in Eq.3.3.

$$f(n_a, P)_{\lim P \to 0} = k_H P \qquad \text{Eq.3.2}$$

$$\left(\frac{\partial n_a}{\partial P}\right)_T = \left(\frac{\partial n_b}{\partial P}\right)_T \text{ when } P = P_e^{\max} \qquad \text{Eq.3.3}$$

To appropriately model absolute and excess behaviour, the bulk quantity of the adsorptive has to be accurately calculated. For this, an equation of state that predicts the state functions of the gas, which includes calculating the density at a given pressure and temperature is necessary. The best available equation of state for molecular hydrogen is the one developed by Leachmann et al. in 2009 [64], which is introduced and explained in the next sub-section.

3.4.2. Determining hydrogen's properties – Leachman's equation of state

Leachman's equation of state (EOS) is a recently published equation of state for hydrogen [64]. Leachman improved on existing EOS for parahydrogen and normal hydrogen and introduced a new EOS for orthohydrogen, which was unavailable before. Parahydrogen, as mentioned in the Background (Chapter 2), is one of the two spin isomers of molecular hydrogen and the one that forms prevalently at low temperatures, corresponding to the lower energy states, with an even rotational level number. Orthohydrogen is the spin isomer that corresponds to higher energy states and high temperatures, with an odd rotational level number. Equilibrium hydrogen is the ratio of ortho- to parahydrogen molecules at a given temperature, with the room temperature ratio called normal hydrogen.

Orthohydrogen and parahydrogen properties differ mostly in two aspects – ideal gas values associated with heat properties, which include specific heats (constant volume specific heat and constant pressure specific heat), thermal conductivity and derived properties such as enthalpy and entropy, and values calculated near or in the critical region. One of Leachman's EOS merits is that it applied the quantum law of corresponding states to determine properties near the critical region. This improved on

the existing formulation for normal and parahydrogen, which was a 32-term Benedict-Webb-Rubin EOS developed by Younglove [217].

Classical EOS based on the virial equation are usually explicit in pressure, meaning that the input independent variables are temperature and density, with the output being pressure. The Leachman EOS is explicit in the Helmholtz free energy, a thermodynamic fundamental property, allowing for other thermodynamic properties to be determined through differentiation. The Leachman EOS is a 14-parameter Helmholtz energy equation, where the Helmholtz free energy a_H can be expressed as:

$$\frac{a_H(T,\rho)}{RT} = \alpha_H(\tau,\delta) \qquad \text{Eq.3.4}$$

Where α_H is the reduced Helmholtz energy and τ and δ are the reduced temperature and reduced density, with the subscript *c* indicating critical-point property:

$$\tau = \frac{T_c}{T} \qquad \text{Eq.3.5}$$

$$\delta = \frac{\rho}{\rho_c} \qquad \text{Eq.3.6}$$

The reduced Helmholtz free energy consists of two parts, the ideal-gas contribution ${\alpha_H}^0$ and the residual contribution ${\alpha_H}^r$:

$$\alpha_H(\tau,\delta) = {\alpha_H}^0(\tau,\delta) + {\alpha_H}^r(\tau,\delta) \qquad \text{Eq.3.7}$$

The ideal gas contribution is based on nonlinear regression data of calculated ideal-gas heat capacity from literature and it can be calculated using the following equation:

$$\alpha^0(\tau,\delta) = \ln\delta + 1.5\ln\tau + a_1 + a_2\tau + \sum_{k=3}^{N} a_k \ln\left[1-\exp(b_k\tau)\right] \qquad \text{Eq.3.8}$$

Where a_k and b_k are ideal-gas capacity coefficients taken from Leachman [64]. The residual contribution for the reduced Helmholtz free energy is:

$$\alpha^r(\tau,\delta) = \sum_{i=1}^{l} N_i \delta^{d_i} \tau^{t_i} + \sum_{i=l+1}^{m} N_i \delta^{d_i} \tau^{t_i} \exp(-\delta^{p_i}) + \sum_{i=m+1}^{n} N_i \delta^{d_i} \tau^{t_i} \exp\left[\varphi_i (\delta - D_i)^2 + \beta_i (\tau - \gamma_i)^2\right] \quad \text{Eq.3.9}$$

This residual contribution has 3 summations. The first one is a simple polynomial comprising seven terms, with d_i and t_i the exponents on reduced density and temperature. The second summation has two terms, contains an exponential density component and is for liquid and critical regions property calculations. The third summation contains five terms, which are modified Gaussian bell-shaped terms and is aimed at improving the property calculations in the critical region. In Eq.3.9, l=7, m=9, n=14 with N_i, d_i, t_i, p_i, φ_i, β_i, γ_i and D_i coefficients and parameters taken from regression and available from Leachman's paper [64]. These parameters are different for parahydrogen, orthohydrogen and normal hydrogen, meaning that the Helmholtz free energy and the corresponding thermodynamic functions can be derived for both spin isomers and for the equilibrium ratio of diatomic hydrogen at any temperature and density that is within the range of the EOS.

Leachman's EOS are implemented in the REFPROP software [218], replacing the older Younglove's equation of state for hydrogen [217] and are available through the NIST Chemistry Webbook . All three EOS (parahydrogen, orthohydrogen and normal hydrogen) have an upper pressure limit of 2,000 MPa or when a density of 38,200 mol m^{-3} is reached and the temperature range is between 13.957 K and 1,000 K. The uncertainties in density are 0.04 % in the region between 250 and 450 K, at pressures from 0.1 to 300 MPa. The uncertainty in vapour pressures and saturated liquid densities varies from 0.1 to 0.2 % [64]. Hydrogen, at cryogenic temperatures and high pressures, deviates from ideal gas behaviour, and the lower the temperature, the more pronounced is this difference, as seen in Figure 3.6.

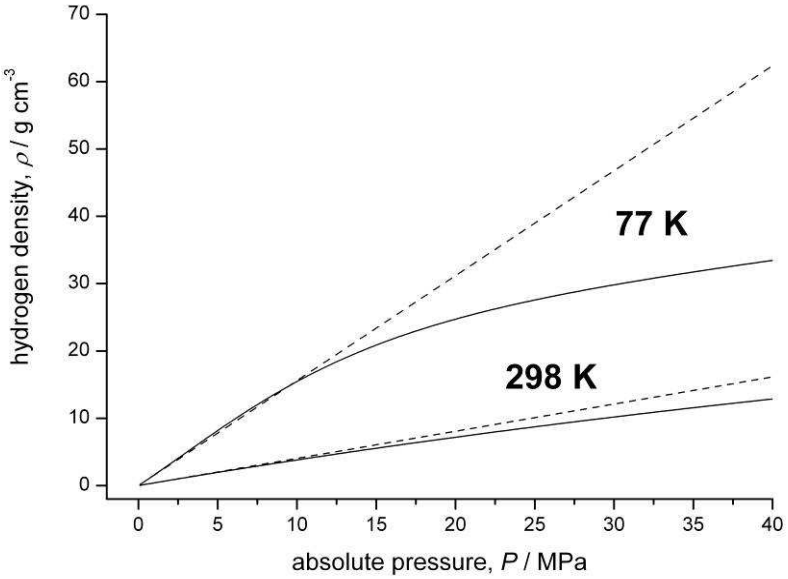

Figure 3.6 – Density of hydrogen up to 40 MPa at 77 and 298 K. The solid lines are the density using the rational function fit to the data for the compressibility factor *Z*, the dashed lines are the densities calculated using the ideal gas equation. Adapted from Bimbo et al. [216].

The complexity of Leachman's equation of state makes it difficult to integrate it with other fitting tools, hence the need for a simpler yet equally accurate way of calculating densities for hydrogen at different pressures and temperatures. Using the properties for hydrogen calculated with the REFPROP software available in the NIST Chemistry Webbook for a given temperature, a 4-term rational was fitted in the pressure ranges required to obtain the compressibility factor *Z*. The compressibility factor is then calculated as a rational function, which in this case is the ratio of two quadratics in pressure:

$$Z(P) = \frac{1 + A_1 P + A_2 P^2}{1 + A_3 P + A_4 P^2} \qquad \text{Eq.3.10}$$

Where A_1, A_2, A_3 and A_4 are temperature-dependent parameters. The density of hydrogen at different temperatures and pressures is then calculated using Eq.3.11:

$$\rho_{H_2}(P,T) = \frac{1}{Z}\frac{P}{RT} \qquad \text{Eq.3.11}$$

As observed in Figure 3.6, the deviations from ideal behaviour are much more pronounced in the low-temperature, high-pressure range. These operating conditions

are the most appropriate for studying hydrogen storage, so an accurate determination of the state functions of molecular hydrogen is needed at these conditions to appropriately use the model. Leachman's EOS is the best available equation of state for hydrogen at the time of writing and the approximation using the rational function in Eq.3.10 yields an excellent fit in the necessary range, as it can be observed in Figure 3.7.

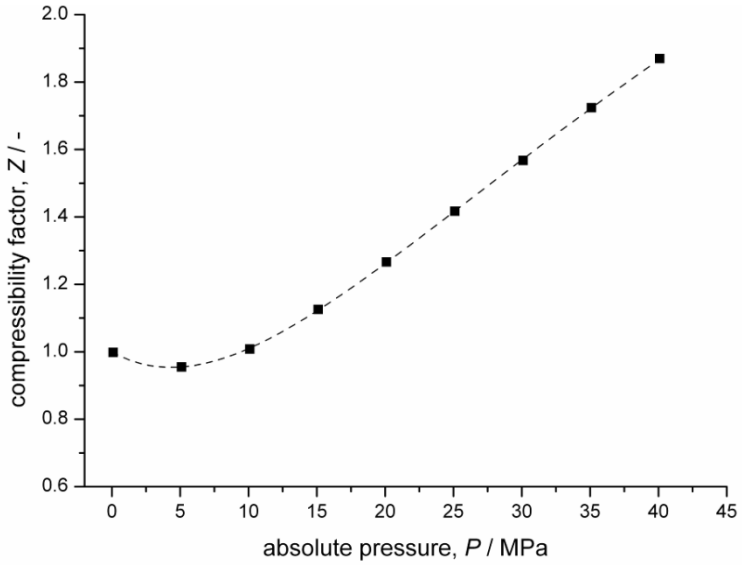

Figure 3.7 – A rational function fit to data from the Chemistry Webbook available in NIST. The square black points are the compressibility factor values taken from NIST and calculated using REFPROP (fewer values than the ones fitted for clarity in the image) and the dashed line is the fit from Eq.3.10 to those same points.

3.4.3. Introducing the methodology

The two previous sections introduced the critical points in supercritical, high-pressure adsorption and Leachman's EOS, its use and the simplification adopted in this work for an approximation of the densities of hydrogen at any given pressure and temperature.

This section introduces the model and methodology used to analyse experimental excess isotherms. In this thesis, the model is applied to hydrogen storage in porous materials, but it could in principle be used for any adsorptive above its critical point. As already mentioned in section 3.4.1, the absolute amount for a supercritical fluid monotonically increases while the excess reaches a maximum at high pressures and then starts to decrease. The adsorbed phase (adsorbate) is the absolute amount

adsorbed n_a and can be partioned into excess n_e and bulk n_b contributions, as shown in Figure 3.4:

$$n_a = n_e + n_b \qquad \text{Eq.3.12}$$

The bulk quantity n_b can be expressed using the density at a given P,T and the specific pore volume v_A, which is expressed in specific units of adsorbent ($cm^3\ g^{-1}$), that is, the available volume per gram of adsorbent. The molecular mass of hydrogen is included so that the density can be introduced in mols (the molecular mass of H_2 will be omitted from the equations from this point on).

$$n_b = \rho_b v_A M(H_2) \qquad \text{Eq.3.13}$$

In Eq.3.13, the density can be calculated using the rational function described in the previous sub-section. The v_A is the specific pore volume for the gas and the absolute adsorbed amount can be calculated if v_A is determined. The specific accessible (or pore) volume can be characterised using CO_2 or N_2 adsorption but there are some diffusional problems which imply great care and lengthy procedures to be accurate [89]. Also, the specific pore volumes determined using CO_2 and N_2 are gas-specific, which means that due to the different sizes of molecules they yield different results depending on the probe molecule used. Also, for hydrogen, the narrower pores which are only accessed by small molecules are thought to be the ones contributing the most for H_2 adsorption. Incorrect determination of the pore volume leads to an inaccurate quantification of the absolute amount adsorbed. While there are techniques to determine v_A accurately for hydrogen, such as using liquid hydrogen [208], using an experimentally determined specific pore volume means that no analytical function is modelled for the system, which precludes extrapolation to other operating conditions. Our methodology is applied to excess experimental data and extracts parameters that define the excess and absolute isotherms for the whole pressure range. The model also determines a pore volume v_A which is independent from experimental measurements and is a parameter from the fit. Myers and Monson demonstrated a methodology for converting absolute variables to excess variables [219] and referred that the opposite situation (extracting absolute variables from excess) was in principle impossible.

However, based on their work, and on Eq.3.12, we can rearrange it to the following form:

$$n_e = n_a - n_b \qquad \text{Eq.3.14}$$

The absolute adsorption n_a is assumed to follow a IUPAC type I behaviour, as illustrated in the diagram in Figure 3.5. This type I behaviour, monotonically approaching an asymptote, can be modelled using any IUPAC type I equation. IUPAC Type I equations are also called saturation isotherms because at very high pressures they saturate and have a limiting quantity (the limiting absolute capacity n_a^{max}). A IUPAC type I equation seems to physically describe the system well, if a nanoporous material is used, because the pores in the system are narrow and will eventually fill up, meaning that there is a limiting adsorptive capacity for the material. There are a number of different IUPAC type I equations and the most common in literature are the Langmuir [220], the Sips [221], the Tóth [222-228], the BET [87], the UNILAN [229], the Jovanović-Freundlich [230], the Dubinin-Astakhov [231] and the Dubinin-Radushkevich [120]. The choice of isotherm will depend on the system being used and despite some equations being derived for subcritical adsorption, like the BET or the Dubinin-Astakhov, they have been applied to supercritical systems. For example, the DA has been applied to hydrogen adsorption [175, 176, 232, 233] assuming fictional vapour-pressures determined by the relation provided by Amankwah and Schwarz [201]. The IUPAC type I equations are usually expressed as a fractional filling θ, varying between zero and 1 and expressed as a relation between absolute amount adsorbed n_a and limiting capacity n_a^{max}.

$$\theta = \frac{n_a}{n_a^{\max}} \qquad \text{Eq.3.15}$$

If the fractional filling θ is expressed as an IUPAC type I equation, we can define n_a with n_a^{max} and the parameters from the IUPAC type I equation.

$$n_a = n_a^{\max}\theta \qquad \text{Eq.3.16}$$

And if we replace Eq.3.14 with Eq.3.16 and 3.13:

$$n_e = n_a^{\max}\theta - \rho_b v_A \qquad \text{Eq.3.17}$$

The density of the bulk adsorptive ρ_b is determined using Eq.3.11, where the compressibility factor Z is replaced with the rational function in Eq.3.10.

$$n_e = n_a^{\max}\theta - \frac{1}{Z}\frac{P}{RT}v_A \qquad \text{Eq.3.18}$$

If the Langmuir equation is used, which is a simple IUPAC type I equation for the fractional filling θ:

$$n_e = n_a^{\max}\frac{bP}{1+bP} - \frac{1}{Z}\frac{P}{RT}v_A \qquad \text{Eq.3.19}$$

In Eq.3.19, the b in the Langmuir equation is called the affinity parameter [234]. The experimental data are then fit with Eq. 3.18, with different IUPAC type I equations used, as it will be discussed in the next sub-section of this chapter, section 3.4.4.

The analysis is done using OriginPro software (version 6.1, OriginLab, Northampton, MA, USA). The model is fitted using the nonlinear regression tool available in Origin, which is based on the Levenberg-Marquardt damped least squares algorithm [235, 236]. The algorithm is explained in more detail in Additional Information B.

Pairs of experimental values (n_e, P) for the experimental excess isotherms, which are the dependent and independent variable, respectively, are fit with the described algorithm and using Eq.3.18. The unknown parameters are determined with initial estimates and successive iterations of the algorithm, until no change is observed in the reduced chi-square (χ^2_{red}). The χ^2_{red} indicates the goodness of fit and is explained in more detail in Additional Information B. These parameters are n_a^{max}, v_A and those that are specific to the IUPAC type I equation used, which describe the absolute isotherm.

3.4.4. Different type I equations

The fractional filling θ is a ratio between the absolute adsorbed amount and the limiting capacity of the material, as already defined in Eq.3.15. This ratio varies between zero and 1 and it is modelled using a IUPAC type I equation, with the asymptote for the limiting capacity being n_a^{max}. There are a number of IUPAC type I equations in the literature, the most commonly used being the Langmuir [220] (Eq.3.27), the Sips [221] (Eq.3.28), the Tóth [222-228] (Eq.3.29), the UNILAN [229] (Eq.3.30), the Jovanović-Freundlich [230] (Eq.3.31), the Dubinin-Astakhov (DA) [231] (Eq.3.32) and the Dubinin-Radushkevich (DR) [120] (Eq.3.33). The Langmuir equation was proposed by Irving Langmuir and it is the first attempt at quantifying adsorption. The equation was originally developed for the adsorption in flat surfaces of glass, mica and platinum [220]. Irving Langmuir was awarded a Nobel Prize in Chemistry "for his discoveries and investigations in surface chemistry" . The Sips equation, also called the Langmuir-Freundlich equation, was developed by Sips as an extension of the Freundlich equation and reduces to the Freundlich at low pressures. However, the Sips equation saturates at large pressures and its energy distribution function is of Gaussian type [221]. The Tóth equation is an empirical equation developed by Tóth as an equation that would fulfil three important requirements - it would reduce to Henry's law in the low pressure limit, have a finite value at high pressures and could easily be used for heterogeneous adsorbents whose adsorption potential changes as a function of coverage [238]. The UNILAN equation was developed assuming a uniform distribution of adsorption energy (hence the name, uniform Langmuir) which reduces to the Langmuir equation when the heterogeneity parameter is zero. The Jovanović-Freundlich is a semi-empirical model for single component adsorption, which reduces to the Jovanović equation when the surface is homogeneous. It also reduces to a monolayer isotherm at high concentrations but it fails to obey Henry's law in the low pressure limit. The energy distribution is a quasi-Gaussian function [239]. The DR and DA were both developed by Dubinin and co-workers as part of the concept of micropore filling [240]. An assumption of fractional filling of the micropore volume is assumed and the isotherm is represented using a constant temperature "characteristic curve" [121]. The DA equation was developed as a more general case of the DR, introducing an additional parameter.

All these equations have a finite limit at very high pressures and because of that, are also designated as saturation isotherms. Both the DA and DR equations are used in their modified forms, as reported by Richard et al. [175].

$$\theta = \frac{bP}{1+bP} \qquad \text{Eq.3.27}$$

$$\theta = \frac{(bP)^c}{1+(bP)^c} \qquad \text{Eq.3.28}$$

$$\theta = \frac{bP}{\left[1+(bP)^c\right]^{\frac{1}{c}}} \qquad \text{Eq.3.29}$$

$$\theta = \left(\frac{1}{2c}\right)\ln\left[\frac{1+bP\exp(c)}{1+bP\exp(-c)}\right] \qquad \text{Eq.3.30}$$

$$\theta = 1-\exp-(bP)^c \qquad \text{Eq.3.31}$$

$$\theta = \exp\left(\frac{RT}{\alpha_E+\beta_E T}\right)^m \ln\left(\frac{P_0}{P}\right)^m \qquad \text{Eq.3.32}$$

$$\theta = \exp\left(\frac{RT}{\alpha_E+\beta_E T}\right)^2 \ln\left(\frac{P_0}{P}\right)^2 \qquad \text{Eq.3.33}$$

The *b* parameter in Eqs.3.27, 3.28, 3.29, 3.30 and 3.31 is called the affinity constant and the *c* parameter in Eqs. 3.28, 3.29, 3.30 and 3.31 is called the heterogeneity parameter [234]. The heterogeneity parameter characterises the heterogeneity of the system, which can be the structural or chemical heterogeneity of the surface, and it varies between zero and one for the Sips and Tóth equations. If equal to one, both equations reduce to the Langmuir equation, meaning that the heterogeneity parameter equal to one reflects the homogeneous surface case. The *m* parameter in Eq.3.32 is also related to the energetic surface heterogeneity, like parameter *c*. The parameter P_0 is the vapour pressure, which does not apply for a supercritical fluid, but for this work was used as a parameter from the fit. It has been used for hydrogen [175, 186] with the relation provided by Amankwah and Schwarz [201], shown in Eq.3.34, where P_0 is the vapour pressure, P_c and T_c are the critical pressure and temperature and *k* is a parameter from the fit.

$$P_0 = P_c\left(\frac{T}{T_c}\right)^k \qquad \text{Eq.3.34}$$

For the DA and DR equations, R is the molar gas constant in J mol^{-1} K^{-1}, T is the absolute temperature in K, α_E is the enthalpic factor and β_E is the entropic factor [175]. Both factors are determined from the fitting and the enthalpic factor is related to the isosteric enthalpy of adsorption.

3.4.5. Modelling excess isotherms

Myers and Monson [219] showed that one can obtain excess isotherms from absolute variables and that this conversion is precise, as long as the pore volume is defined. The reverse process of calculating absolute adsorption by experimental methods is "impossible in principle" according to the same authors, because there is no way of determining experimentally the space lying within the potential field of the solid. One can, however, assuming the absolute follows a IUPAC type I behaviour which monotonically increases and asymptotes at higher pressures, see which is the best absolute isotherm that fits the experimental excess isotherm, based on the principles introduced in section 3.4.2. The density of the adsorbate is unknown and since the potential field of the solid is impossible to measure, estimating absolute adsorption is not an easy task, but one can ask what are the parameters for the absolute isotherm that, taking into account Eq.3.18, best fit the available experimental excess isotherm. The estimation of the specific pore volume (v_A) from experiment is also unnecessary since it can be one of the unknown parameters from the model. Provided there are enough experimental excess points covering both the low and high ends of pressure, we can fit Eq.3.18 using any of the IUPAC type I equations mentioned in the previous sub-section and estimate the limiting capacity n_a^{max}, the specific pore volume v_A and the corresponding parameters for the IUPAC type I equation.

If we use Eq.3.18 with the Tóth as the IUPAC type I equation:

$$n_e = n_a^{\max} \frac{bP}{\left[1+(bP)^c\right]^{\frac{1}{c}}} - \frac{1}{Z}\frac{P}{RT} v_A \qquad \text{Eq.3.35}$$

The Levenberg-Marquardt algorithm is used to extract the parameters n_a^{max} and v_A and the parameters specific to the Tóth, which are b and c. The excess isotherm is described with Eq.3.35. The absolute isotherm is described with the parameters estimated from the fit and it is:

$$n_a = n_a^{\max} \frac{bP}{\left[1+(bP)^c\right]^{\frac{1}{c}}} \qquad \text{Eq.3.36}$$

In this work, units relating to sorption capacities and absolute and excess are sample-specific, that is, per unit mass of adsorbent in some reference state m^0_{ads}, with the reference state being the dry mass. The units for reporting hydrogen sorption quantities for excess and absolute capacities (n_e and n_a) and limiting capacity n_a^{max} in this work are:

$$wt.\% = \left(\frac{m_{H_2}}{m^0_{ads}}\right) 100 \qquad \text{Eq.3.37}$$

The pressure units used in this work are MPa, so units for P and b are in MPa and MPa^{-1}, respectively. The compressibility factor Z is adimensional. The molar gas constant R is in 10^{-6} J mol^{-1} K^{-1} (because of the MPa units for P), T is in K and v_A is in cm^3 g^{-1}. The heterogeneity factor for the Tóth equation is related to the heterogeneity of the surface and it is adimensional.

The methodology then consists of, for an isotherm at a given temperature, fitting the rational function parameters (Eq.3.10) to density data taken from the Chemistry Webbook at that temperature. Once these parameters (A_1, A_2, A_3 and A_4) are determined, the experimental excess data is fit using Eq.3.18 and n_a^{max} and v_A are calculated, as well as the parameters for the IUPAC type I equation. Once the parameters for the IUPAC type I equation are known, the absolute isotherm can be

determined for all the pressures of that temperature. In Figure 3.8, we can see experimental excess data for the MAST TE7 carbon beads at 77 K up to 17 MPa being fit using this methodology. The black squares are the data points, the fitted excess is the solid line and the absolute is the dashed line.

After the fitting is applied to the excess, we can extrapolate for different conditions (pressure and temperature) and we can estimate the total amount of hydrogen that is contained in a material.

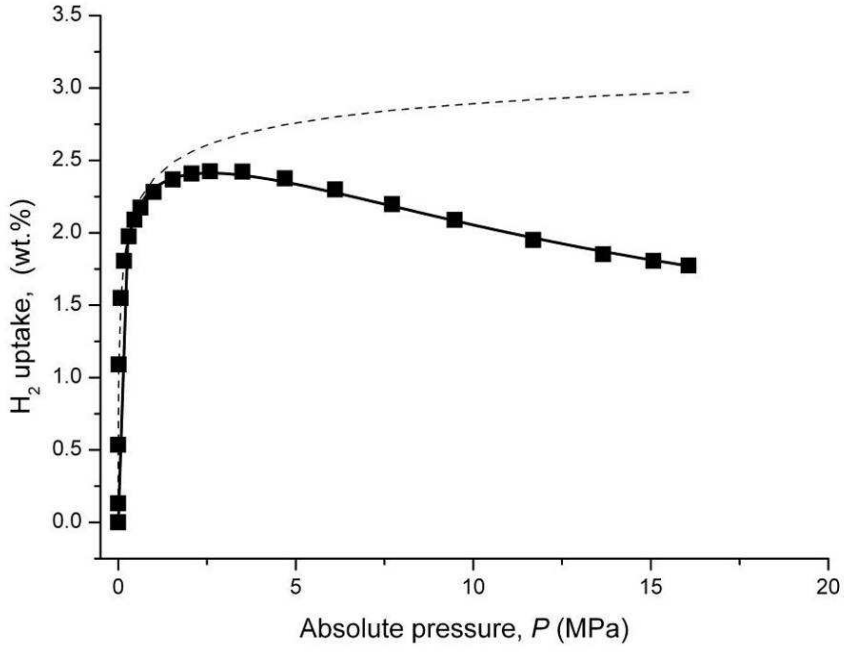

Figure 3.8 - MAST TE7 carbon beads hydrogen adsorption data at 77 K. The square points are the experimental excess points, the solid black line is the fitted excess using Eq.3.18 (using the Tóth as the IUPAC Type I equation) and the dashed line is the estimated absolute using the parameters from the fitting to the excess.

As the next chapter shows, the choice of IUPAC type I equation is very important and can lead to drastic differences in estimated absolute amounts. Also in the next chapter, the temperature dependence of the different parameters and the corresponding multiple fitting to isotherms for the same material collected at different temperatures is studied.

3.5. Summary

The methodology to apply to experimental excess data, as well as the experimental methods and materials' synthesis, characterisation and activation were discussed in this chapter. The methodology was introduced and explained, providing the theoretical basis for the model, its application to experimental data and some of the information that can be derived from fitting hydrogen excess sorption points. Since a prediction of the properties of hydrogen at different temperatures and pressures was necessary, and this prediction needed to be as accurate as possible, the Leachman's EOS was introduced, which is the best available equation of state for hydrogen. Due to the complexity of the equation, density data at different temperatures was fitted using a rational function to account for the non-ideal behaviour of hydrogen at different operating conditions. This made it possible to accurately calculate the densities in a wide range of pressures and temperatures.

The model is very sensitive to the IUPAC type I equation used, which is why further investigation was necessary to address this. The next chapter includes an in-depth discussion of which IUPAC type I equation to use. The last part of this chapter was the application of the methodology to experimental excess data and an example fit using the Tóth as the IUPAC type I equation was performed and explained.

Chapter Four

Results and Analysis

4. Results and Analysis

4.1. Introduction

In this chapter, the model and methodology explained in the previous chapter are applied to hydrogen sorption data for different porous materials. Excess hydrogen sorption data for TE7, AX-21, MIL-101 and NOTT-101 are analysed and fit using the methodology. The temperature dependence of the parameters is studied, investigating if there are any significant trends and multiple fitting of the different isotherms is done, with some relevant parameters collected for the different materials.

The analysed materials are benchmarked and evaluated against conventional methods, especially compression at the same temperature. A break-even point, which is the point in equal volume containers where the quantity stored by adsorption equals the quantity stored by compression at the same temperature, is identified for all the materials for a range of temperatures. The densities of the adsorbed hydrogen for all the materials are compared with densities of liquid and solid hydrogen. A ratio of the adsorbed density over the bulk density is also plotted to show the density enhancement for adsorption and the operating pressures where there is a density gain over the bulk gas.

Finally the chapter finishes with the investigation of the thermodynamics of adsorption for one system, NOTT-101. The isosteric enthalpies of adsorption, important from both an applied and fundamental point of view, are calculated using the Clausius-Clapeyron method, a widely used method in adsorption and compared with the isosteric enthalpies calculated using the Clapeyron equation, which is the exact thermodynamic equation for phase changes. This was done to verify if the assumptions present in the Clausius-Clapeyron equation are valid for isosteric enthalpies calculation in the conditions used for hydrogen storage, which are cryogenic temperatures and high pressures.

4.2. Analysis of experimental excess sorption data

4.2.1. Datasets, temperature dependence and multiple fitting

The analysed materials are the MAST TE7 carbon beads, the "superactivated" carbon AX-21 and the metal-organic frameworks NOTT-101 and MIL-101, described in the Materials and Methods section (Chapter 3) of this thesis. The excess data for the materials were acquired in the high-pressure range at cryogenic temperatures. The excess datasets are presented in Fig.4.1.

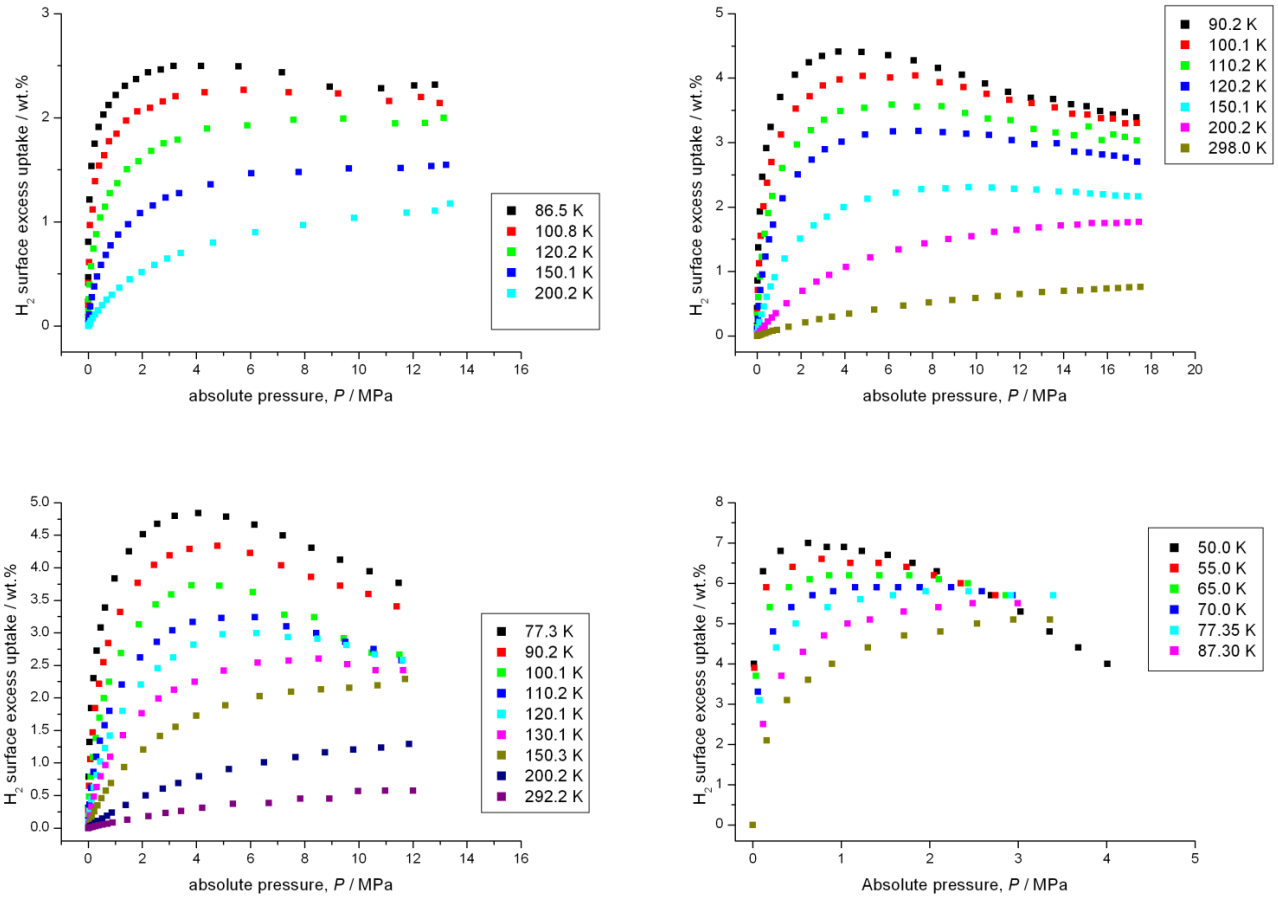

Figure 4.1 – Excess data for the TE7 (top left plot), AX-21 (top right plot), MIL-101 (bottom left plot) and NOTT-101 (bottom right plot) for a range of temperatures.

For the TE7, the hydrogen isotherms were collected up to 14 MPa at 86.5, 100.8, 120.2, 150.5 and 200.2 K. The isotherms for the AX-21 were collected at 90.2, 100.1, 110.2, 120.2, 150.1, 200.2 and 298.0 K up to 16 MPa. The isotherms for the MIL-101 were collected at 77.3, 90.2, 100.1, 110.2, 120.1, 130.1, 150.3, 200.2 and 292.5 K up

to 12 MPa. The temperatures are the average for all the points in the isotherm. The hydrogen isotherms for the NOTT-101 were generously provided by Dr Anne Dailly and were collected at 50.0, 55.0, 60.0, 65.0, 70.0, 77.35 and 87.30 K and up to 4 MPa in the General Motors Research Laboratories (Chemical and Environmental Sciences Laboratory, General Motors Corporation, Warren, MI 48090, USA).

The hydrogen excess data can be fit individually, that is, each isotherm, using the methodology introduced in the Materials and Methods section. For any isotherm at any temperature, the excess can be fit so that the unknown parameters can be determined. The extracted parameters are different according to the type I equation used. Once the parameters are determined, the absolute isotherm can be calculated and both the excess and the absolute can be extrapolated to higher pressures. Extrapolation to other temperatures requires knowledge of the temperature dependence of the parameters. Ideally, an analytical model should be able to predict the uptake for a given material for any operating conditions, that is, any temperature or pressure. For an analytical model to predict for any operating conditions, the isotherms for a material at different temperatures should be collected and the methodology employed separately on single isotherms. After fitting to the different isotherms, the temperature dependence of the resulting parameters should be examined.

We have studied the parameter dependence of the Tóth equation applied to the experimental excess isotherms of different materials. In Fig 4.2, as an illustration of the temperature dependence of the parameters, the limiting absolute quantity n_a^{max}, the c parameter (the heterogeneity parameter) and the specific pore volume v_A using the Tóth equation for the TE7 and the NOTT-101 are plotted against the temperature. From the figure, and if both materials are considered, no obvious temperature dependence is observed for the limiting absolute quantity n^a_{max}, for the heterogeneity parameter c nor for the specific pore volume v_A. Although the results seem to indicate some linear dependence on temperature for all the parameters in the TE7, if both materials are taken into account, no temperature dependence that can be modelled using a simple relation can be found.

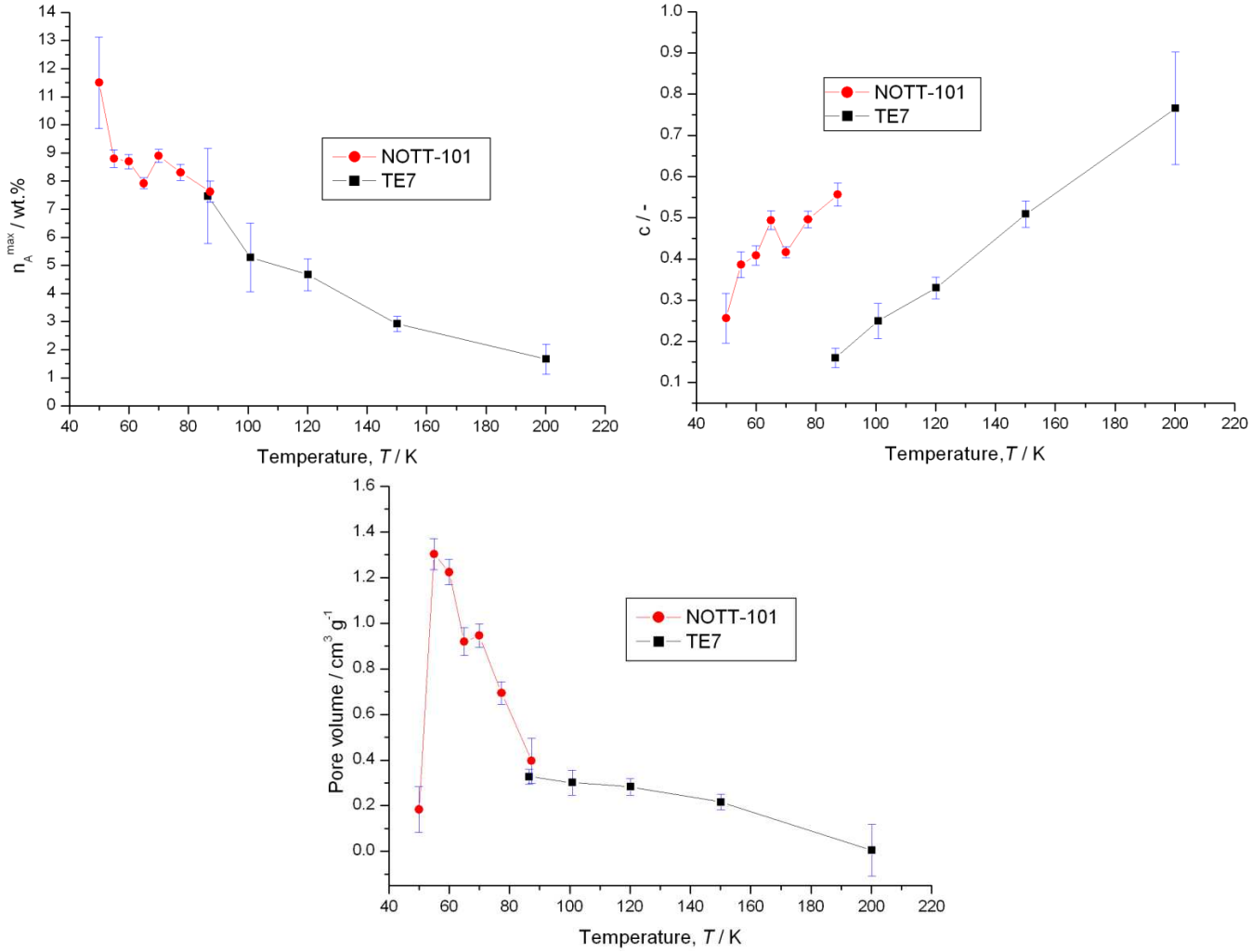

Figure 4.2 – Temperature dependence of the parameters determined using the Tóth equation as the type I equation for the NOTT-101 and the TE7. The parameters are the limiting absolute capacity n_a^{max}(top left plot), the heterogeneity parameter *c* (top right plot) and the specific pore volume v_A (bottom plot). Errors correspond to the standard error and they are derived from the fits.

This temperature dependence is based on the methodology applied to the data at each unique temperature, using the Tóth equation as the type I equation and then plotting the values and errors as a function of temperature.

For both materials, an activated carbon and a MOF, no obvious temperature dependence was observed for the *c* parameter, the pore volume v_A and the limiting absolute quantity n_A^{max}. For the model to predict uptakes at different temperatures, it was necessary to build in temperature dependence on one or more parameters. The affinity constant *b* was expected to show some temperature dependence for all the materials [228] and, as observed in Figure 4.3, if it is plotted logarithmically against the inverse of temperature, it seems to display a slight curve-like behaviour for the

TE7 and a straight line for the NOTT-101. Despite the curve-like behaviour for the TE7, the results suggest that the affinity constant could be modelled for all materials using the van't Hoff relation, as it is the parameter most likely to exhibit temperature dependence [228] and since no temperature dependence that could be modelled using a simple relation was seen for both materials in any of the other parameters.

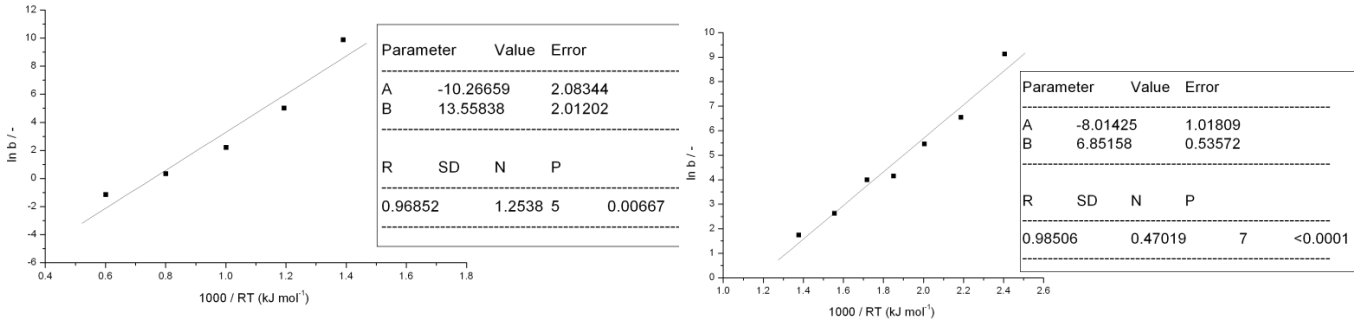

Figure 4.3 – Affinity constant *b* from the Tóth fits to the TE7 (left hand side plot) and NOTT-101 (right hand side plot) material on a logarithmic scale against the inverse of temperature. The points are the affinity constant from the fits to single isotherms and the line is a simple linear fit to those points.

The van't Hoff relation is a chemical thermodynamics relation for the temperature dependence of an equilibrium constant. The derivation of the van't Hoff relation from the Gibbs free energy is explained in Additional Information C. A rearranged version of the van't Hoff equation, with the abscissa at zero being related to the entropic factor b_0 is shown in Eq.4.1.

$$\ln b = \frac{1}{RT} Q_{st}^{O} + \ln b_0 \qquad \text{Eq.4.1}$$

In Eq.4.1, b is the affinity constant, R is the molar gas constant, T is temperature, b_0 is the entropic factor and Q^0_{st} is the characteristic energy of adsorption. The affinity constant b exhibits strong temperature dependence which can be modelled using a van't Hoff relation. The experimental excess isotherms can be fit using our methodology and the analytical model can be used to predict capacities and extrapolate to the whole pressure range. Once the temperature dependence is determined for every single parameter, extrapolation to other temperatures also becomes possible.

After fitting every isotherm individually and determining the temperature dependence of the parameters, the model can be set to fit different isotherms of the same material using the fitting of multiple datasets tool. The multiple fitting tool is available in the nonlinear fitting analysis tool of OriginPro software (OriginLab, Northampton, MA, USA) allowing the fit of multiple datasets to the same function, with the option of selecting which parameters are to be shared between the different datasets. This means that if no temperature dependence is observed for the heterogeneity parameter *c*, it can be assumed as constant for different temperatures, so it will be shared (*i.e.*, it will have the same value) for all the isotherms that are being fit. If, on the other hand, the affinity constant *b* is assumed to have temperature dependence, then the parameter will not be shared between the different isotherms and *b* will have a different value for any single isotherm. The excess experimental isotherms were fit using Eq.3.18. The limiting absolute quantity and specific pore volume were assumed to be temperature independent and constant for all the isotherms. The heterogeneity parameter *c* is also assumed to be temperature independent. The affinity constant *b* is the only temperature dependent parameter for the fitting of the multiple datasets. The temperature dependence is modelled according to the van't Hoff equation for the Langmuir, Sips, Tóth, UNILAN and Jovanović-Freundlich, and *b* is assumed to vary with temperature according to Eq.4.2, which is a modification of Eq.4.1.

$$b = b_0 \exp\left(\frac{Q_{st}^{\circ}}{RT}\right) \qquad \text{Eq.4.2}$$

The affinity constant *b* is modelled using Eq.4.2 and substituted for the fitting of multiple datasets, when using the Langmuir, Sips, Tóth, UNILAN and Jovanović-Freundlich equations. The entropic factor b_0 and the characteristic energy of adsorption Q_{st}° are also temperature independent, so they will remain constant for every single isotherm. The molar gas constant *R* will also remain constant and equal to 8.314 J mol^{-1} K^{-1}. The units for the entropic factor b_0 and the characteristic energy of adsorption Q_{st}° are MPa^{-1} and J mol^{-1}, respectively. The different materials were fit using the Tóth as the type I equation, assuming temperature independence for the limiting absolute quantity n_a^{max}, the pore volume v_a, the heterogeneity parameter *c*, the

entropic factor b_0 and the characteristic energy of adsorption Q_{st}°, with T in Eq.4.2 changing for the different temperatures.

For the temperature dependence of the Dubinin equations, a different approach was taken. The DA can be represented in the form of Eq.4.3.

$$\theta = \exp\left[-\left(A_P / bQ_{st}^0\right)^m\right] \qquad \text{Eq.4.3}$$

In Eq.4.3, b is the affinity parameter, Q^0_{st} is the characteristic energy of adsorption and the parameter A_P is Polanyi's adsorption potential, as shown in Eq.4.4.

$$A_P = RT \ln\left(\frac{P_0}{P}\right) \qquad \text{Eq.4.4}$$

The affinity parameter b and the characteristic energy of adsorption Q^0_{st} were modelled using an entropic and enthalpic contribution, as shown in Eq.4.5.

$$bQ_{st}^0 = \alpha_E + \beta_E T \qquad \text{Eq.4.5}$$

The Dubinin equations were then used in this work in their modified form, as other researchers have applied [175] and as shown in Eq.4.6.

$$\theta = \exp\left[-\left(\frac{RT}{\alpha_E + \beta_E T}\right)^m \ln\left(\frac{P_0}{P}\right)\right] \qquad \text{Eq.4.6}$$

The DA equation was used with the heterogeneity parameter m as a parameter from the fit, while the DR was used with the heterogeneity parameter m with a fixed value equal to 2. The temperature dependence was already built-in the modified form of the equations, while the other parameters (α_E, β_E, P_0 and m for the DA) were considered constant throughout the temperature range. In the Dubinin equations, R is the molar gas constant (equal to 8.314 J mol^{-1} K^{-1}). The units for T are K, for the enthalpic factor α_E are J mol^{-1}, for the entropic factor β_E are J mol^{-1}K^{-1}, and for P_0 and P are MPa. The

entropic and enthalpic contribution in the form of Eq.4.5 for the DR and DA equations are also temperature independent and T is the only parameter that changes with temperature. The characteristic energy of adsorption and the enthalpic factor in the Dubinin equations are related to the isosteric enthalpy of adsorption. It should be emphasised that assuming no temperature dependence for the remaining parameters apart from the affinity constant b makes the model simpler, as opposed to building in a temperature dependence (which can be a linear relation or an even more sophisticated relation, like a polynomial) for the other parameters, making the model and the equation to fit to data more complex. There is the danger of putting in too many parameters in the model, making it excessively complicated. Also, temperature dependence on some parameters might not make much sense physically, for instance, if one assumes a temperature dependence of the pore volume. While it is true that some materials have the phenomenon of "breathing" [129, 241] and opening up of the pores with temperature and/or pressure changes, this is hardly likely to be the case for an activated carbon due to its structural rigidity.

After fitting the multiple datasets for each material and extracting parameters that are constant for all temperatures, an analytical model that can be used to extrapolate to the whole pressure and temperature range can be constructed. In addition to the temperature dependence of the parameters, it is also important to ensure the equation used to model the fractional filling is the most appropriate one. The multiple datasets for the different materials are fitted using different equations and this is discussed in the next section.

4.2.2. Using different type I equations

This analysis and methodology, as already mentioned, are quite sensitive to the type I equation used. This can be explained on different theoretical footings of different equations, with some developed for subcritical systems – the Dubinin equations, DA and DR, were developed for the analysis of micropore filling - others, like the Tóth, originally developed for monolayer adsorption [121]. In this section, analysis of their differences applied to the same datasets is performed to determine and characterise the use of different equations.

The experimental datasets were all fit using the methodology and changing the type I equation to describe the fractional filling, using the equations mentioned in section 3.4.4. The parameters from the fit to the TE7 carbon beads are in Table 4.1 and 4.2 for all the different equations. The errors are the standard errors from the fitting algorithm, which were obtained using the variance-covariance matrix, as explained in Additional Information B.

Table 4.1 - Parameters from the fitting to the TE7 carbon beads using different type I equations. Errors correspond to the standard error and they are derived from the fits.

	n_a^{max} / wt. %	c / -	b_0 / MPa^{-1}	Q_{st}° / kJ mol^{-1}	v_A / cm^3 g^{-1}
Langmuir	2.25 ± 0.05	1	0.0015 ± 0.0003	7.0 ± 0.2	0.03 ± 0.03
Sips	2.78 ± 0.04	0.59 ± 0.01	0.00083 ± 0.00008	7.0 ± 0.1	0.09 ± 0.01
Tóth	2.97 ± 0.05	0.44 ± 0.01	0.0065 ± 0.0007	7.0 ± 0.1	0.14 ± 0.01
UNILAN	2.71 ± 0.04	3.35 ± 0.08	0.00084 ± 0.00007	7.1 ± 0.1	0.11 ± 0.01
Jovanović-Freundlich	2.52 ± 0.05	0.46 ± 0.01	0.00046 ± 0.00006	7.0 ± 0.1	0.09 ± 0.02

Table 4.2 - Parameters from the fitting to the TE7 carbon beads using Dubinin type I equations. Errors correspond to the standard error and they are derived from the fits.

	n_a^{max} / wt. %	m / -	P_0 / GPa	β_E / kJ mol^{-1} K^{-1}	α_E / kJ mol^{-1}	v_A / cm^3 g^{-1}
DR	4.60 ± 0.09	2	1.4 ± 0.2	11.3 ± 0.9	5.31 ± 0.08	0.37 ± 0.01
DA	3.9 ± 0.1	3.1 ± 0.2	31 ± 20	34 ± 6	6.10 ± 0.13	0.27 ± 0.02

As can be observed in Table 4.1 and 4.2, the limiting absolute capacity n_a^{max} is very different when using the DR or the Langmuir equation, for example. This limiting capacity is very similar when using the Tóth, Sips, UNILAN and Jovanović-Freundlich equations. The Langmuir equation gave a slightly lower value, with the DA and DR giving higher limiting capacity values. The heterogeneity parameter c and the entropic factor b_0 were different for the Tóth, Sips, UNILAN and Jovanović-Freundlich, with the characteristic energy of adsorption Q_{st}° having a value similar for all of these equations. As already mentioned, both the enthalpic term α_E on the DA and DR equation and the characteristic energy of adsorption Q_{st}° are related to the

isosteric enthalpies of adsorption. The values for the characteristic energy of adsorption from the Tóth, Sips, UNILAN and Jovanović-Freundlich equations are all in the range of the limiting isosteric enthalpy of adsorption at zero coverage for activated carbons [88, 178, 242]. The specific pore volumes v_A have very low values for the Langmuir, Tóth, Sips, UNILAN and Jovanović-Freundlich, when compared to experimental specific pore volumes obtained for the same material, which, as noted in the Materials and Methods section (Chapter 3), is 0.43 $cm^3\ g^{-1}$. The Dubinin equations yielded closer values to the experimental ones for the specific pore volumes, but still lower than the reported experimental pore volume.

Tables 4.3 and 4.4 show the parameters for the different type I equations applied to the experimental hydrogen excess dataset of the AX-21.

Table 4.3 - Parameters from the fitting to AX-21 using different type I equations. Errors correspond to the standard error and they are derived from the fits.

	n_a^{max} / wt. %	c / -	b_0 / MPa^{-1}	Q_{st}^{o} / kJ mol^{-1}	v_A / $cm^3\ g^{-1}$
Langmuir	4.9 ± 0.1	1	0.0021 ± 0.0002	5.7 ± 0.1	0.45 ± 0.04
Sips	6.2 ± 0.1	0.685 ± 0.009	0.00130 ± 0.00007	5.62 ± 0.07	0.64 ± 0.02
Tóth	6.7 ± 0.1	0.52 ± 0.01	0.0052 ± 0.0003	5.61 ± 0.06	0.65 ± 0.02
UNILAN	6.3 ± 0.1	2.80 ± 0.05	0.00127 ± 0.00006	5.61 ± 0.06	0.66 ± 0.02
Jovanović-Freundlich	5.5 ± 0.1	0.539 ± 0.009	0.00080 ± 0.00008	5.6 ± 0.1	0.60 ± 0.03

Table 4.4 - Parameters from the fitting to AX-21 using Dubinin type I equations. Errors correspond to the standard error and they are derived from the fits.

	n_a^{max} / wt. %	m / -	P_0 / GPa	β_E / kJ $mol^{-1}\ K^{-1}$	α_E / kJ mol^{-1}	v_A / $cm^3\ g^{-1}$
DR	14.2 ± 0.4	2	2.8 ± 0.3	20.2 ± 0.5	3.4 ± 0.05	1.29 ± 0.03
DA	9.5 ± 0.4	4.7 ± 0.6	4313 ± 6000	77 ± 11	4.8 ± 0.1	0.88 ± 0.04

Tables 4.3 and 4.4 show the parameters for the AX-21 dataset. Again, the limiting absolute capacity for the material changes according to the equation used and takes values that seem rather unreasonably high for the Dubinin equations, with a limiting absolute capacity in excess of 14 wt.% when using the DR equation. The

characteristic energies of adsorption Q_{st}° for all the equations in Table 4.4 are in the same range (~5.6 kJ mol^{-1}), while the DR and DA equations had a lower enthalpic factor α of 3.398 and 4.755 kJ mol^{-1} respectively. The pore volumes are all fairly similar for the equations in Table 4.3, slightly higher for the DA equation and much higher when using the DR equation. The reported micropore volume for this material, as mentioned in the Materials and Methods section, is 1.03 cm^3 g^{-1}. All the equations in Table 4.4 give similar results for the different parameters, apart from the Langmuir, the DR and DA equations, whose parameters diverged from the others.

Tables 4.5 and 4.6 present the parameters from the fit to the MIL-101 experimental excess hydrogen data using the different equations.

Table 4.5 - Parameters from the fitting to the MIL-101 using different type I equations. Errors correspond to the standard error and they are derived from the fits.

	n_a^{max} / wt. %	c / -	b_0 / MPa^{-1}	Q_{st}° / kJ mol^{-1}	v_A / cm^3 g^{-1}
Langmuir	5.6 ± 0.2	1	0.0040 ± 0.0004	4.5 ± 0.1	0.70 ± 0.07
Sips	7.1 ± 0.2	0.73 ± 0.02	0.0023 ± 0.0002	4.5 ± 0.1	0.88 ± 0.05
Tóth	7.8 ± 0.3	0.55 ± 0.02	0.0073 ± 0.0006	4.46 ± 0.09	0.89 ± 0.05
UNILAN	7.4 ± 0.3	2.7 ± 0.1	0.0021 ± 0.0002	4.44 ± 0.09	0.91 ± 0.05
Jovanović-Freundlich	6.3 ± 0.2	0.59 ± 0.01	0.0016 ± 0.0002	4.4 ± 0.1	0.85 ± 0.07

Table 4.6 - Parameters from the fitting to the MIL-101 using Dubinin type I equations. Errors correspond to the standard error and they are derived from the fits.

	n_a^{max} / wt. %	m / -	P_0 / GPa	β_E / kJ mol^{-1} K^{-1}	α_E / kJ mol^{-1}	v_A / cm^3 g^{-1}
DR	17.6 ± 0.7	2	2.0 ± 0.7	20.6 ± 0.7	2.65 ± 0.06	1.75 ± 0.06
DA	18 ± 2	1.9 ± 0.3	1 ± 1	19 ± 4	2.6 ± 0.3	1.8 ± 0.1

The MIL-101 is a high surface area MOF and this is indicated by a higher limiting absolute capacity than the two activated carbons. The Sips, UNILAN and Tóth equation all give similar values for the limiting absolute capacity, with the values obtained from the Jovanović-Freundlich and Langmuir a bit lower when compared with these equations. The limiting absolute capacities have substantially higher values

for the Dubinin equations and they are more likely to be an artefact of the fitting. Also, for all the equations in Table 4.6, all the characteristic energies of adsorption are in the same range (~ 4.4 kJ mol^{-1}), while the Dubinin equations exhibit a much lower enthalpic factor. Finally, the pore volumes are around 0.90 $cm^3\ g^{-1}$ for the equations in Table 4.5, while the Dubinin equations have a pore volume of around 1.70 $cm^3\ g^{-1}$. This compares with a micropore volume of 1.51 $cm^3\ g^{-1}$ determined experimentally for this material, as indicated in Chapter Three.

Finally, Tables 4.7 and 4.8 show the parameters for the different type I equations applied to the experimental datasets of NOTT-101.

Table 4.7 - Parameters from the fitting to NOTT-101 using different type I equations. Errors correspond to the standard error and they are derived from the fits.

	n_a^{max} / wt. %	c / -	b_0 / MPa^{-1}	Q_{st}^0 / kJ mol^{-1}	v_A / $cm^3\ g^{-1}$
Langmuir	6.97 ± 0.09	1	0.005 ± 0.001	4.2 ± 0.1	0.89 ± 0.05
Sips	7.8 ± 0.1	0.67 ± 0.02	0.008 ± 0.001	3.91 ± 0.09	1.22 ± 0.06
Tóth	8.2 ± 0.1	0.57 ± 0.02	0.040 ± 0.008	3.56 ± 0.08	1.39 ± 0.05
UNILAN	7.64 ± 0.09	2.7 ± 0.1	0.009 ± 0.001	3.87 ± 0.09	1.19 ± 0.05
Jovanović-Freundlich	7.45 ± 0.09	0.43 ± 0.01	0.0044 ± 0.0007	3.8 ± 0.1	1.14 ± 0.05

Table 4.8 - Parameters from the fitting to NOTT-101 using Dubinin type I equations. Errors correspond to the standard error and they are derived from the fits.

	n_a^{max} / wt. %	m / -	P_0 / GPa	β_E / kJ $mol^{-1}\ K^{-1}$	α_E / kJ mol^{-1}	v_A / $cm^3\ g^{-1}$
DR	9.6 ± 0.2	2	0.066 ± 0.000	-9 ± 2	4.4 ± 0.1	1.79 ± 0.05
DA	9.5 ± 0.3	2.1 ± 0.2	0.07 ± 0.03	-8 ± 4	4.4 ± 0.1	1.7 ± 0.1

The NOTT-101 dataset is slightly different from the other datasets. They were not obtained in the University of Bath and the temperature range is different than previous datasets – 50.0 to 87.0 K. Although this could have implications for the fitting and the parameters obtained for this experimental dataset, Tables 4.8 and 4.9 show a grouping of parameters that is not dissimilar from the ones obtained for the MIL-101, which is

another high surface area MOF. The limiting absolute capacities obtained for the different equations are around 7.0 wt.% for the Langmuir, Sips, Tóth, UNILAN and Jovanović-Freundlich, with the characteristic energy of adsorption ranging from 3.8 to 4.2 kJ mol^{-1} for the same equations. The Dubinin equations show a higher limiting absolute capacity of around 9 wt.%. The enthalpic factor for both the DR and DA is almost identical, with a value of 4.39 kJ mol^{-1}. The pore volumes are sparser for the equations in Table 4.8 than in previous datasets and they range from 0.89 for the Langmuir to 1.39 g cm^{-3} for the Tóth. The pore volumes obtained from the DR and DA equations are in excess of 1.7 g cm^{-3}. The reported crystallographic micropore volume is 1.083 g cm^{-3} and most of the values obtained from the different equations are in excess of this value (in fact, only the Langmuir equation provides with a lower pore volume estimate than the crystallographic one). This might be due to defects in the structure, external surface adsorption or due to "breathing" phenomena, which has been observed in other MOFs and in some cases consists on opening the pore volume upon the influence of an external pressure [129, 241]. The choice of type I equation to apply to the data is an important one, because it will greatly influence results.

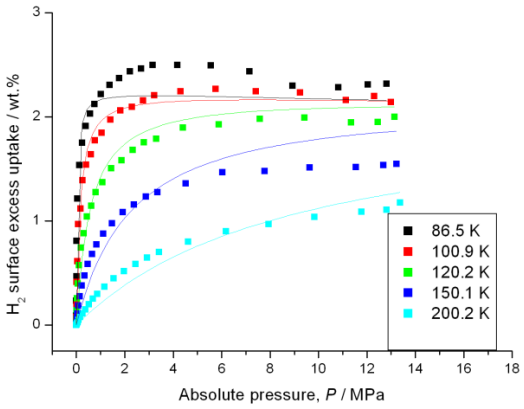

Figure 4.4 - Fitting of the TE7 in the 87 to 200 K range up to 14 MPa using the Langmuir. (adapted from [243] and used with permission from Elsevier).

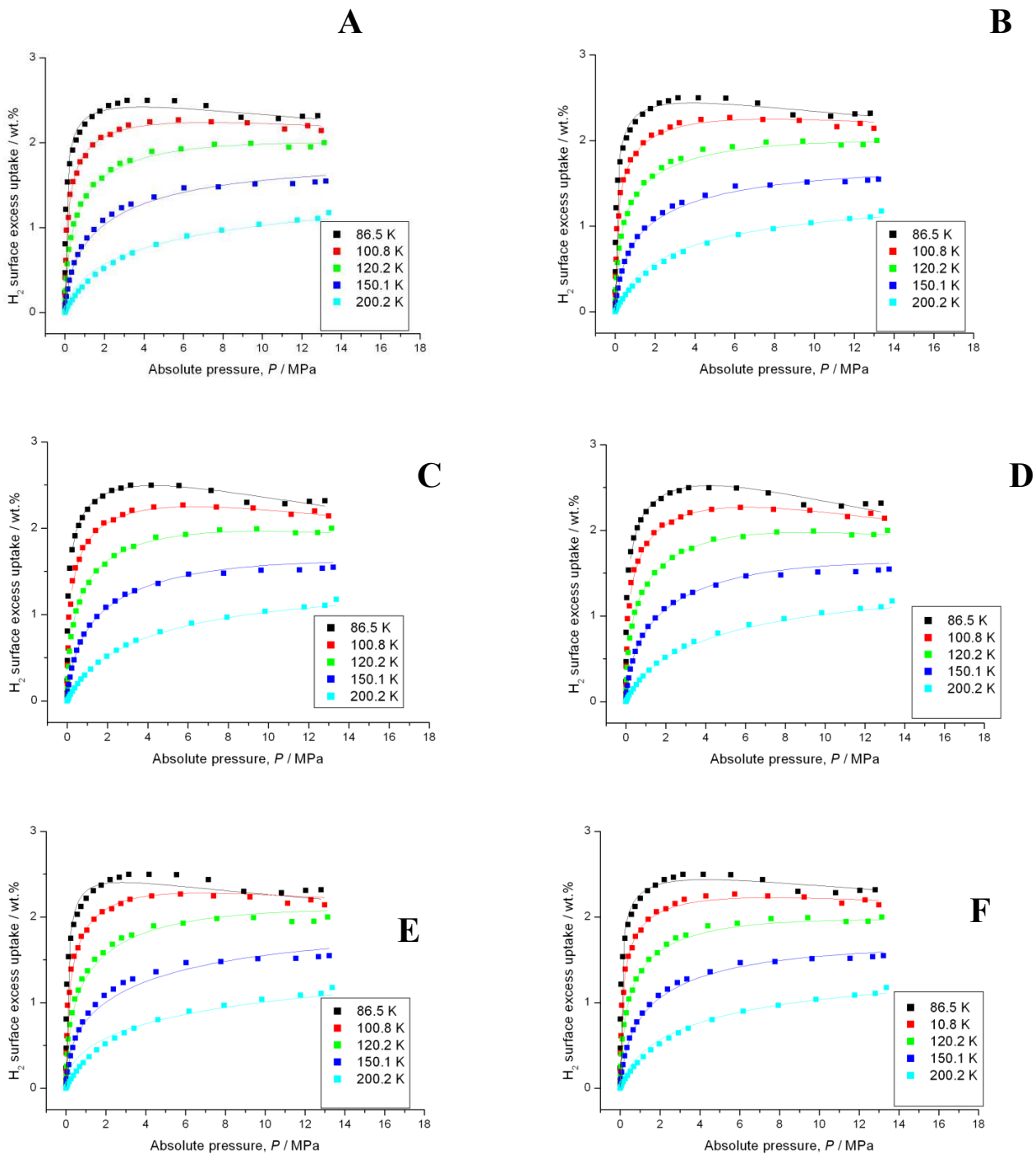

Figure 4.5 – Fitting of the TE7 in the 87 to 200 K range up to 14 MPa using the different type I equations. Type I equation: A - Sips, B - UNILAN, C - Dubinin-Astakhov, D - Dubinin-Radushkevich, E - Jovanovic-Freundlich, F - Tóth. (adapted from [243] and used with permission from Elsevier).

This choice can be done with the analysis of the fits to data and the observation of how close to the model comes to the actual values, the examination of the residuals and the analysis done on the statistical coefficients, like the reduced chi-square (χ^2_{red}) or the coefficient of determination R^2. Both these are a measure of the goodness of fit

and they are explained in Additional Information B. All the remaining equations seem to approximate well the experimental isotherms. Fig 4.4 presents a fit to the TE7 carbon beads with the Langmuir isotherm and Fig.4.5 presents the remaining type I equations. From the figure, it is obvious that the Langmuir equation underpredicts experimental data, with the Jovanović-Freundlich also underpredicting the isotherms in the lower temperature range. Tables 4.9 and 4.10 present the statistical coefficients to help with the analysis of which equation best fits the data. As it can be observed from the table, the χ^2_{red} is lower (the lower the value the better the fit) and the R^2 closer to one (indicating a better fit) for the Dubinin equations, but, in the case of the DA equation, there is an extra parameter in the model in comparison with the other equations (Tóth, Sips, UNILAN and Jovanović-Freundlich), since the vapour pressure P_0 in this analysis is a parameter from the fitting. The Tóth and UNILAN also gave lower values for χ^2_{red} and values of R^2 closer to 1 when compared with the other equations.

Table 4.9 - Reduced chi-square for all the type I equations for the TE7, AX-21, MIL-101 and NOTT-101.

	Langmuir	Sips	Tóth	UNILAN	Jovanović-Freundlich	DR	DA
TE7	0.02055	0.00303	0.00262	0.00261	0.00544	0.00146	0.00104
AX-21	0.0492	0.01089	0.00722	0.0068	0.02381	0.0071	0.00451
MIL-101	0.06548	0.03016	0.02637	0.02637	0.04568	0.01379	0.01386
NOTT-101	0.07422	0.02496	0.02517	0.02424	0.02767	0.01302	0.01319

Table 4.10 – Coefficient of determination of all the type I equations for the TE7, AX-21, MIL-101 and NOTT-101

	Langmuir	Sips	Tóth	UNILAN	Jovanović-Freundlich	DR	DA
TE7	0.97114	0.99578	0.99636	0.99636	0.99242	0.99782	0.99845
AX-21	0.97452	0.99439	0.99628	0.9965	0.98773	0.99619	0.99759
MIL-101	0.96793	0.98531	0.98715	0.98715	0.97775	0.99314	0.99315
NOTT-101	0.97784	0.99264	0.99155	0.99285	0.99184	0.98908	0.98909

With the parameters determined from the fitting of multiple datasets, a comparison of the different equations can be done, by plotting the corresponding absolute isotherm.

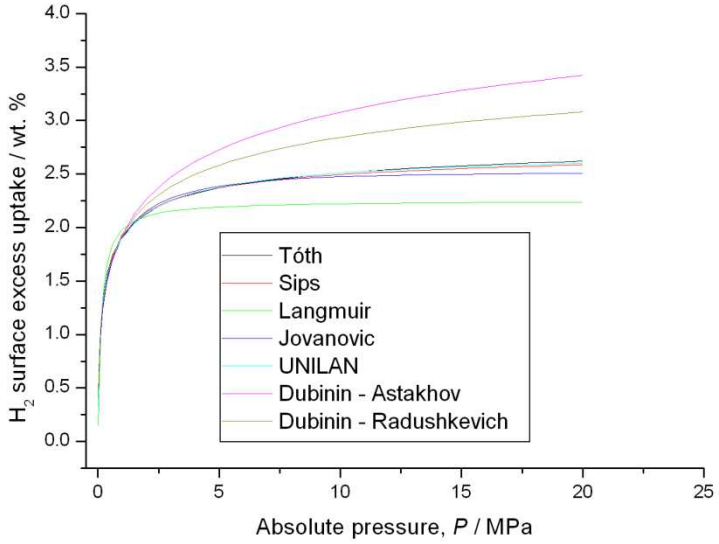

Figure 4.6 – Absolute isotherms determined from the multiple fitting parameters of the different equations up to 20 MPa. The absolute isotherms are in the order of the caption, with the highest capacity at 20 MPa equation being the DR and the lowest the Langmuir equation (adapted from [243] and used with permission from Elsevier).

The absolute isotherms up to 20 MPa determined with the different type I equations are shown in Fig.4.6. Even if the Dubinin equations provide the best χ^2_{red} and R^2 for all the materials analysed in this study, there are some things to consider. The Dubinin equations were developed mostly for subcritical adsorption and they account for vapour pressure. In the modification used in this study P_0 has no physical meaning and comes as a parameter from the fit. The Dubinin-Astakhov equation has more parameters than the others, although both the χ^2_{red} and R^2 are calculated based on the number of variable parameters. The limiting capacities for both equations do not seem reasonable for some materials, being much larger than the ones observed using other equations. The pore volumes obtained with the Dubinin equations were close to the expected value for the TE7, but they were very high for the other materials, and in some cases unreasonable. The limiting absolute capacities, for instance, in the MIL-101, were extremely high, with values close to 19 wt.%, which does not seem to be indicative of the real limiting capacity of those materials.

The equations that yield the most plausible results are the Sips, Tóth and UNILAN. All these equations display similar values for the limiting capacities, pore volumes and characteristic energies of adsorption. In a recent published paper, the UNILAN was considered the best equation to apply to experimental datasets of MOF-5 composites, when compared to the Tóth and the Dubinin-Astakhov equations [190]. Elsewhere, the Tóth was considered the most suitable for fitting data when compared with the Sips for carbons, MOFs, zeolites and porous polymers [189]. We have determined, using single fits for the NOTT-101 material, that the Tóth was the most appropriate equation, when compared with the UNILAN, Sips, Langmuir and Jovanović-Freundlich [216]. In a recently published paper by our research group, Sharpe et al [244] and using a modified version of the methodology presented here – assuming a density profile for the adsorbate within the pore, equal to the one proposed in Chapter 5 of this thesis – and testing it on 6 different materials with a total of 216 fits, the Tóth was considered the equation with the lowest root mean squared residual (RMSR) of all the equations tested, which included the Langmuir, Tóth, Sips, Generalised Freundlich, Jovanović-Freundlich, Dubinin-Astakhov and the UNILAN-b and UNILAN-Q (our terminology, the UNILAN-Q equation is a novel equation presented in the paper).

From our experience, the Tóth seems to be a robust and flexible equation, meaning that it works and converges to a statistically significant result on most datasets and that it can be applied with good results to datasets of different materials, from carbons to MOFs. It is also easy to use and to input into calculations, with the parameters providing meaningful and interpretable results. For these reasons, the Tóth is the equation used in the remainder of the analysis presented in this thesis.

4.3. Comparison with alternative storage methods

4.3.1. Alternative technologies for storing hydrogen

One of the advantages of fitting an analytical model to the experimental data is that the adsorptive capacities of the different materials can be estimated for a range of operating conditions. Since the absolute capacity can be quantified for different

conditions, a comparison between adsorptive storage in different materials and alternative methods of hydrogen storage can be done. The most obvious comparisons to be made are the ones with mature methods, such as compression, cryogenic compression and liquefaction. This is especially important from an applied science perspective, because it could help assessing adsorptive storage in different materials against mature methods. While there are many issues to consider, if adsorptive storage could provide a less energy-intensive method and hence, more economical, a case could be made to implement this technology as opposed to methods currently in use. It would also be important to identify in which operating ranges of *P* and *T* adsorption could store more quantity than other methods, especially compression, which seems to be the store of choice for mobile applications.

There are many issues to consider, including price of materials, systems balance-of-plant (piping, instrumentation, fixings, etc.), diffusion and charge/discharge times for hydrogen, safety and stability when considering and comparing different alternatives. This section only compares quantities stored and comparisons are made between different methods, focusing on adsorptive storage and compression at the same temperature. This is because the operating conditions can be modelled to be the same for both methods, with the difference that in adsorptive storage an adsorbent material is in the container.

Adsorptive storage is very dependent on operating conditions, so it would be quite important to assess which are the optimum ones, *i.e.*, the ones more beneficial for hydrogen storage using adsorption. In the following section we have identified the pressures and temperatures where there is more quantity stored in comparison with compression at the same temperature and these are the conditions that maximise the use of an adsorbent in the container. There is also a point, for any given temperature, where the use of an adsorbent in a container is no longer advantageous. This is because the material displaces a volume in the container and after a certain pressure, more quantity of hydrogen will be stored by simply compressing the H_2 in the same volume at that temperature than by using an adsorbent. This is defined as the break-even point and it is different depending on the material and temperature.

Another important aspect is the comparison using different quantities of adsorbent in the container. A study on different filling ratios – which are the volume of container occupied by the solid adsorbent – is done to evaluate how different quantities of adsorbent influence the gain over compression at the same temperature. Finally, to complement the comparison, the adsorbed densities for the different materials are discussed and compared with liquid and solid H_2 densities. The ratio of adsorbed to bulk hydrogen over increasing pressures is also shown, to underscore the importance of optimum operating conditions.

4.3.2. Volumetric comparisons with compression

In order to compare adsorptive storage with other conventional methods, it is important to quantify the total amount of adsorbate contained in a material. With the parameters determined from the multiple fitting of the different datasets, we can calculate the absolute amount adsorbed and compare it with alternative methods. The Tóth equation was used for the experimental excess isotherm fitting of the different materials and an extrapolation to higher pressures and different temperature ranges was done, using the temperature dependence of parameters discussed in the previous sub-section.

It is also crucial to estimate bulk quantities of hydrogen as accurately as possible. For this, the aforementioned rational approximation for the compressibility factor calculated using the Leachman's equation of state will be used to estimate the densities of hydrogen. To obtain the quantity in the bulk, the bulk density needs to be multiplied by the specific pore volume υ_A, as shown in Eq.4.7.

$$n_B = \frac{1}{Z}\frac{P}{RT}\upsilon_A \qquad \text{Eq.4.7}$$

In Eq.4.7, n_B is the total quantity in the bulk, Z is the compressibility factor, P is pressure in MPa, R is the molar gas constant, which is equal to 8.314 J mol^{-1}, T is temperature in K and υ_A is the specific pore volume in $cm^3\ g^{-1}$.

The mass of hydrogen m_{H_2} within a container of internal volume V_C can be calculated if the volume of bulk gas V_B with density ρ_B and the displaced volume V_D, which is the volume displaced by the adsorbent – that is, the volume of the adsorbent plus the volume of the adsorbate - are factored in the equation. The filling factor f is a relation between the displaced volume V_D and the volume of the container V_C, as shown in Eq.4.8.

$$f = \frac{V_D}{V_C} \qquad \text{Eq.4.8}$$

A comparison between the quantities stored using an adsorbate and the quantities stored by simply compressing the adsorbate at the same temperature can be done for any quantity of adsorbent in a container by using Eq.4.9. A full explanation of this equation is shown in Additional Information D.

$$\frac{m_{H_s}}{V_C} = f\overline{\rho_A}\left(\frac{\rho_S \upsilon_A}{\rho_S \upsilon_A + 1}\right) + \rho_B(1-f) \qquad \text{Eq.4.9}$$

The container is full of adsorbent when $f = 1$ and empty when $f = 0$. The quantity of hydrogen m_{H_2} / V_C can be determined for every given f, as the average density of the adsorbed phase $\overline{\rho_A}$ can be determined by dividing the mass of adsorbent m_{Ads} by the volume of the adsorbed phase V_A, in which the adsorbed mass m_{Ads} is calculated using Eq.4.10.

$$m_{Ads} = m_S n_A M \qquad \text{Eq.4.10}$$

In Eq.4.10, m_S is the mass of the solid adsorbent, n_A is the absolute uptake, as calculated using the methodology applied to excess isotherms and M is the molecular weight (2.016 g mol^{-1}) of H_2. The parameter ρ_S, which is the skeletal density of the solid, is determined using helium pycnometry, ρ_B is the bulk density of hydrogen calculated using the rational function fit to Leachman's equation of state for hydrogen and υ_A is determined from the DR analysis of the nitrogen isotherm at 77 K data,

using the relative pressure range 0.0001 to 0.05. At the break-even point, that is, when m_{H_2} / V_C equals ρ_B, Eq.4.9 can be re-arranged into Eq.4.11.

$$\rho_B = f\overline{\rho_A}\left(\frac{\rho_S \upsilon_A}{\rho_S \upsilon_A + 1}\right) + \rho_B(1-f) \Leftrightarrow f\rho_B = f\overline{\rho_A}\left(\frac{\rho_S \upsilon_A}{\rho_S \upsilon_A + 1}\right) \qquad \text{Eq.4.11}$$

The filling factor f disappears from both sides of the equation, and Eq.4.12 is obtained.

$$\rho_B = \overline{\rho_A}\left(\frac{\rho_S \upsilon_A}{\rho_S \upsilon_A + 1}\right) \text{ when } \; P = P_{BE} \qquad \text{Eq.4.12}$$

As it can be noted from Eq.4.12, the break-even pressure P_{BE} is independent of the filling factor. This means that for any given temperature T, the pressure at which the total quantity stored in an adsorbent is equal to the total quantity when the container is empty, regardless of how much adsorbent is present. That is, for different quantities and displaced volumes in a container, the pressure at which the absolute amount stored through adsorption equals the amount stored in an empty container is the same. This break-even pressure, P_{BE}, however, is temperature and materials dependent.

Densities obtained for compressed gas cylinders at 35 and 70 MPa were also calculated using the rational function fit to the Leachman's equation of state. These densities are in line with published densities for compressed gas at the same conditions (23.3 kg m^{-3} at 35 MPa and 39.2 kg m^{-3} for 70 MPa both at 298.15 K [72]. The Tóth type I equation was used for all datasets in this section to obtain the absolute amounts, using the parameters from the multiple fitting of datasets shown in section 4.2.2.

Hydrogen loadings for the MAST TE7 carbon beads, AX-21 and MIL-101 are shown in Fig.4.7 at three different temperatures (77, 120 and 200 K). It can be seen in the figure that adsorptive storage is competitive with compression at the same temperature in the low-pressure range. This is due to the density enhancement achieved through adsorption, which is more prominent in the low-pressure region and

then plateaus at higher pressures. At the break-even point P_{BE}, however, this gain obtained using an adsorbent disappears and after that point, there is more H_2 quantity stored by just simply compressing it at the same temperature. This is due to the displaced volume of the solid adsorbent, which at high densities of hydrogen reduces the space available, hence, the quantity stored at those operating conditions.

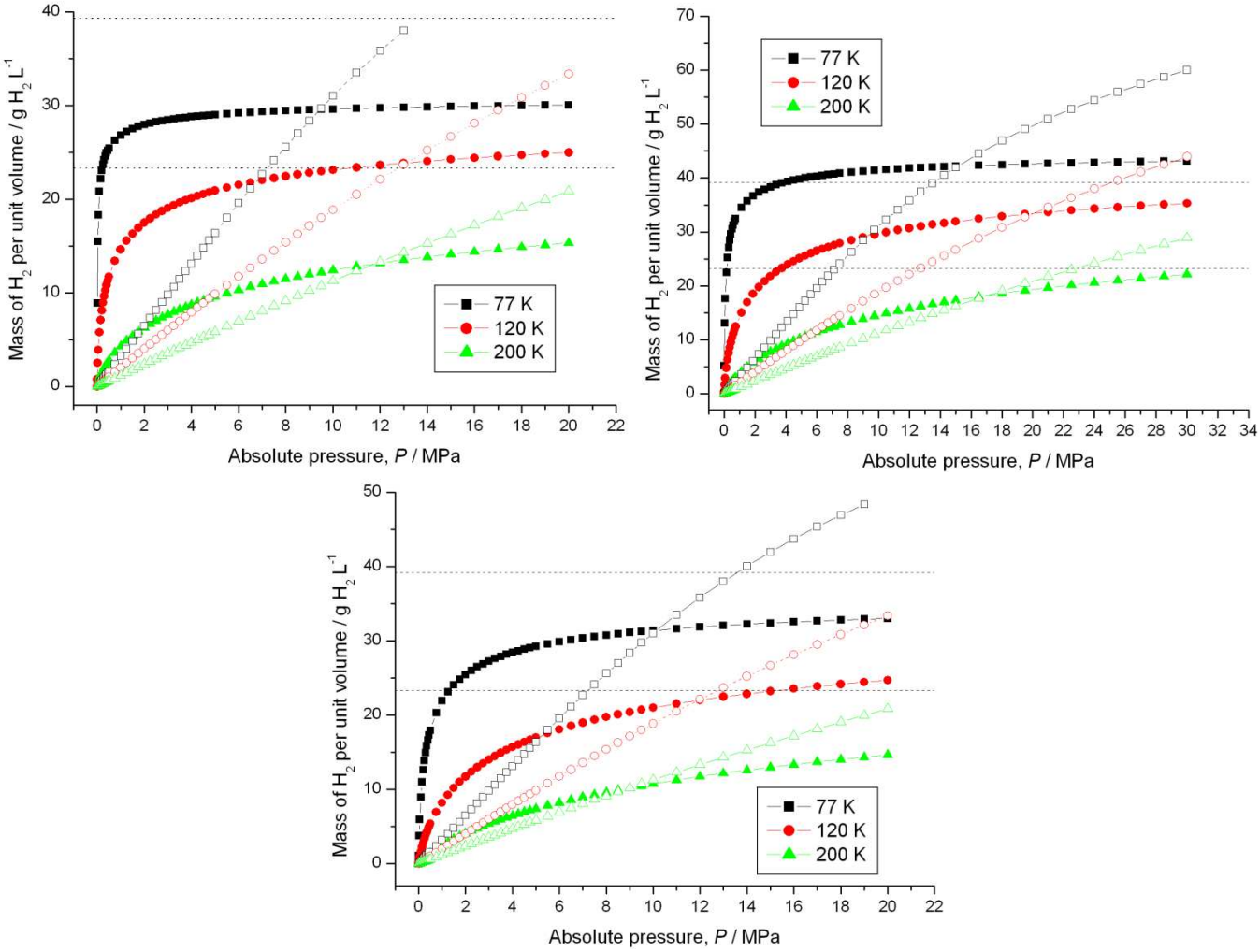

Figure 4.7 – Comparison of adsorptive storage and compression at the same temperature for the TE7 (top left), AX-21 (top right) and MIL-101 (bottom). The closed symbols are the quantities stored through adsorption and the open symbols are the quantities stored with compression at the same temperature. The horizontal dashed lines correspond to the densities in cylinders - 35 (bottom) and 70 MPa (top) at 298.15 K. The equation used to obtain the absolute capacities was the Tóth equation. Adapted from Bimbo et al [243] and used with permission from Elsevier.

This complements other studies, as the one by Hardy and co-workers [199], which also observed that for each temperature there is a cross-over point after which the amount stored in an empty container exceeds the amount that can be stored in a simple container full of adsorbent. This point exists because the solid adsorbent

occupies space that could otherwise contain more hydrogen (*i.e.*, the skeletal volume of the adsorbent reduces the effective storage volume in the container). Also in the figure are the densities of hydrogen for compressed cylinders at 35 and 70 MPa for comparison. Fig.4.7 illustrates that using adsorptive storage in different materials can store more H_2, when compared with compressed cylinders at 35 MPa and when compared with compression at the same temperature. This is especially important, since, as discussed in the Background chapter (Chapter 2), cryogenic insulated pressure vessels are also studied as prospective hydrogen storage solutions [245-248]. The figure shows that for all the materials in the figure, the operating pressures for storing equal quantities of hydrogen are lower for adsorptive storage, thus reducing the energy penalty of compressing the gas.

For AX-21, adsorptive storage requires lower pressures for the same quantities stored when comparing with compression at the same temperature and at 35 MPa. It can also be seen that AX-21 performs better in terms of quantities stored than the TE7 carbon beads and it actually stores similar quantities on a volumetric basis than compressed cylinders at 70 MPa, at around a tenth of the pressure of those cylinders. The break-even pressures are also higher than the ones observed for the TE7 carbon beads, indicating that there are greater quantities stored through adsorption in a higher range of pressures than for the TE7. The MIL-101, perhaps due to its lower skeletal density in comparison with the AX-21, has a volumetric capacity that is closer to the TE7 carbon beads. The break-even points for MIL-101 are also closer to the TE7 ones. It can be seen that the MIL-101 also performs better than the 35 MPa compressed cylinders for 77 and 120 K, needing a much lower pressure to attain the same volumetric capacities.

The break-even point P_{BE} is temperature and material-dependent, as already observed. In Fig.4.8, P_{BE} is plotted for the different materials, and for different temperatures. One interesting inference from Fig.4.8 is that an optimum condition might be observed, because this break-even point P_{BE} seems to reach a maximum between 100 and 150 K for the AX-21 and the TE7 carbon beads, while it seems to reach a maximum between 100 and 120 K for the MIL-101. This suggests that for every material, there might be an optimum operating range of pressures and temperatures for adsorptive storage.

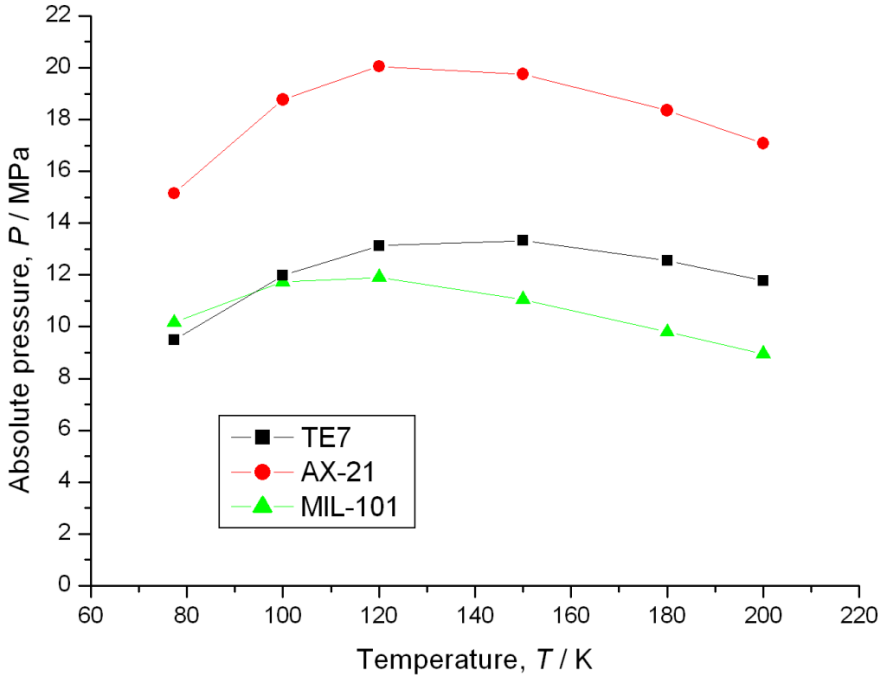

Figure 4.8 – The break-even point P_{BE} for the TE7, the AX-21 and the MIL-101 shown for 77, 100, 120, 150, 180 and 200 K. Adapted from Bimbo et al. [243] and used with permission from Elsevier.

In Fig.4.9, the comparison between the different volumetric capacities of the TE7, the AX-21 and the MIL-101 at 100 K and with different filling factors *f* is shown.

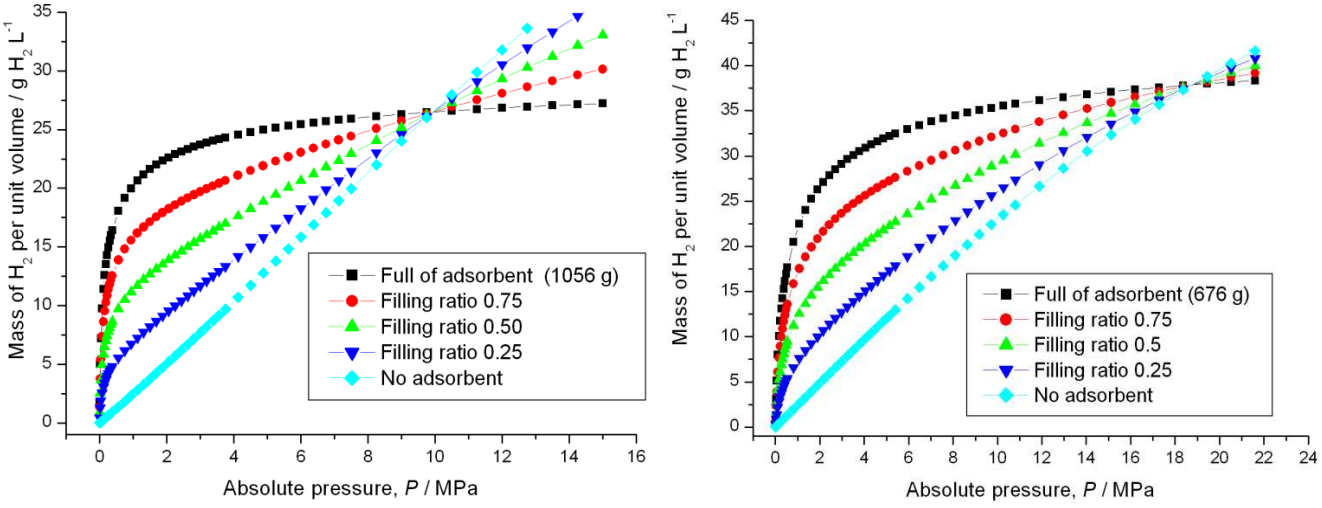

Figure 4.9 – Quantities stored in a container using different filling factors for the TE7 (left figure), AX-21 (right figure) at 100 K, using the Tóth as the type I equation. Lines between symbols are to guide the eye. Adapted from Bimbo et al. [243] and used with permission from Elsevier.

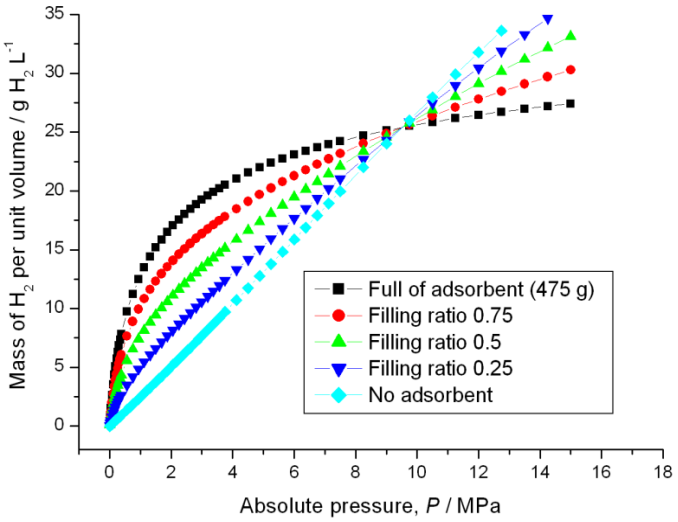

Figure 4.10 - Quantities stored in a container using different filling factors for MIL-101 at 100 K, using the Tóth as the type I equation. Lines between symbols are to guide the eye. Adapted from Bimbo et al. [243] and used with permission from Elsevier.

The above figures Fig.4.9 and 4.10 show a comparison of quantities stored from containers with no adsorbent (diamond symbols) to full of adsorbent (squares). There are three intermediate ratios, 0.25, 0.5 and 0.75, which represent 25, 50 and 75 % of the volume occupied by an adsorbent, respectively. For all the materials at 100 K, adding an adsorbent to the container improves on the quantity stored up to the break-even point P_{BE}. All the three different materials in the above figure reinforce the point made in Eq.4.12, that the break-even point P_{BE} is independent from the filling factor. It is also important to note the volumetric gain from adsorption over compression at the same temperature and that this gain is verified for every single filling factor. The gain is highest with the container full of adsorbent, with the intermediate filling factors storing more quantity the higher they are. Since the volumetric quantities in the *y*-axis do not reflect the total gain from adsorption over compression at the same temperature, the volumetric capacities obtained through adsorption need to be normalised by subtracting the volumetric quantities obtained from simple compression.

In Figure 4.11, a normalisation of Figs.4.9 and 4.10 was done by subtracting the volumetric capacities at each pressure obtained using the equation of state. This was done to quantify the gain over compression throughout the pressure range until the break-even point.

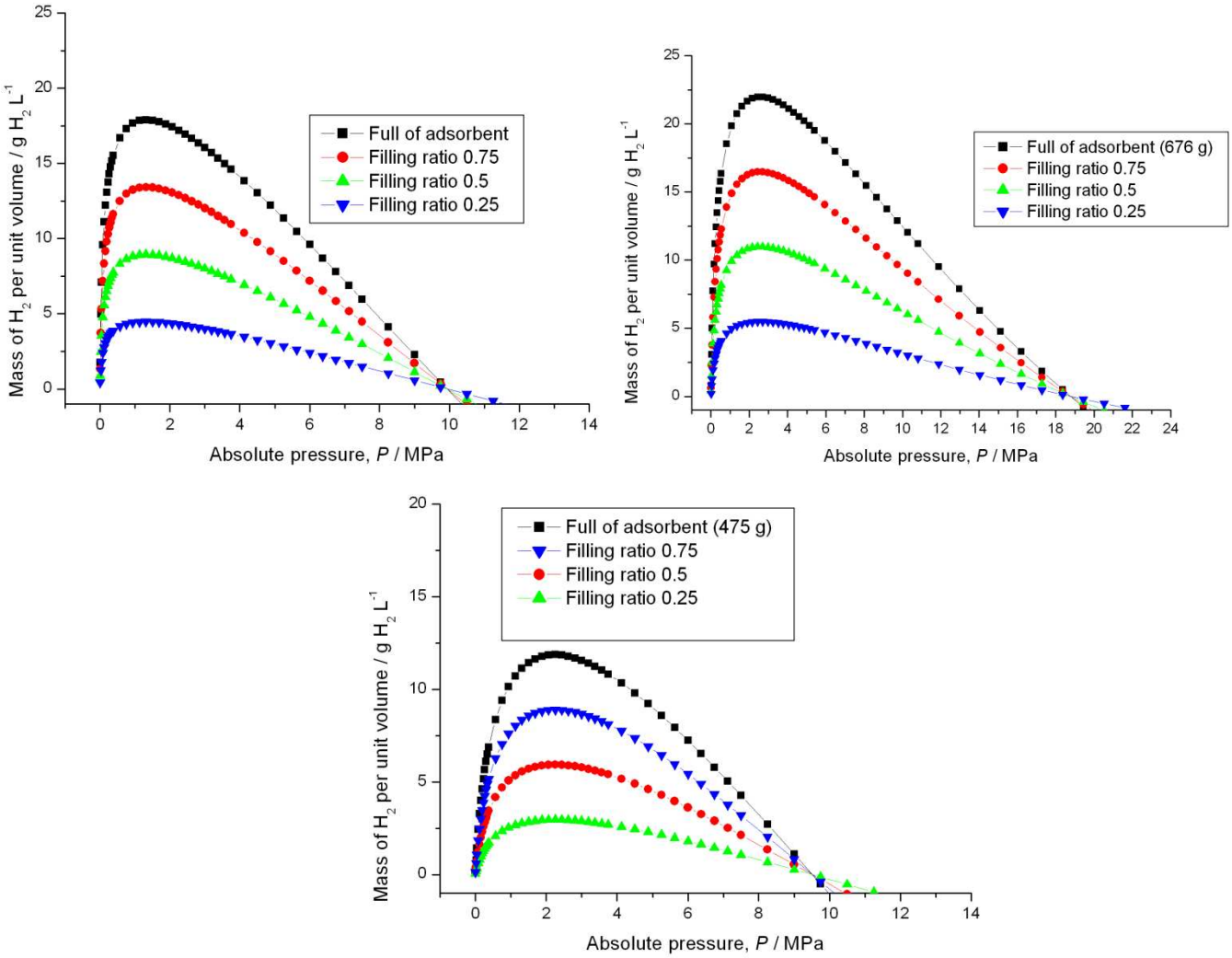

Figure 4.11 – Quantities stored in a container using different filling factors for the TE7 (top left figure), AX-21 (top right figure) and MIL-101 (bottom figure) at 100 K, using the Tóth as the type I equation, normalised by subtracting the volumetric quantities obtained by compression. Lines betwewen symbols are to guide the eye. Adapted from Bimbo et al [243] and used with permission from Elsevier.

For all the materials, the maximum gain against standard compression at the same temperature is in the low-pressure region and, at higher pressures, the quantities stored from adsorptive storage are just slightly more than the ones stored using compression at the same temperature. In all materials, the highest gains are verified between 1 and 5 MPa. These gains are zero at the break-even point, but this figure highlights that, even if adsorptive storage does store more quantity up to the break-even point, the gain over simple compression is not very significant in the high-pressure range, and this gain might not be enough for practical applications, since it has to offset the cost and weight of the adsorbent in the container.

The figure also stresses that operating in the high-pressure (>10 MPa) range might be detrimental for adsorptive storage in these systems. An illustration of this is if a material with an impressive maximum capacity only reaches that capacity at, *e.g.*, 15 MPa, this might result in marginal gains over compression at the same pressure and temperature in an empty container. However, and as noted by the differences in these three materials, properties like density, maximum capacity and enthalpy of adsorption all greatly influence this analysis.

4.3.3. Densities of adsorbed hydrogen

Hydrogen is a low-density gas at ambient conditions and, as noted, the challenge is to enhance its volumetric density without incurring in large energy and materials penalties, which is the case when using compression or liquefaction. Normal hydrogen has a low normal boiling point of 20.369 K [249] and a low normal melting point of 14.025 K [67], with its triple point being 13.957 K and 0.007 MPa and a corresponding density of 77.01 kg m^{-3} [64]. The vapour-liquid critical point is 33.145 K and 1.296 MPa, with the density at that point of 31.26 kg m^{-3} [64].

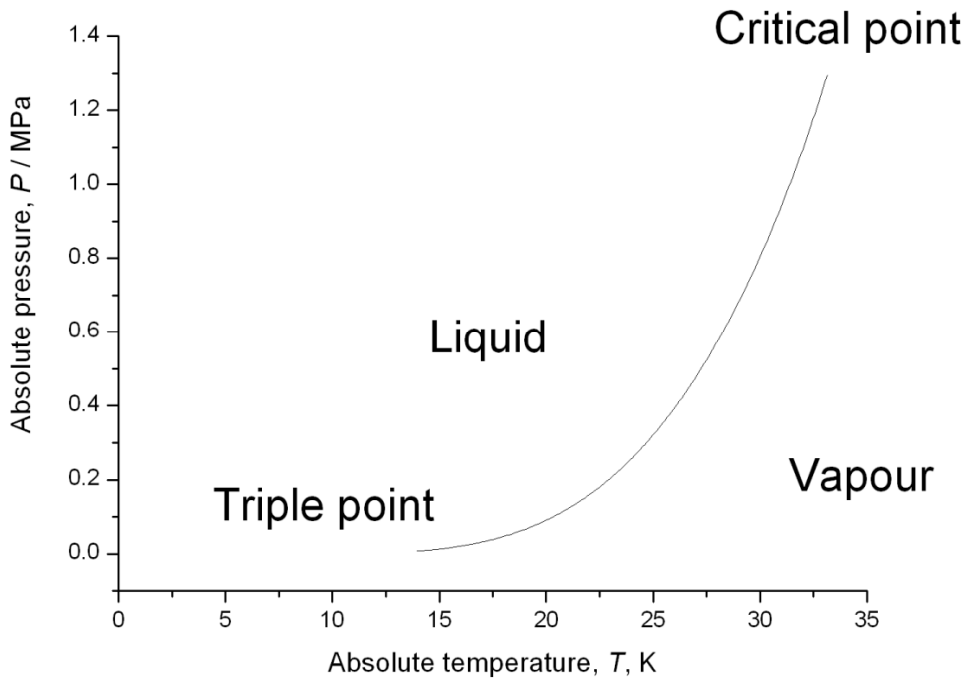

Figure 4.12 – P-T saturation curve for normal hydrogen (from NIST [249]).

Between the vapour-liquid critical and triple point, hydrogen coexists as a vapour and liquid in the saturation curve, which is represented in Fig.4.12. Its density changes accordingly and it is denser at the triple point (density of 77.01 kg m^{-3}). After the vapour-liquid critical point of 33.145 K, hydrogen only exists as a gas and its density changes with increasing pressure.

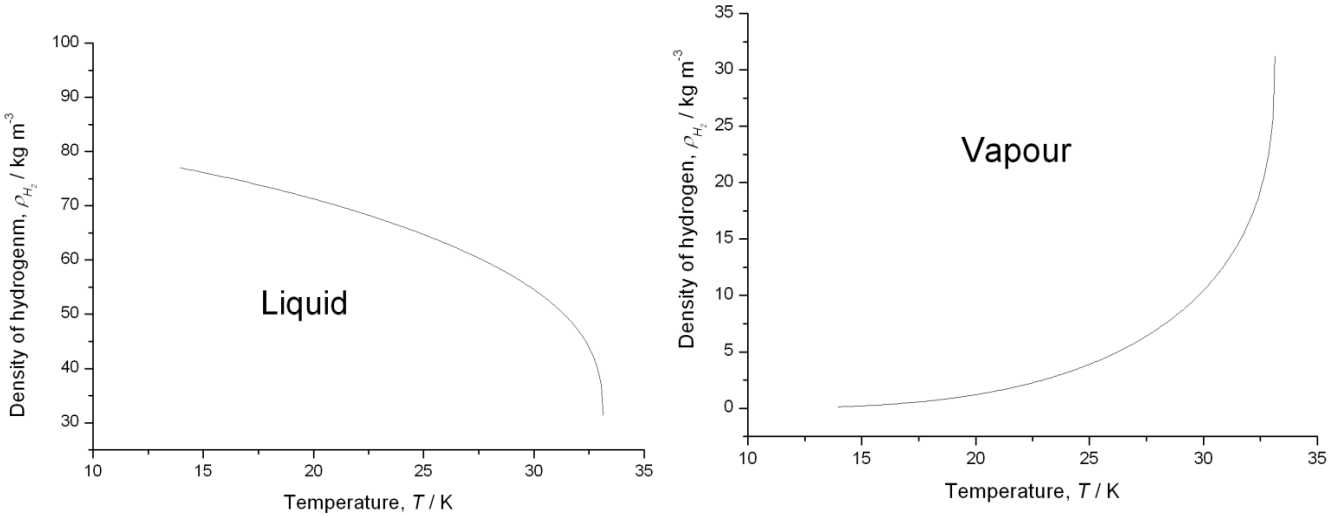

Figure 4.13 – Liquid and vapour densities of normal hydrogen in the saturation curve.

The density profile as a function of temperature for both the liquid and the vapour are shown in Fig.4.13. As it can be seen, the density of the liquid is higher at the triple point and diminishes progressively until it reaches the vapour-liquid critical point, at 33.145 K. The exact opposite is displayed in the density profile of the vapour phase, which has a density close to zero at the triple point and reaches 31.26 kg m^{-3} at the vapour-liquid critical point.

The density at the triple point is not the maximum liquid density for hydrogen, however. Since liquid hydrogen is a highly compressible liquid, its density can go to as high as 80.21 kg m^{-3} at pressures above 10 MPa, for 20.38 K [250]. The range for liquid densities in the saturation curve is from 31.26 kg m^{-3} to 77.01 kg m^{-3}. Apart from compression of liquid hydrogen, higher densities of hydrogen can also be observed for solid hydrogen. Importantly, it should be noted that hydrogen density is extremely low, since even as a solid at 4 K and zero pressure, it has a density of only 87.08 kg m^{-3} [251], which is less than a tenth of liquid water's density at normal pressure and temperature.

Below its triple point of 13.957 K, hydrogen exists mostly as a solid. Its solid properties are the topic of a seminal paper by Silvera [251], which is the common reference for solid hydrogen properties and the limiting value for solid parahydrogen density of 87.08 kg m^{-3}. It should be noted that this value is only the value for the density of solid hydrogen at zero pressure and 4 K and, as indicated in the publication, solid hydrogen is compressible and has a variable density according to pressure. In Figure 4.14, the variation of solid density, from 87.08 kg m^{-3} at 0 MPa to around 110 kg m^{-3} at 120 MPa, and for pressures up to 3,000 MPa, where densities reach 220 kg m^{-3}. As it can be seen from the figure, hydrogen is a highly compressible solid.

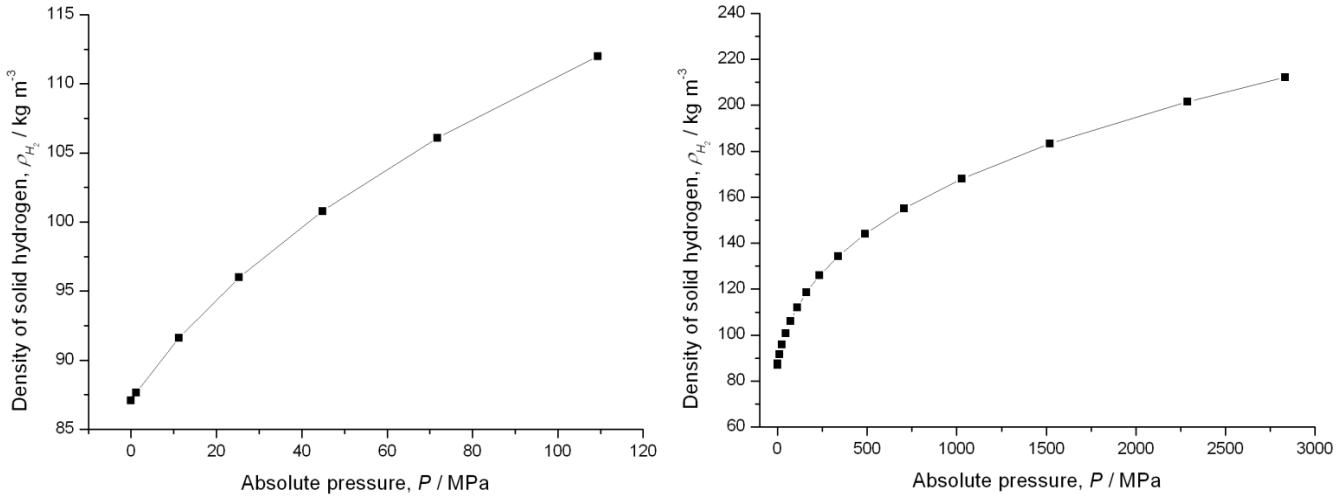

Figure 4.14 – Solid hydrogen density for para-hydrogen at 4 K. Left hand side figure is density up to 120 MPa and right hand side figure is density up to 3,000 MPa. Data taken from Silvera [251].

Adsorptive storage is being considered a hydrogen storage alternative to current methods because it increases its density at milder operating conditions than its alternatives, mainly compression and liquefaction. Due to the surface heterogeneity of the adsorbents, it is difficult to estimate the local density of the adsorbate and even for homogeneous surfaces, densities are not homogeneous in the pore, because they are a function of the distance to the solid wall. In Chapter 5 of this thesis, this problem is approached using an analytical model to account for a density variation in the pore. In this chapter an average density for the adsorbate in the pore $\overline{\rho_A}$ is assumed, which is calculated using the absolute capacity n_a and the specific pore volumes v_A determined from the application of the model. Comparing the adsorbed densities for the different

materials could help assessing those same materials and provide insights on the nature of the hydrogen adsorbed into the surface. This is especially interesting since the adsorbed phase density can be related to the porous structure of the materials.

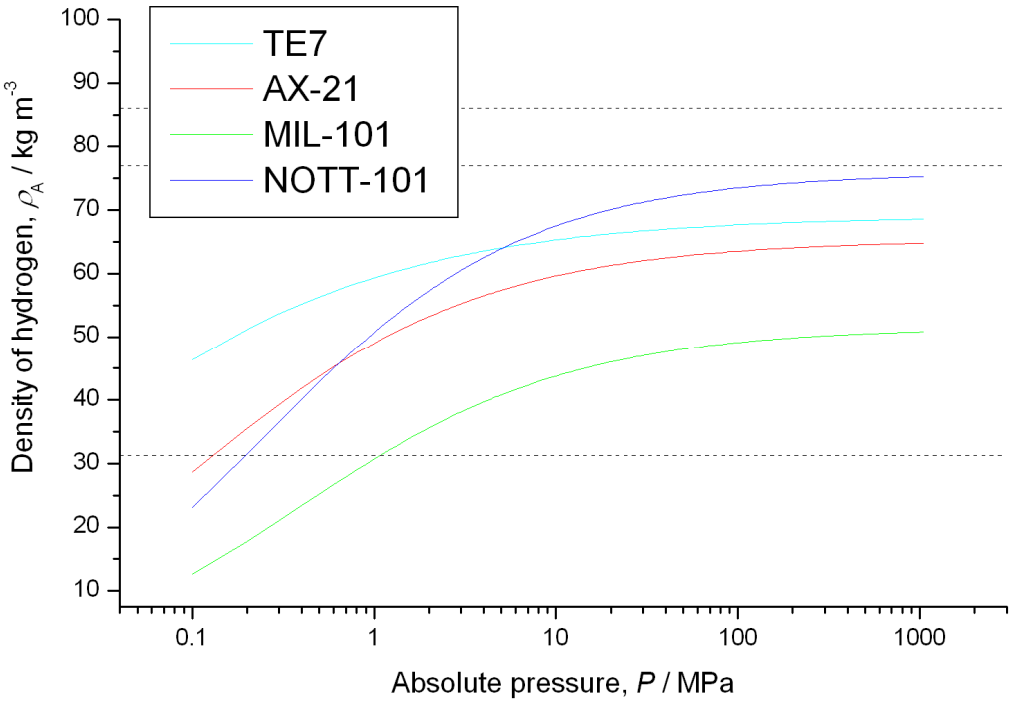

Figure 4.15 – Densities of adsorbed hydrogen for the different materials on a logarithmic scale up to 1000 MPa, using the Tóth as the type I equation. Dashed horizontal lines are solid hydrogen density (87.08 kg m^{-3}, top dashed horizontal line), maximum liquid hydrogen density at saturation (77.01 kg m^{-3}, middle dashed horizontal line) and minimum liquid hydrogen density at saturation (31.26 kg m^{-3}, bottom dashed horizontal line).

In Fig.4.15, a logarithmic plot of the density of the adsorbed hydrogen as a function of pressure can be observed for the TE7 carbon beads, the AX-21, the MIL-101 and the NOTT-101 at 77 K up to 1,000 MPa. This was again calculated using the Tóth as the type I equation and using the parameters determined from the multiple fit to different datasets. To calculate the average pore density $\overline{\rho_A}$, the specific pore volumes used were the ones determined experimentally and presented in Table 3.1. The maximum average adsorbed density corresponds to the NOTT-101 material, which reaches almost 80 kg m^{-3} at 1,000 MPa. All the densities seem to have reached a plateau by 1,000 MPa. The results also have to take into account the limiting densities $\overline{\rho_A}^{LIM}$ calculated using the limiting absolute capacity and the specific pore volume, as indicated in Eq.4.13.

$$\overline{\rho_A}^{LIM} = \frac{n_a^{\max}}{\upsilon_A} \qquad \text{Eq.4.13}$$

The limiting absolute capacities are listed Table 4.11, with the data taken from the Tóth equation fitting to the multiple datasets, as shown in Table 4.1, 4.3, 4.5 and 4.7 for the TE7, AX-21, MIL-101 and NOTT-101, respectively.

Table 4.11– Limiting absolute capacities, pore volumes determined from modelling using the Tóth and experimentally and their corresponding calculated limiting average adsorbed density.

	$n_a^{\max}$	υ_A^*	$\overline{\rho_A}^{LIM*}$	υ_A	$\overline{\rho_A}^{LIM}$
	wt.%	$cm^3\ g^{-1}$	$kg\ m^{-3}$	$cm^3\ g^{-1}$	$kg\ m^{-3}$
TE7	2.97	0.14	212.1	0.43	69.1
AX-21	6.73	0.65	103.5	1.03	65.3
MIL-101	7.77	0.89	87.3	1.51	51.5
NOTT-101	8.22	1.39	59.1	1.083	76.0

The specific pore volumes υ_A* are a parameter from the fit and the limiting densities $\overline{\rho_A}^{LIM*}$ are the calculated limiting adsorbate density using that specific pore volume. The specific pore volumes are the ones calculated experimentally (as in Table 3.1) and the limiting densities $\overline{\rho_A}^{LIM}$ are the corresponding calculated densities using those specific pore volume. From the table, the densities calculated using the specific pore volumes determined as parameters from the fitting offer disparate results, ranging from 59.1 kg m^{-3} for the NOTT-101 to 212.1 kg m^{-3} for the TE7. The limiting density value for the NOTT-101 is in the liquid hydrogen range, which is between 33.2 and 77.0 kg m^{-3}. All the other materials' densities have values far in excess of the solid density of hydrogen at zero pressure, which has a value of 87.08 kg m^{-3}. The limiting densities $\overline{\rho_A}^{LIM}$ calculated using the experimental pore volumes have a closer range of values, spanning from 51.5 kg m^{-3} for the MIL-101 to 76.0 kg m^{-3} for the NOTT-101. As expected, the limiting average adsorbed densities correlate well with the adsorbed densities of Fig.4.15, since for both sets the densities were calculated using the experimental pore volume. The pressure range in Fig.4.15, which goes up to

1,000 MPa in pressure, shows the average adsorbed density values approaching the limiting average adsorbed densities, which represent the average density in the pore at the limit of saturation.

It does seem that for the materials studied and using the pore volumes determined experimentally, the densities of the adsorbed phase are in the high range of liquid densities (> 60 kg m^{-3}), as indicated by Fig.4.15. It is clear that adsorptive storage can greatly enhance the densities of hydrogen, and can achieve an adsorbed phase density which is comparable to high liquid densities and perhaps even, for optimum pore-sized materials with high capacity, achieve densities closer to solid hydrogen in the pore. This will be further discussed in the next chapter of this thesis.

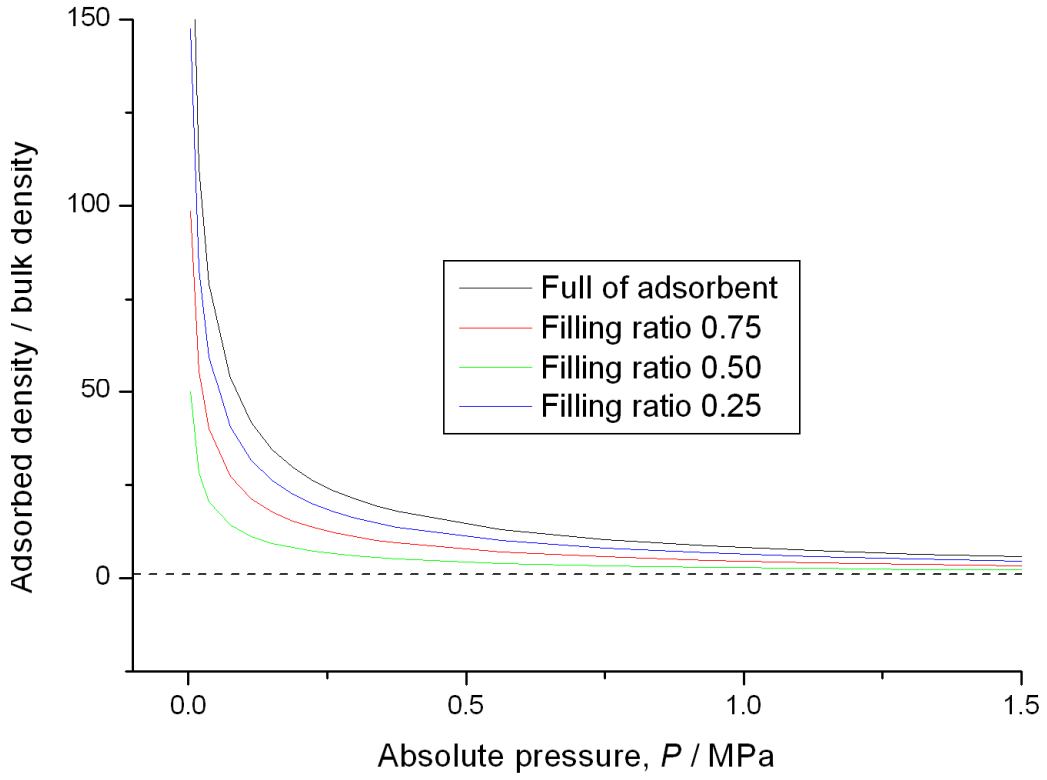

Figure 4.16 – Ratio of adsorbed hydrogen to bulk hydrogen for the TE7 calculated for different filling ratios using the Tóth equation at 100 K. Horizontal dashed line is unity. Adapted from Bimbo et al. [243] with permission from Elsevier.

The adsorbed phase density compared with the density in the bulk phase can be another metric of interest and provide more insights into the optimum operating conditions for adsorptive storage. In Fig.4.16, the ratio of the density of the adsorbed

over the bulk phase was plotted as a function of pressure up to 1.5 MPa for the TE7 carbon beads. The adsorbed phase was calculated using the Tóth equation and the bulk density determined from the rational function fitted to the Leachman's equation of state.

The ratio is adimensional and was obtained by simply dividing one density by the other, as explained in Eq.4.14.

$$\frac{\rho_A}{\rho_B} \qquad \text{Eq.4.14}$$

Fig.4.16 shows the ratio between the adsorbed density and the bulk density. This diminishes with increasing pressure and, for pressures above 2 MPa, the ratio is close to unity. This means that the density enhancement will be more pronounced in the low pressure region, as observed previously for Fig.4.11. However, Fig.4.16 presents an even lower pressure region (to 0.5 MPa) because, while Fig.4.11 compares mass quantity, Fig.4.16 compares densities. The ranges are different since the densities will be equal at a different point than the break-even point (in this case, at lower pressures) because the adsorbed quantity and the bulk quantity occupy different volumes.

4.4. Isosteric enthalpies of adsorption

The enthalpies of adsorption are the thermodynamic measure of the heat exchanged upon adsorption. Adsorption is an exothermic process, meaning that heat is released when the bulk gas undergoes a phase change and condenses to form the adsorbate. This heat release upon adsorption can be measured experimentally and creates problems for the temperature control of the experiment. If a hydrogen adsorption experiment is done at 77 K and some heat is released upon adsorption, bringing the overall temperature up, then the capacity of the material will diminish.

For practical applications, it is important to quantify the enthalpy of adsorption, due to the relevance of the system's thermal management. Adsorptive storage of hydrogen will likely require a low temperature, so any increase in temperature has to be closely

controlled. It is important to calculate the enthalpies of adsorption as accurately as possible for the different materials, to design thermal management systems that can withstand the heat released from adsorption. Also, a more accurate determination of the isosteric enthalpies can help design better storage materials, since the isosteric enthalpies are closely related to the temperature of the storage system, and as reported by Bhatia and Myers, isosteric enthalpies have to be higher in order for storage systems to operate at conditions closer to ambient [97].

The isosteric method for calculating the enthalpies of adsorption implies calculating the pressures for constant amount adsorbed at different temperatures. In the literature, it is common to use two temperatures, typically 77 and 87 K and calculate the isosteric enthalpies of adsorption using the Clausius-Clapeyron approximation and the excess amount adsorbed [121, 189]. As explained in the Background (Chapter 2), the excess quantity is a partition of the total quantity of adsorbate in the pore. It is not a separate phase, so there is some thermodynamic inconsistency in calculating isosteric enthalpies using excess quantities, even if some efforts have been made to define them unambiguously [252]. Furthermore, if calculated based on the excess quantity, which is by definition smaller than the absolute quantities, they will underestimate the real values for the isosteric enthalpies. In addition to this, for hydrogen adsorption the Clausius-Clapeyron approximation might not be the most reliable method since it assumes ideal gas behaviour. In the experimental conditions used for testing hydrogen storage materials, typically cryogenic temperatures and high pressures, hydrogen's behaviour significantly deviates from ideal, as observed in Fig.3.7 of Chapter 3. To study the effect of using the Clausius-Clapeyron approximation on the calculation of the isosteric enthalpies of adsorption, the isosteric enthalpies for NOTT-101 using both methods were calculated and compared.

4.4.1. The Clausius-Clapeyron approximation

The model was applied to individual excess isotherms of the NOTT-101 material, at 50, 55, 60, 65, 70, 77 and 87 K. The equation used in the model was the Tóth equation. Using the methodology, an analytical model for the absolute quantity adsorbed at each temperature was obtained. Since the isosteres are the pressure points

at constant amount adsorbed and an analytical model for the absolute was available, these equations could be solved for constant amount adsorbed using Maple® (Maple 16, Maplesoft, Ontario, Canada). This implied using the analytical model for the equation, solving it for a specific amount adsorbed n_A and obtaining the isostere, that is, the pressure P corresponding to that amount adsorbed. So, and as indicated in Eq.4.15, the pressure points at different amounts adsorbed were calculated for each temperature.

$$P = f(n_A)_T \qquad \text{Eq.4.15}$$

The equations were solved for 0.1, 0.5, 1, 2, 4, 6 and 7 wt. %. After the pressure points for each temperature and each amount adsorbed were calculated, the Clausius-Clapeyron approximation could be applied to the data.

The Clausius-Clapeyron approximation is an equation for phase changes at equilibrium. It is a simplification of the Clapeyron equation, which is the exact thermodynamic equation for phase change calculations at equilibrium and the simplification is based on two assumptions – the gas is ideal and the molar volume of the adsorbate is insignificant in comparison with the molar volume of the adsorptive.

$$\left(\frac{\partial P}{\partial T}\right)_{n_A} = \frac{\Delta h_{ab}}{T \Delta v_{ab}} \qquad \text{Eq.4.16}$$

The Clausius equation, shown in Eq.4.16, relates the enthalpy changes Δh_{ab} in the transition of a bulk gas a to adsorbed phase b, with the rate of change in P with T at constant absolute amount adsorbed n_A (isosteric), the difference in molar volume Δv_{ab} and T. If the molar volume of the adsorbate is much smaller than the molar volume of the adsorptive, the molar volume variation can be assumed as being approximately the molar volume of the adsorptive.

$$\Delta v_{ab} = v_b - v_a \Leftrightarrow \Delta v_{ab} \cong -v_a \qquad \text{Eq.4.17}$$

And if it is an ideal gas, the molar volume of the adsorptive can be approximated using the ideal gas equation.

$$\Delta v_{ab} \cong -\frac{RT}{P} \qquad \text{Eq.4.18}$$

In all the equations in this chapter, R is the molar gas constant, equal to 8.314 J mol^{-1} K^{-1}, T is temperature and P is pressure. If this simplification is done in the Clausius equation (Eq.4.16), Eq.4.19 can be obtained, which is the Clausius-Clapeyron approximation.

$$\left(\frac{\partial P}{\partial T}\right)_{n_A} = -\frac{\Delta h_{ab}}{T\dfrac{RT}{P}} \qquad \text{Eq.4.19}$$

This can be further simplified in Eq.4.20.

$$\left(\frac{\partial \ln P}{\partial \dfrac{1}{T}}\right)_{n_A} = -\frac{\Delta h_{ab}}{R} \qquad \text{Eq.4.20}$$

The above equation is a common representation of the Clausius-Clapeyron approximation, with Δh_{ab} being the differential molar isosteric enthalpy of adsorption. To evaluate the isosteric enthalpies of adsorption for a group of isotherms, the isosteres need to be determined and the slope of the logarithmic isosteres at constant amount adsorbed is related to the enthalpy change, as shown in Eq.4.20. Using the isosteres determined from Maple®, these can be plot as a function of 1000 / RT and the corresponding negative gradient for each isostere will be the differential isosteric enthalpy of adsorption, which is determined for different coverages, as indicated in Fig.4.17.

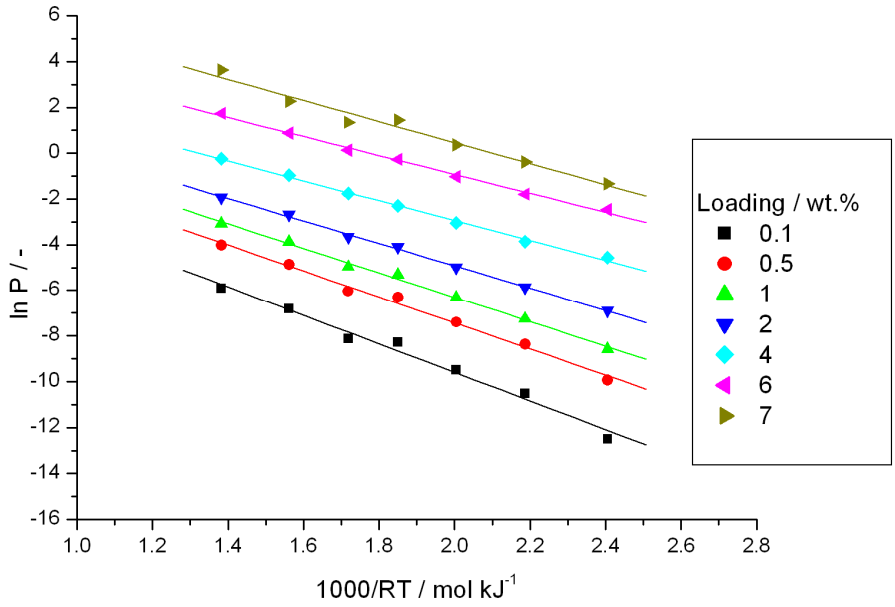

Figure 4.17 – The isosteres and linear fits for the absolute quantities estimated using the Tóth equation for the NOTT-101. The slope of the linear fit equals the isosteric enthalpy of adsorption calculated using the Clausius-Clapeyron method. Figure adapted from Bimbo et al.[216] and used with permission from the Royal Society of Chemistry.

The above figure shows the linear fits on the logarithmic isosteres as a function of the inverse of temperature. The negative of the e slope in the linear fit is the differential molar isosteric enthalpy of adsorption Δh_{ab} calculated using the Clausius-Clapeyron approximation, as indicated in Eq.4.20. The coefficient of determination R^2 for the linear fits diminishes with with loading, which means that the linearity decreases as the loading (and therefore, the pressure) increases. This might have to due with the assumptions present in the Clausius-Clapeyron approximation, the ideal gas assumption and the negligible molar volume, both of which are unlikely to hold at higher pressures in these operating conditions.

To observe how the isosteric enthalpies vary as a function of coverage, they were plotted as a function of absolute amount adsorbed, as shown in Fig.4.18.

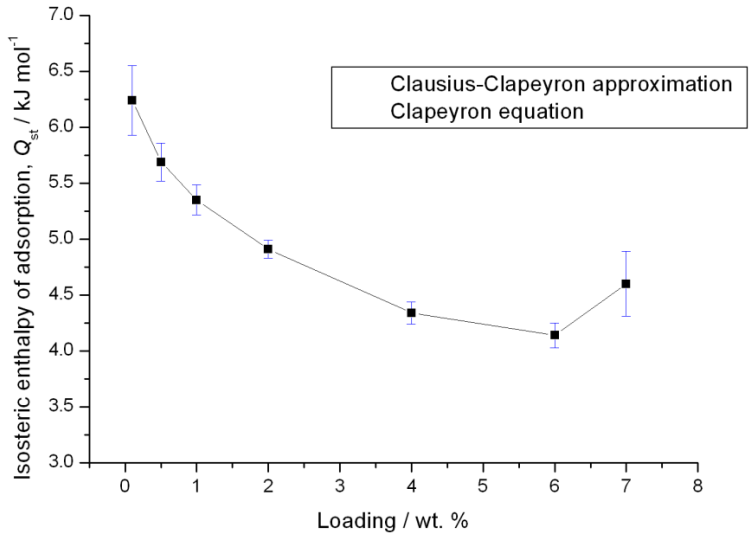

Figure 4.18 – The isosteric enthalpy of adsorption as a function of coverage calculated using the Clausius-Clapeyron equation for the NOTT-101.The error bars are the standard deviation from the linear regression.

In Fig.4.18 the isosteric enthalpies are around 6.5 kJ mol^{-1} for 0.1 wt.% for the NOTT-101, which is in the range of MOFs' isosteric enthalpies of adsorption at zero coverage [189, 204]. The isosteric enthalpies diminish to around 4.5 kJ mol^{-1} at 4 wt.%, reflecting the nature of this adsorbent, which has a higher zero coverage enthalpy of adsorption because of the heterogeneity present in its structure. The high zero coverage enthalpy of adsorption, which significantly decreases with coverage can be attributed to the presence of metal centres, which are very high energy adsorption sites. To assert the correctness of the isosteric enthalpies of adsorption calculated using the Clausius-Clapeyron method, the isosteric enthalpies using the Clapeyron equation had to be evaluated and compared using the same data.

4.4.2. The exact Clapeyron equation

As already said, the Clapeyron equation is the exact thermodynamic equation for enthalpy calculation in phase changes at equilibrium. While the Clausius-Clapeyron equation is widely used in adsorptive studies, its underlying assumptions of ideal gas and negligible adsorbate molar volume are not likely to apply in the conditions used for hydrogen storage. For this reason, it was necessary to assess if there were any

significant differences in calculating the isosteric enthalpies using both methods. To our knowledge, the exact Clapeyron equation has not been tested and compared with the Clausius-Clapeyron approximation for hydrogen adsorption or for any other adsorbed gas. The analytical model is available for the absolute quantity, so the isosteres can be easily calculated, as they were for the Clausius-Clapeyron method. Also because of the analytical model and since the pore volume estimation is available using the methodology, the molar volume of the adsorbate can be quantified. Instead of assuming a molar volume variation Δv_{ab} equal to the molar volume of the bulk phase, as indicated in Eq.4.17, Δv_{ab} can be precisely calculated as the difference in the molar volume of the adsorptive and the molar volume of the adsorbate, as indicated in Eq.4.21. The difference is always negative, because the molar volume of the adsorptive is always bigger than the molar volume of the adsorbate.

$$\Delta v_{ab} = v_b - v_a \Leftrightarrow \Delta v_{ab} = \frac{1}{\rho_b} - \frac{1}{\rho_a} \qquad \text{Eq.4.21}$$

Due to the model, ρ_a can be calculated using the absolute amount adsorbed n_A and the specific pore volume v_A, both parameters determined from the fitting. The bulk density ρ_b can be calculated using the rational function approximation to Leachman's EOS. The difference in molar volumes Δv_{ab} can be quantified for every isostere.

$$\left(\frac{\partial P}{\partial T}\right)_{n_A} T\Delta v_{ab} = \Delta h_{ab} \qquad \text{Eq.4.22}$$

In Eq.4.22, which is a re-arrangement of the Clapeyron equation shown in Eq.4.16, the differential isosteric enthalpies of adsorption can be calculated if the molar volume is determined and if the rate of pressure change as a function of temperature for constant amount adsorbed n_A is calculated. Since an analytical function is available, this rate of pressure change can be determined, because once the isosteres are determined, these can be plotted as a function of temperature for constant amount adsorbed. The gradient for each point can be calculated using OriginPro software. This method yields a differential isosteric enthalpy of adsorption for each amount adsorbed and at each temperature, as opposed to the Clausius-Clapeyron method

detailed in the preceding section, which determines an isosteric enthalpy for each loading using the gradient of the linear fit of the isosteres. For this reason and to compare the different values, the isosteric enthalpies determined using the Clapeyron equation had to be averaged for the temperature range, for constant amount adsorbed n_A.

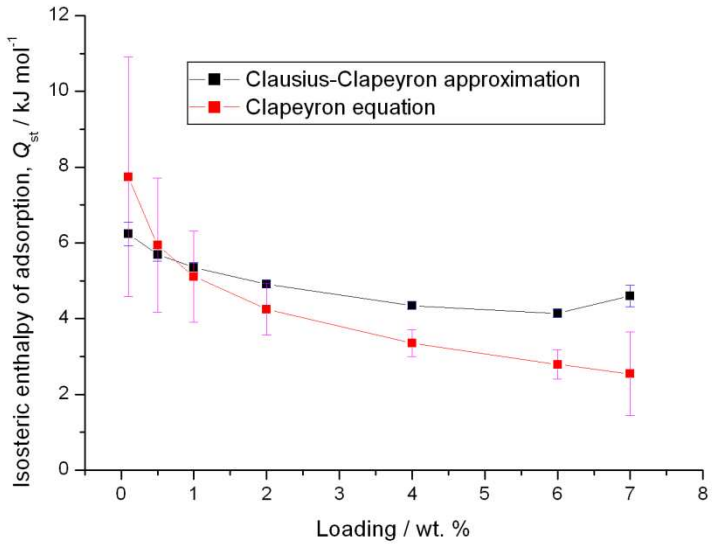

Figure 4.19 – The isosteric enthalpies of adsorption as a function of coverage calculated using the Clausius-Clapeyron approximation and the Clapeyron equation for the NOTT-101 material. The error bars for the Clapeyron equationare the standard deviation calculated from the average of values for the isosteric enthalpies. Adapted from Bimbo et al. [216] and used with permission from the Royal Society of Chemistry.

The isosteric enthalpies calculated both the Clausius-Clapeyron approximation and the Clapeyron equation are shown in Fig.4.19. For the error calculation in the plot the following assumptions were done – the experimental error is the same for all the points that were modelled and which the isosteres were calculated from, so it was ignored. The modelling error associated with non-linear fitting was also considered the same for every point and ignored. This is justified since the absolute quantity and the experimental points were the same for the two methods. For the Clausius-Clapeyron, the error bars are the standard deviations calculated in Origin. An explanation of the calculation of this error is in Additional Information B (copy equation to Additional Information). For the Clapeyron equation, the errors were the calculated standard deviation of the average of values of the Clapeyron equation. There was no error associated with the numerical differentiation of the isosteres and

the error in the calculation of the bulk density is very small (according to Leachman et al. [64], the error is 0.04 % for densities estimated between 250 and 450 K and up to 300 MPa). A convergence at low loadings can be observed, with a gap increasing with higher loadings. Also, the isosteric enthalpies range from 8 kJ mol^{-1} to 3 kJ mol^{-1} with increasing coverage. This is much more than the range of values observed for the Clausius-Clapeyron approximation. The gap with increasing loadings would be expected, since higher loadings correspond to higher pressures, so more deviations from ideal gas behaviour would be expected at these conditions. The convergence at lower loadings can be explained using the same reasoning, since in the low pressure range at these temperatures, hydrogen's behaviour more closely resembles that of an ideal gas and the molar volume of the bulk phase is considerably higher than the molar volume of the adsorbed phase. According to this analysis, the assumptions in the Clausius-Clapeyron make this equation inappropriate for isosteric enthalpy calculation in conditions that are not adequate for the ideal gas approximation. At higher pressures, the isosteric enthalpies calculated using the approximation diverge from those calculated using the exact equation. The adsorbate molar volumes obtained in the pressures corresponding to higher loading can be as high as 30 % of the molar volumes of the adsorptive at the same pressure, so the negligible adsorbate molar volume assumption is not verified. This effect is also more pronounced with increasing pressure, since the adsorptive density approaches the adsorbate density with an increase in pressure. The Clapeyron equation portrays a more accurate profile across the whole coverage range and it is the average value for the whole coverage range that is important, not just the value at low loadings [97].

4.5. Conclusions

The methodology described in the previous chapter was applied to experimental datasets in this chapter. The temperature dependence for the parameters in the different type I equations was studied with the application of the methodology to the datasets. It was concluded that the affinity parameter was the variable most likely to have temperature dependence and this was input into the model. Fitting of the multiple datasets, corresponding to the whole isotherm range for each material was done using a number of different type I equations. The ones that showed the best fits

to the data were the DR, the DA, the UNILAN and the Tóth. Based on the results presented, our experience and from reports in our group and elsewhere, the Tóth was chosen as the type I equation of choice and the modelling of data for the rest of the chapter was done using this equation.

A comparison with alternative storage methods was also studied, particularly compression at the same temperature as adsorptive storage. The break-even point P_{BE} was shown to be an interesting feature of the materials, because it can indicate the pressure up until adsorption can store more quantities of the gas than compression at the same temperature. This break-even pressure P_{BE} was shown to be independent of the fraction of volume occupied by the adsorbent in the container but it is temperature and material-dependent. Because P_{BE} varies with temperature and it reached a maximum for all the materials studied, it seemed to indicate that there might be optimum conditions for adsorptive storage. This is further supported by the study of the gain over simple compression, for the same material and at the same temperature. The gains of adsorptive storage over compression are much more evident in the low-pressure region, especially between 2 and 4 MPa for the different materials, and they reach a maximum of gain over compression at the same temperature at these pressures, with the gain then diminishing with increasing pressures and becoming zero at the break-even point P_{BE}. Operating in the high-pressure range for these materials and at these conditions might prove detrimental, because of the displaced volume by the solid adsorbent.

The densities of hydrogen were also discussed in this chapter. The adsorbed density for the different materials was calculated and plotted up to 1000 MPa, and the limiting average density of the different materials was also shown and discussed. The NOTT-101 seemed to have the highest adsorbed density of all the materials but all the average densities were in the liquid hydrogen range, with some approaching solid hydrogen density. Also, an illustration of the ratio of adsorbed density over the bulk density was done for the TE7, reinforcing that adsorptive storage is more beneficial in the low-pressure range, with higher pressures not representing much gain over compression at the same temperature.

Finally, the chapter ends with the isosteric enthalpies of adsorption and explains two methods to calculate these. The Clapeyron equation, which is the exact thermodynamic equation for phase changes in equilibrium and the Clausius-Clapeyron equation, which simplifies the former with an ideal gas approximation and negligible adsorbed phase molar volume. Using data from the NOTT-101, it was shown that the Clausius-Clapeyron approximation is not the most accurate method to calculate the isosteric enthalpies, especially in conditions that deviate significantly from ideal. Since the isosteric enthalpies diverged significantly at higher loadings for the NOTT-101, it would be more accurate to determine isosteric enthalpies of adsorption using the Clapeyron equation. The application of the Clapeyron equation is stressed in conditions that ideal gas behaviour is unlikely to be the case, as it is in most cases for hydrogen storage, which involve cryogenic temperatures and high pressures. To our knowledge, this comparison was not reported in the literature for hydrogen or for any other adsorbed gas.

Chapter Five

Validation of the Methodology Using Experimental Techniques

5. Validation of the Methodology Using Experimental Techniques

5.1. Introduction

To estimate the total amount of adsorptive within the pore, which is commonly referred to as the absolute adsorbed amount, some assumptions on the pore volume and on the density of the adsorbate have to be made. Without these assumptions, it is impossible to estimate the absolute isotherm by conventional gravimetric or volumetric methods. The nature and density of the adsorbed phase and the available space for hydrogen adsorption in the porous structure are not easy to estimate experimentally, thus precluding an accurate determination of the total amount of hydrogen stored in a porous material. Our methodology overcomes this by assuming a type I equation fractional filling and estimating the parameters of the absolute isotherm that best fit the available experimental excess data. Additionally, since an analytical model is fitted to the data, the absolute and excess quantities can be estimated over the whole pressure range. If the temperature dependence of the different parameters is built into the model, the uptakes can be estimated for different temperature ranges. The analysis in the previous chapter of the isosteric enthalpies of adsorption and the comparisons with alternative methods for storing hydrogen depend on an accurate estimation of the absolute isotherm, so it would be extremely important to obtain experimental validation of these estimated absolute isotherms. If impossible by conventional adsorption equipment, namely gravimetric and volumetric methods, other alternative experimental techniques have to be used to verify and validate our methodology.

One of the techniques that could be used for this purpose is Nuclear Magnetic Resonance (NMR). NMR is a spectroscopic technique that consists in applying a large magnetic field and electromagnetic radiation to a sample in order to determine its physical and chemical properties. It has been applied to adsorption, mainly for studying diffusion in porous materials, but it has recently been applied for hydrogen adsorption to determine absolute uptakes. NMR spectroscopy could experimentally validate our methodology to determine absolute uptakes if the same conditions are

used for obtaining the NMR spectra and sorption data[3]. If the absolute uptakes determined through NMR spectroscopy are similar to our absolute isotherm estimations, it would corroborate our methodology and its estimation of the absolute isotherm.

Another experimental technique that could be used to estimate absolute quantities is Inelastic Neutron Scattering (INS). INS is a technique usually employed to study atomic and molecular motion. Neutron scattering techniques use neutrons scattered onto a sample and depending on the collision of the neutrons with the sample, they can be elastic – neutron diffraction – or inelastic – inelastic neutron scattering. The elastic or inelastic refers to the conservation of momentum after the collision of the neutron with the sample. Neutron scattering techniques have been employed in hydrogen storage studies to identify preferential sites of adsorption at temperatures ranging from 4 to 25 K but, if used at the same temperatures and pressures of sorption experiments, they could quantify the adsorbed amount in the pore and hence verify the absolute isotherm calculated from our model[1].

In this chapter, NMR and INS techniques are introduced. Their application to adsorption studies is reviewed, with special emphasis on prior hydrogen sorption studies. The experimental setups for both the NMR spectroscopy studies and the INS are explained, as well as the results obtained. Finally, since both methods could provide an indication of the absolute uptake of a porous material, an attempt at validating our methodology experimentally is discussed.

[3] The absolute isotherms could be estimated for different temperature or pressure ranges, although this would not be a direct comparison.

5.2. Nuclear magnetic resonance

5.2.1. Nuclear Magnetic Resonance spectroscopy

Nuclear Magnetic Resonance spectroscopy is one of the most powerful analytical tools to elucidate molecular structure and it has been widely used in medicine, chemistry, physics, biology, biochemistry, geology, as well as other fields of science. Its discovery is usually attributed to Nobel laureates Isidor Rabi, Edward Purcell and Felix Bloch, with Rabi receiving the Nobel Prize in Physics in 1944 "for his resonance method for recording the magnetic properties of atomic nuclei" and Edward Purcell and Felix Bloch sharing the 1952 Nobel Prize in Physics for "their development of new methods for nuclear magnetic precision measurements and discoveries in connection therewith" .

NMR spectroscopy relies on a physical property present in nuclei with a nonzero spin, *i.e.*, that have intrinsic magnetic and angular moment. Outside a magnetic field, the nuclear spins of magnetic nuclei orient randomly. Once a magnetic field is applied to these nuclei, they adopt specific orientations, much the same way a compass needle points towards the earth's magnetic field. The spinning nuclei orient themselves in a way that their magnetic field (or spin) is aligned with (parallel to) or opposed to (anti-parallel) the external magnetic field. The two orientations do not have the same energy and so they are unequal in their populations. These nuclei are then irradiated with electromagnetic radiation, and on a specific frequency they absorb the radiation and "flip" from the lower-energy state to the higher energy state. When this occurs, the nuclei are said to be in resonance with the applied radiation, hence the name for the technique, nuclear magnetic resonance [255]. The specific frequency is characteristic of the nucleus, which means that each will resonate at a different frequency. The frequency is also proportional to the strength of the applied magnetic field, and because the energy difference between the two spin states is very small, very large magnetic fields have to be applied to have sufficient resolution [256]. The spectra can be obtained on a constant magnetic field with varying frequency of electromagnetic radiation or at constant frequency of electromagnetic radiation with a varying magnetic field [257].

As said, all nuclei for the same element should resonate – absorb a specific frequency of electromagnetic radiation – under the same magnetic field at the same frequency, but what happens is, because of electrons orbiting nuclei, a small local magnetic field around them is generated which opposes or enhances the applied external magnetic field. This is called shielding (or deshielding) and it depends on the electron density around the nuclei. Shielding alters the frequency at which nuclei resonate and since this change can be measured, those shifts can be used to characterise the environment of the nuclei, that is, to resolve the chemical structure of the molecule [256].

An NMR spectrometer could be explained in the following way. A sample is placed under a strong magnetic field and any of the nuclei in the sample with a nonzero spin will have different energy levels, the exact number depending on the value of the nuclear spin (the more common ^{1}H and ^{13}C NMR have two energy levels). The sample will then be irradiated with a short pulse of electromagnetic radiation, which disturbs the equilibrium and "flips" some of the nuclei in the lower energy level to a higher energy level. When the nuclei fall back to the lower energy level, this energy given out is detected by a sophisticated radio receiver. The results are then displayed in the form of intensity against frequency, the latter expressed in fractional units δ, parts per million, relative to the shifts of a normal compound [256]. The chemical shift of a nucleus is the difference between its resonance frequency and that of a reference standard, which for ^{1}H, ^{13}C and ^{29}Si is commonly tetramethylsilane, $Si(CH_3)_4$ or TMS [258]. As opposed to other spectroscopic methods, which use frequency or wavelength of absorption, NMR uses the chemical shift in ppm from a known substance (usually TMS) as the frequencies of NMR lines are proportional to the magnetic field strength, so if the field strength were to be doubled, so would the frequency of absorption. If a chemical shift scale is used, the peaks in the NMR spectra are independent of the field strength [259].

Being such a powerful technique, NMR spectroscopy found many applications in catalysis and adsorption studies [260-266]. The majority of NMR studies on adsorption have been on research applied to organic substances and water adsorbed on carbon structures [266]. These studies have focused on three major areas – measurement of chemical shifts for adsorbed molecules, dynamic studies (diffusion and mobility) and investigations of thick layers of liquid adsorbed on a surface. The

measurement of chemical shifts values was used to determine the position of molecules on carbon surfaces [261, 264]. Dynamic studies focused on determining the temperature dependence of relaxation times and on measurements of self-diffusion coefficients by applying the pulsed-gradient spin-echo method [261, 263, 266]. Each of the former techniques estimates the mobility of molecules in pores, which relate to the activation characteristics of these molecules. They are crucial for application of adsorbents as catalyst supports, since they determine the diffusion of reagent molecules towards the active sites of a catalyst and the rate of product removal. The investigations on the thick layers of liquid adsorbed on a surface are of great importance for colloidal chemistry and adhesion processes [266].

Despite intense research in hydrogen storage in porous materials, NMR studies on adsorbed hydrogen are relatively scarce. The operating conditions required, which involve cryogenic temperatures and high-pressures, make NMR a rarely used experimental technique to probe hydrogen storage in porous materials, since the NMR spectrometer has to be able to withstand high pressures and extremely low temperatures. Nonetheless, some work has been done on hydrogen adsorption in porous materials using NMR spectrometers.

5.2.2. NMR for hydrogen adsorption

Despite the wide applicability of NMR and its use in adsorption studies, experimental reports of adsorbed hydrogen analysed with NMR are lacking in the literature. The low condensation point of hydrogen has excluded its use as a probe molecule to study the pore size distributions and surface areas of the different adsorbents, unlike other molecules (mainly organic molecules and water) which have been extensively used in combination with NMR. Hydrogen adsorption has been studied on carbon nanotubes and some isotherms were constructed, but because the experiment lacked a mass calibration, no correlation with volumetric or gravimetric studies of hydrogen adsorption could be done [267]. Recently, a research group at the University of North Carolina in Chapel Hill studied hydrogen adsorption on carbon materials [268] and, due to a calibration method developed in-house [269], were able to construct experimental isotherms based on the NMR spectra. Their work highlighted the

importance of probing nanostructures using ^{1}H-NMR and their method was tested on different PEEK carbons (where PEEK stands for poly(ether ether)ketone). The samples of PEEK carbons were burned in a CO_2 or steam atmosphere at 900^{o}, using different times, which resulted in different degrees of burn-off, as measured by the resulting mass after pre-activation [147].

The research group at the University of North Carolina at Chapel Hill had a custom-built NMR spectrometer for studying hydrogen adsorption in porous materials, which could pressurise the sample up to 10 MPa, at room temperature and 100 K with a flow cryostat [268, 269]. With the objective of validating our methodology using experimental techniques other than gravimetric and volumetric sorption equipment, the research group in the University of North Carolina at Chapel Hill was approached for a joint collaboration. Dr Robert J Anderson[4] , Prof Alfred Kleinhammes and Prof Yue Wu[5] agreed to test a sample of TE7 carbon beads. Data for seven PEEK carbons from published work [268] was also sent, as well as samples of PEEK carbons [147] to be tested for sorption at the same conditions (100 K and high pressures) of the NMR experiment in the University of Bath. The idea behind the experiment was to compare experimental excess data for materials under the same conditions of the NMR experiment and apply the methodology to the obtained experimental isotherms.

To calibrate the NMR signal intensity for mass uptake, a glass capillary was placed in the sample tube, as previously done [269]. The TE7 carbon beads were placed in the sample holder and the free volume was calculated, taking into account both the intergranular volume and the free volume in the capillary. The sample was heated to 350^{o} C for 8 hours under vacuum, which according to our research, is the best preparation for degassing this sample [203]. Details for the experimental setup are given in Additional Information E, as written by Dr Robert J Anderson. The NMR spectra were acquired at 100 K and 290 K, with the background spectrum collected before any H_2 was introduced in the sample at 290 K. At 100 K, the background

[4] now at the Department of Medicine, John A. Burns School of Medicine, Honolulu, University of Hawai'i, USA.
[5] both from the Department of Physics and Astronomy at the University of North Carolina in Chapel Hill, NC, USA.

spectrum was collected last, after the spectra for all the different pressures was collected and after a 20 min vacuum evacuation of the sample. The isotherms were collected using a basic Free Induction Decay (FID) pulse sequence, with the intensity of the NMR signal directly proportional to the number of nuclei. All spectra were normalised to 1024 (1k) scans.

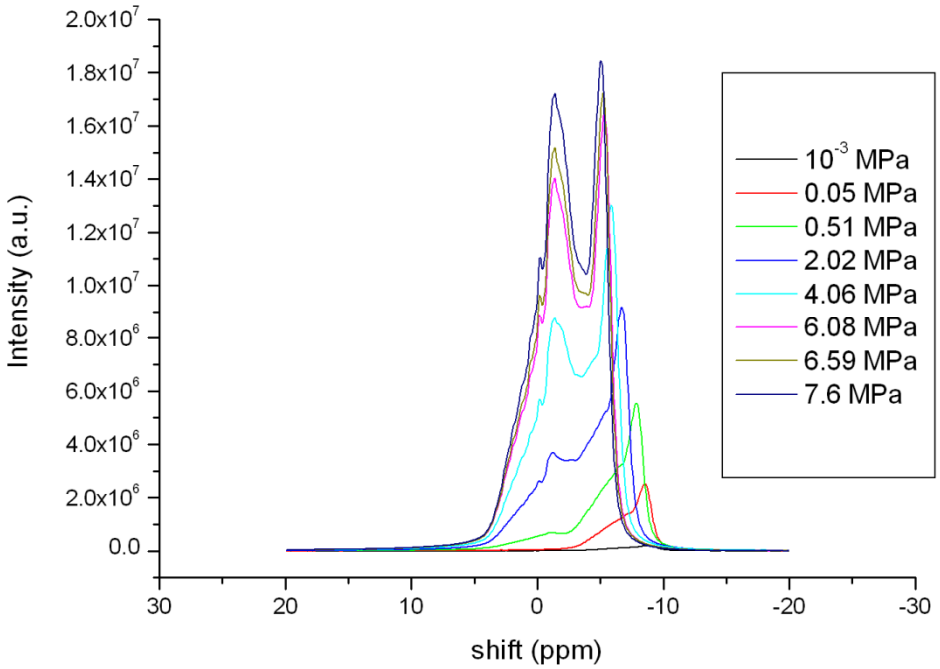

Figure 5.1 – NMR spectra for the TE7 carbon beads at 100 K.

NMR spectra were acquired for 24 different pressure points from 0.001 to 7.6 MPa, but for clarity only the pressure points in the legend were included in the graph. There are two prominent peaks for each pressure at 100 K in the NMR spectra, as depicted in Fig.5.1. At low pressures, the contribution to the spectra will mostly come from adsorbate in the micropores, so the right hand side peak (Peak B) is assigned to the adsorbate in micropores, while the left hand side peak (Peak A) represents the free gas in the sample, *i.e.*, non-adsorbed hydrogen. Peak B, the one corresponding to the H_2 in the micropores, is not Gaussian or Lorentzian in shape, with two or three different peaks comprising it. It is very likely that the shape of Peak B is actually from a type of powder pattern due to the bulk distribution of the carbon beads, which have a

disorganized and random particle size and distribution. To calibrate against mass uptake, the peaks in the NMR spectra need to be resolved.

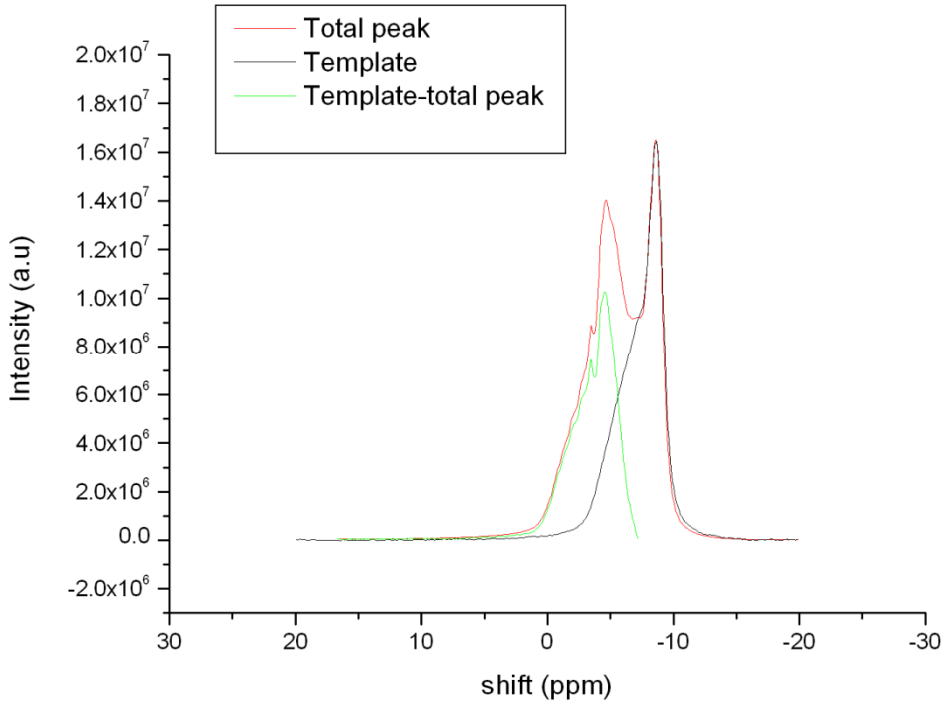

Figure 5.2– Deconvolution of the spectra using the "template method" at 100 K and 6.08 MPa.

The method applied previously, the "template method" [269] to resolve the NMR peaks was applied to the NMR TE7 spectra. Since Peak B is known and present at all pressures, a lower pressure (0.009 MPa) was used to scale and shift a low-pressure spectrum to approximate Peak B at higher pressures. Peak B was then subtracted to the spectrum and the remainder of the spectrum thus corresponds to Peak A, which is the non-adsorbed hydrogen. The "template method" can be seen in Fig.5.2, with the two peaks A and B and the scaled and shifted Peak B obtained from a lower pressure. Peak A, which corresponds to the free gas in the sample, should follow the equation of state. Since the volume that Peak A occupies can be calculated using intergranular and free volume and the quantities at a given pressure and temperature can be calculated using the EOS, a correspondence between the intensity of the scans (in arbitrary units) and the mass uptake was found. Once this was done, the mass uptakes could be calculated both in the free gas and in the micropores, by integrating the spectrum. This was then translated to mass uptake, using the mass of sample to

convert to units of specific mass of adsorbent (wt. %). More details of the analysis and deconvolution are provided in Additional Information E.

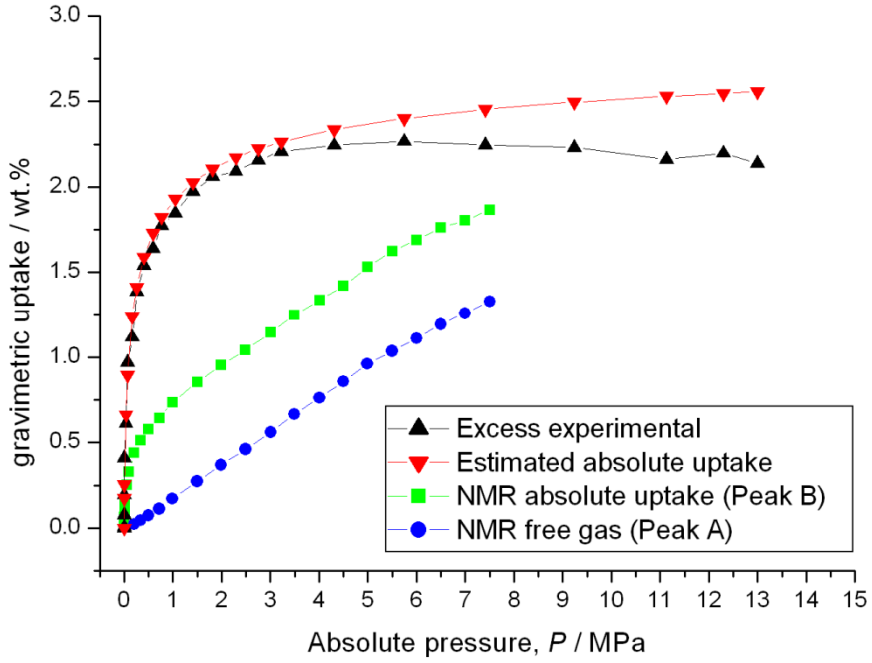

Figure 5.3 – Estimated NMR for the absolute uptake (hydrogen in micropores) and estimated NMR for the quantity of free gas in the TE7 carbon beads at 100 K. The experimental excess for the TE7 and the absolute uptake using the parameters from the multiple fitting of isotherms from Table 4.1 are shown for comparison.

In Fig.5.3, the isotherm for 100 K for the TE7 carbon beads up to 7.6 MPa can be seen, with Peak B corresponding to hydrogen in the micropores and Peak A corresponding to the free gas. The TE7 excess for the same temperature (as measured and shown in Chapter 3 and 4) and the estimated absolute from the methodology, calculated using the Tóth equation and the parameters from the multiple fitting of isotherm are also depicted. Unfortunately, although Peak A shows a linear relation with pressure – as one would expect from a free, non-adsorbed gas – the absolute estimated using NMR spectra and the estimation of the absolute using our methodology do not show good correspondence. The NMR estimation of the absolute uptake is in fact even lower than the measured experimental excess for the same conditions of pressure and temperature. Furthermore, it seems that the NMR estimated hydrogen in micropores does not saturate and reach a plateau, even at pressures as

high as 7.6 MPa. Instead, it increases almost linearly with pressure, which, as noted for Peak A, seems to be indicative of a free gas.

The results from the NMR analysis on the TE7 carbon beads were inconclusive, so data for the published journal article on the PEEK carbons were kindly provided by Dr Robert J Anderson. Some samples of the tested PEEK carbons were sourced and tested on the volumetric HTP-1 at the University of Bath, aiming at comparing the obtained uptakes from NMR to the estimated absolute isotherm using the volumetric excess quantity.

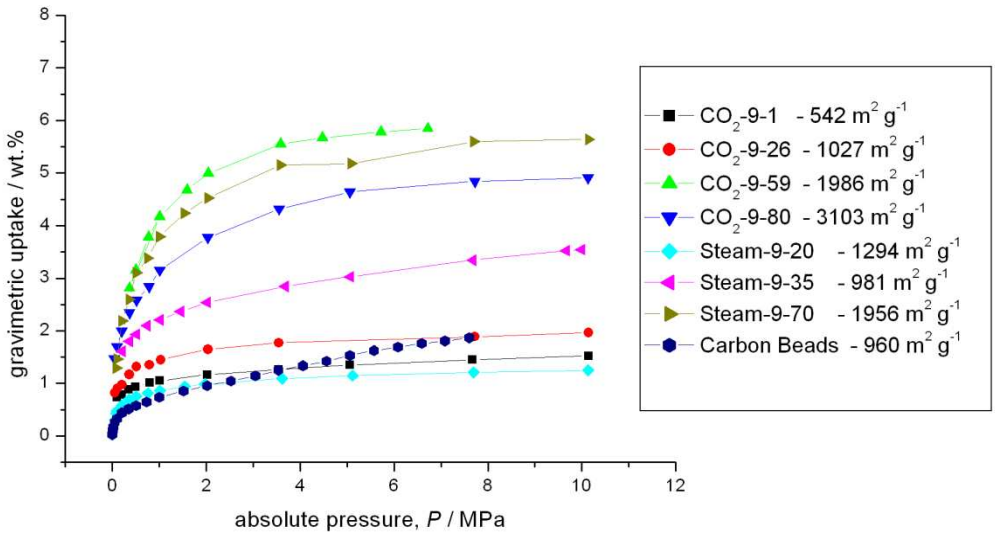

Figure 5.4 – Absolute uptakes determined at 100 K for the PEEK carbons using NMR. Absolute uptake determined for the TE7 is shown for comparison. Data for the PEEK carbons absolute uptake was provided by Dr Robert J Anderson and was published in Anderson et al. [268].

In Fig.5.4, the NMR absolute isotherms for the PEEK carbons are shown. For comparison, the NMR absolute isotherm for the TE7 is also in the figure. As it can be inferred from the figure, the PEEK carbon results and the TE7 are inconsistent and the shape of the absolute isotherm for the TE7 does not match the one expected from a microporous carbon. On the other hand, the absolute isotherms for the PEEK carbons seemed to have the shape (type I isotherm) characteristic of an absolute isotherm for a supercritical gas in a microporous material. Since NMR absolute uptakes were already available from published data [268], the PEEK carbons were sourced from the University of North Carolina at Chapel Hill and tested at the University of Bath in the volumetric, high-pressure sorption Hiden HTP-1 apparatus.

The sourced PEEK carbons were the PEEK ST-9-20 and ST-9-35 samples, where ST indicates steam activated, the atmosphere in which they were burned, and 20 and 35 indicate the percentage of burn-off as measured by the resulting mass after activation. Details on the preparation of the PEEK carbons and on the NMR are given in McNicholas et al. [147] and Anderson et al. [268], respectively. The excess data for hydrogen was obtained after a degas cycle under vacuum at 573 K for 12 hours. The hydrogen excess isotherms were collected using the same experimental methodology detailed in Chapter 3 for high-pressure sorption data acquisition, at 100 K and up to 20 MPa. After the excess data were obtained, the model was applied using the Tóth equation to estimate the absolute isotherm, with the parameters obtained from fitting the excess experimental isotherms for each material at a single temperature (100 K).

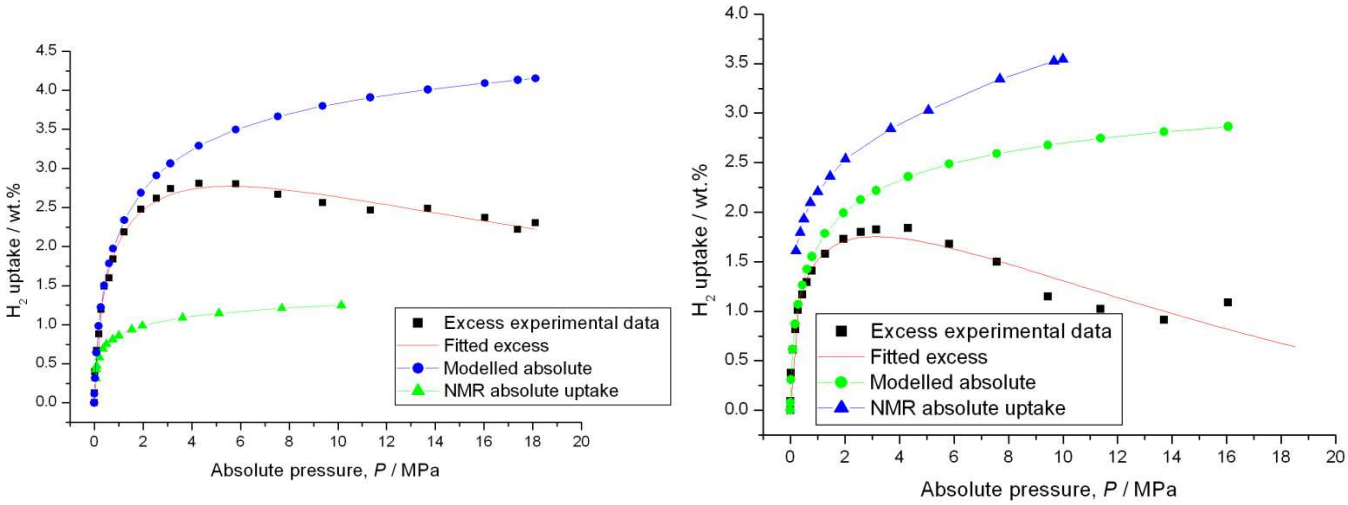

Figure 5.5 – Comparison of the NMR absolute uptakes determined for the PEEK carbons by the "template method" with the excess and estimated absolute from experimental data. The excess was fitted using the model and the Tóth equation, with a fit at a single temperature (100 K). PEEK-ST-9-20 is the left-hand side plot and PEEK-ST-9-35 is the right-hand side plot.

The NMR absolute isotherm, the excess isotherm obtained experimentally in the HTP-1 and the absolute estimated from our methodology for the PEEK-ST-9-20 and the PEEK-ST-9-35 are shown in Fig.5.5. The results shown are again unexpected. It is remarkable that for the PEEK ST-9-20 carbon, the NMR absolute is lower than the experimental excess, as was also evident in the TE7 comparison. Analysis of Fig.5.4 reveals that the PEEK carbons, synthesised the same way except for the atmosphere in which they were burned (steam or CO_2) and degree of burn-off, showed different NMR absolute uptakes. Interestingly, absolute uptakes did not correlate with the BET

specific surface area. The "Chahine rule" of hydrogen excess uptake of 1 wt.% at 77 K and 0.1 MPa *per* 500 m^2 g^{-1} BET specific surface area [88, 157, 182, 270], was not verified for the measured PEEK carbons shown in Fig.5.4[6]. In Figure 5.5, for the PEEK-ST-9-20 and the PEEK–ST-9-35, with surface areas of 1294 m^2 g^{-1} and 981 m^2 g^{-1}, respectively, the excess uptakes are fairly similar as measured in the HTP-1, being somewhat higher for the ST-9-20, which has a higher surface area. The "template method" used to calibrate the NMR signal seems to offer disparate results for absolute uptakes and shows inconsistency when compared to the excess uptake for the same material.

A qualitative comparison between the absolute uptakes determined by NMR and the absolute uptakes estimated using our methodology is presented in Fig.5.6. This time, the signal calibration for the NMR uptake was ignored and the uptakes were scaled using the absolute estimation from the model instead. The NMR estimated absolute was scaled to the absolute isotherm for each single point and the Sum of the Root Squared Residuals (SRSR) was calculated for every scaling. The scaling for the point that had the lowest SRSR for each material is shown in Fig. 5.6, again for the PEEK-ST-9-20 and the PEEK-ST-9-35.

$$SRSR = \sum_{i=1}^{i=n} \sqrt{\left[\left(x_m - x_n\right)\right]^2} \qquad \text{Eq.5.1}$$

In Eq.5.1, n is the number of points, x_m is the absolute calculated using our methodology and x_n is the absolute calculated using NMR.

[6] Chahine's rule is commonly quoted as 1 wt.% hydrogen uptake at 77 K and 0.1 MPa *per* 500 m^2 g^{-1} BET N_2 at 77 K specific surface area, although Thomas and Panella [88] K.M. Thomas, Catal Today, 120, 389 (2007), [270] B. Panella, M. Hirscher, S. Roth, Carbon, 43, 2209 (2005). found that this is very dependent on the material and it should be taken as a rule of thumb, even for porous carbons.

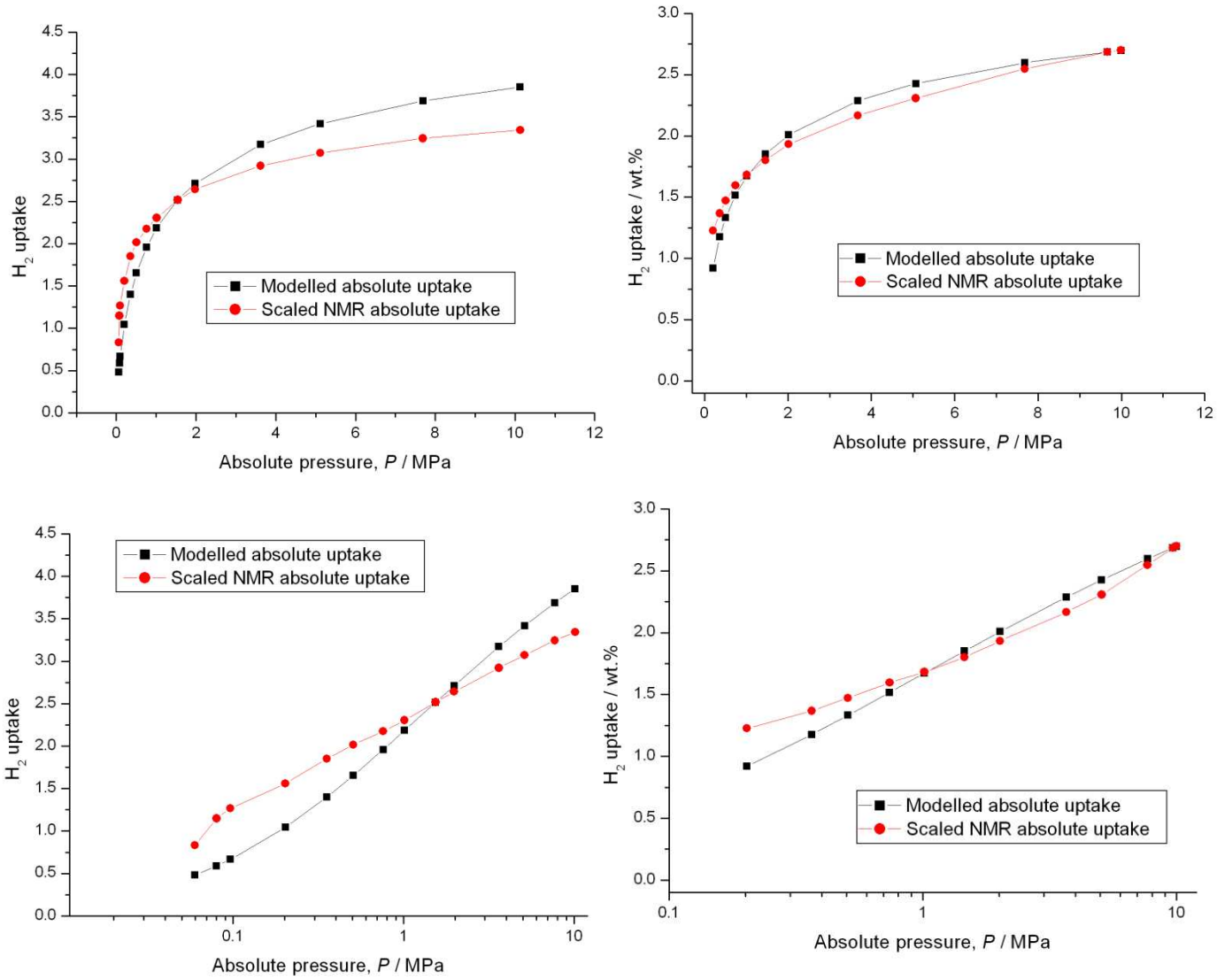

Figure 5.6 – Scaling of the absolute NMR to the estimated absolute uptake from the modelling using the Tóth equation and the parameters for single fits at 100 K. The scaling was done to the point in the modelled absolute that had the lowest SRSR for the NMR absolute uptake. Left-hand side plots are the PEEK-9-20 and right-hand side plots are the PEEK-9-35. Plots in the top are the data in a normal scale and plots in the bottom are in a logarithmic ($\log_{10}$) scale.

In Fig.5.6, we can see that the agreement in the lowest SRSR for the absolute NMR uptake and the estimated one is good for both sets and logarithmic scale, being slightly better for the PEEK-ST-9-35 (right-hand side), as also indicated by the lower SRSR for that material.

Unfortunately, the "template method" developed at the University of North Carolina applied to NMR hydrogen adsorption did not validate our proposed methodology of estimating absolute quantities quantitatively. For the TE7, the behaviour displayed by the absolute isotherm is incompatible with what would be expected from a microporous material and therefore a correlation to our methodology was

impracticable. For the PEEK carbon data, even if the isotherms display a saturation and plateau, consistent with a type I behaviour of adsorption of supercritical hydrogen in a microporous material, a quantitative correlation was also not possible. Strangely, for both the TE7 and for one of the PEEK carbons tested, the NMR absolute uptakes were even lower than the measured experimental excess. A closer look at published data for the NMR on PEEK carbons reveals some inconsistency of uptakes with surface areas, which should approximately linearly correlate, as observed by other authors for a range of materials [88, 182, 270]. Correlation with the scaled NMR uptakes using the estimated absolute isotherms offered better agreement.

The results on the PEEK isotherms indicate that qualitative good agreement can be reached between those and our estimated absolutes from excess experimental data. NMR can be a powerful tool to study hydrogen adsorption and, based on the PEEK carbon results and other reports from the group [268, 269], it seems to measure the adsorbate in the micropores. Nevertheless, the "template method" developed at the University of North Carolina for quantifying the NMR absolute uptakes did not corroborate our methodology. There is a lack of literature on NMR for hydrogen adsorption and experimental or computational validation of the NMR absolute determined using this method is necessary. These results indicate that the "template method" for calibrating absolute hydrogen uptakes and estimating adsorbed hydrogen in terms of mass uptakes in the micropores might need further refinement.

5.3. Inelastic neutron scattering

5.3.1. Neutron scattering

Neutrons are sub-atomic uncharged particles, with approximately the same mass as the proton. They were theoretically predicted by Ernest Rutherford, who hypothesised that, based on the differences between atomic number and atomic mass on the chemical elements, a particle with approximately the same mass as the proton but no charge had to constitute the nuclei of elements [271]. This supposition was experimentally proven by James Chadwick, who in 1932 proved that the radiation

coming from beryllium when bombarded with α-particles from polonium could not be ascribed to quantum radiation but instead to an uncharged particle that would constitute the nuclei of atoms [272]. While the atomic number is the number of protons in a nucleus, the atomic mass is given by both the number of protons and neutrons. Isotopes are elements with the same number of protons and different number of neutrons, hence, different mass.

Neutrons are widely used in research and they are generated in a neutron source, which can be mainly of two types – nuclear fission reactors generate neutrons upon fission of uranium-235 as part of a nuclear reaction; and spallation sources, which accelerate a proton beam to high-energy using a linear accelerator and a synchrotron. The proton beam then collides against a heavy metal target, releasing neutrons upon collision. In both cases, the generated neutrons are directed towards instruments. The biggest spallation neutron sources are the Spallation Neutron Source (SNS) at Oak Ridge, USA; the ISIS neutron source at the Rutherford Appleton Laboratory, UK; the Paul Scherrer Institute Spallation Neutron Source (SINQ) in Switzerland; the KENS neutron scattering facility in Japan; the Los Alamos Neutron Science Centre in the USA and the European Spallation Source, which is under construction and will be the most powerful neutron source in the world, located in Lund, Sweden. Important neutron sources that work on nuclear fission reactors are the Institute Laue-Langevin (ILL) in Grenoble, France; the Intense Pulsed Neutron Source (IPNS) at Argonne National Laboratory, USA; the NIST research reactor in the USA and the High Flux Australian Reactor (HIFAR).

Neutrons are widely used for research, mainly on condensed matter. There are several reasons why neutrons are used, the main ones are the fact that, when cooled, they can have a wavelength of the order of interatomic distances and, since they are uncharged, they can penetrate matter and come closer to the nuclei, as opposed to other techniques that probe the electron cloud, like X-rays. Another important reason is that the energy of neutrons can be of the same order as many excitations in condensed matter. This means that, when inelastically scattered, the neutron will exhibit a change of energy that is a large fraction of its initial energy. Finally, the neutron has a magnetic moment, which means it can interact with unpaired electrons in magnetic atoms [273]. Detection of neutrons is done indirectly, because they have no charge

and they react weakly with matter. Neutrons are detected with nuclear reactions that are caused upon collision of the scattered neutron with an unstable isotope. Typically, detection is done using one of following ionisation reactions.

$$^{3}_{2}\mathrm{He}+^{1}_{0}\mathrm{n}\rightarrow ^{3}_{1}\mathrm{H}+^{1}_{1}\mathrm{H}+0.76\mathrm{MeV} \qquad \text{Eq.5.2}$$

$$^{10}_{5}\mathrm{B}+^{1}_{0}\mathrm{n}\rightarrow ^{7}_{3}\mathrm{Li}+^{4}_{2}\mathrm{He}+2.8\mathrm{MeV} \qquad \text{Eq.5.3}$$

$$^{6}_{3}\mathrm{Li}+^{1}_{0}\mathrm{n}\rightarrow \left(^{7}_{3}\mathrm{Li}\right)\rightarrow ^{3}_{1}\mathrm{He}+^{4}_{2}\mathrm{He}+4.8\mathrm{MeV} \qquad \text{Eq.5.4}$$

When the neutron hits the detector, the energy released in the ionisation reactions can be measured [274]. The wave-particle duality of neutrons enables the measurement of nuclear positions of elements and allows for the characterisation of the structural information of molecules, because the wavelength is a scalar quantity but the neutron wave has a defined direction. The nuclear positions can be resolved through the scattering of the incident neutron beam from the sample nuclei, since the scattering intensity is a function of the incident and scattered neutron wave vectors and of the scattering angle [275]. One advantage of neutron scattering is that the wavefunction of the scattered neutron has a scattering length, which is independent of the angle of scattering. This scattering length varies from nuclide to nuclide erratically and, due to the lack of a proper nuclear theory, cannot be calculated or predicted from other properties of the nuclei, and instead has to be determined experimentally [273]. This scattering length is also a fingerprint of a nuclide, allowing for neutrons to identify the elements and determine their positions in the molecule. In an experiment, scattering will depend on the different scattering lengths associated with different nuclei.

If neutrons are to be used in investigating the arrangement of atoms in a solid, their wavelengths have to be adjusted to that they are of the same order as the distance between the different atoms. For this to be achieved, their temperatures have to be brought down, which is usually done using a moderator [276]. In the high-flux reactor at the Institute Laue-Langevin, liquid deuterium is used to cool the neutrons and their wavelength adjusted for the experiment. In neutron diffraction experiments, a crystal is used to monochromatise the neutron beam, that is, to reflect a small band of wavelengths towards the sample and then measure the scattering from specific wavelengths. One important thing to distinguish in neutron scattering is the coherent

and incoherent scattering of neutrons. Coherent scattering is the scattering that the same system (same nuclei at same position and motion) would give if all the scattering lengths were equal. The neutron wave interacts with the whole sample and, because the scattered waves from each nucleus interfere with each other, there is interference from the different scattered waves. Incoherent scattering is the term we must add to this to obtain scattering in the actual system and in it, the neutron wave interacts independently with each nuclei, so the scattered waves do not interfere with each other. Incoherent scattering can therefore carry information about diffusion or rotation [276]. For most experiments, incoherent and coherent scattering are simultaneous.

Neutron diffraction is used to determine crystal structures, in which a neutron beam with an appropriate wavelength falls on a crystalline sample having a periodic array of crystals. The interference is created when, on a right wavelength, all the scattered waves add up in phase to create a new plane wavefront. This occurs when the angle of incidence equals the angle of reflection, according to Bragg's law. In spallation neutron sources, the time-of-flight for the neutron can be measured and, since the diffractrometer covers a range of angles, the atomic structure of the material can be resolved [275]. In addition to coherent or incoherent scattering, the neutron scattering can be of elastic or inelastic nature. In neutron diffraction, the underlying assumption is that the nuclei are of infinite mass and the incident neutron has an elastic collision with the nuclei, that is, there is no loss of momentum from the incident neutron [276]. In a real crystal, the atoms are not of infinite mass and their positions are not rigid, since they have some motion because of their thermal energy. Because of this, the incident neutron can gain or lose energy upon collision with some of the atomic nuclei. This will alter the wavelength of the incident neutron and, because these changes are large enough to be measured, important information of the structure can be acquired [276]. Inelastic neutron scattering is widely used for vibrational spectroscopy, that is, the study of the vibrational spectra of molecules [277].

The importance of both elastic and inelastic neutron scattering for condensed matter was recognised by the award of the Nobel Prize in Physics in 1994 for "pioneering contributions to the development of neutron scattering techniques for studies of condensed matter" to Bertram Brockhouse for "the development of neutron

spectroscopy" and to Clifford Shull for "the development of the neutron diffraction technique".

5.3.2. Inelastic neutron scattering and hydrogen storage

INS is a technique that can be used to study hydrogen storage materials. As mentioned in the previous section, it is used for vibrational spectroscopy because of its characteristics, since neutrons have mass of the order of the proton (unlike photons or electrons)[7] and are deeply penetrating, meaning that they interact weakly with matter and can pass easily through the walls of containers, like aluminium or stainless steel. They can also span a wide range of energies, from the microwave to the ultraviolet regions of the electromagnetic spectrum. Other techniques, like Raman or infrared spectroscopy, are subject to the selection rule that only transitions at zero wavelength are observable, as opposed to neutron scattering, which is allowed for all wavevectors, so not subject to selection rules [277].

Neutrons are an excellent probe for some materials, due to their sensitivity to low atomic number elements and their scattering by the nuclei, instead of the electron cloud. They can be used to measure structure and dynamics and they are ideal for hydrogen studies, since hydrogen has a large incoherent cross-section, which is about ten times the cross-section of other elements [278]. For these reasons, INS has been used to study hydrogen storage in hydrides and other hydrogen storage materials. Some examples are the study of thermal treatment or the identification of the catalysing substances for sodium alanates [279, 280]. Another material studied by INS were magnesium hydrides, where INS supported some previous assertions on improved kinetics and reversibility by cycling the material [281].

Another good example of using neutrons for adsorption studies is the use of small angle neutron scattering for pore structure determination and characterisation [282]. INS in particular has also found applications in adsorptive studies and physisorption

[7] Photons have no mass, the mass of the electron is 9.109 382 x 10^{-31} kg, the mass of the neutron is approximately 10 000 times higher and it is 1.674 927 x 10^{-27} kg.

of hydrogen on porous materials [283]. Most of the work done using INS for hydrogen adsorption has concentrated on identifying the individual sorption sites on adsorptive materials and determine their binding energy [127]. There are many recent reports on metal-organic frameworks studied using INS, to determine the strong binding sites, which usually correspond to the unsaturated metal centres [284-288]. The controversial spillover has also been studied using INS, on platinum, ruthenium and platinum/ruthenium catalysts on carbon supports to identify dissociated hydrogen on the surfaces. INS provided evidence of hydrogen in the edges of the carbon support and in a weakly bound layer of mobile H atoms after dissociation of the molecular hydrogen [289].

INS is a powerful tool for studying dynamics and structure and, due to the cross-section of hydrogen, ideal for hydrogen studies. Since neutrons are deeply penetrating, INS can be done in conditions similar to sorption experiments - cryogenic temperatures and high-pressures. The large incoherent scattering cross section of hydrogen enables the use of INS to study the binding strength of the atoms and molecules even when using a bulk disordered material. A proposal to the TOSCA instrument, one of the inelastic neutron scattering instruments at the ISIS Facility at the Rutherford Appleton Laboratory (RAL), Didcot, Oxfordshire, UK, was submitted to study hydrogen adsorption and validate the model for absolute isotherm determination. TOSCA was chosen because it can simultaneously track the inelastic and elastic region of the spectrum and it had been recently upgraded with new low energy capabilities, which also enabled tracking of the shape of the recoil features. This would allow quantification of the hydrogen in the porous structure of the adsorbent, both the adsorbed and the free gas. Since this could be done at the same operating conditions of sorption experiments, INS could experimentally validate our models for predicting absolute capacities from experimentally obtained excess through volumetric or gravimetric methods. The material that was tested was our standard reference material, the TE7 carbon beads from MAST Carbon International. The idea was to use neutrons to study the material under different hydrogen pressures at cryogenic temperatures and then construct an isotherm at different pressure points, which would correspond to an absolute isotherm obtained from neutrons. For maximisation of the vibrational spectra, INS measurements are typically done below 25 K, but a more relevant temperature – and one that could directly compare to

hydrogen sorption measurements in the same material – of 77 K was used. If a lower temperature was to be used, temperature dependence on the model had to be inserted, instead of direct comparison at the same temperature. If the experiment was done at a subcritical temperature of 25 K, this would have rendered the results even more difficult to compare, because of phase changes to liquid hydrogen in the INS experiment.

5.3.3. Solid hydrogen – a new model for hydrogen adsorption

INS studies on the TE7 carbon beads were done using the TOSCA instrument at RAL, Didcot, Oxfordshire, UK. Due to time allocated in the instrument, the slow frequency of the neutrons and the statistical significance needed for neutron counts in each pressure point, only the collection of one isotherm with different pressure points was possible, coupled with single pressure measurements at the lowest pressure at 4 and 100 K. INS spectra were measured at 77 K, with eight gas pressure points, from 0.016 to 3.5 MPa. TOSCA had recently been modified, which allowed high resolution of the instrument over a wide range of energy transfer, higher than any INS instrument in the world. This high resolution at low energies permitted the quantitative analysis of the elastic region, which is the region of the spectra where little or no energy is lost by the scattered neutron. This information was collected for a number of different pressure points. The inelastic region was monitored at the same time, and both regions contain information regarding the phase of the adsorptive.

The TE7 carbon beads were activated under high vacuum and 623 K for 8 hours and then loaded into a Ar glovebox. The sample (~ 10 g) was then changed to a high pressure (7 MPa) stainless steel can, with temperature control provided by a standard cryofurnace ancillary. The hydrogen gas (Air Liquid, 99.999% purity) was dosed into the sample and equilibrated at 77 K. The pressure was recorded using a baratron and a high-pressure transducer. The spectra was collected at the TOSCA instrument, covering the energy range from -3 to 500 meV, with a resolution in the 3 to 500 meV range of $\Delta E/E < 1.25\%$. In the elastic region (-3 to 3 meV), the full width at half-maximum instrumental resolution is 300 μeV. The background scans were done for 12 hours in the degassed sample under a dynamic vacuum at 77 K. These were later

subtracted from the spectra to correct for the presence of terminal H atoms in the sample. The pressures used were 0.016, 0.070, 0.160, 0.301, 0.630, 0.998, 2.070 and 3.5 MPa of hydrogen pressure with 12 hours collection periods. Due to the paramagnetic nature of activated carbons, the room temperature mixture of parahydrogen and orthohydrogen rapidly equilibrated to 50:50, which is the ratio of *para*-to-*ortho* hydrogen at 77 K. Both spin isomers were needed while collecting the spectra, since they provide different features in the elastic and inelastic regions of the spectra.

The INS spectra for the TE7 carbon beads at 77 K are shown in Fig.5.7.

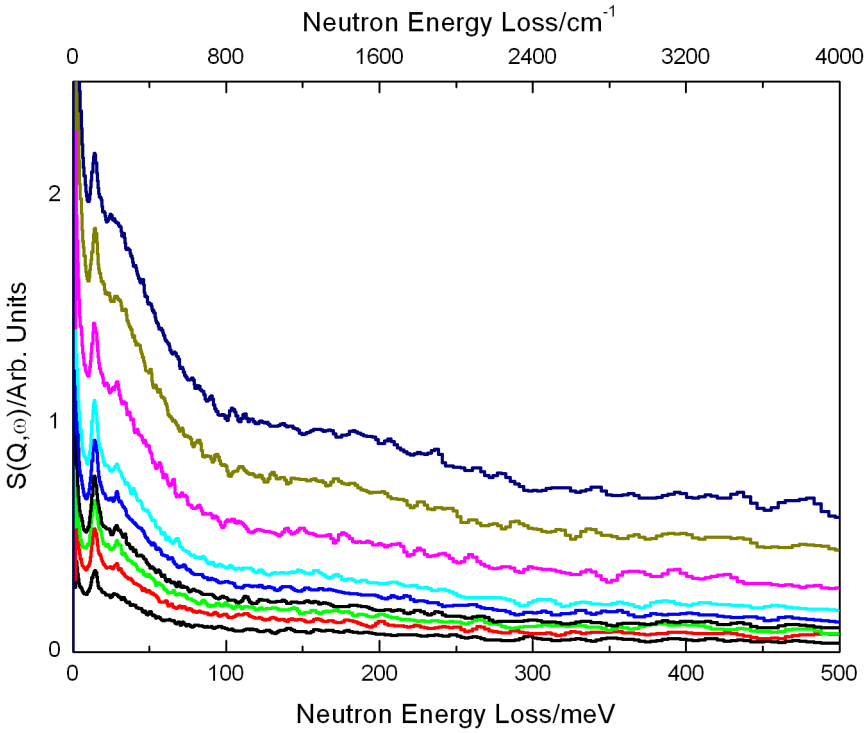

Figure 5.7 - INS spectra for the TE7 carbon beads at 77 K from -10 to 500 meV, with pressures 0.016, 0.070, 0.160, 0.301, 0.630, 0.998, 2.070 and 3.5 MPa, from bottom to top.

The INS spectra at 77 K for the carbon beads revealed very interesting information. In the elastic region of the spectra (~ 0 meV), an intense, sharp peak was noticeable, due to the scattering of neutrons by orthohydrogen. This peak indicates a highly dense phase for hydrogen, since liquid and solid phases show a sharp elastic peak on the elastic region, due to higher densities of adsorbate. If the hydrogen is in a liquid phase, the peak will have a more broadened shape than in the solid phase, due to its

mobility and quasielastic interactions. The elastic peak in the lowest pressure point (0.016 MPa) had a full-width at half-maximum that neared the instrument's resolution (~ 0.3 meV), as it can be seen in Fig.5.8. This feature points to an immobile hydrogen in the pores, in a solid-like phase. Interestingly, the INS spectra also showed a clear peak at ~ 14.7 meV, which is a distinct fingerprint of the *para*-to-*ortho* transition. This peak, clearly seen in Fig.5.8 in the logarithmic scale, is commonly referred to as the "rotor peak", and it is twice the rotational constant for hydrogen (rotational constant is 7.35 meV). A peak at ~ 14.7 meV indicates a free rotation of molecular H_2 and it is a clear feature of solid hydrogen. The presence of this peak indicates that the hydrogen is immobilised in the pores and lacks translational freedom [251, 278, 290, 291]. This peak is not present in liquid or gaseous parahydrogen [292] and it is present in every measured pressure in the 77 K INS spectra for the TE7. This peak was also present in the spectra measured at 100 K and 0.016 MPa for the same material (figure in Additional Information F).

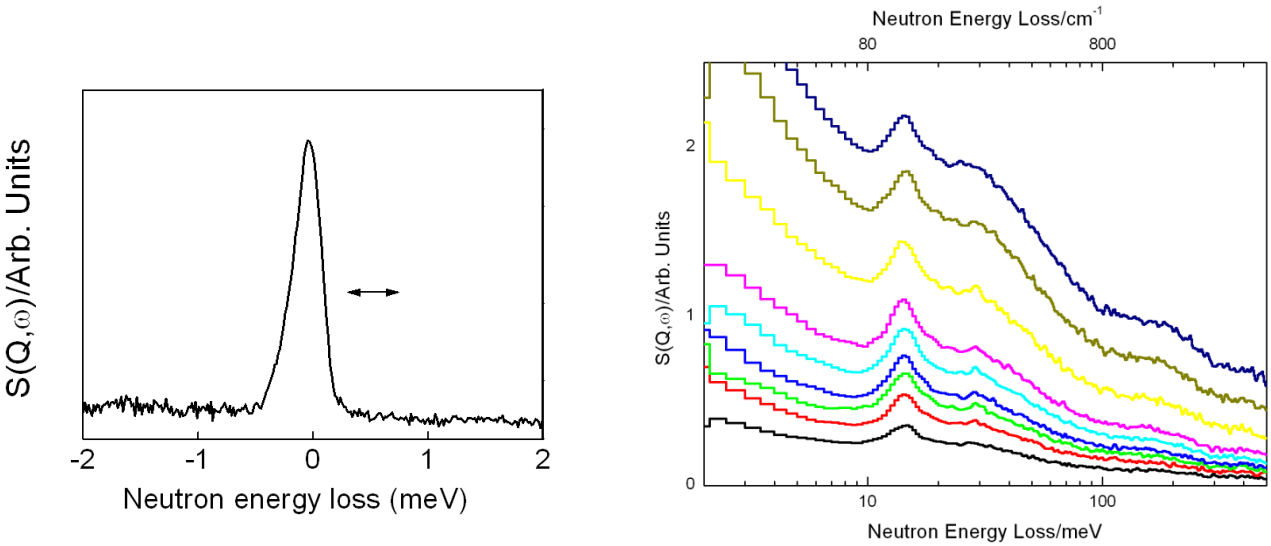

Figure 5.8 – INS spectra for the TE7 carbon beads at 77 K. Left-hand side plot is the elastic peak (from -2 to 2 meV at 0.016 MPa, with horizontal line indicating full width at half maximum. Right-hand side plot is the INS spectra, with the same range and order of pressures as Fig.5.7, in a logarithmic scale. The rotor line peak at 14.7 meV is clear in the logarithmic plot.

Both these features in the spectra strongly support solid-like, immobilised hydrogen in the pores of TE7. This is an outstanding development on the understanding of supercritical adsorption in a porous material and could be a new paradigm for hydrogen storage. The peaks were quantified, both the elastic region, – corresponding

to high-density liquid or solid-like density hydrogen – the inelastic region, – corresponding to the adsorbed and non-adsorbed hydrogen gas in the sample - and the region under the 14.7 meV – corresponding to solid-like hydrogen - were integrated for the different pressure points and are shown in Fig.5.9. The total intensity in the inelastic region was integrated from 2-500 meV, the elastic region was numerically integrated from -2 to 2 meV after subtraction of the linear background and the 14.7 meV peak integration was determined using a Gaussian peak shape after subtraction of a fourth-order polynomial background.

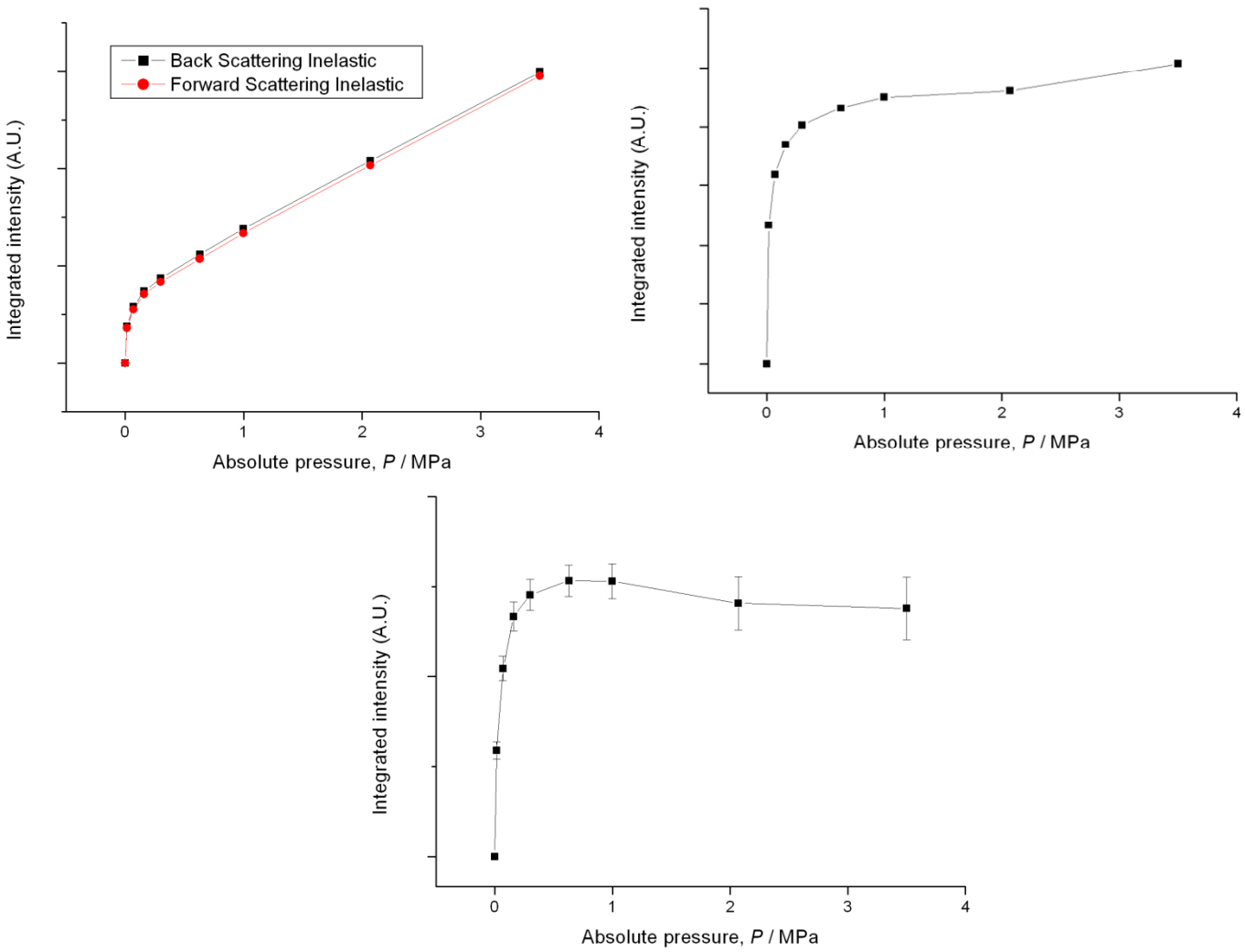

Figure 5.9 – Integrated area in the inelastic region, both back and forward detector (top left hand side plot), in the elastic region from the forward detector (top right hand side plot) and integrated area under the rotor peak (~ 14.7 meV) from 0 to 3.5 MPa (bottom plot). The *y*-axis units are arbitrary units. Errors for the top plots are within the data markers.

As observed in Fig.5.9, in the top left hand side plot, the integration of the whole inelastic region would yield the total amount of hydrogen in the sample. This

corresponds to both the adsorbed and non-adsorbed hydrogen, and the spectra should be dominated by the amount of free gas, obeying the equation of state, that is, it should have linear behaviour that rises with increasing pressure. This was exactly what was observed for the integrated spectra of the inelastic region. The integrated elastic peak and the integrated peak below the 14.7 meV showcased a behaviour that is consistent with a type I isotherm, which is what an adsorbed species on a microporous material at that temperature should have. This means that the quantification of solid-like adsorbed hydrogen correlates very well with adsorption on a material, analysed using volumetric or gravimetric equipment. Rather than a gaseous phase that increases in density with increasing pressure, the presence of the rotor peak at even the lowest pressures shows that a mechanism of direct accumulation of solid-like H_2 with increasing pressures is more likely in light of this evidence. Both the elastic peak and the area under the 14.7 meV peak integrated intensities are very similar, within the margins of error, with the uncertainty margin in the area under the rotor resulting from the lower count statistics on the lower-intensity rotor line. The existence of these two peaks and their similarity indicates that the same phenomenon is behind these results. These results indicate that orthohydrogen and parahydrogen are both densifying in the pores, resulting in solid-like phase for the adsorbed hydrogen.

This defies current understanding of hydrogen adsorption and also impacts on our methodology for estimating absolute isotherms from experimental data. Whereas in our former methodology, the excess plus the bulk in the pore would be the absolute isotherm and the total quantity of adsorbate in the pore, now a more immobilised adsorbate layer with a solid-like density of hydrogen has to be considered for modelling purposes. Excess data for the TE7 at the same temperature of the INS experiment was modelled using a further development of the methodology, which distinguishes between excess, absolute and total adsorption.

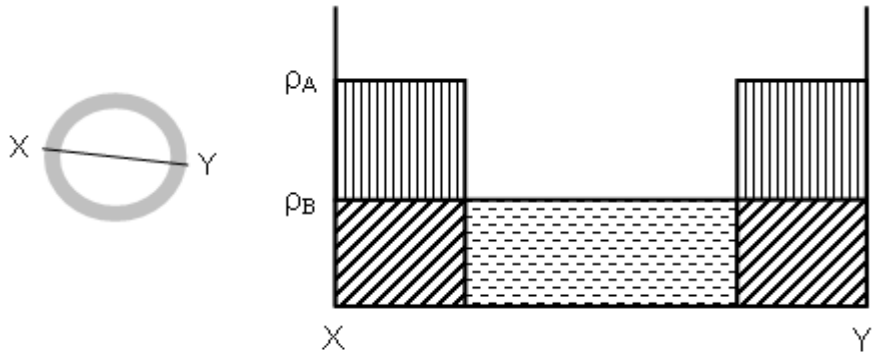

Figure 5.10 – Diagram distinguishing between excess, absolute and total adsorption in the pore. Left hand side figure is the cross-section (X-Y) of the pore. Right hand side is the density profile. The mass density of the adsorbate is ρ_A and the mass density of the bulk adsorptive is ρ_B. The sum of areas with vertical lines correspond to the excess, the sum of areas with vertical and diagonal lines correspond to the absolute and the sum of areas with vertical, diagonal and horizontal dashed lines correspond to the total.

In this new methodology, the absolute isotherm is the amount of densified H_2 in the pore and this quantity plus the bulk quantity of gas within the pore represents the total isotherm. In the modelling, the adsorbed phase density was considered constant and a parameter from the fit and an adsorbate volume was also introduced, which is the fraction of the pore volume that is occupied by the adsorbed layer. The adsorbed layer, which is the absolute isotherm, represents the area in which the density in the pore differs significantly from the bulk. The mechanism of accumulation of solid-like hydrogen was modelled as a fractional filling of the adsorbed layer in the pore, which was modelled using a type I equation. This corresponds to the filling of the pore by the adsorbed volume in relation to the pore volume.

$$\theta = \frac{V_A}{V_P} \qquad \text{Eq.5.5}$$

The excess, absolute and total are represented in Eqs.5.6, 5.7 and 5.8, respectively.

$$m_E = (\rho_A - \rho_B)\theta_A V_P \qquad \text{Eq.5.6}$$

$$m_A = \rho_A \theta_A V_P \Leftrightarrow m_E + \rho_B \theta_A V_P \qquad \text{Eq.5.7}$$

$$m_P = \rho_A \theta_A V_P + \rho_B V_P (1 - \theta_A) \Leftrightarrow m_E + \rho_B V_P \qquad \text{Eq.5.8}$$

For all the equations, m_E, m_A and m_P are the excess, absolute and total amounts in wt.%. The densities ρ_A and ρ_B are the adsorbed and bulk density, respectively, both in kg m^{-3}. The fractional filling is unitless and it is modelled using a type I equation. The adsorbed volume V_A and the pore volume V_P are in units of cm^3 g^{-1}. As shown previously, the excess experimental data is fitted using Eq.5.6, with the rational function approximation for the Leachman's EOS used to quantify the density of bulk hydrogen. The parameters are given initial estimates and iterated until their χ^2_{red} no longer changes. Once the parameters are determined, the absolute and total isotherm can be estimated using Eqs.5.7 and 5.8.

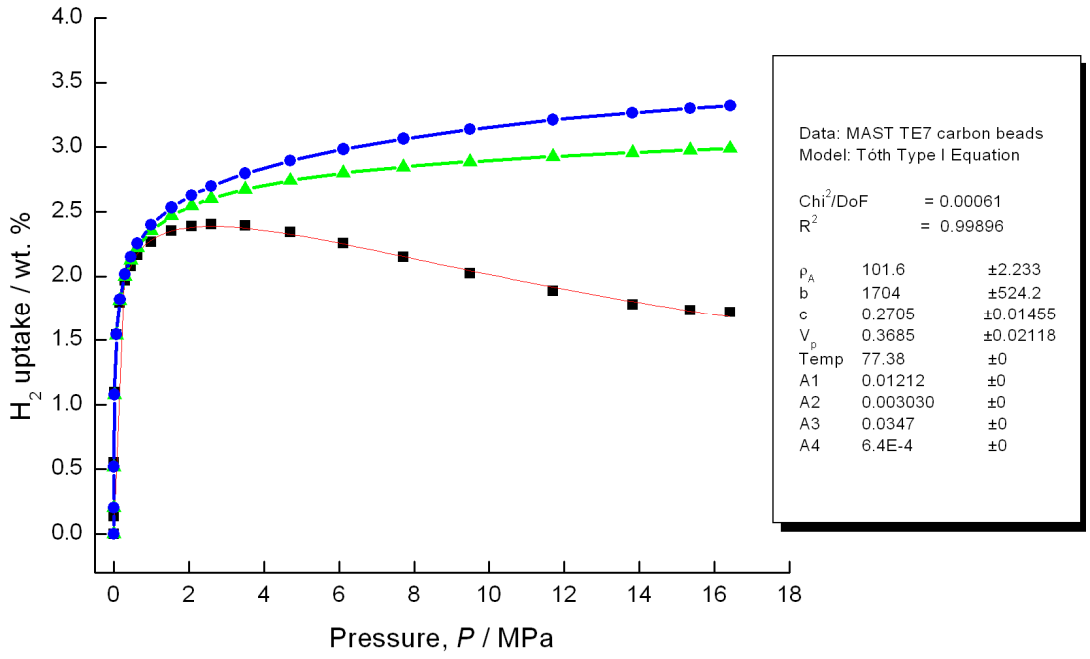

Figure 5.11 – Excess experimental sorption data for the TE7 up to 17 MPa at 77 K fitted using the new methodology, with the Tóth as the type I isotherm. The black squares are the excess experimental data, the red line is the fitted excess using Eq.5.6, the green line and triangles are the calculated absolute isotherm using Eq.5.7 and the blue line and circles are the total isotherm.

The fitting of the excess data for the TE7 carbon beads at the same temperature of the experiment and up to 17 MPa using the Tóth as the type I isotherm yielded some interesting results. In Fig.5.11, the *Chi²/DoF* is the reduced Chi-square, the R^2 is the coefficient of determination, ρ_A is the adsorbed phase density in kg m^{-3}, *b* and c are the affinity factor (in MPa^{-1}) and heterogeneity parameter (unitless) for the Tóth equation, respectively, V_P is the pore volume in cm^3 g^{-1}, *Temp* is the absolute

temperature in K and A_n are the parameters for the rational function to the Leachman's equation of state. The adsorbed density ρ_A, which is assumed constant and comes from the fitting as a parameter, has a value of 101.6 kg m^{-3}, a value which is well in excess of the maximum density of liquid H_2, which is 77.01 kg m^{-3} at the triple point (solid-liquid-vapour) of 13.96 K and 0.00736 MPa [64] and also higher than the solid density of parahydrogen at 4 K and zero pressure, which is 87.08 kg m^{-3} [251]. The application of the new methodology further suggests the solid-like density assumption, because when assuming a constant adsorbate density and an adsorbed volume different than the pore volume, the estimation of density from the model is higher than solid hydrogen density at 0 MPa and 4 K.

To study the pressure dependence of the solid-like accumulation and compare it to the sorption experimental results, the parameters from the fit to the excess data were used to estimate the absolute isotherm, which according to our model represents the adsorbate layer with a higher density than the bulk quantity. The absolute isotherm was estimated using Eq.5.7 and the INS integrated elastic region in Fig.5.9 was used, because it had better count statistics than the area under the rotor peak. The INS data has the intensity of signal estimated in arbitrary units normalised to neutron counts, so it was scaled using the methodology already exemplified for the scaling of the NMR data for the PEEK carbons. Every point in the INS integrated elastic line was scaled to a point in the absolute isotherm and the one with the lowest SRSR was used to illustrate the correlation.

As indicated in Fig.5.12, the INS integrated elastic line strongly correlates with the estimated absolute isotherm, which represents the quantity in the pore which has a higher density than the bulk. Furthermore, the density estimated from the use of the model is well within the solid range and higher than the density of solid hydrogen at 4 K and 0 MPa. The plateau region in the INS spectra might indicate that this accumulation of solid-like hydrogen in the pores has an upper limit, much as it would be expected from a microporous material.

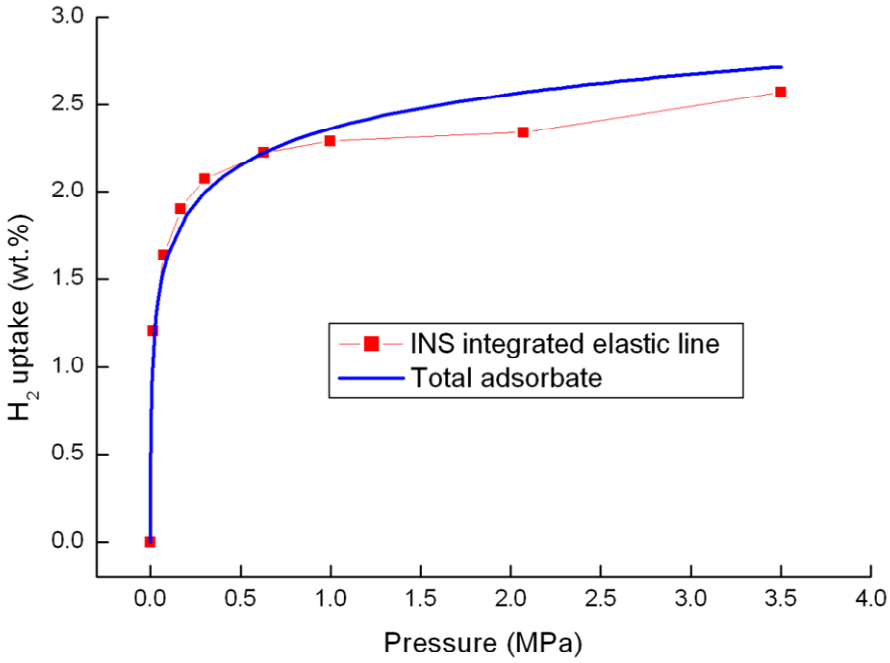

Figure 5.12 – Absolute isotherm estimated from experimental data and the integrated elastic line from the forward detector scaled to the point in the absolute isotherm corresponding to the lowest SRSR.

The two features in the INS spectra of the peak at 14.7 meV and the broad sharp peak in the elastic region; the fact that the integration beneath both curves shows a behaviour that is much compatible with sorption measurements for hydrogen at the same temperature; the constant adsorbate density from the model that estimates higher than solid hydrogen for the adsorbed phase; and the correlation of the elastic region with the absolute isotherm all provide persuasive evidence that the adsorbed hydrogen is indeed in a solid-like phase and that this bulk accumulation of solid is the mechanism for hydrogen adsorption in a microporous material with optimum pore sizes. The TE7 beads have modal pore size diameter of 0.7 nm, which is believed to be the optimal pore size for H_2 interactions [89, 93, 95] and the INS and modelling results indicate that hydrogen is solid-like when confined in those small nanopores.

The solid-like density of adsorbed hydrogen has been reported before [284, 293, 294], but it was ascribed to specific adsorption sites, which had a higher strength of interaction and were believed to immobilise the hydrogen adsorbed on those particular sites. This was observed in unsaturated metal centres in MOFs. In zeolites, this peak was also observed, but it showed an energy shift due to the adsorption of hydrogen on strong sites in the zeolite [278, 295]. In activated carbons, which have limited

interactions with hydrogen molecules, this effect was not seen before and it is most likely due to the confinement of the adsorbed hydrogen in optimally sized pores. This is in line with previous studies in literature, which reported higher densities of hydrogen in microporous adsorbents with small pores. These observations were made experimentally and computationally [194, 296-298].

5.3.4. Conclusions

In this chapter, an experimental validation of the model proposed in this thesis is presented. NMR spectroscopy and INS are presented as powerful experimental techniques used for a range of subjects in science and each technique and its applications are briefly reviewed. Previous experiments in hydrogen storage materials are also discussed and a novel way to use both techniques to quantify adsorbate quantities is introduced. This quantification could provide validation of the absolute isotherms estimated using experimental excess sorption data, which is used for the analysis presented in this thesis.

NMR spectroscopy analysis was carried on our standard material, the TE7 carbon beads. The results were inconclusive, because the behaviour displayed by the NMR estimated absolute isotherm was not compatible with a type I behaviour, expected from the adsorption of hydrogen in a microporous carbon. Previous data from the PEEK carbons was used to correlate with the experimental measurements done at Bath. The results from the comparison of the PEEK carbons were more encouraging, since the estimated absolute from the NMR showed behaviour more in line with adsorption for this system. The “template method” previously reported for the mass quantification of the absolute isotherm was, on the other hand, difficult to conciliate with our estimated absolute isotherms. A qualitative comparison, in which the isotherms were scaled to our absolute isotherm showed better correlation, indicating that, while the NMR method might be measuring the adsorbate in the pore, the “template method” needs refinement, which could be provided with more comparisons to experimental sorption data and computer simulations.

INS results provided strong experimental evidence for a new paradigm in hydrogen storage in porous materials, since, when using appropriate pore sizes, hydrogen can be immobilised in the pores and display solid-like behaviour. This complements some results already shown for modelling and simulation of adsorbed phases, in which the density of hydrogen can be in the liquid and perhaps even in the solid range. Design of materials with high-surface areas and with pores that provide for high-liquid range or solid-like densities for hydrogen could provide a very competitive storage solution in comparison with other methods already in use. Our methodology was developed to accommodate this new insight and a model designed to distinguish between excess, absolute and total was devised to fit to experimental data. This model further supported the evidence already shown by the INS measurements, yielding an adsorbate density which is higher than solid density of parahydrogen at 4 K and 0 MPa. The INS elastic line, which has arbitrary units for intensity, was correlated with this model, showing very good correspondence.

The novel way in which both experimental techniques were used was just a first step in the use of the two approaches for estimating quantities for adsorbed hydrogen. Our results provided some evidence that the NMR actually measures the adsorbed phase but the methods need to be further developed. There is very little literature available for hydrogen adsorption on a porous material studied by NMR. More studies should be done using this technique, which can then be coupled with INS measurements and experimental sorption data. INS studies, at the pressures and temperatures of a sorption experiment for hydrogen are also, to our knowledge, non-existent, so we hope proper dissemination of these results will encourage other researchers to use INS and NMR and then compare the results to experimental excess sorption data. Computer simulations are a very active field of research for adsorption of hydrogen in a porous material, mainly Grand Canonical Monte Carlo (GCMC) simulations for adsorbed phases, which are used to study hydrogen uptakes by different materials. The importance of GCMC and their widespread use for hydrogen adsorption studies require that GCMC simulations are benchmarked against our methodology. GCMC simulations for hydrogen adsorption and a comparison to our methods are the subject of the next chapter.

Chapter Six

Validation of the Methodology Using Computational Techniques

6. Validation of the Methodology using Computational Techniques

6.1. Introduction

Computer simulations are ubiquitous in science, and are present in diverse areas from meteorology to genetics. They have been widely used in chemistry and physics for the study of liquids, gases and solids and they are a favoured tool in materials science, where they are used to study materials' characteristics and behaviour. Computer simulations can predict the behaviour of single or many atoms and molecules, and they can aid in the elucidation of the macroscopic properties exhibited by those systems.

Hydrogen storage in porous materials has been studied using computer simulations. Of interest to this work are equilibrium simulations for adsorbed phases that predict uptakes by purely computational methods, since they can be compared with the methodology proposed in this thesis. This chapter introduces the background for the computer simulations and presents computational and experimental results obtained for silicalite-1. The simulations were done using four different assumptions, which yielded four different sets of results. The assumptions were accounting for quantum effects on hydrogen adsorption and molecular hydrogen simulated using a united atom and a two-centre model. The high-pressure excess hydrogen experimental results were obtained and further treated to estimate absolute quantities, using the conventional methodology and the development of the model that accounts for constant adsorbed density. The experimental and simulated results were then compared to assess the validity of the methodology and of the assumptions present in the computer simulations.

6.2. Molecular simulations for hydrogen storage

There are many different types of molecular simulations that can be applied to predict the behaviour of molecules. The methods usually differ on what properties are to be

studied, and, for instance, molecular dynamics methods are used primarily to study diffusion or mechanics of molecules. One of the main advantages of molecular simulations is that, with a small number of parameters that are input into the simulation, a great variety of properties can be analysed. They are a useful tool for studying properties of many-body systems, with the drawback that not all properties can be measured directly in a simulation [299]. This means that sometimes, the information calculated by simulations cannot be directly related to experimental results [299]. Experiments usually measure an average property, averaged over a large number of particles, within an averaged time of measurement. For computer simulations, if the goal is to compare with experimental results, there is the need to know what averages are to be computed. Statistical mechanics relates simulations in a small number of atoms or molecules with macroscopic observables. For simulation of equilibrium phases, Grand Canonical Monte Carlo (GCMC) methods are usually used, as will be explained next.

6.2.1. Grand Canonical Monte Carlo - basics

To relate computer simulations with experiments, the language of statistical mechanics needs to be introduced. Statistical mechanics is a discipline in molecular science which aims to relate the microscopic behaviour of atoms and molecules with observed macroscopic variables using statistical methods [300]. Computer simulations simulate the behaviour of a small group of atoms or particles and then extrapolate that behaviour to observable quantities in experiments, so statistical mechanics are the keystone of molecular simulations. Due to the size of the whole discipline of statistical mechanics, a thorough review and discussion of the field is inappropriate for the scope of this thesis. Instead, a brief overview of statistical mechanics and its applications to molecular simulations, especially to Monte Carlo methods, are presented in the next pages.

Statistical mechanics are used to relate observable macroscopic properties of systems with microscopic properties of individual atoms. In statistical mechanics, to calculate thermodynamic properties, the value of the mechanical properties in each and every quantum state that is compatible with the few parameters necessary to specify the

system in a macroscopic sense needs to be calculated [300]. The average of these properties is taken, giving each different quantum state the same weight. The postulate is that the average of mechanical properties calculated for each single quantum state will correspond to a parallel thermodynamic macroscopic observable [300].

One way of interpreting statistical mechanics is to think of the systems as ensembles, as introduced by J.W. Gibbs. An ensemble is a virtual collection of a very large number of systems, each constructed to be a replica on a thermodynamic macroscopic level of the particular thermodynamic system of interest [300]. If the system is assumed to have a number of molecules N, energy E and volume V, the number of quantum states that obey these conditions can be calculated. While the systems are identical in the thermodynamic point of view, they are not identical in the molecular level [300]. In statistical mechanics, the principle of equal *a priori* probability is applied, which states that each and every one of the different quantum states that obey the conditions is represented an equal number of times in the ensemble [300]. It follows that the ensemble average of a mechanical property can be related to the corresponding thermodynamic property. To relate mechanical properties with measurable thermodynamic variables, the energy distribution is necessary [300]. The Boltzmann distribution (or Gibbs distribution) is the distribution function that relates the equilibrium occupation probability p in a state i [301]:

$$p_i = \frac{\exp\left(-E_i/(k_b T)\right)}{Z(T)} \qquad \text{Eq.6.1}$$

In equation 6.1, the equilibrium occupation probability of a state i is p_i, E_i is the energy of state i, k_b is Boltzmann's constant (1.38×10^{-23} J K^{-1}) and T is temperature [301]. The partition function $Z(T)$ is a function of temperature and it describes the statistical properties of a system in thermodynamic equilibrium [301]. The distribution of an assembly of identical systems over the possible states in which the system can find itself, given that the energy of the assembly is a constant E is perhaps the central problem in statistical mechanics [300] and for each different ensemble, there is a corresponding partition function. The ensembles are named according to the variables that are kept constant and the N, E and V ensemble is called the microcanonical

ensemble. The most common ensemble in statistical mechanics is the canonical ensemble, which has N, V and T fixed [300, 301].

Another common ensemble is the Grand Canonical ensemble, which is specified by constant V, T and the chemical potential μ. The Grand Canonical ensemble is typically used for conditions of chemical equilibrium in an open system, since one of the prerequisites for chemical equilibrium is constant chemical potential. The partition function for the Grand Canonical ensemble is shown in Eq.6.2 [300].

$$Z(V,T,\mu) = \sum_{N}\sum_{j} \exp(-E_{Nj}(V)/k_bT \exp(\mu N/k_bT) \qquad \text{Eq.6.2}$$

To solve the partition functions, it is required that the equations are summed on a large number of quantum states, so a very large number of calculations are necessary to compute the averages. It is often not practical to do all the necessary calculations, so a computer simulation which could sample a small fraction of states in the system and get accurate estimates of the macroscopic quantities would be extremely useful [301]. The Monte Carlo method was developed precisely with this in mind. In Monte Carlo methods, instead of calculating the sum for all possible states, the states are sampled according to the Boltzmann probability distribution, in what is called importance sampling [301]. Instead of summing all quantum states, only the states that are believed to impact more the sum of the integral are taken into account. Another important issue in Grand Canonical Monte Carlo simulations (GCMC) is to create a random chain of states, which are independent of the previous states. For this, a Markov chain of states needs to be generated in which new states are created randomly, which are independent of all previous states except for the one immediately before [301]. The Markov process generates new states according to a transition probability and, if run for long enough, it will generate a succession of states which appear with the probabilities given by the Boltzmann distribution [301]. Another thing to specify in Monte Carlo simulations is the acceptance ratios. The acceptance ratio stipulates a percentage of acceptances for randomly generated states after an initial given state, which should be accepted a fraction of the time by the algorithm. [301].

The Metropolis algorithm is perhaps the most used and famous algorithm for Monte Carlo simulations and it was proposed by Nicholas Metropolis and Stanislaw Ulam in 1949 [301, 302]. The Metropolis algorithm requires the input of the transition probabilities and of acceptance ratios. The additional feature of the Metropolis algorithm is that, when new states are generated, their energies are compared with the energies of the current state. If the energy of the newly generated state is lower than that of the current, the transition to that state should always be accepted [301]. In the Metropolis algorithm applied to molecular simulation, there are trial moves to generate new states for the system. For GCMC simulations, since the number of molecules of the system can change, as opposed to temperature, volume and chemical potential, which remain constant, the trial moves can be a random translation, change of orientation, insertion or deletion of a molecule. If any trial move minimises the energy of the system, then the move is accepted and the system changes to this new state. The Metropolis algorithm is used to solve the Grand Canonical ensemble and estimate the partition function and energy distribution that obeys the macroscopic requirements of the system. For a given system, which operates at constant V, T and chemical potential μ, a computer simulation generates a succession of states, which are accepted or rejected depending on the variation of energy. After enough states have been simulated and if no change is observed, the system is at equilibrium and the number of molecules in the simulation cell is recorded, as it corresponds to the equilibrium number of molecules that obeys the requirements.

6.2.2. GCMC for hydrogen adsorption

GCMC has been used extensively for hydrogen adsorption in porous materials [303-308]. The Grand Canonical ensemble can be used for studying adsorption, since it can estimate uptakes at a given pressure and temperature. The ensemble has a fixed V, T and μ and can vary the number of molecules in the system, which means that it is an appropriate representation of adsorption in a porous material. In an adsorption experiment, the isotherm is obtained when the system equilibrates at a fixed volume and temperature, so T, V and chemical potential μ are constant. Once the system equilibrates at these conditions, the excess adsorbed molecules are calculated.

GCMC computer simulations are usually set out in the following way – a simulation cell, which is usually one or more unit cells of the adsorbent are input into the programming code or software. This simulation cell is supposed to mimic the atomic structure of the adsorbent, so simulations are more easily done on crystalline materials. For amorphous materials, such as activated carbons, some assumptions on the atomic structure of the pores have to be done to simulate uptakes. In most GCMC experiments, the simulation cell is set up in periodic boundary conditions, which means that it is an infinite periodic lattice of identical cells. These conditions mean that the simulation is done on an infinite, perfect crystal. For crystalline materials, the crystallographic coordinates are used as a description of the framework of the material [305]. The adsorptive species are modelled in different ways, depending on their nature. In some cases, the adsorptive is modelled using an united-atom approach, in which the species has a simpler geometrical representation, for instance, methane is modelled as a single sphere [305].

Along with the definition of the unit cell, the intermolecular potentials are also described *a priori*, and they define the potential energies for the system. For GCMC simulations, van der Waals and Coulombic interactions are typically taken into account, with the former usually modelled using Lennard-Jones (LJ) potentials. The LJ potential is an intermolecular potential [309], defined as a function of the intermolecular separation and shown in Eq. 6.3 [306].

$$u_{LJ}(r) = 4\varepsilon\left[\left(\frac{\sigma}{r}\right)^{12} - \left(\frac{\sigma}{r}\right)^{6}\right] \qquad \text{Eq.6.3}$$

The potential energy u_{LJ} as a function of the intermolecular separation distance r is defined using the potential well depth of interaction ε (where the attractive force is at its maximum) and the collision diameter σ (where the potential u_{LJ} is equal to zero). The r^{-12} represents the intermolecular repulsive forces and the r^{-6} represents the attractive forces. Force fields are used to describe the energetic interaction between the adsorbent and the adsorbate. LJ parameters for individual atoms are usually taken from generic force fields, usually UFF [310] and DREIDING [311] which contain parameters for most of the elements in the periodic table. The values taken from the

force fields are ε and σ for a specific element. The LJ potential is short-ranged, meaning that the interactions are negligible after a certain distance, so a cut-off radius is introduced in the simulation to reduce the interactions that are calculated. Coulombic interactions, when present, are calculated using quantum chemistry methods and then input in the simulation [305].

To simulate the interaction between the adsorptive and the adsorbent material, the potentials for the atoms in the adsorbent and the adsorptive taken from the generic force field have to be mixed. The most common method for mixing the parameters is the Lorentz-Bertholot mixing rules, which involve standard geometric combination rules for the well depth as shown in Eq.6.4 and geometric mean combination rule for the distance, as shown in Eq. 6.5 [310].

$$\varepsilon_{ij} = \sqrt{\left(\varepsilon_i \varepsilon_j\right)} \qquad \text{Eq.6.4}$$

$$\sigma_{ij} = \frac{1}{2}\left(\sigma_i + \sigma_j\right) \qquad \text{Eq.6.5}$$

In a simulation insertion, deletion, translation and, depending on the simulation, orientation trial moves are done in the simulation cell of the material until equilibrium is reached at a certain pressure after a number of iterations. GCMC can therefore construct simulated isotherms for a given adsorptive in a specified material, simply by knowing its crystal structure and the force field LJ parameters. Computer simulations generate the total amount of adsorptive that is equilibrated in the material, so the output of the simulation is the absolute amount of adsorptive within the material, as opposed to experimental techniques, which yield the excess amount of adsorptive within the material. MOFs and other materials have been studied using GCMC methods and some of the most promising materials for hydrogen storage have been first designed *in silico* and then tested using GCMC. Good examples of using GCMC simulation to calculate uptakes in new materials are the MOFs NU-100 and MOF-210 [118, 119].

Hydrogen is an extremely light molecule and at very low temperatures, quantum effects cannot be ignored for the treatment of the hydrogen molecule [312]. One

approach to introduce the quantum effect in adsorption simulations has been to correct them using the Feynman-Hibbs (FH) path integral effective potential method [313-315]. The correction takes the following form, shown in Eq.6.6 [316].

$$u_{FH}(r) = \left(\frac{6\mu_m}{\pi\beta_T\hbar^2}\right)^{3/2} \int dRu\left(|r+R|\right) \times \exp\left(-\frac{6\mu_m}{\beta_T\hbar^2}R^2\right) \qquad \text{Eq.6.6}$$

In Eq.6.6, $U_{FH}(r)$ is the FH effective potential between a pair of molecules, $\hbar$ is the reduced Planck's constant ($h/2\pi$), μ_m is the reduced mass (m_1m_2/m_1+m_2), β_T is equal to the inverse of Boltzmann's constant k_b (1.38 x 10^{-23} J K^{-1}) multiplied by temperature (β_T = 1/ k_bT). This integral is computationally very hard to solve, so a Taylor expansion is usually done in $U(|r + R|)$ and truncated in either the quadratic [317] or fourth order term [318]. If truncated at the quadratic term, the approximate FH effective potential becomes Eq.6.7.

$$u_{FH}(r) = u(r) + \left(\frac{\beta_T\hbar^2}{24\mu_m}\right)\nabla^2 u(r) \qquad \text{Eq.6.7}$$

For LJ parameters, the Laplacian $\nabla^2 u(r)$ becomes Eq.6.8.

$$\nabla^2 u(r) = u''(r) + \frac{2}{r}u'(r) = 4\varepsilon\left(\frac{132\sigma^{12}}{r^{14}} - \frac{30\sigma^6}{r^8}\right) \qquad \text{Eq.6.8}$$

The FH effective potential corrects for quantum effects at low temperatures for low weight molecules. The quantum correction results in lower adsorption when compared to the classical system [319].

6.3. Silicalite-1: a case study

For the purpose of this thesis, the proposed methodology to analyse excess experimental data needs to be compared with computational methods. GCMC

simulations for adsorption yield the absolute amount adsorbed for a material, which is compared with the quantities obtained through the methodology on hydrogen excess isotherms for the same material. For this comparison, a rigid, simple system, which adsorbs moderate amounts of hydrogen, was used. A sample of silicalite-1 was sourced and tested for hydrogen sorption, with the purpose of comparing simulations done at the same operating conditions with absolute uptakes obtained when applying the models to experimental data.

6.3.1. GCMC simulations of hydrogen on silicalite-1

The GCMC simulations were done for hydrogen adsorption on silicalite-1 using different assumptions. The two-centred model and united atom approach were used to model the molecular hydrogen, and the FH effective potential was applied to account for quantum effects. The LJ potential was done to simulate isotherms without quantum effects, which resulted in four different sets of simulated results. The simulation results were compared to assess the different assumptions and then compared with experimental results. An important issue when comparing simulated results with experimental ones is that the simulations are done on a perfect, infinite and pure crystal. Experimental samples are neither pure nor perfect materials, which precludes a straightforward comparison. It is reasonable to expect some differences between simulated values and experimental ones, even when measuring the same property at the same conditions.

Silicalite-1 was first reported in 1978 [320] and it consists of a polymorph of silicon dioxide (SiO_2). The framework structure is classified as MFI (Morderite Inverted Framework), similar to zeolite ZSM-5, with an orthorhombic crystallite shape. Silicalite-1 is a pure silica oxide framework, with a hydrophobic structure that can act as a molecular sieve [320]. Silicalite-1 has been extensively studied, experimentally and computationally, for gas separations, contaminant removal or gas storage [321].

GCMC simulations were carried out using the MUSIC (Multipurpose Simulation Code) code developed by Professor Randall Snurr and his group at Northwestern University, USA [322]. MUSIC has been used extensively for the simulation of

hydrogen uptakes in MOFs [323-326]. The GCMC simulations were done in the Aquila High-Performance Computer at the University of Bath. For all the simulations, Coulombic interactions were ignored and non-Coulombic interactions were modelled using LJ parameters, with the simulations accounting for the quantum effects done using the FH path integral effective potential. The simulations were done on an atomistic model, in which molecular hydrogen is modelled using two LJ spheres (two-centre model) and a united-atom model, in which molecular hydrogen is modelled as one LJ sphere. In the two-centre model, the hydrogen atoms are separated by 0.74 Å [327].

The GCMC method was used for the simulations, as implemented in the MUSIC code. Random insertion, deletion and translational moves were done, all with the same weight and for the two-centre model, a rotational move was included with the same weight as the remaining moves. For every simulation, a potential map was created first which stores the potential energy of interaction between the sorbate and the sorbent in a grid, with a spacing of 0.1 Å. MUSIC runs a potential map prior to running the GCMC simulation to save computational time, as during the GCMC simulation it interpolates the potentials between grid points. Both the potential map and the simulations were done using a simulation cell which had dimensions of 2 unit cells in the *x*, *y* and *z* directions. The potential map and GCMC simulations were done using 2 x 10^6 iterations, with the steps on the GCMC simulations including random insertion, deletion, translation and rotation (when using the two-centre model) moves. To calculate the uptakes at simulated pressure points and to convert from ideal to real gas, the pressures were converted to fugacities using the Peng-Robinson equation of state [328]. The interactions above 17 Å were ignored and the molecule-molecule interactions for silicon and oxygen were taken from the UFF generic force field [310]. Hydrogen molecule parameters for the two-centred and united atom model were taken from Rossin et al. [307] and from Darkrim et al. [327] respectively.

There were 26 pressure points used in the simulations, between 0.1 and 40 MPa. The conversion from molecules *per* unit cell to wt. % was done using the following molecular weights:

M(silicalite-1) = 11,536.19 g mol^{-1}

M(H_2) = 2.01588 g mol^{-1}

The isotherms were calculated at 77, 90, 100, 120, 150 and 200 K. The molecule-molecule interaction parameters for the united atom model and the two-centre model taken from UFF [310], Rossin et al. [307] and Darkrim et al. [327] and mixed according to the Lorenz-Berthelot rules are shown in Table 6.2 and Table 6.1, respectively.

Table 6.1 – Molecule-molecule parameters for the LJ united atom model simulation.

	σ Å	ε / k_B K	Reference
H-H	2.958	36.700	[327]
H-Si	3.392	86.164	[310, 327]
H-O	3.038	33.288	[310, 327]

Table 6.2 - Molecule-molecule parameters for the LJ two-centred model simulation.

	σ Å	ε / k_B K	Reference
H-H	2.720	10.000	[307]
H-Si	3.273	44.977	[307, 310]
H-O	2.919	17.376	[307, 310]

The results from the simulations using the LJ potentials and the united atom and two-centre model are shown in Figure 6.1 and Figure 6.2. The results are broadly in line with what was expected from hydrogen adsorption in a microporous material at the tested temperatures. The absolute adsorption, which is output from the simulation, monotonically approaches an asymptote for every temperature.

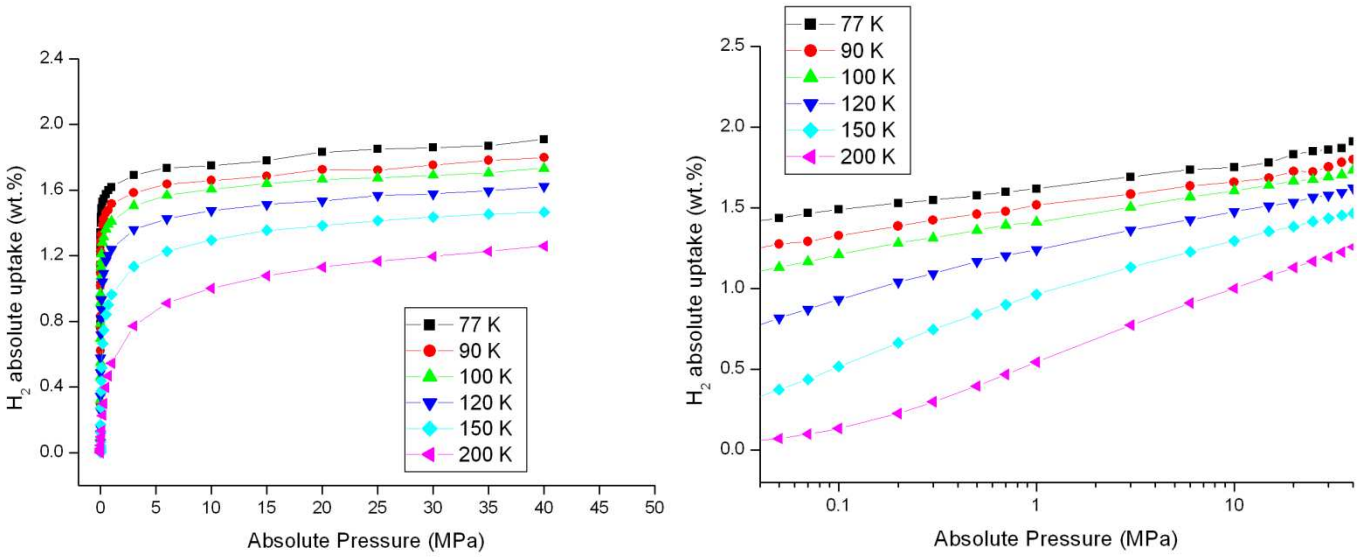

Figure 6.1 - GCMC simulations on silicalite-1 using the united-atom model with LJ parameters for a range of temperatures. The absolute hydrogen uptake is shown in weight percent. Right-hand side plot is the same data plotted in a logarithmic (log_{10}) scale.

In Figure 6.1, the isotherms in the 77 to 200 K range for the silicalite-1 using LJ parameters and united atom model as a representation of the molecular hydrogen. The uptakes were converted to weight percent using the crystalline density of silicalite-1 (1.797 g cm^{-3}) and both molar masses of silicalite-1 and molecular hydrogen.

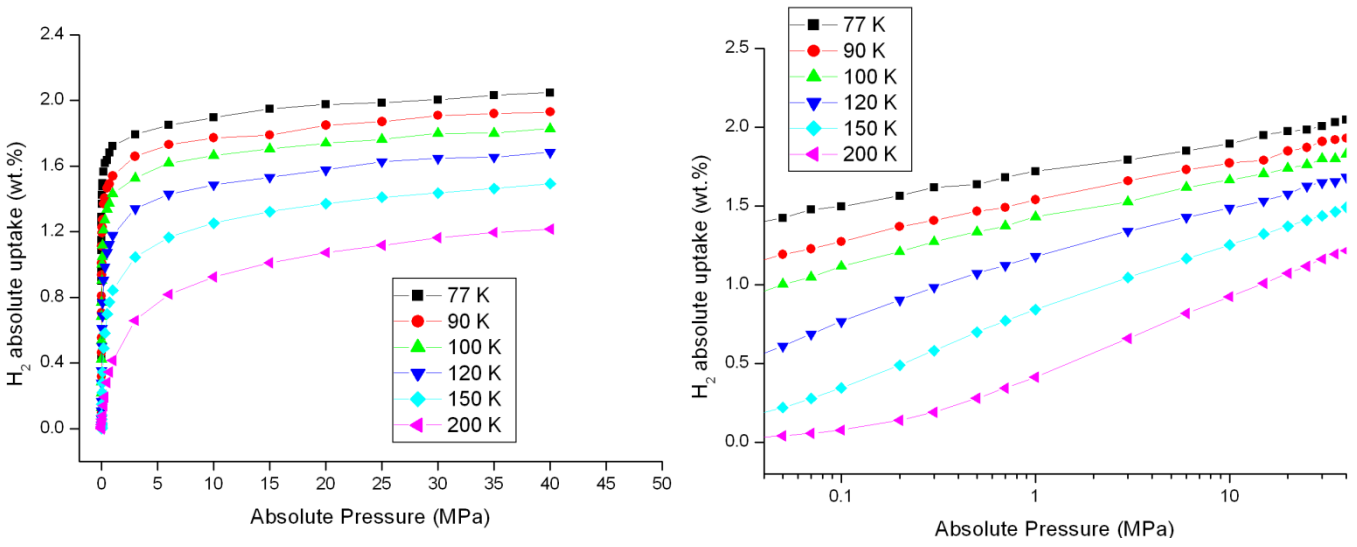

Figure 6.2 - GCMC simulations on silicalite-1 using the two-centre model with LJ parameters for a range of temperatures. The absolute hydrogen uptake is shown in weight percent. Right-hand side plot is the same data plotted in a logarithmic (log_{10}) scale.

In Figure 6.2, the absolute uptake using LJ potentials and the two-centre model for the silicalite-1 for temperatures ranging from 77 to 200 K is plotted. Experimental reports

for hydrogen uptake for ZSM-5, which has a silicon to aluminium ratio of 140, so also an MFI structure but not purely siliceous [329], are of 0.75 wt. % at 77 K and 0.1 MPa. Elsewhere, an excess experimental hydrogen uptake of 0.73 wt. % was observed for silicalite-1 at 77 K and 0.092 MPa [330]. GCMC simulations on silicalite-1 show 1.2 wt. % at 77 K and 1 MPa [331]. The results presented here for both the united atom and two-centre model are higher than those reported for both experiments and simulations.

As it is acknowledged in literature [317, 332, 333], there are differences, especially at low temperatures, if quantum corrections are included, due to the low molecular weight of hydrogen. A good way to include quantum effects is to use FH effective potential, as already discussed in this chapter. GCMC simulations were done using the FH potential, at the same temperatures and for the same pressure points as with the LJ potentials. The parameters are the same as shown in Table 6.1 and Table 6.2 for the united atom and two-centre model. The results for the united atom model are shown in Figure 6.3.

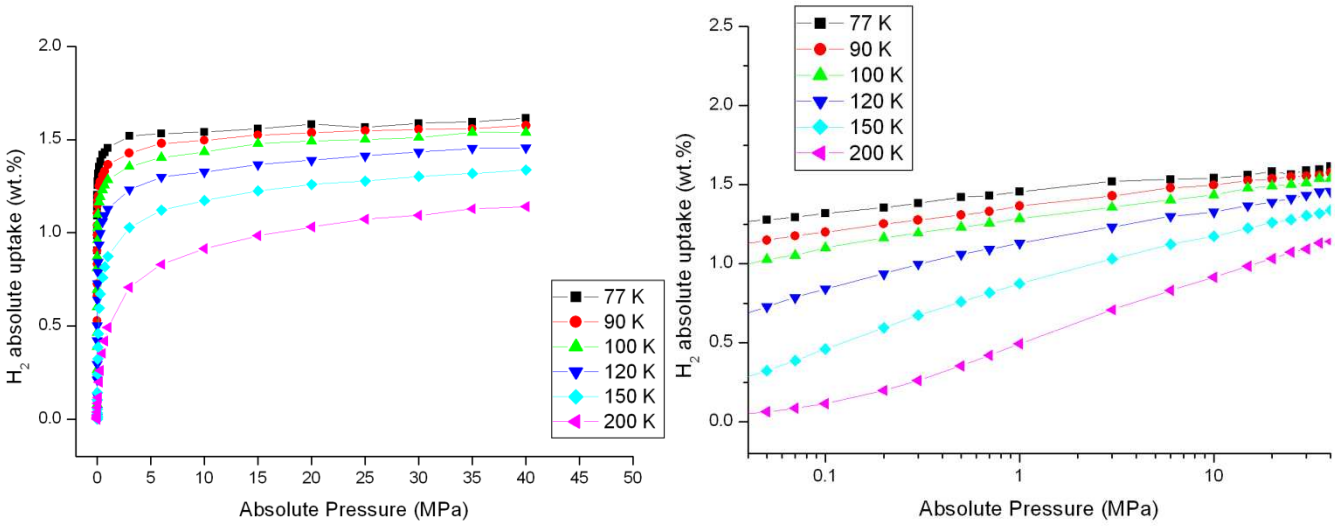

Figure 6.3 - GCMC simulations on silicalite using the united-atom model and the FH potential for a range of temperatures. The absolute hydrogen uptake is shown in weight percent. Right-hand side plot is the same data plotted in a logarithmic (log_{10}) scale.

The FH potential was also used to estimate the uptakes for the two-centre model. The results for the simulation with the FH potential and the two-centre model are presented in Figure 6.4.

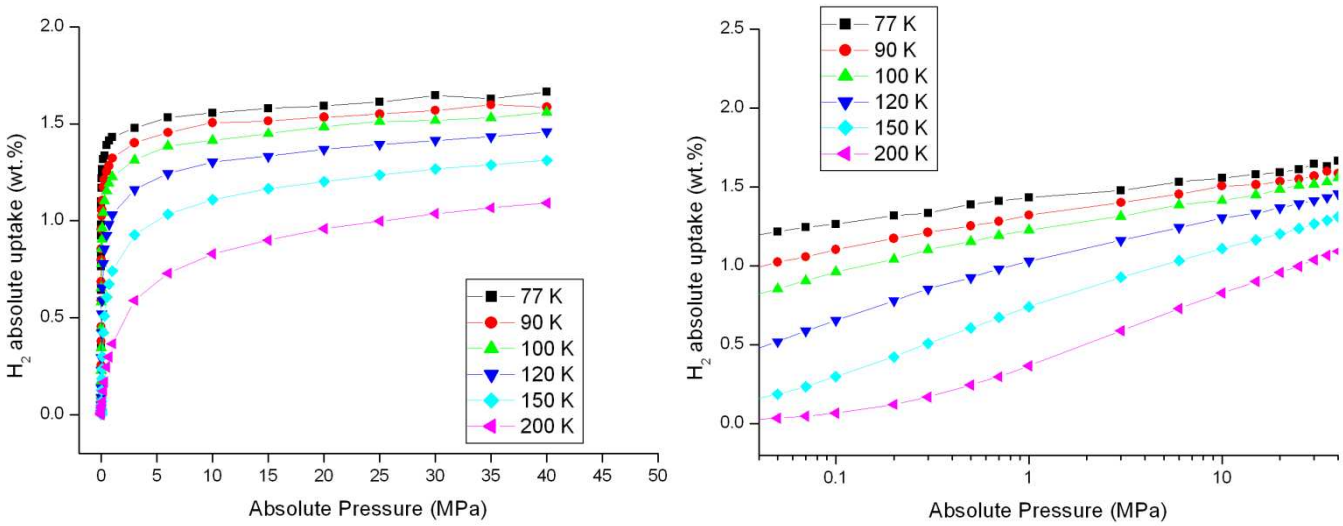

Figure 6.4 - GCMC simulations on silicalite using the two-centre model and the FH potential for a range of temperatures. The absolute hydrogen uptake is shown in weight percent. Right-hand side plot is the same data plotted in a logarithmic (log_{10}) scale.

There are some differences in the results for the LJ and FH potentials and for the united atom and two-centre model. In Figure 6.5, the 4 different sets of results are analysed at 77 K. As it can be seen from the figure, the LJ parameters exhibit higher uptakes, with a significant difference between the uptakes of the united atom and two-centre model. The FH potential results display lower uptakes, with the differences between the united atom and two-centre model not being very significant.

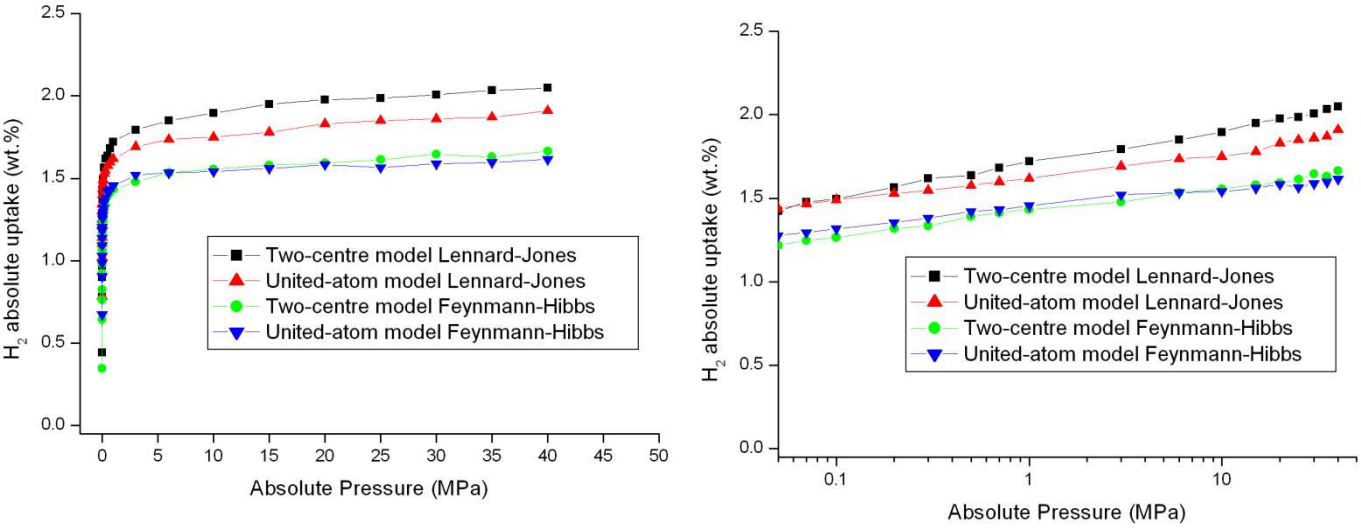

Figure 6.5 - Comparison of two-centre and united-atom model using LJ and FH potentials at 77 K. Right-hand side plot is the same data plotted in a logarithmic (log_{10}) scale.

In Figure 6.6, the same comparison is done for both the united atom and two-centre model using the LJ and FH potential at 200 K. As expected, the quantum effects correspond to lower uptakes, but these differences become less distinct the higher the temperature.

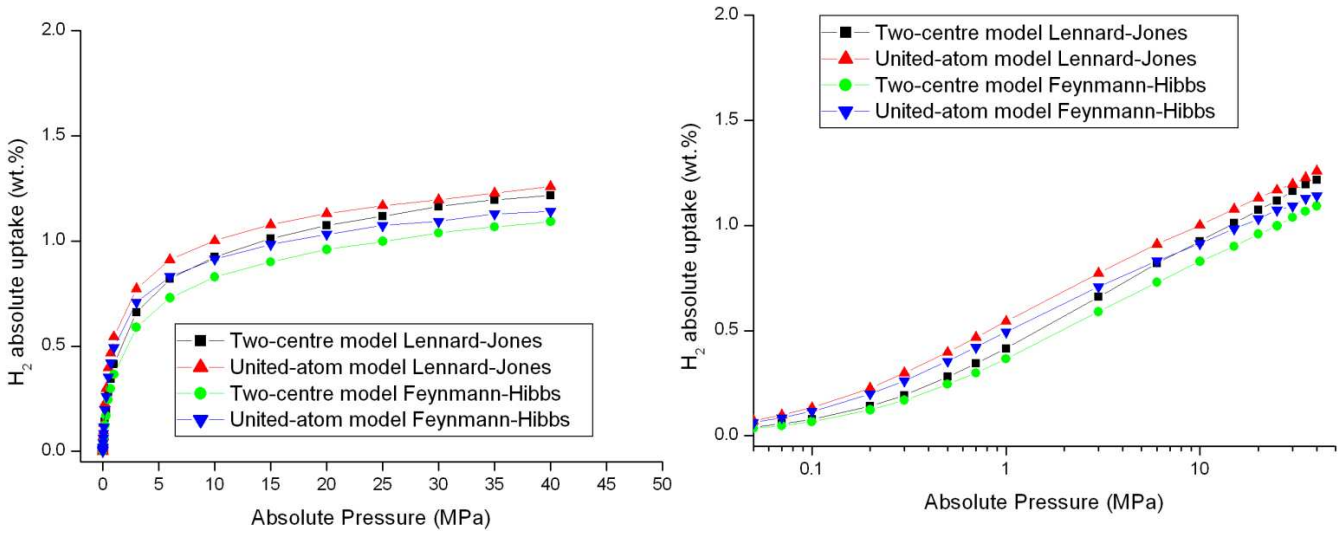

Figure 6.6 - Comparison of two-centre and united-atom model using LJ and FH potentials at 200 K. Right-hand side plot is the same data plotted in a logarithmic (log_{10}) scale.

It seems the quantum correction is more prevalent at lower temperatures, as it would be expected. The results also show that the choice of model (united-atom or two-centred) is more pronounced without the quantum correction, which means that the path-integral formalism actually blurs the differences between a two-centre and a united-atom approach. The uptakes calculated with the quantum correction are also smaller than the ones calculated without it. Interestingly, it also seems that the uptakes calculated with the two-centred model are higher at lower temperatures for both methods (Lennard-Jones and Feynmann-Hibbs), but with increasing temperatures the united-atom model uptakes begin to equal the two-centre model, and at 200 K, there is clearly a distinction, with the united-atom model's uptakes being slightly higher than the two-centre ones. This is more pronounced in the calculation without quantum effects.

The BET specific surface area was also simulated using computational methods. The BET simulated surface area was calculated using the crystallographic information and the accessible surface area code made available by Dr Tina Düren from the University

of Edinburgh [324, 334, 335]. The program uses a probe molecule rolling on the surface to estimate the accessible surface area and it has compared well with the experimental BET specific surface area determined using the consistency criteria in good samples [334]. The program was used with a probe molecule diameter of 3.681 Å, which is the reported value for the molecule diameter of diatomic nitrogen. The density of the crystal was determined using the crystallographic file and it was determined at 1.797 g cm^{-3}, which compares with the reported density of silicalite-1, which in the original report was 1.76 g cm^{-3} [320]. The BET accessible surface area was simulated with the code using 10,000 iterations. The accessible area was calculated as 480.74 m^2 g^{-1} using the crystallographic determined density, with the accessible surface area in $Å^2$ as 921.25 and the accessible surface area per volume as 863.88 m^2 cm^{-3}.

6.3.2. Experimental high-pressure hydrogen sorption results for silicalite-1 and comparison with GCMC simulations

Experimental hydrogen excess isotherms were obtained for a sample of silicalite-1 to compare with the simulated results. The silicalite-1 was obtained from Zeochem ® (Zeochem AG, Uetikon am See, Switzerland), characterised and tested for high-pressure hydrogen adsorption at the University of Bath. The technical specification sheet provided by Zeochem is in Additional Information G. The silicalite had traces of sodium, potassium, calcium, magnesium and iron and aluminium and had a SiO_2: Al_2O_3 ratio of 759:1.

The material was degassed at 350 ^oC for 8 hours prior to the measurement of the BET specific surface area. The BET specific surface area was measured in the ASAP 2020 (Micromeritics Instrument Corporation, Norcross, GA, USA) using the British Standard method, so in the 0.05 to 0.3 P / P_0 range. The excess hydrogen isotherms were collected as described in the Materials and Methods section for other materials, with a 6 hours degassing at 350 ^oC prior to sorption experiments. The excess hydrogen isotherms were collected at 77 K using the HTP-1 volumetric gas sorption analyser (Hiden Isochema, Warrington, UK), with high-purity hydrogen (Air Products BIP-Plus, 99.99996 % purity). An immersion reactor with liquid nitrogen was used to

maintain the temperature at 77 K, with the reactor and sample being fully immersed in the liquid nitrogen dewar. The skeletal density of the sample was measured at room temperature using a helium pycnometer (Micromeritics AccuPyc 1330, Micromeritics Instrument Corporation, Norcross, GA, USA).

The BET specific surface area was measured twice, and resulted in specific surface area values of 301.6 ± 4.5 and 282.6 ± 9.9 $m^2\ g^{-1}$, in which the error is the standard error of the measurements. The value calculated at Zeochem, using a Micromeritics ASAP 2000 ((Micromeritics Instrument Corporation, Norcross, GA, USA) and in the range 0.06 to 0.2 P / P_0 after degassing for 8 hours at 450 ^oC was 371 and 321 $m^2\ g^{-1}$ (see Technical Specifications sheet in Additional Information G). The density determined through the pycnometer after 10 runs and fitted using an exponential model was 2.35 $g\ cm^{-3}$.

The temperature was controlled at 77 K, with an average of 77.14 K for all the pressure points and a calculated standard deviation of 0.0069 K. The adsorptive compressibility was determined as reported in the Materials and Methods chapter and as published in Bimbo et al. [216] using a rational fit of compressibility data obtained using the Leachman's equation of state [64] available through the NIST website . The excess isotherm was fitted using both the proposed methodology and the development to include the constant adsorbed phase reported in the previous chapter (Chapter 5) of this thesis and the Tóth equation [224, 228]. The experimental excess isotherm for the silicalite-1 at 77 K and both the absolute determined using the methodology and the constant adsorbate density are shown in Figure 6.7.

Table 6.3 – Fitting parameters for the Tóth simple model and the Tóth with constant adsorbed density model to the Silicalite-1 experimental data.

	n_a^{max} wt.%	ρ_A kg m^{-3}	b MPa^{-1}	c -	v_A g cm^{-3}	R^2	X^2_{red}
Tóth simple model	1.36 ± 0.05	-	381 ± 104	0.35 ± 0.02	0.111 ± 0.005	0.99787	0.00013
Tóth with constant adsorbed density	-	110 ± 2	346 ± 84	0.36 ± 0.02	0.119 ± 0.006	0.99796	0.00012

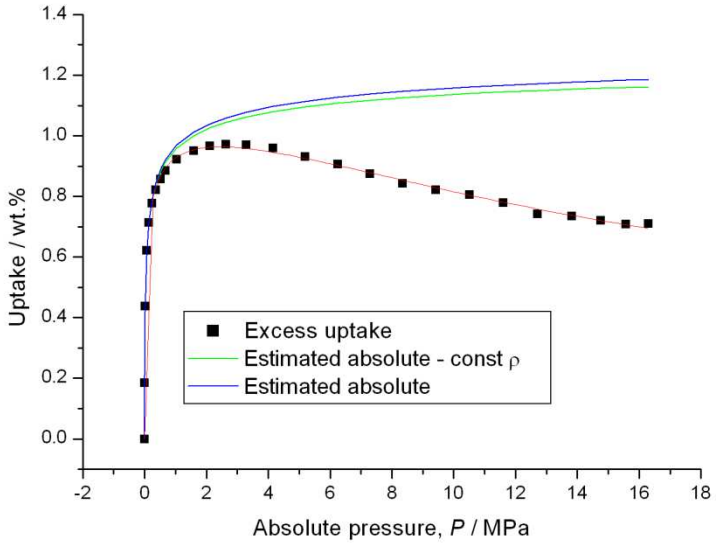

Figure 6.7 - Experimental excess hydrogen uptake for silicalite-1 and estimated absolute using the methodology and the constant density of the adsorbate. The Tóth was the equation used for both absolute estimates.

The results from the fit are shown in Table 6.3 with the errors corresponding to the errors calculated from the fitting and deduced from the Variance-Covariance matrix (Additional Information B).

The statistical differences between the two models are marginal, and it is interesting to note that both models predict a pore volume around 0.11 g cm^{-3}, which compares to the reported micropore volumes for silicalite-1 in the 0.176 and 0.199 cm g^{-1} range [320, 336-338]. The adsorbed H_2 density calculated from the model is 110.18 kg m^{-3}, which is higher than the solid parahydrogen density at 4 K and zero pressure of 87.08 kg m^{-3} [251]. This value can also be compared to the adsorbed density observed for the TE7 carbon beads, which was calculated at 101.6 kg m^{-3} in the previous chapter of this thesis.
The two estimated absolutes were compared with the four sets of simulated results and the outcome is Figure 6.8.

In Figure 6.8, the disparity between the excess hydrogen uptakes, the two absolute isotherms estimated using experimental data and the simulated isotherms can be

observed. It has also already been noted in this chapter that the uptakes predicted by simulation are far from others observed in experiments and simulations. One explanation for this difference could be the fact that simulations were carried out on a perfect, periodic crystal, which could mean that the uptakes would be different than those observed experimentally on imperfect (defective) samples. In addition, the calculated surface areas from the crystal file and experimental ones are also different, and so is the calculated crystal density (1.797 g cm^{-3}) and the experimentally obtained one (2.35 g cm^{-3}).

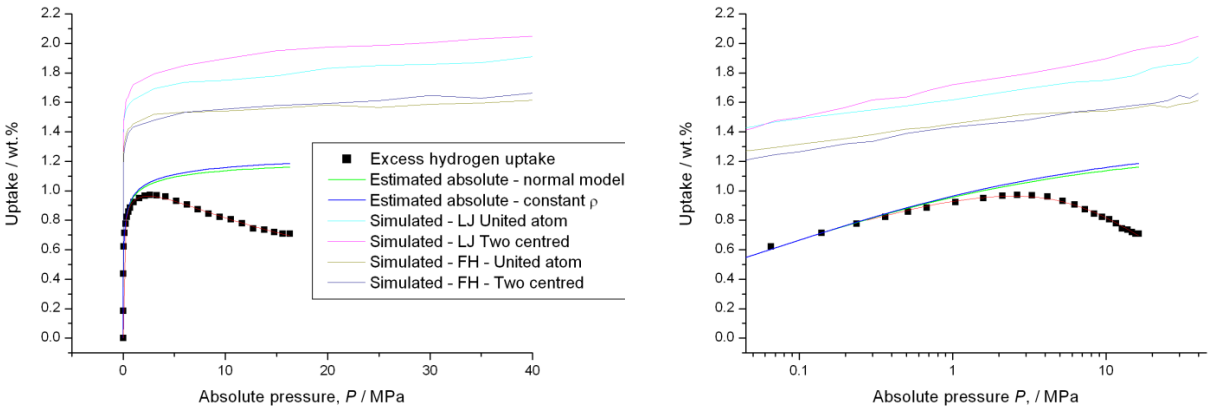

Figure 6.8 – Comparison between the estimated absolutes using the normal methodology and the constant adsorbed density and the simulated isotherms using the LJ and FH potentials and the two centred and united atom models. Right-hand side plot is the same data plotted in a logarithmic (log_{10}) scale. The caption is the same for both figures.

A straightforward comparison between the simulated isotherms and the experimental and modelled absolutes is not possible. Since the simulated isotherms show a higher uptake than reported elsewhere and from what is expected for a material with these characteristics, an alternative would be to correct the simulated isotherms. As observed, simulations are done on a perfect, pure, periodic crystal of the material, so a correction that could be done to account for the non-ideality of the sample could enable a comparison between the uptakes. The tested silicalite-1 sample, as it can be seen from the Technical Specifications sheet in Additional Information G has some impurities and is only 95 % crystalline.

The crystal density is obtained in a simple way with just the crystallographic coordinates and the experimental density is also measured in a simple way by using He pycnometry. Since they can easily be related to the singularities of the simulations

and experiment, respectively, they could provide a relation between the non-ideality of the sample and the perfectness of the simulation. If the density obtained from the crystal coordinates (1.797 g cm^{-3}) is divided by the density obtained for the experimental sample (2.35 g cm^{-3}), a factor of 0.765 is obtained. This factor can be applied to the simulated isotherms to correct them, enabling a comparison between the simulations and the experimental results. The corrected simulated isotherms, the excess hydrogen uptake and the absolute estimated from both the normal methodology and the constant adsorbed density development are presented in Figure 6.9.

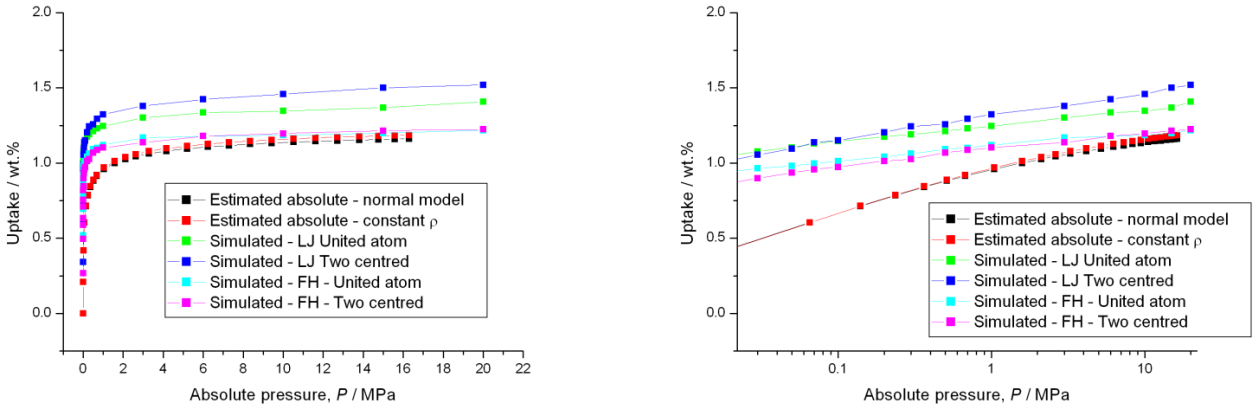

Figure 6.9 - Comparison between the estimated absolute using the normal methodology and the constant adsorbed density and the simulated isotherms using the LJ and FH parameters and the two centred and united atom model. The simulated isotherms were scaled using the ratio of densities. Right -hand side plot is the same data plotted in a logarithmic (log_{10}) scale.

When applying a factor, there is good correspondence between the simulated isotherms and the models applied to the experimental data. As evident from the measured density, the simulated material and the sample have some differences. This can be seen also in the simulated BET specific surface area, which is 481 m^2 g^{-1}, as indicated in the last section. The experimental BET specific surface areas was 371 and 321 m^2 g^{-1} as measured in Zeochem and specified in the Technical Datasheet in Additional Information G. The BET specific surface area was also measured twice in Bath, yielding values of 302 m^2 g^{-1} and 282 m^2 g^{-1}. If we compare the simulated BET specific surface areas with the experimental ones, we obtain a ratio of 0.77 and 0.66 for the BET specific surface area measured in Zeochem. The first measurement of 371

$m^2\ g^{-1}$ yields a ratio very similar to the ratio of densities of 0.765. The ratios with the BET specific surface areas measured in Bath are 0.627 and 0.586, respectively.

The comparison with the simulated isotherms in Figure 6.9 shows that, when using a ratio of densities to compensate for the differences between the perfect simulated crystal of silicalite-1 and the absolute obtained from experimental data, the models show very good correspondence with the simulated isotherms using the FH potential. There are no great differences between the two models that estimate the absolute and the two simulated isotherms using the united atom and two-centre model with the FH potentials. The absolute estimated isotherms and the FH simulated isotherms show some differences in the 1 to 4 MPa range, but show good correspondence afterwards, becoming almost equal at pressures above 10 MPa. The simulated isotherms using the LJ parameters show some difference between the united atom and two-centre model after 1 MPa. The results shown in Figure 6.9 are not unforeseen, since it has been reported in the literature that hydrogen at low temperatures needs to take into account the quantum effects [317, 332, 333] and perhaps the best way of including these in GCMC simulations are to use the path integral formulation described by Feynmann and Hibbs [313-315].

As observed in this section, the validation of the methodology is rendered meaningless if no correction is applied on simulated results. As seen in Figure 6.8, the simulated results for the same material are much in excess of the uptakes observed for experiments. One possible explanation for this is the fact that the simulations are done assuming a perfect, pure and periodic crystal. Experiments, even in crystalline samples, are done on imperfect materials, which have impurities, might not have been properly degassed and have defects in their crystal structures. The characterisation of the material further emphasises this, since the densities and BET specific surface areas are also different from simulated results and experimental techniques. For this reason, a ratio of experimentally measured densities and simulated ones was applied to the simulated isotherms, which in turn showed good correspondence. One interesting outcome of the comparison is the confirmation that the use of the FH potential, as proven in other cases [317], seems to yield better results than simply using LJ potentials.

6.4. Conclusions

Computational simulations are a distinct alternative to conventional experimental techniques. They can probe hypothetical and real materials with more ease and simulate results at different operating conditions. GCMC simulations have been used for hydrogen adsorption in porous materials and they can provide some helpful results and guide the synthesis of new materials.

For the purpose of this thesis, GCMC simulations could provide a good benchmark and an alternative validation technique for the methodology employed to study hydrogen sorbent materials. The methodology has been evaluated using NMR and INS in the previous chapter and, due to the nature of simulations and the fact that the absolute amount adsorbed is the output for GCMC simulations, these methods can serve as an additional technique to validate the estimation of absolute uptakes. However, GCMC simulations have some drawbacks, since the underlying assumptions are that the material is a perfect, infinite crystal, which could result in significant differences when comparing with experimental gas sorption techniques. GCMC simulations are also very dependent on input parameters and models and, for this reason, two different assumptions on the hydrogen molecule were used. The two-centre and united atom model were used, which are based on different potentials. It would also be important to verify if quantum effects are significant for hydrogen adsorption, so absolute uptakes were calculated with and without the quantum correction, by means of the FH potential. The tested material was silicalite-1, a rigid, simple material, with moderate hydrogen uptakes. Silicalite-1 was chosen exactly due to its material and crystallographic simplicity and to the ease of sourcing and testing it, enabling a comparison of computational simulations with experimental uptakes.

The simulations done on silicalite-1 show that the quantum correction is prevalent at low temperatures, as it would be expected. This makes uptakes at 77 K calculated using the correction lower than the ones using LJ parameters. This difference blurs with increasing temperatures and it less significant at 200 K. At 77 K, the differences between the united atom and two centred model are substantial when using the LJ potential but not very important for the set of results that employed the FH potential.

At 200 K, the simulations indicate that there is no great difference between the united atom and two-centre models for both the LJ parameters and the FH parameters.

Experimental results were obtained for the silicalite-1 at 77 K and up to 17 MPa, to compare and possibly validate the methodology proposed in this thesis using computational simulations. The experimental results were treated using the aforementioned methodology, with both the conventional model proposed in the Results and Analysis chapter and the development that was introduced in Chapter Five, which assumes a constant density of the adsorbed phase. The fitting and parameters obtained using both methods were very similar, as shown in Table 6.3 and Figure 6.7. The hydrogen uptakes output by the simulation and the estimated absolutes from experimental data resulted in Figure 6.8, which shows a large difference between simulation and absolutes determined by experiment. As discussed in this chapter, GCMC simulations have some assumptions like perfect, pure, periodic materials, which can make comparisons with experiment troublesome. For this reason, the simulated results were converted using a ratio obtained with the simulated density of the material and the experimental density estimated using He pycnometry. When the uptakes are converted, the estimated absolutes are in good agreement with the simulated results using the FH potential after 10 MPa, as shown in Figure 6.9. In the low pressure range however, there are some noticeable differences.

The proposed methodology shows good agreement with the simulated isotherms, as long as a ratio for converting simulated isotherms is taken into account. The agreement is clearer when comparing with isotherms simulated using the FH potential, so taking into account quantum corrections, as it has been reported for hydrogen adsorption at these temperatures.

Chapter Seven

Discussion - A Model to Apply to Hydrogen Adsorption in Nanoporous Materials

7. A model to apply to hydrogen adsorption

7.1. Introduction

In the four preceding chapters, the modelling and analysis which are the subject of this thesis were introduced, applied to excess hydrogen sorption data and discussed. The methodology was also compared with experimental techniques, namely NMR and INS and with computational simulations such as GCMC simulations. The methodology proposed in this thesis and the validation and comparison with experimental and computational techniques are critically discussed in this chapter.

7.2. The context of the work

As discussed in the Background chapter (Chapter 2), energy is crucial for our living. We have mainly relied on fossil fuels to power our economies but there is an amass of social, economic and environmental reasons, at the top of which stands anthropogenic climate change, that compels societies to migrate as soon as possible to a clean, sustainable energy system. This is a herculean task, since fossil fuels are right at the core of our economic system and governments, companies and consumers have come to rely on these straightforward, cheap and available sources of energy. A clean, sustainable energy system will have to be built around renewable sources of energy which, despite all the benefits they carry, still have some technical and economic issues to be dealt with if they are to provide energy in a bigger share. While it is uncertain which forms of renewable energy will provide most of the energy generation of the future, some issues are transversal across the majority of renewable sources of energy. Two such issues are the intermittency and unpredictability of renewable energies, which create the need for proper energy storage in the electric grid, to cope with the imbalances observed between an intermittent supply provided by renewable energies and the fluctuation of demand, which varies throughout the day depending on consumers. The type of energy storage depends on specific requirements, such as duration, availability, power and rate of discharge, so a variety

of methods exist to store excess energy, which range from pumped hydroelectric storage to conventional lead-acid batteries.

Hydrogen can be used as an energy storage method. Furthermore, it can also be used as a fuel in vehicles to decarbonise the transport sector, since when combusted with pure oxygen only produces water. The wide applicability and features of hydrogen make it ideal to use as a wide-scale energy vector in a clean and sustainable future energy system. This has coined the expression “hydrogen economy”, which is a future energy scenario where hydrogen is sustainably produced through renewable sources of energy and widely used as an energy store and as fuel for the transport sector.

The rationale for the “hydrogen economy” is built upon the following pillars – availability and ease of producing hydrogen, efficient use in a fuel cell or steam engine and no harmful emissions at end use. Hydrogen is ubiquitous in nature, in the form of water, biomass or hydrocarbons, so there is a widespread availability of it. Any source of energy can be used to produce hydrogen but, if the goal is sustainable production, a renewable source of energy has to be used so that the hydrogen is clean and sustainable. Hydrogen is the most energetic of any chemical fuel on a mass basis and can be efficiently used in a fuel cell or in an internal combustion engine, with the added feature that it does not produce any harmful emissions when used in either device. If pure hydrogen is used, nothing apart from water is produced when combusted in a heat engine or used in a fuel cell.

Despite the obvious benefits of using hydrogen as a wide-scale, sustainable energy vector, there are still issues to solve, which include economic, social, technical and scientific problems. Whereas the infrastructure issue, the price and efficiency of fuel cells and the efficient and sustainable production of hydrogen are all difficult questions to address and remain unanswered so far, storage has been identified as probably the biggest technical barrier precluding wide-scale application of hydrogen in light-duty vehicles. The hydrogen storage problem has puzzled scientists and engineers for some decades now and a hydrogen storage system that fits all the stringent requirements is still elusive. Storage of hydrogen can be done using conventional methods like compression or liquefaction and there is research underway on other alternatives, including hydrides, liquid fuels or storage in porous materials.

Storage in porous materials through adsorption has known considerable developments in the last decades, mainly due to the development of new synthetic materials. Synthetic chemistry has developed to a point where it is possible to molecularly tailor materials which possess pores in the nanoscale range. There are a wide variety of novel synthetic, highly porous materials, which includes porous polymers, templated nanoporous carbons and MOFs.

Analysis and modelling of hydrogen storage in a porous material can play an important role in clarifying the alternatives for proper storage of hydrogen. Developments have been considerable in the synthesis of new hydrogen storage materials, with new synthetic high-surface materials having porous features that were unthinkable a decade ago, so ways of assessing and comparing them with other storage alternatives are of utmost importance. Modelling and analysis of hydrogen uptakes in porous materials can shed light on the mechanisms of hydrogen adsorption and will help to identify which are the most promising materials for hydrogen storage. In addition, they can be used to compare uptakes with other mature storage methods, like compression, cryogenic compression and liquefaction. A better understanding of the thermodynamics of adsorption is also facilitated by modelling. Thermodynamics are crucial when designing adsorptive storage systems, especially if a tight control has to be maintained at cryogenic temperatures.

7.3. The methodology as a benchmark to evaluate hydrogen storage materials

The operating conditions at which adsorptive storage occurs, the structural and chemical heterogeneity of surfaces, the nature of adsorption in porous materials and the way experimental techniques used to assess quantities stored were designed make the estimation of the total amount of hydrogen in a material hardly as straightforward as it might initially seem. The proposed methodology aims at obtaining an estimate of the absolute amount of adsorbate in a material and, while tested on hydrogen in this thesis, can in principle be applied to any fluid above its critical point adsorbed in a microporous material. If enough experimental excess data is available at different

temperatures, the methodology can also estimate the absolute and excess amounts for higher pressures and different temperatures, relying only on a small number of parameters that were determined through nonlinear fitting.

Adsorption in a microporous material usually follows IUPAC type I behaviour, which means that its uptake as a function of pressure is a monotonic convex function with a horizontal asymptote, indicative of the limiting adsorptive capacity. In a supercritical fluid, as hydrogen is at temperatures above 33 K, the excess measured in experiments reaches a maxima and then starts to decrease with increasing pressures, while the absolute follows an IUPAC type I behaviour. The estimation of the absolute isotherm from experimental excess presented in this work uses an IUPAC type I equation and estimates the parameters that under those conditions would best fit the available experimental excess points. It is a simple way of estimating the absolute isotherm, since it only needs the experimental excess input, the definition of the type I equation and a nonlinear fitting tool to determine the parameters of the isotherm. These parameters are then used to determine excess and absolute uptakes under different conditions.

One of the advantages of the model is that it can be applied regardless of the porous morphology of the adsorbent, which means that it can be applied whether the material is crystalline or amorphous, and regardless of the chemical composition of the surface. This proves especially useful when considering the vast number of materials being considered as prospective hydrogen storage materials. This versatility of the methodology is verified in the Results and Analysis chapter (Chapter 4), with the application of the method and analysis to four sets of results – isotherms from MOFs (MIL-101 and NOTT-101) and isotherms from microporous carbons (AX-21 and TE7), with overall good results for the tested materials. Temperature dependence was also built into the model for the different equations and they were compared based on their uptakes and fitting parameters. The Tóth and the UNILAN equations were considered the most suitable to apply to the experimental data, based on the statistical results from the fitting and on analysis of the estimated isotherms.

One interesting development of the methodology was the constant adsorbed density model, which was developed based on the observations provided by the INS. As the

INS indicated a solid density of adsorbate within the micropores of TE7, a model was developed that takes into account three different quantities in the pore – the excess, the total and the absolute amount adsorbed. The difference is that the absolute amount adsorbed became the amount adsorbed that has constant density and the total is the total amount of adsorbate within the pore, which includes the absolute amount with constant density and the adsorbate gas in equilibrium with the adsorbate. This is an exciting new development for hydrogen adsorption and has been confirmed with the application of this new method to experimental data, since fitting results also yielded a density above 87.08 kg m^{-3}, which is the reported density for solid parahydrogen at 4 K and zero pressure. This adsorbed density might be due to the optimally sized pores of the material, which greatly compresses hydrogen and packs it in the pore, enhancing its density to levels not seen before. This new development of the model needs to be tested in more experimental excess data, to search for similar solid-like density in other hydrogen storage materials.

The thermodynamic analysis of the NOTT-101 data showed that there might be some differences when calculating the differential enthalpies of adsorption using the isosteric method by the Clausius-Clapeyron approximation and the Clapeyron equation, which are significant at higher pressures. This is probably because of the assumptions present in the Clausius-Clapeyron approximation, which assume ideal gas behaviour and negligible molar volume for the adsorbate. As observed in the Results and Analysis chapter (Chapter 4), both these assumptions might not hold at the conditions observed for hydrogen adsorption, which are typically high pressures and cryogenic temperatures. For this reason, while both methods have similar results at low coverage, there is a growing discrepancy with increasing coverage between the two methods, with the isosteric enthalpies calculated using the exact Clapeyron equation showing a sharper decrease in enthalpies at higher coverage.

One of the most useful aspects of the model is the comparison to alternative storage methods. The methodology allows the estimation of uptakes at different operating conditions and can be used to calculate and compare uptakes with conventional storage methods, which include liquefaction, standard and cryogenic compression. One useful comparison is the one drawn with cryogenic compression, which has been proposed as a storage alternative that is more beneficial than compression or

liquefaction of hydrogen. From the analysis on the Results and Analysis chapter (Chapter 4), adsorptive storage has greater quantities stored in comparison with cryogenic compression up to a certain pressure. This means that hydrogen storage in a porous material can be an alternative solution to the methods currently in use, since it can lower the pressure requirements of the system for the same stored amounts up to a certain pressure. This comparison of adsorption to other storage methods and the identification of the break-even point are some of the most interesting results of this work, since they provide a number and a simple and straightforward comparison between alternative methods. It also shows that adsorptive storage can be used and is beneficial for practical applications, at least when compared against cryogenic compression.

Interestingly, the densities of the adsorbed hydrogen inferred from the application of the model seem to suggest extremely high densification of hydrogen in the pores. The densities obtained from the analysis for adsorbed hydrogen in most materials point towards densities in the high-end of liquid hydrogen, which has also been observed in other studies. However, the INS studies from Chapter 5, along with the development of the methodology suggest that provided the adsorbent has optimally-sized pores for hydrogen adsorption, the hydrogen can attain even higher densities than liquid hydrogen, some even surpassing the density of solid parahydrogen at 4 K and zero pressure. This is an extremely encouraging result, which indicates that hydrogen can be highly compressed in optimally sized pores.

7.4. Validation of the methodology by a combined experimental and computational approaches

Most of the conclusions drawn in the Results and Analysis section (Chapter 4) are dependent on the estimation of the absolute isotherm. The verification of the absolute isotherm using other methods would strengthen most of the conclusions garnered in that chapter by validating the proposed model and analysis. Experimental methods, which could quantify the adsorbate that is adsorbed in the pores of a solid material and computational simulations, which yield the absolute amount adsorbed in a

material, could provide interesting insights and be used to compare with the model and analysis presented in this thesis.

The experimental validation of the model relied on two different experimental techniques, NMR and INS. There are rare reported instances of using these techniques at conditions that would be relevant to validate the model, probably due to difficulties in the experimental setup. These conditions, which are the ones used for adsorption of hydrogen, typically involve cryogenic temperatures between 77 and 200 K and pressures higher than 1 MPa.

The NMR results were difficult to reconcile with predictions from the model, even if the NMR measured the absolute amount adsorbed. The proposed quantification of adsorbed amounts of hydrogen seems to need additional calibration. As explained in the corresponding chapter (Chapter 5), the observed hydrogen absolute uptakes are not in line with what was expected from tested materials. The TE7 carbon beads, which is one of the materials our research group has fully characterised, and one of the materials analysed and modelled in the Results and Analysis chapter (Chapter 4), were shipped and tested using NMR in the University of North Carolina at Chapel Hill. The absolute isotherm determined using NMR was compared to the excess and estimated absolute using the model, but the results diverged significantly. Not only was the uptake less than the experimental excess, the shape of the isotherm did not follow an IUPAC type I behaviour. Instead, the isotherm showed almost linear dependence on the pressure, so it did not even saturate at the highest pressure, which was 8 MPa. The PEEK carbons, which had already been tested with the NMR equipment and published, were sourced and tested in Bath for high-pressure hydrogen adsorption. The experimental excess hydrogen uptake was determined and the model applied to experimental data, which allowed for the estimation of the absolute isotherm. Again, as was the case for the TE7, the PEEK carbons exhibited absolute uptakes determined from the NMR that did not compare well with absolute isotherms estimated using the model and the experimental excess. For the PEEK-ST-9-20, the excess and estimated absolute isotherms determined using the methodology were comparatively much higher than the estimated absolute determined by NMR techniques. For the other tested material, the PEEK-ST-9-35, the excess and estimated absolute isotherms were smaller than the NMR estimated absolute. The materials are

very similar in their properties and characteristics, and they were tested in the same way for NMR hydrogen studies and for excess hydrogen sorption, so the results are very inconsistent for the two PEEK materials. Furthermore, as it can be observed for the PEEK carbons and their absolute isotherm determination by NMR, the uptakes do not correlate to their BET specific surface area nor do they compare with the respective pore volumes. The shape of the NMR measured uptake, on the other hand, seemed to be compatible with an IUPAC type I equation, so the NMR determined absolute was scaled to the absolute determined with the model, and the two isotherms showed good correspondence. The conclusion is that a qualitative comparison with the absolute uptake determined through NMR and the one determined using the model applied to experimental data is possible. A quantitative comparison cannot be made using our models and, from the observations made in the chapter, it is strongly suggested that the "template" method used to quantify the absolute hydrogen might need further refinement in light of these results.

The INS experiment was also done with the same purpose of comparing and validating the proposed models, especially for obtaining a validation of the absolute isotherm determined from the methodology. The TE7 were again the material chosen for the comparison and the INS revealed some interesting results. The INS spectra for the TE7 carbon beads, measured at 77 K with increasing pressures up to 3.5 MPa, showed two very interesting features. The spectra had a sharp, intense peak in the elastic region due to the scattering of orthohydrogen. This peak has a full-width at half-maximum in the lowest pressure point measured (0.016 MPa) which neared the instrumental resolution (0.3 meV). A sharp, intense peak in the elastic region with this width indicates a solid-like phase for the adsorbed gas in the solid material. To reinforce this observation, an even more distinct fingerprint of solid hydrogen was seen in the spectra, with a clear, well resolved peak at ~ 14.7 meV, for every pressure, which is only present in the *ortho*-to-*para* transition and is commonly called the "rotor line", since it corresponds to the unperturbed rotation of molecular hydrogen. The INS experiment pointed to a solid-like adsorbed phase density of hydrogen, which is a very interesting development and has not been seen before at these operating conditions. Both the integration of the elastic peak and the integration of the area under the "rotor line" showed a behaviour that is compatible with the shape of an IUPAC type I equation, since they monotonically approach a horizontal asymptote.

Taking these observations into account, the model was improved to include a constant adsorbed phase density and to distinguish between excess, absolute and total adsorption. When this model was applied to TE7 experimental data, it yielded an adsorbed density that was higher than 87.08 kg m^{-3}, which is the solid density of parahydrogen at 4 K and zero pressure. The INS results, together with the application of this new model, suggest that the optimally sized pores of TE7 confine the adsorbed hydrogen into a solid-like phase, which can have densities superior to solid density of parahydrogen at zero pressure and 4 K. The integrated elastic peak from the INS experiment was also scaled to the absolute determined from the model using the constant density of adsorbate and it provided very good correspondence, showing that the absolute amount adsorbed (which is different when using the constant adsorbed density model, since it corresponds to the adsorbed phase that has the same density) predicted from the experimental excess compares well with the immobile hydrogen adsorbed into the pores, which the INS indicates has a solid-like behaviour. A quantitative measure of the absolute adsorbed quantity from INS was very hard to obtain, since it required the calculation of the exact amount of sample that was under the INS beam, so the scaling with the absolute isotherm determined through the modelling was the only available option for comparison. For this reason, only a qualitative validation of the methodology was possible, but the comparison between the integrated elastic peak and the absolute isotherm determined from the experimental excess correlated very well.

The computational validation of the methodology also showed interesting results. The GCMC simulations were done on silicalite-1, and were then compared to the absolute determined from the modelling using both the simple methodology and the development to include the constant adsorbed density. The GCMC simulations of adsorbed hydrogen in silicalite-1 also had different assumptions, since they were done with classical potentials (Lennard-Jones potential) and accounting for quantum effects (Feynman-Hibbs effective potential). Furthermore, the simulations were also run using a united-atom and two centre model for molecular hydrogen. This added an interesting element to the comparison with the modelling applied in this thesis, since the GCMC simulations also had different assumptions, yielding different results. Thus, a two-way comparison to the modelling could be done, since the experiments and modelling could provide guidance on which assumptions were more likely to be

true for GCMC simulation of hydrogen adsorption in silicalite-1 at those conditions. In the simulations it was expected that, at cryogenic temperatures, the quantum effects would make a difference to the hydrogen uptakes, as had been reported in the literature. The results from GCMC simulations showed that quantum effects were significant at lower temperatures and the uptakes calculated using the Feynman-Hibbs were lower than the ones calculated using Lennard-Jones potentials. This difference vanished with increasing temperatures. The united atom and two-centre approach to molecular hydrogen was significant only when using the Lennard-Jones potentials at low temperatures, since at 200 K, the four sets of results were all very similar.

To compare with the simulations, the silicalite-1 was experimentally tested at 77 K and high pressures, up to 17 MPa and the modelling was applied to the obtained excess, using both the simple model and the constant adsorbed density model. Straightforward analysis of the results did not show a great correlation, since the uptakes seen in the GCMC simulations were much higher than the ones observed from modelling applied to the experiment. This might have to do with the nature of the simulations, which are done on a perfect, pure, periodic crystal, making it hard to compare with experiments. For this reason, and to compare both the experiment and the simulation, a simple measurement that could indicate the differences was carried out. The density is a simple physical property of the material, which could be determined for both the sample and the simulated crystal. The density of the two was divided to obtain a ratio, which was used to scale the simulated isotherms and compare with the absolutes determined through the modelling. When this method was used to scale the simulated isotherms, the modelled absolute matched quite well with the GCMC simulations. In addition, the comparison indicated that the uptakes estimated at 77 K for the silicalite-1 seem to be more precise if quantum effects are included, that is, the correlation is better using the simulated absolute isotherms determined from the Feynman-Hibbs effective potential. While in the low pressure region there seems to be some disparity between the modelled absolutes and the simulated ones, the results showed close similarity around 10 MPa, and are almost equal beyond that pressure.

In summary, the absolute isotherms estimated using the methodology were compared with other techniques, which were NMR, INS and GCMC simulations. A full,

straightforward quantitative validation was not possible using any of the techniques, since it was either not possible to calculate (INS), it did not compare well with the modelling (NMR) or a straightforward comparison with computer simulations did not correlate due to prior assumptions (GCMC simulations). For the NMR studies, even though a quantitative method was developed at the University of North Carolina at Chapel Hill and published, their proposed method did not match our models and results. The INS validation was also not straightforward, since an exact calculation of the sample and of the hydrogen that is under the beam is necessary. For the GCMC simulations, the assumption of the perfect, pure, periodic crystal is difficult to reconcile with experiments, since samples contain impurities and defects, making the simulation results difficult to compare with experiments. However, for all the techniques used, a qualitative comparison was possible. The NMR estimated absolute was scaled to the absolute isotherm for two PEEK carbons and showed good correspondence. The INS integrated elastic peak was scaled to an absolute model determined from experimental excess data, which accounted for a constant adsorbed density, and both results correlated well. The GCMC simulations, if corrected using a ratio which indicated the relation between physical properties of experiment and simulation, also showed good results. The densities, determined from He pycnometry and from the crystal structure, were the property chosen to provide the relation between experiment and simulation. If the absolute simulated isotherms were scaled using that ratio, they provided a good match to the model applied to the experimental excess data of silicalite-1. This comparison also indicated that quantum effects, at those temperatures, should not to be ignored when simulating hydrogen adsorption.

Chapter Eight

Concluding Remarks

8. Concluding remarks

8.1. Conclusions

This thesis' aim was to model and analyse the hydrogen storage in nanostructured solids for sustainable energy systems and the following conclusions can be drawn from this work:

1) The methodology and analysis proposed in this thesis can be applied to a variety of hydrogen adsorbent materials without any great changes to the model, provided the materials are microporous. The model uses only a small number of parameters and yields significant results, which can provide information on the available pore volume, heterogeneity of the surface and energetics of adsorption, depending on the type I equation used. This conclusion is directly related to objectives I, II and III that were set at the end of Chapter 2 (Background) and related to the development of an analytical model with a small number of parameters (objective I) that could predict over different operating ranges (objective II) and test this on a number of experimental excess hydrogen datasets (objective III).

2) The model can be used to predict both absolute and excess uptakes at different pressures than the ones fitted. If temperature dependence is included in the analysis, extrapolation to different temperatures also becomes available.

3) The Tóth equation and the UNILAN equation are the ones that work better with the available experimental datasets. The Tóth is the type I equation used in the analysis on this thesis, since it is robust, simple to use and has parameters that have physical meaning. The Tóth equation also showed, along with the UNILAN, the best statistical results for the same number of parameters. The DA and DR equations also had good statistical coefficients for the available datasets, but showed unreasonable values for some parameters.

4) When comparing with compression at the same temperature, adsorption in a porous material is beneficial only up to a certain pressure, called the break-even point. This break-even point is temperature dependent and the uptake gains are only marginal at pressures close to the break-even point, being much more pronounced in the low pressure range. This conclusion is directly related to objective IV, set in Chapter 2 (Background) which was the comparison of adsorptive storage with alternative storage methods.

5) The hydrogen densities seen for adsorptive storage and calculated from the methodology are in the high liquid hydrogen density range, with estimated values of ~ 70 kg m^{-3} for the adsorbed density. Using the development of the analysis that assumes constant adsorbed density, the calculated values are above solid parahydrogen density at 4 K and zero pressure (> 87.08 kg m^{-3}).

6) The differential isosteric enthalpy of adsorption has to be calculated using the absolute isotherm, because the excess is not a separate phase. In addition, the assumptions present in the Clausius-Clapeyron approximation are only valid for calculation at low coverage, since at higher coverage hydrogen's behaviour deviates from ideal. This means that differential isosteric enthalpies are calculated with more accuracy using the Clapeyron equation, which is the exact thermodynamic equation for phase changes. This conclusion is related to objective V set in Chapter 2 (Background), which was the estimation of the thermodynamic properties of a material and the improvement on currently used methods.

7) The TE7 results from the NMR were not compatible with the excess and determined absolute from the model. The TE7 results did not showed a type I behaviour, which was the expected one from adsorption of hydrogen in a microporous material.

8) The PEEK results from the NMR offered a qualitative confirmation of the absolute isotherm determined from the modelling. The "template" method, which was used to quantify the adsorbed hydrogen in a porous material, proved difficult to compare with the obtained experimental results and the

absolute isotherms determined from the model. This conclusion is directly related to objective VI that was set in Chapter 2 (Background), which was the validation of the methodology using experimental techniques.

9) The INS spectra showed two features that indicate solid-like density in the hydrogen adsorbed in TE7 at 77 K. These are a sharp, intense elastic peak with a full width at half-maximum that approximates the instrument's resolution and a "rotor line" peak at 14.7 meV for all pressures. Both are a clear indication of solid hydrogen present in the material, at temperatures much higher than the critical point of hydrogen (which is 33 K).

10) The solid like signal from the "rotor line" and from the elastic line increases with increasing pressures until it saturates, a behaviour that mirrors what happens in adsorption of a supercritical fluid in a microporous material. This shows that the solid hydrogen accumulation is a feature of adsorption of hydrogen into a optimally-sized pore of a porous material.

11) The solid hydrogen observation prompted a development in the model, which accounts for constant density of the adsorbate and distinguishes between total, absolute and excess adsorption. The absolute isotherm, which in this development corresponds to the adsorbed phase that has constant density, was compared with the integrated elastic line from the INS spectra. When this integrated elastic line was scaled, the results were very similar to the absolute isotherm determined from the development of the model. The fitting also indicated that the density of the adsorbed phase was well in excess of solid hydrogen density (> 87.0 kg m^{-3}). This conclusion is directly related to objective VI that was set in Chapter 2 (Background), which was the validation of the methodology using experimental techniques.

12) The comparison of the model applied to experimental results and the GCMC simulations showed differences if applied without any treatment. Scaling the simulated isotherms by using a ratio of experimental and simulated density showed a good correspondence between the absolute isotherms calculated from the model and the simulated isotherms calculated using the Feynman-

Hibbs potential. This corroborates other findings in the literature that indicate that, in those temperatures, quantum effects have to be taken into account for hydrogen adsorption. This conclusion is directly related to objective VI that was set in Chapter 2 (Background), which was the validation of the methodology using computational techniques.

8.2. Future work

This work showed the importance of applying modelling and analysis to hydrogen adsorption in microporous materials. It would be of particular interest to follow up some of the results and conclusions presented herein and the following points are suggested as future work, some of which are already being developed or planned.

- The proposed methodology was solely applied using hydrogen as the adsorbate. It would be of scientific and technical interest, especially in the context of energy gases for storage or separation, to expand this methodology and use experimental datasets of other supercritical gases. The prime candidates to be tested, owing to their current interest in industry, energy applications or greenhouse gas concerns, are carbon dioxide, methane, oxygen and nitrogen. It is already been discussed in our research group the planning of some experiments and application of our models on the materials presented here for other gases in the near future.

- The methodology proposed here has been applied assuming a fixed pore volume for the adsorbate. Our research group is working on expanding this analysis to include flexible adsorbents, so experimental excess isotherms are being collected and analysed for some flexible materials, including flexible MOF MIL-53.

- The use of the limiting absolute capacity, which corresponds to a horizontal asymptote, means that the isotherm will never reach saturation, except at extremely high pressures. Saturation might be reached at more reasonable pressures, so the model is currently being applied with the saturation equations

proposed by Tóth [238]. This work is already being developed in our research group.

- The thermodynamic analysis of the differential isosteric enthalpies needs further refinement. The results observed for the NOTT-101 should be replicated in other materials and they should include other equations reported in the literature, especially the virial equation, which has been used extensively for the calculation of isosteric enthalpies. Work on this topic is currently ongoing and the author has an accepted abstract for an oral presentation at the *Fundamentals of Adsorption 11* in Baltimore in May 2013 on this topic, entitled *Isosteric Enthalpies for Hydrogen Adsorbed on Nanoporous Materials at High Pressures.*

- INS proved a very valuable tool to probe hydrogen storage materials. Further studies at the temperature of sorption experiments are required to see if the solid density of adsorbate is seen on other materials. At the time of the writing of this chapter (March 2013) our research group is conducting an experiment in TOSCA using MIL-101 and silicalite-1 as adsorbents, at 77 and 4 K and to pressures up to 5 MPa to confirm the results seen for TE7.

- In addition to INS, additional neutron techniques like small angle neutron scattering and wide angle neutron scattering could provide interesting information on the adsorption of hydrogen in mircroporous materials. Our research group has been awarded beam time on two different instruments to measure hydrogen adsorption in porous materials. The instruments are the SANS2D instrument at ISIS, RAL, which uses small angle neutron scattering and the NIMROD instrument, also at ISIS, RAL, which bridges the gap between small angle and wide angle neutron scattering by covering small and wide angle wavelengths. Our research group was awarded four days at NIMROD and 2 days at SANS2D to study hydrogen adsorption in porous materials and verify the results obtained from TOSCA. The main goal of the two experiments is to clarify the mechanisms to hydrogen adsorption in microporous materials, to assess the state of the adsorbed hydrogen and to

quantify the adsorbed hydrogen and relate it to the models presented in this thesis.

- A proposal for beam time from our research group was also awarded 3 days in the European Radiation Synchrotron Radiation Facility (ERSF) in Grenoble, France. The proposal is aimed at studying the structural dynamics and variation of materials upon hydrogen adsorption. It will use X-rays to probe the structure of different flexible adsorbent materials that our research group has tested and to see the structural changes at cryogenic temperatures and high pressures. This experiment will provide insights on pore variation models currently being developed in our research group.

- The lack of NMR studies on adsorbed hydrogen and the disparate results offered by the "template" method developed at the University of North Carolina at Chapel Hill suggest that some more work could be done on the use of NMR for adsorbed hydrogen. The PEEK carbon results showed that NMR probably measures the adsorbed hydrogen but its quantification might need refinement. New NMR studies, which would be complemented with INS and SANS results, could provide an indication of the state of the adsorbed hydrogen, since NMR can distinguish between the different phases, as well as an additional quantification of the model by another experimental technique.

- GCMC and other computational tools should continue to be used for the study of hydrogen adsorbed in porous materials. An interesting development of this work and one that is currently being explored involves the use of the code DL_MONTE, with the help of Professor Stephen Parker from the Department of Chemistry at the University of Bath. This code could be benchmarked against the MUSIC code and experimental results. Additionally, DL_MONTE is currently being developed to include the possibility of simulating flexible adsorbents, which would allow for the simulation of MOFs with variable volume. If included successfully, this would allow the comparison of the simulated isotherms in a flexible material with the models applied to experimental data and with results provided by X-rays in the ERSF.

9. References

[1] International Energy Agency, in, OECD Publishing, 2008.
[2] United Nations Development Programme, in, Palgrave Macmillan, New York, 2011.
[3] World Bank. *World Bank Indicators*. January 2013]; Available from: http://data.worldbank.org/.
[4] Exxon-Mobil, in, 2012.
[5] International Energy Agency, in: I.E. Agency (Ed.), International Energy Agency, 2010.
[6] U.S. Energy Information Administration, in, 2011.
[7] United Nations Economic and Social Affairs - Population Division, in, New York, 2011.
[8] H. Müller-Steinhagen, J. Nitsch, Process Safety and Environmental Protection, 83, 285 (2005).
[9] F. Barbir, Energy, 34, 308 (2009).
[10] British Petroleum Company., in, British Petroleum Co. plc, London, 2012, pp. 44 p.
[11] P.V. Kamat, The Journal of Physical Chemistry C, 111, 2834 (2007).
[12] P. de Almeida, P.D. Silva, Energ Policy, 37, 1267 (2009).
[13] P. Hanlon, G. McCartney, Public Health, 122, 647 (2008).
[14] M.K. Hubbert, Science, 109, 103 (1949).
[15] J.P. Dorian, H.T. Franssen, D.R. Simbeck, Energ Policy, 34, 1984 (2006).
[16] R.W. Howarth, R. Santoro, A. Ingraffea, Climatic Change, 106, 679 (2011).
[17] A.D. Charpentier, J.A. Bergerson, H.L. MacLean, Environ Res Lett, 4, (2009).
[18] D.A. King, Science, 303, 176 (2004).
[19] I. Dincer, Energ Source, 20, 427 (1998).
[20] I. Dincer, Energ Policy, 27, 845 (1999).
[21] J. Hansen, M. Sato, R. Ruedy, A. Lacis, V. Oinas, P Natl Acad Sci USA, 97, 9875 (2000).
[22] S. Solomon, Intergovernmental Panel on Climate Change. Working Group I, Climate change 2007 : the physical science basis, Published for the Intergovernmental Panel on Climate Change [by] Cambridge University Press, Cambridge, UK ; New York, 2007.
[23] J.C. Orr, V.J. Fabry, O. Aumont, L. Bopp, S.C. Doney, R.A. Feely, A. Gnanadesikan, N. Gruber, A. Ishida, F. Joos, R.M. Key, K. Lindsay, E. Maier-Reimer, R. Matear, P. Monfray, A. Mouchet, R.G. Najjar, G.K. Plattner, K.B. Rodgers, C.L. Sabine, J.L. Sarmiento, R. Schlitzer, R.D. Slater, I.J. Totterdell, M.F. Weirig, Y. Yamanaka, A. Yool, Nature, 437, 681 (2005).
[24] J.A. Curry, J.L. Schramm, E.E. Ebert, J Climate, 8, 240 (1995).
[25] *Climate Change Act*, House of Commons,
[26] *DECISION No 406/2009/EC OF THE EUROPEAN PARLIAMENT AND OF THE COUNCIL of 23 April 2009 on the effort of Member States to reduce their greenhouse gas emissions to meet the Community's greenhouse gas emission reduction commitments up to 2020*, European Parliament, Official Journal of the European Union, 140,136
[27] N. Stern, The economics of climate change : the Stern review, Cambridge University Press, Cambridge, 2007.

[28] World Commission on Environment and Development., Our common future, Oxford University Press, Oxford ; New York, 1987.
[29] R.M. Solow, in: Eighteenth J. Seward Johnson lecture to the Marine Policy Center, Woods Hole Oceanographic Institution, at Woods Hole, Massachussets, June 14, 1991, 1991.
[30] H.M. Wee, W.H. Yang, C.W. Chou, M.V. Padilan, Renew Sust Energ Rev, 16, 5451 (2012).
[31] P. Moriarty, D. Honnery, Renew Sust Energ Rev, 16, 244 (2012).
[32] M. Balat, Energ Source Part B, 2, 381 (2007).
[33] Nuclear Energy Agency, in: O.f.E.C.-o.a. Development. (Ed.), 2012.
[34] S.V. Valentine, Renew Sust Energ Rev, 15, 4572 (2011).
[35] M.I. Hoffert, K. Caldeira, G. Benford, D.R. Criswell, C. Green, H. Herzog, A.K. Jain, H.S. Kheshgi, K.S. Lackner, J.S. Lewis, H.D. Lightfoot, W. Manheimer, J.C. Mankins, M.E. Mauel, L.J. Perkins, M.E. Schlesinger, T. Volk, T.M.L. Wigley, Science, 298, 981 (2002).
[36] I.P.B. Editors, I.P.E.G. Chairs, Co-Chairs, I.J.C. Team, P.I. Unit, Nuclear Fusion, 39, 2137 (1999).
[37] ITER.
[38] H. Ibrahim, A. Ilinca, J. Perron, Renew Sust Energ Rev, 12, 1221 (2008).
[39] N.K.C. Nair, N. Garimella, Energ Buildings, 42, 2124 (2010).
[40] *2012 UK Greenhouse Gas Emissions, provisional figures*, Deparment of Energy and Climate Change,
[41] Environmental Protection Agency. *National Greenhouse Gas Emissions Data*. 2012; Available from: http://www.epa.gov/climatechange/ghgemissions/usinventoryreport.html.
[42] H.S. Chen, T.N. Cong, W. Yang, C.Q. Tan, Y.L. Li, Y.L. Ding, Prog Nat Sci, 19, 291 (2009).
[43] I. Hadjipaschalis, A. Poullikkas, V. Efthimiou, Renew Sust Energ Rev, 13, 1513 (2009).
[44] T.R. Cook, D.K. Dogutan, S.Y. Reece, Y. Surendranath, T.S. Teets, D.G. Nocera, Chem Rev, 110, 6474 (2010).
[45] W.M. Haynes, D.R. Lide, T.J. Bruno, CRC handbook of chemistry and physics : a ready-reference book of chemical and physical data, 93rd ed., CRC, Boca Raton, Fla. ; London, 2012.
[46] P. Häussinger, R. Lohmüller, A.M. Watson, Hydrogen, 1. Properties and Occurence, in: Ullmann's Encyclopedia of Industrial Chemistry, Wiley-VCH Verlag GmbH & Co. KGaA, 2000.
[47] A. Le Duigou, M. Miguet, Y. Amalric, Int J Hydrogen Energ, 36, 8822 (2011).
[48] C.-J. Winter, Int J Hydrogen Energ, 30, 681 (2005).
[49] P. Häussinger, R. Lohmüller, A.M. Watson, Hydrogen, 2. Production, in: Ullmann's Encyclopedia of Industrial Chemistry, Wiley-VCH Verlag GmbH & Co. KGaA, 2000.
[50] R.J. Press, Introduction to hydrogen technology, Wiley ; Chichester : John Wiley [distributor], Hoboken, N.J., 2009.
[51] P. Häussinger, R. Lohmüller, A.M. Watson, Hydrogen, 6. Uses, in: Ullmann's Encyclopedia of Industrial Chemistry, Wiley-VCH Verlag GmbH & Co. KGaA, 2000.
[52] J.W. Gosselink, Int J Hydrogen Energ, 27, 1125 (2002).
[53] I. Dincer, Int J Hydrogen Energ, 37, 1954 (2012).

[54] P.P. Edwards, V.L. Kuznetsov, W.I.F. David, Philos T R Soc A, 365, 1043 (2007).
[55] A. Sartbaeva, V.L. Kuznetsov, S.A. Wells, P.P. Edwards, Energ Environ Sci, 1, 79 (2008).
[56] C. Weidenthaler, M. Felderhoff, Energ Environ Sci, 4, 2495 (2011).
[57] D. Haeseldonckx, W. D'haeseleer, Int J Hydrogen Energ, 36, 4636 (2011).
[58] A. Almansoori, N. Shah, Chem Eng Res Des, 84, 423 (2006).
[59] H. Fayaz, R. Saidur, N. Razali, F.S. Anuar, A.R. Saleman, M.R. Islam, Renew Sust Energ Rev, 16, 5511 (2012).
[60] B.D. McNicol, D.A.J. Rand, K.R. Williams, J Power Sources, 100, 47 (2001).
[61] G.J. Offer, M. Contestabile, D.A. Howey, R. Clague, N.P. Brandon, Energ Policy, 39, 1939 (2011).
[62] S.J. Cherryman, S. King, F.R. Hawkes, R. Dinsdale, D.L. Hawkes, Public Underst Sci, 17, 397 (2008).
[63] M. Goldman, H. Johannesson, O. Axelsson, M. Karlsson, Magn Reson Imaging, 23, 153 (2005).
[64] J.W. Leachman, R.T. Jacobsen, S.G. Penoncello, E.W. Lemmon, J Phys Chem Ref Data, 38, (2009).
[65] L. Schlapbach, A. Zuttel, Nature, 414, 353 (2001).
[66] *NIST Chemistry Webbook*. October 2012]; Available from: http://webbook.nist.gov.
[67] K. Christmann, Surf Sci Rep, 9, 1 (1988).
[68] U. Eberle, M. Felderhoff, F. Schuth, Angew. Chem.-Int. Edit., 48, 6608 (2009).
[69] U.D.o. Energy, O.o.E.E.a.R.E.a.t.F.a.F. Partnership. *Targets for Onboard Hydrogen Storage Systems for Light-Duty Vehicles*. 2009 October 2012]; Available from: http://www1.eere.energy.gov/hydrogenandfuelcells/storage/pdfs/targets_onboard_hydro_storage.pdf.
[70] S.F. Parker, Faraday Discuss, 151, 9 (2011).
[71] D. Anton, T. Motyka, in: US Department of Energy Hydrogen and Fuel Cells Program 2011 Annual Merit Review, 2011.
[72] M. Hosseini, I. Dincer, G.F. Naterer, M.A. Rosen, Int J Hydrogen Energ, 37, 5063 (2012).
[73] J.Y. Zheng, X.X. Liu, P. Xu, P.F. Liu, Y.Z. Zhao, J. Yang, Int J Hydrogen Energ, 37, 1048 (2012).
[74] S.M. Aceves, G.D. Berry, G.D. Rambach, Int J Hydrogen Energ, 23, 583 (1998).
[75] R.K. Ahluwalia, T.Q. Hua, J.K. Peng, Int J Hydrogen Energ, 37, 2891 (2012).
[76] L. Trevisani, M. Fabbri, F. Negrini, P.L. Ribani, Energ Convers Manage, 48, 146 (2007).
[77] G.D. Berry, S.M. Aceves, Energ Fuel, 12, 49 (1998).
[78] A. Züttel, A. Borgschulte, L. Schlapbach, Hydrogen as a future energy carrier, Wiley-VCH, Weinheim, 2008.
[79] J. Yang, A. Sudik, C. Wolverton, D.J. Siegel, Chem Soc Rev, 39, 656 (2010).
[80] D.P. Broom, Hydrogen storage materials : the characterisation of their storage properties, Springer, London ; New York, 2011.
[81] S.I. Orimo, Y. Nakamori, J.R. Eliseo, A. Zuttel, C.M. Jensen, Chem Rev, 107, 4111 (2007).
[82] G. Sandrock, J Alloy Compd, 293–295, 877 (1999).
[83] D.J. Siegel, C. Wolverton, V. Ozolins, Phys Rev B, 76, (2007).
[84] A.W.C. van den Berg, C.O. Arean, Chem Commun, 668 (2008).

[85] K.S.W. Sing, D.H. Everett, R.A.W. Haul, L. Moscou, R.A. Pierotti, J. Rouquerol, T. Siemieniewska, Pure Appl Chem, 57, 603 (1985).
[86] M.D. Donohue, G.L. Aranovich, Fluid Phase Equilibr, 158, 557 (1999).
[87] S. Brunauer, P.H. Emmett, E. Teller, J Am Chem Soc, 60, 309 (1938).
[88] K.M. Thomas, Catal Today, 120, 389 (2007).
[89] G. Laudisio, R.K. Dash, J.P. Singer, G. Yushin, Y. Gogotsi, J.E. Fischer, Langmuir, 22, 8945 (2006).
[90] G. Yushin, R. Dash, J. Jagiello, J.E. Fischer, Y. Gogotsi, Adv Funct Mater, 16, 2288 (2006).
[91] Z.X. Yang, Y.D. Xia, R. Mokaya, J Am Chem Soc, 129, 1673 (2007).
[92] E. Masika, R. Mokaya, J Phys Chem C, 116, 25734 (2012).
[93] Y. Gogotsi, C. Portet, S. Osswald, J.M. Simmons, T. Yildirim, G. Laudisio, J.E. Fischer, Int J Hydrogen Energ, 34, 6314 (2009).
[94] Y. Gogotsi, A. Nikitin, H.H. Ye, W. Zhou, J.E. Fischer, B. Yi, H.C. Foley, M.W. Barsoum, Nat Mater, 2, 591 (2003).
[95] Y. Gogotsi, R.K. Dash, G. Yushin, T. Yildirim, G. Laudisio, J.E. Fischer, J Am Chem Soc, 127, 16006 (2005).
[96] M. Sevilla, R. Mokaya, A.B. Fuertes, Energ Environ Sci, 4, 2930 (2011).
[97] S.K. Bhatia, A.L. Myers, Langmuir, 22, 1688 (2006).
[98] G. Ferey, Chem Soc Rev, 37, 191 (2008).
[99] O.M. Yaghi, M. O'Keeffe, N.W. Ockwig, H.K. Chae, M. Eddaoudi, J. Kim, Nature, 423, 705 (2003).
[100] M.P. Suh, H.J. Park, T.K. Prasad, D.W. Lim, Chem Rev, 112, 782 (2012).
[101] S.Q. Ma, H.C. Zhou, Chem Commun, 46, 44 (2010).
[102] J. Lee, O.K. Farha, J. Roberts, K.A. Scheidt, S.T. Nguyen, J.T. Hupp, Chem Soc Rev, 38, 1450 (2009).
[103] R.J. Kuppler, D.J. Timmons, Q.R. Fang, J.R. Li, T.A. Makal, M.D. Young, D.Q. Yuan, D. Zhao, W.J. Zhuang, H.C. Zhou, Coordin Chem Rev, 253, 3042 (2009).
[104] A.C. McKinlay, R.E. Morris, P. Horcajada, G. Ferey, R. Gref, P. Couvreur, C. Serre, Angew. Chem.-Int. Edit., 49, 6260 (2010).
[105] P. Horcajada, C. Serre, G. Maurin, N.A. Ramsahye, F. Balas, M. Vallet-Regi, M. Sebban, F. Taulelle, G. Ferey, J Am Chem Soc, 130, 6774 (2008).
[106] P. Horcajada, C. Serre, M. Vallet-Regi, M. Sebban, F. Taulelle, G. Ferey, Angew. Chem.-Int. Edit., 45, 5974 (2006).
[107] C.Y. Sun, C. Qin, X.L. Wang, Z.M. Su, Expert Opin Drug Del, 10, 89 (2013).
[108] P. Horcajada, T. Chalati, C. Serre, B. Gillet, C. Sebrie, T. Baati, J.F. Eubank, D. Heurtaux, P. Clayette, C. Kreuz, J.S. Chang, Y.K. Hwang, V. Marsaud, P.N. Bories, L. Cynober, S. Gil, G. Ferey, P. Couvreur, R. Gref, Nat Mater, 9, 172 (2010).
[109] S.S. Kaye, A. Dailly, O.M. Yaghi, J.R. Long, J Am Chem Soc, 129, 14176 (2007).
[110] K.S. Park, Z. Ni, A.P. Cote, J.Y. Choi, R.D. Huang, F.J. Uribe-Romo, H.K. Chae, M. O'Keeffe, O.M. Yaghi, P Natl Acad Sci USA, 103, 10186 (2006).
[111] K. Koh, A.G. Wong-Foy, A.J. Matzger, J Am Chem Soc, 131, 4184 (2009).
[112] H.K. Chae, D.Y. Siberio-Perez, J. Kim, Y. Go, M. Eddaoudi, A.J. Matzger, M. O'Keeffe, O.M. Yaghi, Nature, 427, 523 (2004).
[113] H. Furukawa, M.A. Miller, O.M. Yaghi, J Mater Chem, 17, 3197 (2007).
[114] M. Latroche, S. Surble, C. Serre, C. Mellot-Draznieks, P.L. Llewellyn, J.H. Lee, J.S. Chang, S.H. Jhung, G. Ferey, Angew. Chem.-Int. Edit., 45, 8227 (2006).

[115] P.L. Llewellyn, S. Bourrelly, C. Serre, A. Vimont, M. Daturi, L. Hamon, G. De Weireld, J.S. Chang, D.Y. Hong, Y.K. Hwang, S.H. Jhung, G. Ferey, Langmuir, 24, 7245 (2008).
[116] G. Ferey, C. Mellot-Draznieks, C. Serre, F. Millange, J. Dutour, S. Surble, I. Margiolaki, Science, 309, 2040 (2005).
[117] X. Lin, J.H. Jia, X.B. Zhao, K.M. Thomas, A.J. Blake, G.S. Walker, N.R. Champness, P. Hubberstey, M. Schroder, Angew. Chem.-Int. Edit., 45, 7358 (2006).
[118] H. Furukawa, N. Ko, Y.B. Go, N. Aratani, S.B. Choi, E. Choi, A.O. Yazaydin, R.Q. Snurr, M. O'Keeffe, J. Kim, O.M. Yaghi, Science, 329, 424 (2010).
[119] O.K. Farha, A.O. Yazaydin, I. Eryazici, C.D. Malliakas, B.G. Hauser, M.G. Kanatzidis, S.T. Nguyen, R.Q. Snurr, J.T. Hupp, Nat Chem, 2, 944 (2010).
[120] M.M. Dubinin, E.D. Zaverina, L.V. Radushkevich, Zh Fiz Khim+, 21, 1351 (1947).
[121] F. Rouquerol, J. Rouquerol, K.S.W. Sing, Adsorption by powders and porous solids : principles, methodology, and applications, Academic Press, San Diego, 1999.
[122] H. Li, M. Eddaoudi, M. O'Keeffe, O.M. Yaghi, Nature, 402, 276 (1999).
[123] O.K. Farha, I. Eryazici, N.C. Jeong, B.G. Hauser, C.E. Wilmer, A.A. Sarjeant, R.Q. Snurr, S.T. Nguyen, A.Ö. Yazaydın, J.T. Hupp, J Am Chem Soc, 134, 15016 (2012).
[124] D.J. Collins, H.C. Zhou, J Mater Chem, 17, 3154 (2007).
[125] O.K. Farha, J.T. Hupp, Accounts Chem Res, 43, 1166 (2010).
[126] J.L.C. Rowsell, O.M. Yaghi, Angew. Chem.-Int. Edit., 44, 4670 (2005).
[127] L.J. Murray, M. Dinca, J.R. Long, Chem Soc Rev, 38, 1294 (2009).
[128] X.S. Wang, S.Q. Ma, P.M. Forster, D.Q. Yuan, J. Eckert, J.J. Lopez, B.J. Murphy, J.B. Parise, H.C. Zhou, Angew. Chem.-Int. Edit., 47, 7263 (2008).
[129] A.J. Fletcher, K.M. Thomas, M.J. Rosseinsky, J Solid State Chem, 178, 2491 (2005).
[130] X. Zhao, B. Xiao, A.J. Fletcher, K.M. Thomas, D. Bradshaw, M.J. Rosseinsky, Science, 306, 1012 (2004).
[131] H. Cheng, L. Chen, A.C. Cooper, X. Sha, G.P. Pez, Energ Environ Sci, 1, 338 (2008).
[132] Y. Li, R.T. Yang, J Am Chem Soc, 128, 726 (2005).
[133] Y. Li, R.T. Yang, J Am Chem Soc, 128, 8136 (2006).
[134] R. Campesi, F. Cuevas, M. Latroche, M. Hirscher, Phys Chem Chem Phys, 12, 10457 (2010).
[135] M. Hirscher, Micropor Mesopor Mat, 135, 209 (2010).
[136] S.M. Luzan, A.V. Talyzin, Micropor Mesopor Mat, 135, 201 (2010).
[137] N.P. Stadie, J.J. Purewal, C.C. Ahn, B. Fultz, Langmuir, 26, 15481 (2010).
[138] K.L. Mulfort, J.T. Hupp, J Am Chem Soc, 129, 9604 (2007).
[139] P. Dalach, H. Frost, R.Q. Snurr, D.E. Ellis, J Phys Chem C, 112, 9278 (2008).
[140] S. Yang, X. Lin, A.J. Blake, K.M. Thomas, P. Hubberstey, N.R. Champness, M. Schroder, Chem Commun, 0, 6108 (2008).
[141] U. Mueller, M. Schubert, F. Teich, H. Puetter, K. Schierle-Arndt, J. Pastre, J Mater Chem, 16, 626 (2006).
[142] A.U. Czaja, N. Trukhan, U. Muller, Chem Soc Rev, 38, 1284 (2009).
[143] H. Marsh, F. Rodríguez-Reinoso, Activated carbon, 1st ed., Elsevier, Amsterdam ; Boston, 2006.
[144] Y. Yurum, A. Taralp, T.N. Veziroglu, Int J Hydrogen Energ, 34, 3784 (2009).
[145] R. Strobel, J. Garche, P.T. Moseley, L. Jorissen, G. Wolf, J Power Sources, 159, 781 (2006).

[146] B. Weinberger, F.D. Lamari, Int J Hydrogen Energ, 34, 3058 (2009).
[147] T.P. McNicholas, A.M. Wang, K. O'Neill, R.J. Anderson, N.P. Stadie, A. Kleinhammes, P. Parilla, L. Simpson, C.C. Ahn, Y.Q. Wang, Y. Wu, J. Liu, J Phys Chem C, 114, 13902 (2010).
[148] H. Takagi, H. Hatori, Y. Soneda, N. Yoshizawa, Y. Yamada, Mat Sci Eng B-Solid, 108, 143 (2004).
[149] A.C. Dillon, K.M. Jones, T.A. Bekkedahl, C.H. Kiang, D.S. Bethune, M.J. Heben, Nature, 386, 377 (1997).
[150] V. Tozzini, V. Pellegrini, Phys Chem Chem Phys, 15, 80 (2013).
[151] J.W. Burress, S. Gadipelli, J. Ford, J.M. Simmons, W. Zhou, T. Yildirim, Angewandte Chemie International Edition, 49, 8902 (2010).
[152] H. Nishihara, T. Kyotani, Adv Mater, 24, 4473 (2012).
[153] R. Gadiou, S.E. Saadallah, T. Piquero, P. David, J. Parmentier, C. Vix-Guterl, Micropor Mesopor Mat, 79, 121 (2005).
[154] Z. Yang, Y. Xia, R. Mokaya, J Am Chem Soc, 129, 1673 (2007).
[155] V. Presser, M. Heon, Y. Gogotsi, Adv Funct Mater, 21, 810 (2011).
[156] Y. Gogotsi, S. Welz, D.A. Ersoy, M.J. McNallan, Nature, 411, 283 (2001).
[157] M. Sevilla, R. Foulston, R. Mokaya, Energ Environ Sci, 3, 223 (2010).
[158] M.G. Nijkamp, J.E.M.J. Raaymakers, A.J. van Dillen, K.P. de Jong, Appl Phys A, 72, 619 (2001).
[159] R. Dawson, A.I. Cooper, D.J. Adams, Progress in Polymer Science, 37, 530 (2012).
[160] N.B. McKeown, S. Makhseed, P.M. Budd, Chem Commun, 0, 2780 (2002).
[161] J.-H. Ahn, J.-E. Jang, C.-G. Oh, S.-K. Ihm, J. Cortez, D.C. Sherrington, Macromolecules, 39, 627 (2005).
[162] J.-X. Jiang, F. Su, A. Trewin, C.D. Wood, N.L. Campbell, H. Niu, C. Dickinson, A.Y. Ganin, M.J. Rosseinsky, Y.Z. Khimyak, A.I. Cooper, Angewandte Chemie International Edition, 46, 8574 (2007).
[163] T. Ben, H. Ren, S. Ma, D. Cao, J. Lan, X. Jing, W. Wang, J. Xu, F. Deng, J.M. Simmons, S. Qiu, G. Zhu, Angewandte Chemie International Edition, 48, 9457 (2009).
[164] N.B. McKeown, P.M. Budd, K.J. Msayib, B.S. Ghanem, H.J. Kingston, C.E. Tattershall, S. Makhseed, K.J. Reynolds, D. Fritsch, Chemistry – A European Journal, 11, 2610 (2005).
[165] B.S. Ghanem, K.J. Msayib, N.B. McKeown, K.D.M. Harris, Z. Pan, P.M. Budd, A. Butler, J. Selbie, D. Book, A. Walton, Chem Commun, 0, 67 (2007).
[166] J.-Y. Lee, C.D. Wood, D. Bradshaw, M.J. Rosseinsky, A.I. Cooper, Chem Commun, 0, 2670 (2006).
[167] Q. Chen, M. Luo, T. Wang, J.-X. Wang, D. Zhou, Y. Han, C.-S. Zhang, C.-G. Yan, B.-H. Han, Macromolecules, 44, 5573 (2011).
[168] T. Ben, C.Y. Pei, D.L. Zhang, J. Xu, F. Deng, X.F. Jing, S.L. Qiu, Energ Environ Sci, 4, 3991 (2011).
[169] D. Yuan, W. Lu, D. Zhao, H.-C. Zhou, Adv Mater, 23, 3723 (2011).
[170] A.P. Cote, A.I. Benin, N.W. Ockwig, M. O'Keeffe, A.J. Matzger, O.M. Yaghi, Science, 310, 1166 (2005).
[171] S.S. Han, H. Furukawa, O.M. Yaghi, W.A. Goddard, J Am Chem Soc, 130, 11580 (2008).
[172] H. Furukawa, O.M. Yaghi, J Am Chem Soc, 131, 8875 (2009).
[173] M.A. Richard, D. Cossement, P.A. Chandonia, R. Chahine, D. Mori, K. Hirose, Aiche J, 55, 2985 (2009).

[174] M.A. Richard, P. Benard, R. Chahine, Adsorption, 15, 53 (2009).
[175] M.A. Richard, P. Benard, R. Chahine, Adsorption, 15, 43 (2009).
[176] E. Poirier, R. Chahine, P. Benard, L. Lafi, G. Dorval-Douville, P.A. Chandonia, Langmuir, 22, 8784 (2006).
[177] P. Benard, R. Chahine, P.A. Chandonia, D. Cossement, G. Dorval-Douville, L. Lafi, P. Lachance, R. Paggiaro, E. Poirier, J Alloy Compd, 446, 380 (2007).
[178] P. Benard, R. Chahine, Langmuir, 17, 1950 (2001).
[179] P. Benard, R. Chahine, Int J Hydrogen Energ, 26, 849 (2001).
[180] P. Benard, R. Chahine, Langmuir, 13, 808 (1997).
[181] A. Dailly, E. Poirier, Energ Environ Sci, 4, 3527 (2011).
[182] E. Poirier, R. Chahine, T.K. Bose, Int J Hydrogen Energ, 26, 831 (2001).
[183] E. Poirier, A. Dailly, The Journal of Physical Chemistry C, 112, 13047 (2008).
[184] E. Poirier, A. Dailly, Langmuir, 25, 12169 (2009).
[185] E. Poirier, A. Dailly, Nanotechnology, 20, (2009).
[186] E. Poirier, A. Dailly, Energ Environ Sci, 2, 420 (2009).
[187] E. Poirier, A. Dailly, Phys Chem Chem Phys, 14, 16544 (2012).
[188] K.M. Thomas, Dalton Transactions, 0, 1487 (2009).
[189] S. Tedds, A. Walton, D.P. Broom, D. Book, Faraday Discuss, 151, 75 (2011).
[190] J. Purewal, D.G. Liu, A. Sudik, M. Veenstra, J. Yang, S. Maurer, U. Muller, D.J. Siegel, J Phys Chem C, 116, 20199 (2012).
[191] D. Saha, R. Zacharia, L. Lafi, D. Cossement, R. Chahine, Int J Hydrogen Energ, 37, 5100 (2012).
[192] R. Zacharia, D. Cossement, L. Lafi, R. Chahine, J Mater Chem, 20, 2145 (2010).
[193] D. Saha, R. Zacharia, L. Lafi, D. Cossement, R. Chahine, Chem Eng J, 171, 517 (2011).
[194] E. Dundar, R. Zacharia, R. Chahine, P. Benard, Int J Hydrogen Energ, 37, 9137 (2012).
[195] J.S. Xiao, J.J. Wang, D. Cossement, P. Benard, R. Chahine, Int J Hydrogen Energ, 37, 802 (2012).
[196] J.S. Xiao, M. Hu, D. Cossement, P. Benard, R. Chahine, Int J Hydrogen Energ, 37, 12947 (2012).
[197] J.S. Xiao, Y. Liu, J.J. Wang, P. Benard, R. Chahine, Int J Heat Mass Tran, 55, 6864 (2012).
[198] F. Ye, J.S. Xiao, B.X. Hu, P. Benard, R. Chahine, Physcs Proc, 24, 793 (2012).
[199] B. Hardy, C. Corgnale, R. Chahine, M.A. Richard, S. Garrison, D. Tamburello, D. Cossement, D. Anton, Int J Hydrogen Energ, 37, 5691 (2012).
[200] J.S. Xiao, L.A. Tong, C.H. Deng, P. Benard, R. Chahine, Int J Hydrogen Energ, 35, 8106 (2010).
[201] K.A.G. Amankwah, J.A. Schwarz, Carbon, 33, 1313 (1995).
[202] British Standards Institution, in, BSI, London, 1996.
[203] A. Hruzewicz-Kolodziejczyk, V.P. Ting, N. Bimbo, T.J. Mays, Int J Hydrogen Energ, 37, 2728 (2012).
[204] X. Lin, I. Telepeni, A.J. Blake, A. Dailly, C.M. Brown, J.M. Simmons, M. Zoppi, G.S. Walker, K.M. Thomas, T.J. Mays, P. Hubberstey, N.R. Champness, M. Schröder, J Am Chem Soc, 131, 2159 (2009).
[205] L.F. Wang, R.T. Yang, Carbon, 50, 3134 (2012).
[206] L. Zhou, Y.P. Zhou, Y. Sun, Int J Hydrogen Energ, 29, 319 (2004).
[207] L. Gurvich, J Phys Chem Soc RUss, 47, 805 (1915).
[208] B. Streppel, M. Hirscher, Phys Chem Chem Phys, 13, 3220 (2011).

[209] N. Quirke, S.R.R. Tennison, Carbon, 34, 1281 (1996).
[210] S. Sircar, Ind Eng Chem Res, 38, 3670 (1999).
[211] J.W. Gibbs, The Collected Works of J. Willard Gibbs, Longmans & Co., New York, 1928.
[212] D.D. Do, H.D. Do, J Colloid Interf Sci, 316, 317 (2007).
[213] D.D. Do, H.D. Do, D. Nicholson, J Phys Chem B, 113, 1030 (2009).
[214] P. Malbrunot, D. Vidal, J. Vermesse, R. Chahine, T.K. Bose, Langmuir, 13, 539 (1997).
[215] S. Sircar, Aiche J, 47, 1169 (2001).
[216] N. Bimbo, V.P. Ting, A. Hruzewicz-Kolodziejczyk, T.J. Mays, Faraday Discuss, 151, 59 (2011).
[217] B.A. Younglove, J Phys Chem Ref Data, 11, 1 (1982).
[218] E.W.L.M.L.H. M.O.McLinden, in, National Institute of Standards and Technology, pp. NIST Standard Reference Database 23: Reference Fluid Thermodynamic and Transport Properties.
[219] A.L. Myers, P.A. Monson, Langmuir, 18, 10261 (2002).
[220] I. Langmuir, J Am Chem Soc, 40, 1361 (1918).
[221] R. Sips, J Chem Phys, 16, 490 (1948).
[222] J. Toth, Acta Chimica Academiae Scientarium Hungaricae, 31, (1962).
[223] J. Toth, Acta Chimica Academiae Scientarium Hungaricae, 30, (1962).
[224] J. Toth, Acta Chimica Academiae Scientarium Hungaricae, 32, (1962).
[225] J. Toth, Acta Chimica Academiae Scientarium Hungaricae, 33, (1962).
[226] J. Toth, Acta Chimica Academiae Scientarium Hungaricae, 38, (1963).
[227] J. Toth, Acta Chimica Academiae Scientarium Hungaricae, 39, (1963).
[228] J. Toth, Acta Chimica Academiae Scientarium Hungaricae, 69, (1971).
[229] J.M. Honig, L.H. Reyerson, J Phys Chem-Us, 56, 140 (1952).
[230] I. Quinones, G. Guiochon, J Colloid Interf Sci, 183, 57 (1996).
[231] M.M. Dubinin, V.A. Astakhov, Russ Chem B+, 20, 8 (1971).
[232] E. Poirier, A. Dailly, J Phys Chem C, 112, 13047 (2008).
[233] E. Poirier, A. Dailly, Langmuir, 25, 12169 (2009).
[234] D.D. Do, Adsorption analysis : equilibria and kinetics, Imperial College Press, London, 1998.
[235] K. Levenberg, Quarterly Applied Mathematics, 2, 164 (1944).
[236] D.W. Marquardt, Journal of the Society for Industrial and Applied Mathematics, 11, 431 (1963).
[237] *Nobel Prize in Physics 1994*. Available from: http://www.nobelprize.org/nobel_prizes/physics/laureates/1994.
[238] J. Toth, Adv Colloid Interfac, 55, 1 (1995).
[239] I. Quinones, G. Guiochon, J Chromatogr A, 796, 15 (1998).
[240] M.M. Dubinin, Chem Rev, 60, 235 (1960).
[241] P.L. Llewellyn, G. Maurin, T. Devic, S. Loera-Serna, N. Rosenbach, C. Serre, S. Bourrelly, P. Horcajada, Y. Filinchuk, G. Ferey, J Am Chem Soc, 130, 12808 (2008).
[242] X.B. Zhao, B. Xiao, A.J. Fletcher, K.M. Thomas, J Phys Chem B, 109, 8880 (2005).
[243] N. Bimbo, V.P. Ting, J.E. Sharpe, T.J. Mays, Colloid Surface A (in press), (2012).
[244] J. Sharpe, N. Bimbo, V. Ting, A. Burrows, D. Jiang, T. Mays, Adsorption, 19, 643 (2013).

[245] S.M. Aceves, G.D. Berry, J. Martinez-Frias, F. Espinosa-Loza, Int J Hydrogen Energ, 31, 2274 (2006).
[246] S.M. Aceves, G.D. Berry, J Energ Resour-Asme, 120, 137 (1998).
[247] S.M. Aceves, F. Espinosa-Loza, E. Ledesma-Orozco, T.O. Ross, A.H. Weisberg, T.C. Brunner, O. Kircher, Int J Hydrogen Energ, 35, 1219 (2010).
[248] S.M. Aceves, J. Martinez-Frias, O. Garcia-Villazana, Int J Hydrogen Energ, 25, 1075 (2000).
[249] NIST, NIST Chemistry WebBook, (2012).http://webbook.nist.gov/chemistry/. 08 November 2012
[250] H.L. Johnston, W.E. Keller, A.S. Friedman, J Am Chem Soc, 76, 1482 (1954).
[251] I.F. Silvera, Rev Mod Phys, 52, 393 (1980).
[252] S. Sircar, R. Mohr, C. Ristic, M.B. Rao, The Journal of Physical Chemistry B, 103, 6539 (1999).
[253] *Nobel Prize in Physics 1944*. Available from: http://www.nobelprize.org/nobel_prizes/physics/laureates/1944.
[254] *Nobel Prize in Physics 1952*. Available from: http://www.nobelprize.org/nobel_prizes/physics/laureates/1952/.
[255] J. McMurry, Organic chemistry, 3rd ed. ed., Brooks/Cole Pub ; [London] : [Chapman & Hall], Pacific Grove, Calif., 1992.
[256] J. Clayden, Organic chemistry, Oxford University Press, Oxford, 2001.
[257] J.M. Berg, J.L. Tymoczko, L. Stryer, Biochemistry, 5th ed. / Jeremy Berg, John Tymoczko, Lubert Stryer / web content by Neil D. Clarke. ed., W. H. Freeman and Co. ; [Basingstoke : Palgrave] [distributor], 2001, New York, 2002.
[258] P.W. Atkins, J. De Paula, Atkins' physical chemistry, 8th ed. ed., Oxford University Press, Oxford ; New York, 2006.
[259] J. Keeler, Understanding NMR spectroscopy, Wiley, Chichester, England ; Hoboken, NJ, 2005.
[260] S.G. Allen, P.C.L. Stephenson, J.H. Strange, J Chem Phys, 106, 7802 (1997).
[261] F. Furtado, P. Galvosas, M. Goncalves, F.D. Kopinke, S. Naumov, F. Rodriguez-Reinoso, U. Roland, R. Valiullin, J. Karger, Micropor Mesopor Mat, 141, 184 (2011).
[262] V.M. Gun'ko, V.V. Turov, Langmuir, 15, 6405 (1999).
[263] J. Karger, J. Caro, P. Cool, M.O. Coppens, D. Jones, F. Kapteijn, F. Rodriguez-Reinoso, M. Stocker, D. Theodorou, E.F. Vansant, J. Weitkamp, Chem Eng Technol, 32, 1494 (2009).
[264] M. Krutyeva, F. Grinberg, F. Furtado, P. Galvosas, J. Karger, A. Silvestre-Albero, A. Sepulveda-Escribano, J. Silvestre-Alberto, F. Rodriguez-Reinoso, Micropor Mesopor Mat, 120, 91 (2009).
[265] X. Liu, X.L. Pan, W.L. Shen, P.J. Ren, X.W. Han, X.H. Bao, J Phys Chem C, 116, 7803 (2012).
[266] V.V. Turov, R. Leboda, ^{1}NMR Spectroscopy of Adsorbed Molecules and Free Surface Energy of Carbon Adsorbents, Taylor & Francis, New York, 2001.
[267] K. Shen, T. Pietrass, J Phys Chem B, 108, 9937 (2004).
[268] R.J. Anderson, T.P. McNicholas, A. Kleinhammes, A.M. Wang, J. Liu, Y. Wu, J Am Chem Soc, 132, 8618 (2010).
[269] A. Kleinhammes, R.J. Anderson, Q.A. Chen, Y. Jeong, T.C.M. Chung, Y. Wu, J Phys Chem C, 114, 13705 (2010).
[270] B. Panella, M. Hirscher, S. Roth, Carbon, 43, 2209 (2005).
[271] E. Rutherford, Proceedings of the Royal Society of London. Series A, 97, 374 (1920).

[272] J. Chadwick, Nature, 129, 312 (1947).
[273] G.L. Squires, Introduction to the theory of thermal neutron scattering, Cambridge University Press, Cambridge, 1978.
[274] R. Hempelmann, Quasielastic neutron scattering and solid state diffusion, Clarendon Press, Oxford, 2000.
[275] C.G. Windsor, Pulsed neutron scattering, Taylor & Francis, London, 1981.
[276] G.E. Bacon, Neutron diffraction, 3d ed., Clarendon Press, Oxford Eng., 1975.
[277] S.F. Parker, D. Lennon, P.W. Albers, Appl Spectrosc, 65, 1325 (2011).
[278] A.J. Ramirez-Cuesta, M.O. Jones, W.I.F. David, Mater Today, 12, 54 (2009).
[279] A. Albinati, D. Colognesi, P.A. Georgiev, C.M. Jensen, A.J. Ramirez-Cuesta, J Alloy Compd, 523, 108 (2012).
[280] Q.J. Fu, A.J. Ramirez-Cuesta, S.C. Tsang, J Phys Chem B, 110, 711 (2006).
[281] H.G. Schimmel, M.R. Johnson, G.J. Kearley, A.J. Ramirez-Cuesta, J. Huot, F.M. Mulder, J Alloy Compd, 393, 1 (2005).
[282] J.D.F. Ramsay, Adv Colloid Interfac, 76, 13 (1998).
[283] R.K. Thomas, Prog Solid State Ch, 14, 1 (1982).
[284] Y. Liu, H. Kabbour, C.M. Brown, D.A. Neumann, C.C. Ahn, Langmuir, 24, 4772 (2008).
[285] W.L. Queen, E.D. Bloch, C.M. Brown, M.R. Hudson, J.A. Mason, L.J. Murray, A.J. Ramirez-Cuesta, V.K. Peterson, J.R. Long, Dalton Transactions, 41, 4180 (2012).
[286] N.L. Rosi, J. Eckert, M. Eddaoudi, D.T. Vodak, J. Kim, M. O'Keeffe, O.M. Yaghi, Science, 300, 1127 (2003).
[287] J.L.C. Rowsell, J. Eckert, O.M. Yaghi, J Am Chem Soc, 127, 14904 (2005).
[288] D.J. Tranchemontagne, K.S. Park, H. Furukawa, J. Eckert, C.B. Knobler, O.M. Yaghi, The Journal of Physical Chemistry C, 116, 13143 (2012).
[289] P.C.H. Mitchell, A.J. Ramirez-Cuesta, S.F. Parker, J. Tomkinson, D. Thompsett, The Journal of Physical Chemistry B, 107, 6838 (2003).
[290] P.C.H. Mitchell, Vibrational spectroscopy with neutrons : with applications in chemistry, biology, materials science and catalysis, World Scientific, Hackensack, NJ, 2005.
[291] J.A. Young, J.U. Koppel, Phys Rev, 135, A603 (1964).
[292] M. Celli, D. Colognesi, M. Zoppi, Phys Rev E, 66, 021202 (2002).
[293] J. Luo, H. Xu, Y. Liu, Y. Zhao, L.L. Daemen, C. Brown, T.V. Timofeeva, S. Ma, H.-C. Zhou, J Am Chem Soc, 130, 9626 (2008).
[294] T. Yildirim, M.R. Hartman, Phys Rev Lett, 95, 215504 (2005).
[295] A.J. Ramirez-Cuesta, P.C.H. Mitchell, Catal Today, 120, 368 (2007).
[296] N.C. Gallego, L. He, D. Saha, C.I. Contescu, Y.B. Melnichenko, J Am Chem Soc, 133, 13794 (2011).
[297] J. Jagiello, A. Ansón, M.T. Martínez, The Journal of Physical Chemistry B, 110, 4531 (2006).
[298] Q. Wang, J.K. Johnson, The Journal of Chemical Physics, 110, 577 (1999).
[299] D. Frenkel, B. Smit, Understanding molecular simulation : from algorithms to applications, 2nd ed., Academic Press, San Diego, 2002.
[300] D.A. McQuarrie, Statistical mechanics, Harper & Row, New York, 1975.
[301] M.E.J. Newman, G.T. Barkema, Monte Carlo methods in statistical physics, Clarendon Press ; Oxford University Press, Oxford, New York, 1999.
[302] N. Metropolis, S. Ulam, Journal of the American Statistical Association, 44, 335 (1949).
[303] F. Darkrim, J. Vermesse, P. Malbrunot, D. Levesque, J Chem Phys, 110, 4020 (1999).

[304] D.D. Do, H.D. Do, Adsorpt Sci Technol, 21, 389 (2003).
[305] T. Duren, Y.S. Bae, R.Q. Snurr, Chem Soc Rev, 38, 1237 (2009).
[306] R.B. Getman, Y.S. Bae, C.E. Wilmer, R.Q. Snurr, Chem Rev, 112, 703 (2012).
[307] A. Rossin, D. Fairen-Jimenez, T. Duren, G. Giambastiani, M. Peruzzini, J.G. Vitillo, Langmuir, 27, 10124 (2011).
[308] L.L. Wang, L. Wang, J.J. Zhao, T.Y. Yan, J Appl Phys, 111, (2012).
[309] J.E. Jones, Proceedings of the Royal Society of London. Series A, 106, 463 (1924).
[310] A.K. Rappe, C.J. Casewit, K.S. Colwell, W.A. Goddard, W.M. Skiff, J Am Chem Soc, 114, 10024 (1992).
[311] S.L. Mayo, B.D. Olafson, W.A. Goddard, The Journal of Physical Chemistry, 94, 8897 (1990).
[312] A.V.A. Kumar, H. Jobic, S.K. Bhatia, Adsorption, 13, 501 (2007).
[313] R.P. Feynman, A.R. Hibbs, Quantum mechanics and path integrals, McGraw-Hill, New York,, 1965.
[314] M.B. Sweatman, Phys Rev E, 77, (2008).
[315] L.M. Sese, J Chem Phys, 108, 9086 (1998).
[316] H. Tanaka, D. Noguchi, A. Yuzawa, T. Kodaira, H. Kanoh, K. Kaneko, J Low Temp Phys, 157, 352 (2009).
[317] H. Tanaka, H. Kanoh, M. Yudasaka, S. Lijima, K. Kaneko, J Am Chem Soc, 127, 7511 (2005).
[318] A.V.A. Kumar, S.K. Bhatia, Phys Rev Lett, 95, (2005).
[319] G. Garberoglio, A.I. Skoulidas, J.K. Johnson, J Phys Chem B, 109, 13094 (2005).
[320] E.M. Flanigen, J.M. Bennett, R.W. Grose, J.P. Cohen, R.L. Patton, R.M. Kirchner, J.V. Smith, Nature, 271, 512 (1978).
[321] V.V. Guliants, A.J. Huth, J.M. Stueve, J Porous Mat, 20, 235 (2013).
[322] A. Gupta, S. Chempath, M.J. Sanborn, L.A. Clark, R.Q. Snurr, Mol Simulat, 29, 29 (2003).
[323] H. Frost, R.Q. Snurr, J Phys Chem C, 111, 18794 (2007).
[324] H. Frost, T. Duren, R.Q. Snurr, J Phys Chem B, 110, 9565 (2006).
[325] Y.S. Bae, R.Q. Snurr, Micropor Mesopor Mat, 135, 178 (2010).
[326] Y.S. Bae, R.Q. Snurr, Micropor Mesopor Mat, 132, 300 (2010).
[327] F. Darkrim, D. Levesque, J Chem Phys, 109, 4981 (1998).
[328] D. Peng, D.B. Robinson, Ind Eng Chem Fund, 15, 59 (1976).
[329] S.H. Jhung, J.W. Yoon, J.S. Lee, J.-S. Chang, Chemistry – A European Journal, 13, 6502 (2007).
[330] A. Zecchina, S. Bordiga, J.G. Vitillo, G. Ricchiardi, C. Lamberti, G. Spoto, M. Bjørgen, K.P. Lillerud, J Am Chem Soc, 127, 6361 (2005).
[331] L. Zhao, D. Zhai, B. Liu, Z.C. Liu, C.M. Xu, W. Wei, Y. Chen, J.S. Gao, Chem Eng Sci, 68, 101 (2012).
[332] H. Tanaka, J. Fan, H. Kanoh, M. Yudasaka, S. Iijima, K. Kaneko, Mol Simulat, 31, 465 (2005).
[333] A.V.A. Kumar, S.K. Bhatia, Phys Rev Lett, 96, (2006).
[334] T. Duren, F. Millange, G. Ferey, K.S. Walton, R.Q. Snurr, J Phys Chem C, 111, 15350 (2007).
[335] T. Duren. Available from: http://www.see.ed.ac.uk/~tduren/research/surface_area/.
[336] V.V. Turov, V.M. Gun'ko, K.N. Khomenko, A.Y. Petin, A.V. Turov, P.P. Gorbik, Russ J Phys Chem a+, 84, 70 (2010).

[337] T. Karbowiak, M.A. Saada, S. Rigolet, A. Ballandras, G. Weber, I. Bezverkhyy, M. Soulard, J. Patarin, J.P. Bellat, Phys Chem Chem Phys, 12, 11454 (2010).
[338] D.S. Tomar, M. Singla, S. Gumma, Micropor Mesopor Mat, 142, 116 (2011).

In the accompanying DVD

Additional Information (in electronic format)

- Additional Information A

Additional Background – Energy storage and uses of hydrogen

- Additional Information B

The Levenberg-Marquardt algorithm

- Additional Information C

The van't Hoff relation

- Additional Information D

Filling factor

- Additional Information E

NMR experimental setup, analysis and deconvolution

- Additional Information F

INS spectra at 4 and 100 K and 0.016 MPa

- Additional Information G

Technical specification sheet for silicalite-1

PhD Thesis in electronic format

Figures

References